CRYSTAL QUALITY ENHANCEMENT OF SEMI-POLAR (11-22) InGaN/GaN-BASED LED GROWN ON M-PLANE SAPPHIRE SUBSTRATE VIA MOCVD

OMAR AYAD FADHIL

FACULTY OF SCIENCE
UNIVERSITY OF MALAYA
KUALA LUMPUR

2019

CRYSTAL QUALITY ENHANCEMENT OF SEMI-POLAR (11-22) InGaN/GaN-BASED LED GROWN ON M-PLANE SAPPHIRE SUBSTRATE VIA MOCVD

OMAR AYAD FADHIL

THESIS SUBMITTED IN FULFILMENT OF THE REQUIREMENTS FOR THE DEGREE OF DOCTOR OF PHILOSOPHY

DEPARTMENT OF PHYSICS
FACULTY OF SCIENCE
UNIVERSITY OF MALAYA
KUALA LUMPUR

2019

UNIVERSITY OF MALAYA
ORIGINAL LITERARY WORK DECLARATION

Name of Candidate: **OMAR AYAD FADHIL**

Matric No: **SHC140066**

Name of Degree: **DOCTOR OF PHYLOSOPHY**

Title of Thesis ("this Work"):

CRYSTAL QUALITY ENHANCEMENT OF SEMI-POLAR (11-22) InGaN/GaN-BASED LED GROWN ON M-PLANE SAPPHIRE SUBSTRATE VIA MOCVD

Field of Study:

EXPERIMENTAL PHYSICS

I do solemnly and sincerely declare that:

(1) I am the sole author/writer of this Work;
(2) This Work is original;
(3) Any use of any work in which copyright exists was done by way of fair dealing and for permitted purposes and any excerpt or extract from, or reference to or reproduction of any copyright work has been disclosed expressly and sufficiently and the title of the Work and its authorship have been acknowledged in this Work;
(4) I do not have any actual knowledge nor do I ought reasonably to know that the making of this work constitutes an infringement of any copyright work;
(5) I hereby assign all and every rights in the copyright to this Work to the University of Malaya ("UM"), who henceforth shall be owner of the copyright in this Work and that any reproduction or use in any form or by any means whatsoever is prohibited without the written consent of UM having been first had and obtained;
(6) I am fully aware that if in the course of making this Work I have infringed any copyright whether intentionally or otherwise, I may be subject to legal action or any other action as may be determined by UM.

Candidate's Signature Date:

Subscribed and solemnly declared before,

Witness's Signature Date:

Name:

Designation:

CRYSTAL QUALITY ENHANCEMENT OF SEMI-POLAR (11-22) InGaN/GaN-BASED LED GROWN ON M-PLANE SAPPHIRE SUBSTRATE VIA MOCVD

ABSTRACT

Gallium nitride (GaN) thin films grown along c-plane (polar) direction are extensively employed for III-nitride based LEDs. However, the wurtzite crystal structure of LEDs grown along c-plane direction suffers from the spontaneous and piezoelectric field, resulting in quantum-confined stark effect (QCSE), which impairs the device efficiency towards longer wavelengths. The growth of semi-polar (11-22) epitaxial layer have attracted substantial interest as it circumvents this issue. In this study, the Taiyo Nippon Sanso SR-2000 horizontal metal-organic chemical vapor deposition (MOCVD) was employed to assist the semi-polar (11-22) growth on m-plane sapphire substrate. Two main phases were employed, namely the growth of semi-polar (11-22) unintentionally doped-gallium nitride (uid-GaN) and the LED structure. The former phase consists of nitridation process, aluminum nitride (AlN) nucleation layer, AlN/GaN multi-layer (ML), and the uid-GaN. The ammonia (NH_3) flux for the growth of uid-GaN was varied from 0.7 to 8.3 standard liter per minute (slm). The NH_3 flux of the AlN growth was varied from 1-2.3 slm to investigate its influence towards the crystal quality of the uid-GaN. The AlN/GaN ML was varied from 20-60 to observe the enhancement of the crystal quality and the surface morphology of the semi-polar (11-22) uid-GaN. The second phase of this work was the LED structure, including of the n-type GaN, the InGaN/GaN multi-quantum wells (MQW) and the p-type GaN. The disilane (Si_2H_6) flow rate for the growth of n-type semi-polar (11-22) GaN epitaxial layers was varied from 10 to 20 standard cubic centimeter per minute (sccm). The bicyclopentadienyl magnesium (Cp_2Mg) flow rate for the growth of p-type GaN was varied from 20 to 40 sccm to measure hole mobility and concentrations. Lastly, the trimethylindium (TMI) flow rate was varied at yield triethylgallium, TEG:TMI ratio of 1:1, 1:2 and 1:3 for the growth of InGaN/GaN active region. The compressive stress/strain state of the as-grown uid-GaN was examined by Raman spectroscopy at room temperature. The crystal quality of the epitaxial layers was characterized by high resolution X-ray diffraction (HR-XRD), including phase analysis (PA), on- and off-axis x-ray rocking curve (XRC) and reciprocal space mapping (RSM), and transmission electron microscopy (TEM). The surface morphology analysis was investigated by atomic force microscopy (AFM) and field emission scanning electron microscopy (FESEM). The optical and the electrical properties were analyzed by room temperature photoluminescence spectroscopy (PL), Hall effect and electroluminescence spectrum (EL) analysis. The full-width at half-maximum (FWHM) of semi-polar (11-22) InGaN/GaN LED with the use of AlN/GaN ML template was found to be as low as 0.11° and 0.30° along [-1-123] and [1-100], respectively. The values of root mean square (RMS) surface roughness and the peak-to-valley were obtained as low as 6.30 and 40.24 nm, respectively. Consequently, the semi-polar (11-22) InGaN/GaN LED grown on the AlN/GaN template exhibited superior indium incorporation with enhanced PL and EL emission against its counterparts.

Keywords: Gallium nitride, m-plane sapphire substrate, MOCVD, AlN/GaN multi-layer, semi-polar.

PENINGKATAN KUALITI KRISTAL SEMI-POLAR (11-22) LED BERASASKAN InGaN/GaN PADA SATAH-M SUBSTRAT MELALUI MOCVD

ABSTRAK

Filem nipis Gallium nitride (GaN) yang dihasilkan di sepanjang arah satah-c (polar) telah digunakan secara meluas untuk LED yang berasaskan unsur III-nitride. Walau bagaimanapun, struktur kristal wurtzite LED yang tumbuh di sepanjang arah satah-c mengalami kelemahan dari medan spontan dan piezoelektrik, yang menyebabkan terhasilnya kesan terkurung kuantum (QCSE), di mana ianya menjejaskan kecekapan peranti pada gelombang yang lebih panjang. Pertumbuhan lapisan epitaxy separuh kutub (11-22) telah menarik minat yang ketara kerana ia dapat menyelesaikan isu yang dinyatakan. Dalam kajian ini, pemendapan wap kimia logam-organik - Taiyo Nippon Sanso SR-2000 (MOCVD) digunakan untuk membantu pertumbuhan separuh kutub (11-22) pada substrat satah-m nilam. Dua fasa utama digunakan, iaitu pertumbuhan separuh kutub (11-22) suntikan secara tidak sengaja-gallium nitride (uid-GaN) dan struktur LED. Fasa pertama terdiri daripada proses nitridasi, lapisan nukleasi aluminium nitride (AlN), AlN / GaN lapisan bertingkat (ML), dan uid-GaN. Fluks ammonia (NH_3) untuk pertumbuhan uid-GaN diubah dari 0.7 hingga 8.3 standard liter per minit (slm). Fluks NH_3 digunakan untuk pertumbuhan AlN diubah dari 1-2.3 slm untuk menyiasat kesannya terhadap kualiti kristal uid-GaN. Lapisan bertingkat AlN/GaN juga divariasi dari 20-60 untuk melihat peningkatan kualiti kristal dan morfologi permukaan separuh kutub (11-22) uid-GaN. Fasa kedua pula bermula dari pengstrukturan LED, termasuk GaN jenis n- ,lapisan kuantum berbilang InGaN/GaN (MQW) dan GaN jenis p-. Kadar pengaliran disilane (Si_2H_6) bagi lapisan epitaxy pertumbuhan separuh kutub (11-22) GaN jenis n- diubah dari 10 hingga 20 sentimeter padu per minit (sccm). Kadar aliran bicyclopentadienyl magnesium (Cp_2Mg) untuk pertumbuhan p-GaN diubah dari 20-40 sccm untuk mengukur konsentrasi pembawa serta mobiliti lubang. Akhir sekali, kadar aliran trimethylindium (TMI) diubah untuk mendapatkan nisbah triethylgallium TEG: TMI kepada 1:1, 1:2, dan 1:3 bagi pertumbuhan InGaN/GaN ruang aktif. Taraf tekanan/ketegangan mampat uid-GaN yang telah diteliti dan diperiksa menggunakan spektroskopi Raman pada suhu bilik. Kualiti kristal lapisan epitaxi dicirikan oleh difraksi sinar-X resolusi tinggi (HR-XRD), termasuk analisis fasa (PA), dan keluk ayunan x-ray (XRC) on- dan off-axis dengan pemetaan ruang timbal balik (RSM), dan mikroskop transmisi elektron (TEM). Analisis morfologi permukaan telah diselidik dengan menggunakan mikroskopi daya atom (AFM) dan mikroskop elektron imbas (FESEM). Sifat optik dan elektrik dianalisis dengan suhu bilik fotoluminesen spektroskopi (PL), pengesanan Hall, dan elektroluminesen spektra (EL) analisis. Lebar-penuh pada separuh maksimum (FWHM) bagi separuh kutub (11-22) InGaN/GaN LED yang ditumbuh dengan menggunakan AlN/GaN ML templat ditemui pada kadar terendah iaitu 0.11° dan 0.30° sepanjang [-1-123] dan [1-100]. Kekasaran permukaan dan puncak ke lembah pula ditemui serendah 6.08 dan 40.24 nm. Akibatnya, separuh kutub (11-22) InGaN/GaN LED yang ditumbuh diatas AlN/GaN templat mempamerkan kadar indium inkorporasi yang unggul dengan menunjukkan PL dan EL yang lebih baik berbanding dengan sebaliknya.

Kata Kunci: Gallium nitride, substrat satah-m nilam, MOCVD, AlN/GaN lapisan-pelbagai, satah kutub.

ACKNOWLEDGEMENTS

In the name of God Allah, the most beneficent and the most merciful. First and foremost, all praise is due to God Allah Almighty *subhanahu wa-ta'ala,* on whom we ultimately depend, for his endless blessing and allowing me to achieve what I have achieved today.

I would like to take this opportunity to express my gratitude to my supervisor Dr. Ahmad Shuhaimi Abu Bakar for giving me the opportunity, confidence and guidance during my doctorate candidature. I would like to further extend my deepest thankfulness and appreciation to my supervisor Dr. Azzuliani Supangat for being a great advisor, motivator as well as teacher throughout the period it took to complete this thesis. I owe incredible gratitude to Dr. Azzuliani as she has been tremendously patient and supportive in all situations we have gone through.

I would sincerely love to take this opportunity to express my endless love and appreciation for my lovely wife Sally Abdulateef Jameel Al-Sammarrraie for her unconditional love, support and patience during the period of my study, by which without her I would not be what I am today. Here existence is the best thing happened in my life.

Above all, I would love to deeply express my special gratitude to my family, especially my beloved parents, Ayad Fadhil and Iman Sofi for their unconditional love, encouragements, guidance and support. I would also love to offer my regards and blessings to all my siblings for their unconditional support in all aspects during my life.

Special thanks and gratefulness go to my special friend and brother Abdullah Haaziq Ahmad Makinudin for his never-ending support during the whole study of my doctorate degree. His advice, encouragement and patience were endless and I really owe him

remarkable gratitude. He has been with me through thick and thin, and I really have seen "A friend in need is a friend indeed" in him. As we always say "Let us enjoy the journey".

I like to express my hearty gratitude and appreciations to Adreen and Anas, who stood by through thick and thin.

Special thanks go to go the members in the LDMRC Lab, Afiq, Mazwan, Yus, Sobry, Hilmi, Nazry, Aliff, Ameera, Najwa, Najiha, Dayana and Ismaliza.

Last but not least, I would like to acknowledge University of Malaya for Postgraduate Research Grant (PG267-2015B) and UMRG: RP039B-18AFR, CREST Gallium Nitride on Gallium Nitride Collaboration and the Ministry of Education (MOE) for the Long-Term Research Grant (LRGS) with account/project No: LR001A-2016A.

TABLE OF CONTENTS

LIST OF FIGURES

LIST OF TABLES

LIST OF SYMBOLS AND ABBREVIATIONS

q : Carrier charge

n : Charge density

σ : Conductivity

J : Current density

v : Drift velocity

R_H : Hall coefficient

V_H : Hall voltage

μ : Mobility

P^{pz} : Piezoelectric polarization

P^{sp} : Spontaneous polarization

P_{L}^{SP} : Spontaneous polarizations for the layer

P_{LT}^{SP} : The spontaneous polarizations for the template

d : Thickness

ΔP : Total polarization

AlN : Aluminum nitride

ALD : Atomic layer deposition

APCVD : Atmospheric pressure chemical vapor deposition

BF : Bright field

$\mathrm{Cp_2Mg}$: Bicyclopentadienemagnesium

CVD : Chemical vapor deposition

ELOG : Epitaxial lateral overgrowth

GaN : Gallium nitride

HEMT : High electron mobility transistors

InN : Indium Nitride

LCDs	:	Liquid crystal displays
LD	:	Laser diode
LED	:	Light emitting diode
LPCVD	:	Low pressure chemical vapor deposition
MBE	:	Molecular beam epitaxy
Mg	:	Magnesium
MOCVD	:	Metal organic chemical vapor deposition
MOSFET	:	Metal oxide semiconductors field effect transistor
MQW	:	Multi quantum well
PECVD	:	Plasma enhanced chemical vapor deposition
PSF	:	Prismatic stacking fault
QCSE	:	Quantum-confined stark effect
RLP	:	Reciprocal lattice point
RSM	:	Reciprocal space mapping
Si_2H_6	:	Disilane
TEG	:	Triethylgallium
TEM	:	Transmission electron microscopy
TMA	:	Trimethylaluminum
TMG	:	Trimethylgallium
TMI	:	Trimethylindium
UHCVD	:	Ultra-high vacuum chemical vapor deposition
XRC	:	X-ray rocking curve
WZ	:	Wurtzite
ZB	:	Zinc blend

CHAPTER 1: INTRODUCTION

1.1 Historical Introduction to III-V Semiconductors

III-V group semiconductors such as gallium nitride (GaN), aluminum nitride (AlN) and indium nitride (InN) and their alloys currently are the choice for high power electronics and ultraviolet/visible light emitters. This is attributed to the promising thermal and chemical properties as well as direct band gap. The direct band gaps for these materials range from 0.64 eV (InN) to 3.4 eV (GaN), and to 6.2 eV (AlN) (Wu, 2009). Therefore, most of the range of the solar spectrum is covered by these III-V semiconductors and their alloys. In addition, they are suitable for high frequency, high power and high temperature electron devices due to the high breakdown voltage, high electron saturation velocity, high mobility, high thermal conductivity and chemical stability (DeCuir Jr et al., 2008; Pearton et al., 1999).

The initial growth study of the III-V materials can be traced back in 1907; whereby the synthesis of the AlN was reported by Fichter et al. (Fichter et al., 1907), Johson et al. in 1932 reported the synthesis of GaN (Johson et al., 1932) as well as Juza and Hahn in 1938 reported the InN growth (Juza & Hahn, 1938). The initial breakthrough for development of III-V materials occurred in 1969 by growing GaN on sapphire substrate by hydride vapor phase epitaxy (HVPE) (Maruska & Tietjen, 1969), metal organic chemical vapor deposition (MOCVD) in 1971 (Manasevit et al., 1971) and molecular beam epitaxy (MBE) in 1975 (Yoshida et al., 1975). Maruska & Tietjen reported the use of HCl and Ga as a goup-III material source that were flowed together in carrier gas; in which, they formed $GaCl_3$ and GaCl group-III halide by halide vapor phase epitaxy method. This method is also called hydride vapor phase epitaxy since the hydride-based ammonia (NH_3) is utilized for the group-V source. However, the GaN achievement during that time was conductive (n-type) without dopant. In other words, the lack of the p-type conductivity and the poor crystal quality resulted in hindering development of the III-V materials for device applications.

In addition, Amano and Akasaki reported the two-step growth method in 1986, whereby a deposition of AlN buffer layer at low temperature was achieved, followed by the GaN deposition at high temperature (Amano et al., 1986). This method resulted in high quality GaN with atomically flat surface. In addition, another breakthrough that had a positive impact towards p-type development was reported by Amano et al., in 1989 (Amano et al., 1989). In 1991, Nakamura reported the usage of low temperature GaN buffer layer prior to the growth of high temperature GaN (Nakamura, 1991). This method led to achieving the GaN with mirror-like surface as well as relatively low defect density. After that, a very cost-effective method to acquire p-type GaN was developed by Nakamura, in which the magnesium (Mg) doped GaN was annealed at high temperature under ambience of nitrogen (N_2). Consequently, Nakamura succeeded to accomplish the first GaN-based LED and LD (Nakamura et al., 1994; Nakamura et al., 1996).

Since 1994, the research of the III-V materials has increased rapidly owing to the necessity of the commercial applications such as violet-yellow LEDs (Nakamura et al., 1994; Nakamura et al., 1995; Nakamura et al., 1993; Nishida et al., 2001), and LD (Nakamura et al., 2013; Nakamura et al., 1996). Besides, GaN-based blue LEDs possess key role to fabricate white LEDs, resulting from their high efficiency and long life-time (Park et al., 2003). Hence, it is important to further carry on the research to develop the GaN-based LEDs. However, several fundamental challenges such as substrate issue, quantum-confined stark effect (QCSE), crystal quality and morphological properties might hinder the development for longer wavelength emission (Baker et al., 2005; Khoury et al., 2017; Li et al., 2017; Zhao et al., 2016).

1.2 Challenges

1.2.1 Choice of Substrate

There are four main substrates that can be used for the growth of GaN epitaxial layers, namely free-standing GaN, SiC, Si and sapphire substrates. Substantial crystal qualities could be achieved with the use of free-standing GaN substrates due to the non-extended defects of the epitaxial layers (Fujito et al., 2009a; Fujito et al., et al., 2009b; Schmidt et al., 2007). Therefore, the homoepitaxial growth of GaN using free-standing GaN substrates would promote the best performance of LED and LD applications. However, these substrates can only be obtained through a growth of thick GaN using HVPE, which are expensive (Cao et al., 2004; Khoury et al., 2017; Xu et al., 2002). Hence, it is limiting the development of GaN-based LEDs for mass production.

Alternatively, GaN epitaxial layers can be grown on cost-effective substrates such as Si, which is then called a heteroepitaxial growth. However, Si substrates possess high lattice mismatch of almost 17% towards the GaN (Nakamura et al., 2013). In addition, due to the large thermal expansion coefficients between the GaN and Si substrates would further worsen the situation as a severe cracking might be encountered. Also, the growth of high temperature GaN epitaxial layer would suffers from amorphous meltback-etching (Ishikawa et al., 1998). In contrast, SiC/GaN possesses relatively low lattice mismatch of ~3.5% (Nakamura et al., 2013; Van de Walle, 2012). However, the SiC substrates are quite expensive, whereas they will be less competitive for mass production.

In a remarkable contrast to the aforementioned substrates, GaN epitaxial layers grown on sapphire substrate were accomplished (Alhassan et al., 2016; Narukawa et al., 2010; Sun et al., 2009b; Xu et al., 2009). Despite the high lattice mismatch of 16%, the GaN-based LEDs have commercially been grown along c-plane direction (Li et al., 2017; Narukawa et al., 2010). Therefore, the GaN grown on sapphire substrate still suffer from extended defects and dislocations such as threading dislocations (TDs) as well as basal stacking faults (BSFs). This in turn would lead to impairing the device efficiency (Baker et al., 2005; Cherns et al., 2001; Speck & Rosner, 1999; Zhao et al., 2016).

1.2.2 Quantum-Confined Stark Effect (QCSE)

One of the most crucial impacts that limits the LED performance is the separation of the electron and hole wave-functions by polarization field (Fiorentini et al., 1999). The polarization effect in III-V materials grown along c-plane direction is responsible for the efficiency limitations, especially for longer wavelength emission (Fiorentini et al., 1999; Lee et al., 2014; Leung et al., 2012). This in turn will lead to band bending, which induces the quantum-confined stark effect (QCSE) (Chen et al., 2017). The QCSE is the effect of an external electric field upon the light emission spectrum of multi quantum well (MQW), in which the permitted light emission frequencies is reduced. In turn, the electrons and holes are shifted to opposite sides of well, leading to remarkable decrement in the recombination efficiency of LEDs (Khoury et al., 2017; Xu et al., 2012). Theoretically, the piezoelectric field is maximum along the c-plane orientations as illustrated in Figure 1.1 (Romanov et al., 2006; Scholz, 2012). It is, however, decreased for semi-polar orientations, and eliminated for the planes that are perpendicular to c-plane (non-polar), in which the electron-hole wavefunction overlap is reduced (Scholz, 2012).

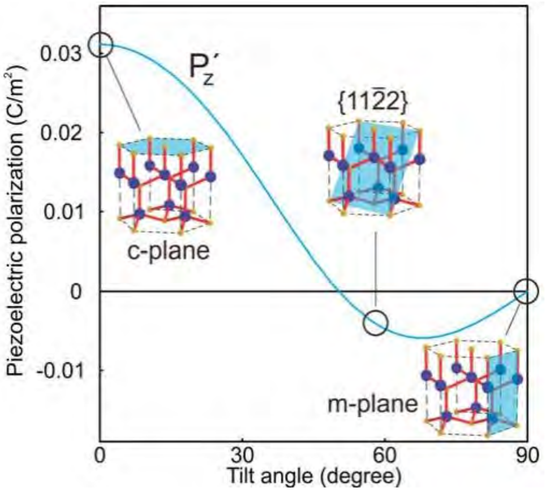

Figure 1.1: Piezoelectric polarization of an $In_xGa_{1-x}N$ quantum well versus tilted angles (Schwarz & Kneissl, 2007).

The non-polar m-plane InGaN/GaN-based LED without polarization fields was firstly proposed in the year of 2000 (Chakraborty et al., 2005). It was reported, however, the indium incorporation efficiency for non-polar is reduced by factor of three as compared to c-plane orientation, resulting in a reduction in the output power for longer wavelength emission (Yamada et al., 2008). This is because that the GaN-based LEDs grow along non-polar orientation exhibits less indium incorporation, which promotes LED device with shorter wavelength emissions (Koleske et al., 2013). However, LED devices grown along semi-polar orientation would promote higher indium incorporation due to the distribution of the terrace-like features as it will be discussed in Chapter 6. This in turn induces the growth along semi-polar, which attracted the attention as a potential efficiency of indium for green emitters (Northrup, 2009).

1.2.3 Crystal Quality Issue

It must be restated that the QCSE is reduced or eliminated by using the growth to be along non- and semi-polar orientations. However, the growth along these orientations on non-native substrates exhibits high density of extended defects, resulting from the high lattice mismatch (different lattice constants) with the substrate (Van de Walle, 2012). In contrast, several groups have suggested the use of free-standing GaN substrates and epitaxial lateral overgrowth (ELOG) to improve the crystal qualities. However, the use of free-standing semi-polar (11-22) GaN substrates require high production cost. While, the latter required additional steps and regrowth process (*ex-situ*). Therefore, the further development of longer wavelength LEDs requires the suitable growth condition as well as defect reduction technique. This will enable high efficiency semi-polar LEDs at relatively low cost.

1.3 Aim and Research Objectives

As discussed in 1.2, the growth of GaN-LEDs suffered from several limitations such as substrate issue, QCSE as well as crystal qualities. These negative impacts significantly affect the LED performance. However, GaN-LEDs grown along the semi-polar (11-22) orientation can reduce the QCSE, which might enhance the LED performance (Mukundan et al., 2014). Furthermore, it was reported that growth of GaN-based LED along the semi-polar (11-22) orientation significantly improved the indium incorporation as compared to polar and non-polar planes, which is very motivational to circumvent the green gap issue (De Mierry et al., 2009; Yamada et al., 2007). Nonetheless, the growth of semi-polar (11-22) GaN epitaxial layer on non-patterned sapphire yielded low crystal qualities and morphological properties. Hence, the aim of this study is to obtain high crystal quality and morphological properties of semi-polar (11-22) epitaxial layers grown on m-plane sapphire substrate. The investigation of crystal, morphological, optical and electrical towards the improvement of the epitaxial layer will be implemented.

The objectives of this study are:

1. To optimize the ammonia (NH_3) flux for the growth of semi-polar (11-22) GaN epitaxial layers grown on m-plane sapphire substrate.
2. To improve the crystal quality of semi-polar (11-22) GaN epitaxial layers using AlN/GaN multi-layer (ML) grown on m-plane sapphire.
3. To investigate the TMI flow rates towards the enhancement of the crystal, morphological, optical and electrical characteristics of the semi-polar (11-22) InGaN/GaN MQW-based LEDs.
4. To compare the full semi-polar (11-22) LED structures deposited on with and without AlN/GaN ML templates.

1.4 Thesis Organization

The thesis is consisted of seven Chapters. A brief introduction to the III-V semiconductors is presented in Chapter 1. Then, the challenges, aim and research objectives as well as the thesis organization are discussed. In Chapter 2, a general background, theories and physics of semiconductor related III-V materials are discussed. A detailed introduction and a current stage of semi-polar epitaxial layer are given. Then, defects in III-nitride epitaxial layer are elaborated with respect to the polar, non- and semi-polar orientations. Finally, the CVD techniques and the epitaxial growth of semi-polar (11-22) are elaborated. Chapter 3 presents the MOCVD working principle and the vapor phase reaction. Thereafter, the experimental procedure including the growth of unintentionally doped-gallium nitride (uid-GaN) template and LED structures are briefly explained with their respective flow charts. Furthermore, the principles of the characterization methods and sample preparations that being utilized in this research are described. The results and discussion of the semi-polar (11-22) epitaxial layers are presented in Chapter 4, including the optimization of the uid-GaN, AlN nucleation layer and number of the pairs used for the AlN/GaN multi-layers. The structural and morphological properties will be discussed in details. Chapter 5 includes the optimization of the disilane (Si_2H_6) and bicyclopentadienyl magnesium (Cp_2Mg) flow rates for the growth of semi-polar (11-22) n- and p-type GaN epitaxial layers, respectively. The enhancement of the structural, morphological and electrical properties will be discussed. The optimization of the MQW thickness using different flow rate ratios (TEG: TMI) and their effect towards the semi-polar (11-22) LED will be discussed in chapter 6. The comparison between the semi-polar (11-22) InGaN/GaN-based LED using different templates will be discussed. The relevant summary of the results in this thesis and the future plans are summarized in Chapter 7.

CHAPTER 2: THEORY AND LITERATURE REVIEW

A general literature review will be discussed in this chapter. In Section 2.1, the introduction of semiconductors is discussed, while the theory of the direct and indirect band gaps is explained in Section 2.2. The physics of the III-N semiconductor material properties such as electrical properties and crystal structures are discussed thoroughly in Section 2.3. Then, the semi-polar and non-polar epitaxial layers are discussed in terms of the spontaneous and piezoelectric polarization, the current stage of semi- and non-polar as well as substrate issues and presented in Section 2.5. In Section 2.5, the types of the defects in III-N materials including polar, semi-polar and non-polar orientations are elaborated. Furthermore, recent techniques of the chemical vapor deposition are discussed in Section 2.6. Finally, the current epitaxial growth techniques for the semi-polar (11-22) epitaxial growth are presented in Section 2.7.

2.1 Semiconductors

2.1.1 Introduction

Materials, in terms of the electrical properties, can be categorized into three groups: i) conductors, ii) insulators, and iii) semiconductors. In a conducting material, the electric charges are allowed to flow, while the electrical charged carriers cannot move easily in an insulating material. However, in a semiconductor, there is an intermediate conductivity between conductors and insulator. This remarkable behavior of the semiconductors can be realized by the band structure, namely the conduction and valence bands. Basically, the conduction band is at the lowest unfilled energy band, whilst the valence band is at the highest filled energy band. These two bands are overlapped in conductors, while in semiconductors and insulators are separated by forbidden gap.

In order to visualize the difference between materials, the energy band gap theory applied. Fundamentally, there are three band regions: i) valence band, ii) conduction band and iii) bandgap. The electron in the valence band are strongly bonded to the atoms, in which they cannot move freely. While, the carriers in the conduction band are free to move throughout the crystal lattice. Therefore, the energy level of the electrons in the conduction band is higher than the one in the valence band. The bandgap is defined as the energy difference between the maximum energy in the valence band and the minimum energy in the conduction band. In contrast, the material is either an insulator when the bandgap is relatively large or semiconductor when the bandgap is relatively small. This in general leads to the fact that the insulators have a relatively larger bandgap than semiconductors.

2.2 Direct and Indirect Bandgaps

In a direct bandgap of a semiconductor, the maximum energy of the valence band and the minimum energy of the conduction band have the same momentum. In an indirect bandgap of a semiconductor, however, the maximum energy in the valence band and the minimum energy of the conduction band might not be at the same momentum. This difference leads to a significant change in the optical properties such as radiative recombination rate. The radiative recombination rates in the direct bandgaps is higher than the indirect bandgaps. This in turn leads to the fact that the generation of the electron-hole pairs in a direct bandgap can easily occur. However, the process of the electron-hole pair recombination or regeneration in an indirect bandgap must be mediated by a phonon in order to lose or gain momentum as schematically depicted in Figure 2.1 (a) & (b). In addition to aforementioned, the recombination process of an electron-hole pair in the direct and indirect bandgaps possesses indifferent manners. Hence, the direct bandgap semiconductors are more preferable for the fabrication of the optical emitters such as light emitting diodes (LEDs) and laser diodes (LDs) (Mokkapati & Jagadish, 2009; Zimmermann, 2000). This is attributed to the higher efficiencies of the radiative recombination in the direct bandgaps than the ones in the indirect band gap.

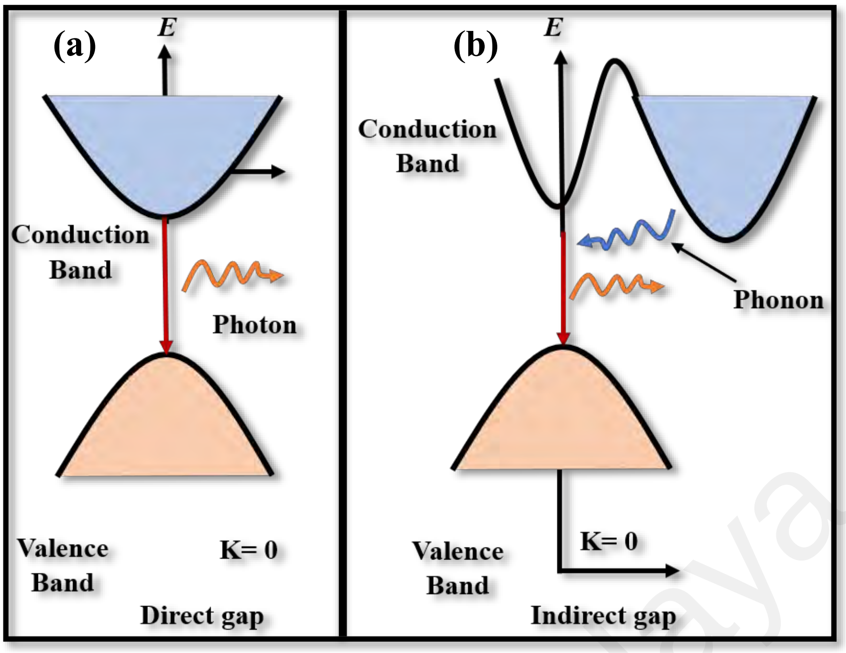

Figure 2.1: Schematic diagram of (a) A direct bandgap semiconductor and (b) An indirect bandgap semiconductor (Fujita, 2013).

Furthermore, the characteristics of an intrinsic semiconductor might be changed by adding impurities, well known as dopants. Upon introducing the donor impurity atoms (valence electrons), it results in n-type semiconductors since the semiconductor is exposed to valence electrons. In contrast, upon adding acceptor impurity atoms (less valence electrons), it leads to a p-type semiconductor, resulting from the acceptance of electron from the semiconductor. It must be noted that the donor impurities are close to the conduction band, while the acceptor impurities are close to the valence band. This in turn suggests that the electrical and optical performance of the semiconductors are greatly influenced. It must be noted that the common dopant are silane and magnesium (Mg) for n-type and p-type, respectively (Pampili & Parbrook, 2017).

2.3 Characteristics of III-nitride Semiconductors

The III-nitride semiconductors possess direct band gaps, covering the range from 0.7 eV (InN) to 6.2 eV (AlN) (Li et al., 2003), which is broad spectrum from infrared to deep ultraviolet. However, a great attention has attracted researchers through huge number of advantages over the conventional II-VI compounds semiconductors, III-Arsenides and III-Phosphides, (Ahmed et al., 2007; Arbouche et al., 2010; Ohtomo et al., 1998). Unlike III-N material, other bandgap semiconductors have a limitation in the spectrum region; whereas either very long wavelength emission such as III-Arsenides and III-Phosphides, or relatively short wavelength emission such as II-VI compounds. In addition, the III-nitride materials considered very strong candidates for the short wavelength application owing to the wide band gaps. Furthermore, due to their large breakdown voltage, reasonable thermal conductivity, tunable bandgap and the ability of operation under high temperature, III-V materials are promising candidates for high power and optoelectronic devices (Jain et al., 2000; Morkoç, 2009; Nakamura et al., 2013). Hence, the III-V semiconductors are perfect for the band gap engineering to understand the optical emitters with dissimilar wavelength emissions as shown in Figure 2.2. Meanwhile Table 2.1 lists the significant parameters for GaN and other semiconductors.

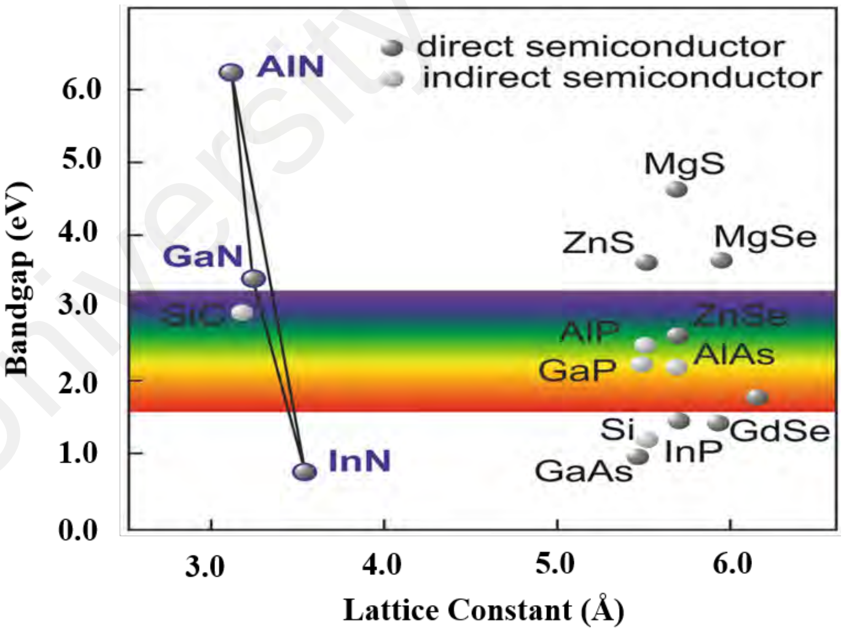

Figure 2.2: Bandgap energies of several semiconductors versus lattice constant (Cimalla, 2017).

Table 2.1: Significant parameters for GaN and other semiconductors (Nakamura et al., 2013).

Parameters	**GaN**	**6H-SiC**	**4H-SiC**	**GaAs**	**Si**
Band gap (eV)	3.39	2.86	3.26	1.42	1.12
Electron mobility (cm^2. V^{-1}. s^{-1})	1200 (Bulk)	400	700	8500	1350
Breakdown voltage ×10^5 (V.cm^{-1})	26	24	20	6	3
Thermal conductivity (W/cm.K)	1.3	4.9	4.9	0.46	1.5

2.3.1 Electrical Properties and Doping

Upon applying an electric field to a semiconductor, negatively charged (electron) as well as positively charged (holes) are accelerated in certain directions, resulting in electric current. The thermally excited electrons for pure GaN at room temperature are very small owing to its large band gap, leading to relatively high resistivity. In contrast, as a dopant of group-IV impurity atoms are utilized, the conductivity increases enormously since some of the gallium (Ga) atoms is replaced by Si atoms. This in turn might supply extra valence electrons rather than the atoms of Ga. Therefore, the electrons will be easily excited to the conduction band as they are bounded weakly to the supplied impurity atom. In this case, the semiconductor is called n-type GaN and the typical material to be used is silane. However, when the group-II impurity atoms substitute Ga atoms, holes will be introduced to the valence band. In this case, the semiconductor is called p-type GaN and magnesium (Mg) is utilized for p-type dopant.

As the hole and the electron move in certain directions upon applying an electric field to a semiconductor, they can be described by their mobilities. It must be noted that the carrier mobility in a semiconductor depends on the carrier concentration and the defect densities. Therefore, the mobility is considered very crucial parameter to investigate the effect of defect densities.

2.3.2 Crystal Structure

The crystal structure of III-V semiconductors can be classified into three types, namely wurtzite (WZ), zinc blend (ZB) and rock salt (Liu & Edgar, 2002; Maruska & Tietjen, 1969; Parthé, 1964; Xia et al., 1993). The structure of the rock salt can be stabilized under high pressure only, whilst the WZ and ZB can be stabilized in the epitaxial growth. Figure 2.3 (a) & (b) illustrates the structures of WZ and ZB, respectively. The structures of WZ and ZB are closely related and quite similar to each other (Nakamura et al., 2013). Nonetheless, the WZ and the ZB lattices differ in the stacking sequence of the close-packed plane (cpp) (Yeh et al., 1992). The WZ structure is more commercially common as compared to ZB structure (Nakamura et al., 2013). The WZ structure possesses a hexagonal unit cell, namely alternative diatomic cpp (0001) of Ga and nitrogen (N) pairs, leading to a stacking sequence as follows:

$$\ldots \mathrm{Ga_AN_AGa_BN_BGa_AN_AGa_BN_BGa_AN_AGa_BN_B} \ldots$$

However, the ZB structure is cubic, in which it has four Ga and four N elements in a single unit cell, resulting in a stacking sequence as follows:

$$\ldots \mathrm{Ga_AN_AGa_BN_BGa_CN_CGa_AN_AGa_BN_BGa_CN_C} \ldots$$

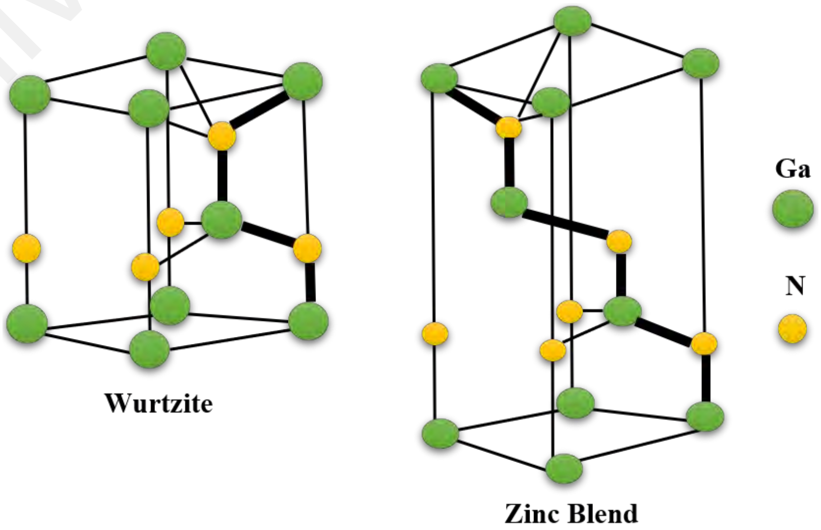

Figure 2.3: Illustrative difference in the unit cell of GaN for (a) WZ and (b) ZB crystal structures (Yeh et al., 1992).

The ZB structure is metastable owing to the difficulty to remain in the same structure (Beyer et al., 2015; Nakamura et al., 2013). Additionally, there are few studies on the ZB structures utilizing epitaxial methods were successfully reported such as GaN, AlN and InN (As et al., 2006; Chandrasekhar et al., 1995; Gerthsen et al., 1999; Lei et al., 1991). However, it was reported that the WZ structure is quite stable and commonly seen for III-V application (Nakamura et al., 2013; Yeh et al., 1992; Zhao et al., 2016). Hence, this study focuses on the WZ crystal structure to deposit semi-polar (11-22) epitaxial layers on m-plane sapphire substrate. The perfect WZ structures have two hexagonal close-packed (hcp) lattices, namely a_0 and c_0. In the WZ structures, the bonding to the next neighbors is tetrahedral, in which the group-III is bounded to four N atoms and vice versa (Nakamura et al., 2013). As reported in the literature, the GaN possesses lattice constants of a = 3.189 Å and c = 5.185 Å, while AlN structure has lattice constants of a = 3.111 Å and c = 4.978 Å. The lattice constants (a, c) as well as the unit cell parameters for GaN, AlN and InN are tabulated in Table 2.2. It was reported that the experimentally calculated values of the lattice constants (a, c) differ from the ideal ones due to the strong ionic bonds (Li et al., 2003), whereby it might be the reason for the difficulties in the doping of AlN.

Table 2.2: The lattice constants for GaN, AlN and InN (Nakamura et al., 2013).

Lattice Constant	**GaN**	**AlN**	**InN**
***a* (Å)**	3.189	3.111	3.544
***c* (Å)**	5.185	4.978	5.718
***u* (Å)**	0.382	0.382	0.379

The crystal planes in the hexagonal unit cell can be identified by four indices (*Miller-Bravais indices*), whereby these indices are designated by *h, k, i* as well as *l* (*hkil*). These indices are in conjunction with the axes of a coordinate system, in which a_1, a_2, a_3 and C indicate the *h*, *k*, *i* and *l* indices, respectively, as shown in Figure 2.4 (a-c). However, the crystallographic directions are commonly designated by four indices, namely *u*, *v*, *t*, and *w*, [*uvtw*]; the index of *w* is the lattice vector in the C direction, while the a_1, a_2 and a_3 are the lattice vectors for the *u, v,* and *t* indices.

As shown in Figure 2.4 (a-c), the wurtzite crystal structures possess the main direction of [0001] (a), which can be utilized as reference to recognize the other crystal planes. However, other planes are either inclined (semi-polar) (b) or perpendicular (non-polar) (c) to the polar plane of (0001). As mentioned in the previous chapter, less indium incorporation would be obtained upon the growth of GaN-based LEDs along non-polar directions, inducing shorter wavelength emission. However, higher indium incorporation would be attained by growing the GaN-based LEDs along the semi-polar (11-22) orientations. In this study, therefore, the semi-polar (11-22) orientation has been chosen to be the main candidate for the epitaxial growth.

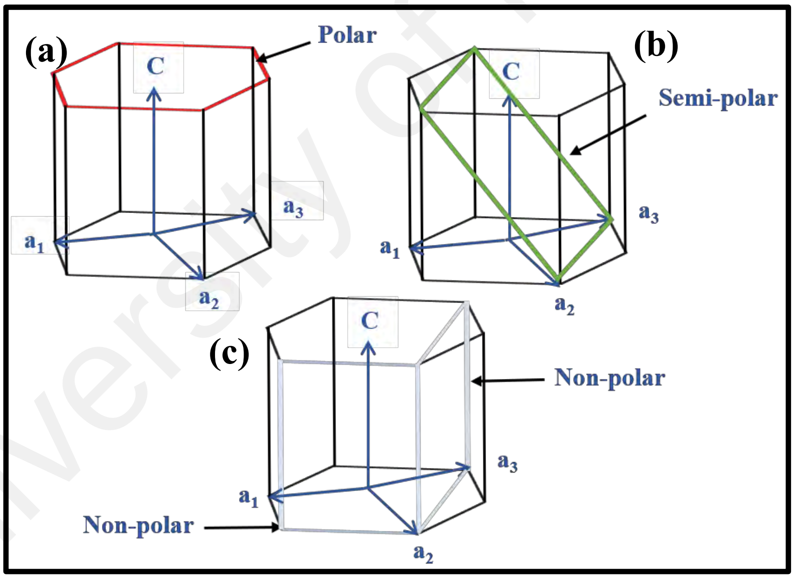

Figure 2.4: Schematic illustration of (a) polar, (b) semi-polar and (c) non-polar planes.

2.4 Semi- and Non-polar Epitaxial Layers

2.4.1 Spontaneous and Piezoelectric Field

III-nitride materials-based emitters have been utilized in a wide spectral range from the ultraviolet (UV) to blue and green wavelengths (Avramescu et al., 2010; Heikman et al., 2003; Nakamura et al., 1993; Narukawa et al., 2010). So far, the achievement is still limited to GaN grown along the conventional c-plane orientation. However, the device grown along the c-plane orientation suffers from polarization effects, which hinders the further enhancement of the device performance. These polarization effects are resulted from the spontaneous (P^{sp}) and piezoelectric polarization (P^{pz}). Basically, the non-symmetry of the wurtzite structure along c-plane causes the P^{sp}, while the P^{pz} is resulted from the biaxial mechanical stress between the heterojunction (Morkoç, 2009).

Figure 2.5 (a) & (b) illustrate the ball and stick configuration of tetrahedral bond between Ga and N in Ga polarity and N polarity, respectively. As shown in the Figure, since the electron cloud is closer to the N atoms, the polarization vector (P_0) direction is from N to Ga and the cumulative *z*-component of the triple bond of the atoms (P_{0zr}) will be along the [0001] direction. In N polarity, however, the P_{0zr} will be along the [000-1] direction.

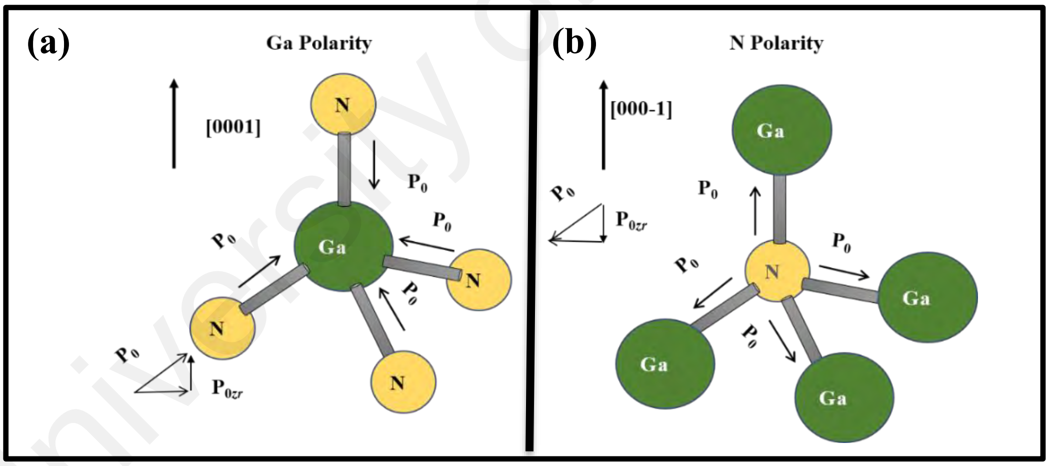

Figure 2.5: Demonstration of ball-and-stick configuration of GaN tetrahedron under in-plane compressive strain with (a) Ga polarity and (b) N polarity (Morkoç, 2009).

Furthermore, when the III-V material is exposed to stress, the lattice constants of *c* and *a* will be changed to compensate the stress. Therefore, the additional polarization in the strained III-V is along [000-1], while for the compressive strain is along [0001] (Bernardini, 1997). It is noteworthy that the large polarization field can affect the III-V semiconductors in many ways. Basically, the polarization results in an electrical field, causing a tilt in the energy band structure of the quantum well (QW), thus spatial separation for the electron-hole wavefunctions (Chen et al., 2017). This in turn increases the probability for the radiative recombination to be lower. Hence, the c-oriented devices will exhibit the quantum-confinement Stark-effect (QCSE), which induces large reduction in the recombination efficiency of GaN-based LEDs (Ryou et al., 2009; Xu et al., 2012; Yamamoto et al., 2010). Figure 2.6 (a) & (b) depicts the schematic illustration of the energy band structure for polar and non-polar InGaN QWs.

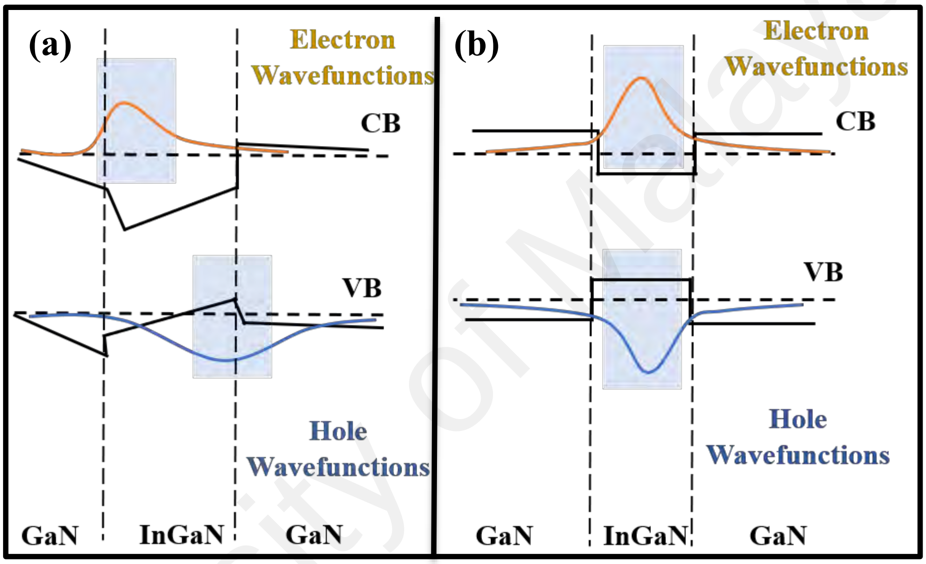

Figure 2.6: Schematic illustration of different energy band structures along (a) polar and (b) non-polar orientations.

This negative impact has attracted the attention to several groups to circumvent this issue, especially with longer wavelength emission. In order to overcome this issue, several groups have proposed the growth of the LEDs along semi- and non-polar orientation (Chitnis et al., 2004; De Mierry et al., 2009; Li et al., 2017; Takeuchi et al., 2000). The orientation-dependent piezoelectric field is calculated by transforming the typical (x, y, z) natural coordinate system into new (x′, y′, z′) primed coordinate system with angle (ϑ) with respect to the polar orientation as shown in Figure 2.7.

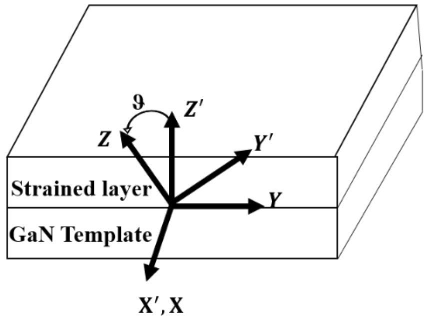

Figure 2.7: Schematic illustration of the crystal lattice mismatch between semi-polar and the template (Romanov et al., 2006). Note: The $\mathbf{X}, \mathbf{Y}, \mathbf{Z}$ and $\mathbf{X}', \mathbf{Y}', \mathbf{Z}'$ are natural coordinate system associated with semi-polar and coordinate system related to the layer, respectively.

The nonzero component of the strain tensor in the primed coordinate system are given in Equation (2.1) as follows (Romanov et al., 2006):

$$\varepsilon_{x'x'} = \varepsilon_{m1}, \ \varepsilon_{y'y'} = \varepsilon_{m2},$$

$$\varepsilon_{z'z'} = \frac{(B_{41}\varepsilon_{m1} + B_{42}\varepsilon_{m2})A_{32} - (B_{31}\varepsilon_{m1} + B_{32}\varepsilon_{m2})A_{42}}{A_{31}A_{42} - A_{32}A_{41}},$$

$$\varepsilon_{y'z'} = \frac{(B_{31}\varepsilon_{m1} + B_{32}\varepsilon_{m2})A_{41} - (B_{41}\varepsilon_{m1} + B_{42}\varepsilon_{m2})A_{31}}{A_{31}A_{42} - A_{32}A_{41}},$$

where

$$A_{31} = C_{11}sin^4\vartheta + \left(\frac{1}{2}C_{13} + C_{44}\right)sin^2 2\vartheta + C_{33}\ cos^4\vartheta,$$

$$A_{32} = [C_{11}sin^2\vartheta + (C_{13} + 2C_{44})cos2\vartheta - C_{33}\ cos^2\vartheta]sin2\vartheta,$$

$$A_{41} = \frac{1}{2}[(C_{11} - C_{13})sin^2\vartheta + 2C_{44}\cos 2\vartheta + (C_{13} - C_{33})cos^2\vartheta] \sin 2\vartheta, \tag{2.1}$$

$$A_{42} = \left(\frac{C_{11} + C_{33}}{2} - C_{13}\right)sin^2 2\vartheta + 2C_{44}\,cos^2 2\vartheta,$$

$$B_{31} = C_{12}\ sin^2\vartheta + C_{13}\ cos^2\vartheta,$$

$$B_{32} = C_{13}(sin^4\vartheta + cos^4\vartheta)\left(\frac{C_{11} + C_{33}}{4} - C_{44}\right)sin^2 2\vartheta,$$

$$B_{41} = \sin 2\vartheta\,\frac{C_{12} - C_{13}}{2}\,\sin 2\vartheta,$$

$$B_{42} = \frac{1}{2}[C_{11}cos^2\vartheta - (C_{13} + 2C_{44})\cos 2\vartheta - C_{33}\,sin^2\vartheta]\sin\ 2\vartheta,$$

Therefore, the coefficients of the elastic stiffness of the layer can be measured (Romanov et al., 2006).

In addition, the nonzero strain can be determined in the natural coordinate system from Equation (2.2), in which the appropriate tensor transformation is applied as follows:

$$\begin{aligned}
\varepsilon_{xx} &= \varepsilon_{x'x'} \\
\varepsilon_{yy} &= \varepsilon_{y'y'} cos^2\,\vartheta + \varepsilon_{z'z'}\, sin^2\vartheta + \varepsilon_{y'z'} \sin 2\,\vartheta_, \\
\varepsilon_{zz} &= \varepsilon_{y'y'} sin^2\,\vartheta + \varepsilon_{z'z'}\, cos^2\vartheta - \varepsilon_{y'z'} \sin 2\,\vartheta_, \\
\varepsilon_{yz} &= \frac{\varepsilon_{z'z'} - \varepsilon_{y'y'}}{2} \sin 2\,\vartheta + \varepsilon_{y'z'} \cos 2\,\vartheta.
\end{aligned} \tag{2.2}$$

The total polarization (ΔP_z) is known as the sum of the P^{sp} and P^{pz}, whereby the III-V semiconductor would possess P^{sp} and P^{pz} even at equilibrium. (Romanov et al., 2006). The as-grown epitaxial layer of the semiconductors are usually under strain, resulting from to the lattice mismatch between the layer and the template (Romanov et al., 2006). This in turn leads to additional P^{pz}, which closely associated with the unit cell symmetry. The layer grown along the c-plane are under in-plane biaxial stretching, resulting in P^{pz}, while semi-polar can be subjected to an arbitrary strain ε_{ij} (Romanov et al., 2006). By considering the symmetry of the space group of WZ III-V ($P6_3mc$), the P^{pz} can be related to strain as follows:

$$P^{pz} = \begin{pmatrix} 0 & 0 & 0 & 0 & e_{15} & 0 \\ 0 & 0 & 0 & e_{15} & 0 & 0 \\ e_{31} & e_{31} & e_{33} & 0 & 0 & 0 \end{pmatrix} \begin{pmatrix} \epsilon_{xx} \\ \epsilon_{yy} \\ \varepsilon_{zz} \\ \varepsilon_{yz} \\ \varepsilon_{xz} \\ \varepsilon_{xy} \end{pmatrix} = \left(e_{31} \begin{pmatrix} e_{15}\epsilon_{xz} \\ \epsilon_{xx} + e_{15}\epsilon_{yz} \\ \epsilon_{yy} \end{pmatrix} + e_{33}\varepsilon_{zz} \right) \tag{2.3}$$

in which the element e_{ij} of the piezoelectric tensor in Voigt notation (Bernardini & Fiorentini, 1999; Romanov et al., 2006). It must be noted that the relations in Equation (2.3) are obtained in the natural coordinate system relative to the *c* axis. Thus, the spatial change in the ΔP_z results in a fixed volume charge density (Romanov et al., 2006):

$$\rho = -\nabla . P. \tag{2.4}$$

Therefore, the longitudinal component of the piezoelectric polarization $P_{LZ'}^{PZ}$ can be written as follows:

$$P_{LZ'}^{PZ} = e_{31} cos\vartheta \epsilon_{X'X'} + \left(e_{31} cos^3\vartheta + \frac{e_{33} - e_{15}}{2} sin\vartheta \; sin2\vartheta\right) \epsilon_{y'y'} + \left(\frac{e_{33} + e_{15}}{2} sin\vartheta \; sin2\vartheta + e_{33} cos^3\vartheta\right) \epsilon_{z'z'} + [(e_{31} - e_{33}) cos\vartheta \; sin2\vartheta + e_{15} sin\vartheta \; cos2\vartheta] \epsilon_{y'z'} \tag{2.5}$$

Hence, the ΔP_z polarization is determined as follows:

$$\Delta P_{Z'} = P_{LZ'}^{PZ} + (P_L^{SP} - P_{LT}^{SP}) cos\vartheta \tag{2.6}$$

whereby the P_L^{SP} and P_{LT}^{SP} are the spontaneous polarizations for the layer and the template, while the $P_{LZ'}^{PZ}$ is the piezoelectric polarization.

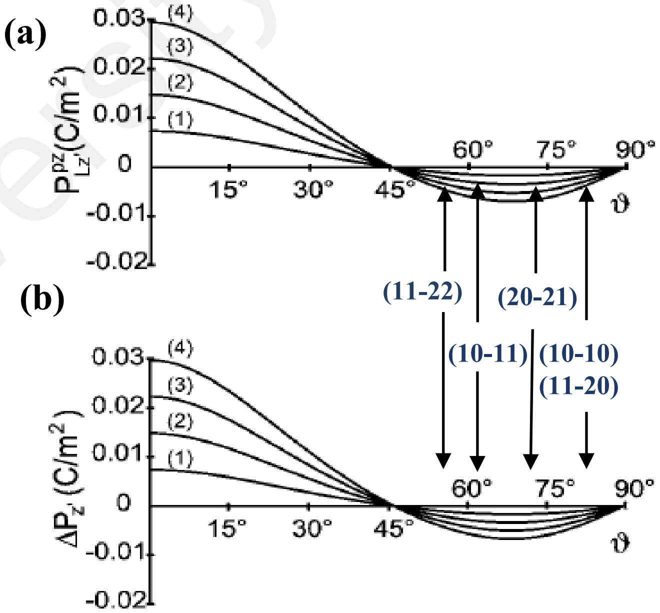

Figure 2.8: Dependence of the orientations on (a) The piezoelectric polarization and (b) The total polarization for In_xGa_{1-x} layers grown on GaN. The indium composition x=0.05 (1), 0.10 (2), 0.15 (3), and 0.20 (4) (Romanov et al., 2006).

Figure 2.8 (a) & (b) illustrates the $P_{LZ'}^{PZ}$ and the ΔP_z for different indium composition (x) with respect to the crystal orientation, respectively (Romanov et al., 2006). As it can be discerned, the polarization field increased tremendously upon the growth along c-direction, while it reached the minimum value along the semi-polar (11-22) and (20-21), and completely suppressed along the m-plane (10-10).

2.4.2 Current Stage of Semi- and Non-polar

As mentioned earlier, other planes than c-plane (0001), there are perpendicular planes with the respect to plane in wurtzite crystal structure, namely non-polar planes (Armitage & Hirayama, 2008; Sasaki & Zembutsu, 1987). Those planes include m-plane (10-10) and *a*-plane (11-20) (Craven et al., 2002; Schmidt et al., 2007). However, the WZ crystal structure between the polar and non-polar are termed as semi-polar such as (10-11), (11-22) and (20-21) (De Mierry et al., 2009; Lee et al., 2016; Young et al., 2010). Some commonly utilized planes were previously depicted in Figure 2.4. The growth along non-polar orientations would exhibit less indium incorporation, resulting in shorter wavelength emission (Koleske et al., 2013; Yamada et al., 2007). For LEDs with longer wavelength emission, however, growth along semi-polar (11-22) orientation possesses efficient indium incorporation (Bai et al., 2015; Funato et al., 2006). This in turn concludes that the growth along semi-polar direction is preferable for longer wavelength emission, might be due to the lower chemical potential for In atoms to accommodate (Northrup, 2009).

However, as previously reported that owing to the lattice mismatched between the epitaxial layer and the sapphire substrate, semi-polar (11-22) epitaxial layers suffer from high densities of defect and dislocations such threading dislocation (TDs) and basal stacking fault (BSFs) (Baker et al., 2005; Koukoula et al., 2012; Vennegues et al., 2007). Furthermore, the on- and off-axis x-ray rocking curve (XRC) of the semi-polar epitaxial layer grown on m-plane sapphire substrate are broad, which is mainly due to high densities of TDs and BSFs (Leung, et al., 2009; Zhao et al., 2016), impairing the device efficiency. Hence, it is crucial to enhance the crystal quality and the morphological properties of the semi-polar (11-22) GaN grown on m-plane sapphire substrate.

2.4.3 Substrate Issue

There are several substrates can be utilized to grow GaN epitaxial layers. These main substrates are free-standing GaN, SiC, Si, and sapphire substrates. The free-standing GaN substrates have been utilized to grow GaN with proper crystal quality, which mainly resulted from the non-extended defects of the epitaxial layers (Fujito et al., 2009a; Funato et al., 2006). Therefore, the free-standing GaN substrates promote best performance for application of GaN-based emitters. However, these free-standing substrates remain expensive and they are available in small sizes (Amilusik et al., 2014; Li et al., 2017; Sun, et al., 2009a). On the other hand, SiC substrates are proper alternative as compared to free-standing GaN substrates. GaN epitaxial layers have been grown on SiC substrates with successful achievement of electronic and optoelectronic devices (Johnson et al., 1996; Kordoš et al., 2005; Murthy et al., 2006; Sun et al., 2017). Nonetheless, these SiC substrates are available in small sizes and more expensive as compared to Si and sapphire substrates.

In contrast, Si substrates have been utilized to grow GaN epitaxial layers (Dadgar et al., 2003; Dadgar et al., 2007; Lee et al., 2016; Rahman et al., 2016; Suzuki et al., 2009). The physical properties as well as the availability of the Si substrate make it very good candidate for GaN growth. However, the growth of GaN epitaxial layer is more challenging as compared to sapphire, which might be attributed to the large lattice and thermal mismatch as presented in Table 2.3. This in turn would result in formation of cracks during cooling stage after the growth (Fu et al., 2000; Li et al., 2019). Furthermore, the GaN/Si reaction might lead to an amorphous meltback-etching (Ishikawa et al., 1998).

Hence, the crystal quality and the morphological properties for GaN growth are far from satisfactory (Drechsel et al., 2012; Reuters et al., 2014).

Table 2.3: Lattice mismatch, thermal mismatch and thermal expansion coefficient between GaN and common utilized substrates (Nakamura et al., 2013; Van de Walle, 2012).

Substrates	**Lattice constant (Å)**	**Lattice mismatch to GaN (%)**	**Thermal expansion coefficient ($10^{-6.}$ K^{-1})**	**Thermal mismatch to GaN (%)**
GaN	a = 3.189 c = 5.185	0	5.59 3.17	0
AlN	a = 3.112 c = 4.982	2.4 (compressive)	4.2 5.3	33
Sapphire	a = 4.758 c = 12.991	16.1 (compressive)	7.5 8.5	-25
6H-SiC	a = 3.080 c = 15.120	3.5 (Tensile)	4.2 4.68	33
(111) Si	a = 5.430	16.9 (Tensile)	3.59	56

Sapphire substrates, in contrast, have been extensively utilized for the epitaxial growth of GaN-based emitters as they possess the best properties for crystal quality and prices (Bae et al., 2011; Lu et al., 2003). Furthermore, m-plane sapphire substrates have widely been employed to attain the growth of semi-polar (11-22) GaN (Xu et al., 2012; Zhao et al., 2016). As mentioned earlier, however, the semi-polar (11-22) epitaxial layers still suffer from defects and dislocations (Lee et al., 2014; Vennegues et al., 2007; Xu et al., 2012; Zhao et al., 2016). Hence, it is important to optimize the growth of semi-polar (11-22) epitaxial layers on non-patterned and inexpensive substrate. In this study, 2-inch m-plane sapphire will be employed to obtain the growth of the semi-polar (11-22) epitaxial layers. The epitaxial relationship between the semi-polar (11-22) epitaxial layers m-plane sapphire is depicted in Figure 2.9.

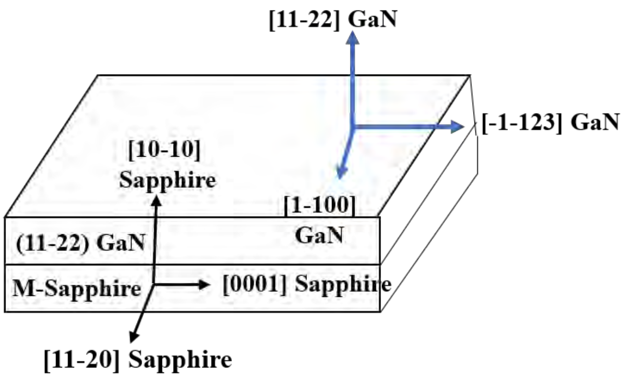

Figure 2.9: The schematic illustration of the epitaxial relationship between the semi-polar (11-22) GaN and the m-plane (10-10) sapphire substrate.

whereby the epitaxial relationship can be written as follows:

$$[11\text{-}22]_{GaN} \parallel [10\text{-}10]_{sap}, [1\text{-}100]_{GaN} \parallel [11\text{-}20]_{sap}, [\text{-}1\text{-}123]_{GaN} \parallel [0001]_{sap} \quad (2.7)$$

2.5 Types of Dislocations and Defects in III-V Materials

The crystal structure is composed by regular arrangement of decorated periodic atoms. The main reason that degrades the optical properties of the optoelectronics devices is the crystal defect, which reveals imperfection of the crystal lattice (Lester et al., 1995; Schubert et al., 2007). In general, two types of dislocations, namely edge and screw dislocations are formed along the growth of c-plane (Narayan et al., 2006; Arslan et al., 2013; Rahman et al., 2016). In addition, these dislocations in most cases are combination of edge and screw dislocations, which is well known to be mixed dislocations (Narayan et al., 2006; Rahman et al., 2016).

The edge dislocations can be conceived to be an extra half plane, which accommodated a lattice twist, while the screw dislocations can be visualized as the atoms are dislocated from the lattice (accommodated in a lattice tilt) as illustrated in Figure 2.10 (a) & (b) (Arslan et al., 2009; Moram & Vickers, 2009; Narayan et al., 2006). These dislocations are parallel to the orientation, resulting in crystals to be distorted. Therefore, they propagate through the epitaxial layer, known as TDs, and reach the surface of the growth.

Therefore, the existence of the TDs will impair the device performance by causing carrier scattering effect (Weimann et al., 1998), nonradiative recombination (Hangleiter et al., 2005; Rosner et al.,1997) and diffusion of dopant and impurities (Lebedev et al., 2005).

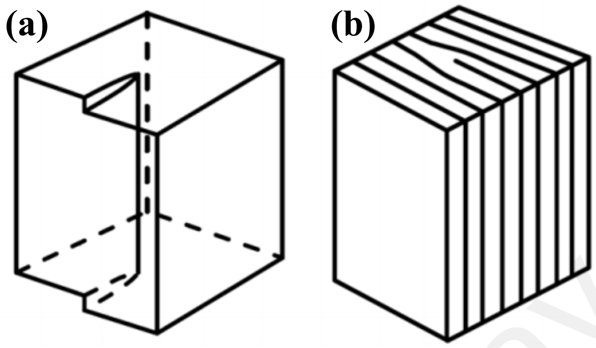

Figure 2.10: Illustration of (a) edge and (b) screw dislocations (Moram & Vickers, 2009).

However, the typical planar defect in the semi- and non-polar epitaxial layer are the BSFs. These types of defects might be resulted from the atomic stacking of a crystal structure (Lähnemann et al., 2014). There are three distinguished types of BSFs reported in the literature (Frank & Nicholas, 1953; Hirth et al., 1982; Lähnemann et al., 2014); in which a change from one hcp to another , i.e. from AB to BC (I_1) or AC (I_2) stacking sequence would lead to the formation of intrinsic BSFs, whilst an extrinsic layer insertion results in the extrinsic BSFs, i.e. AC (*E*) in an AB sequence as schematically illustrated in Figure 2.11 (a-c). The types of BSFs as follows:

a) The intrinsic I_1 type of BSFs: One breach in the wurtzite (WZ) stacking rule occurred, resulting in a stacking sequence of ABABCBCBC. . .
b) The intrinsic I_2 type of BSFs: Two breaches in the WZ stacking rule, leading to the stacking sequence of ABABCACAC. . .
c) The extrinsic *E* type of BSFs: Three breaches in the WZ stacking rule, leading to the stacking sequence of ABABCABAB. . .

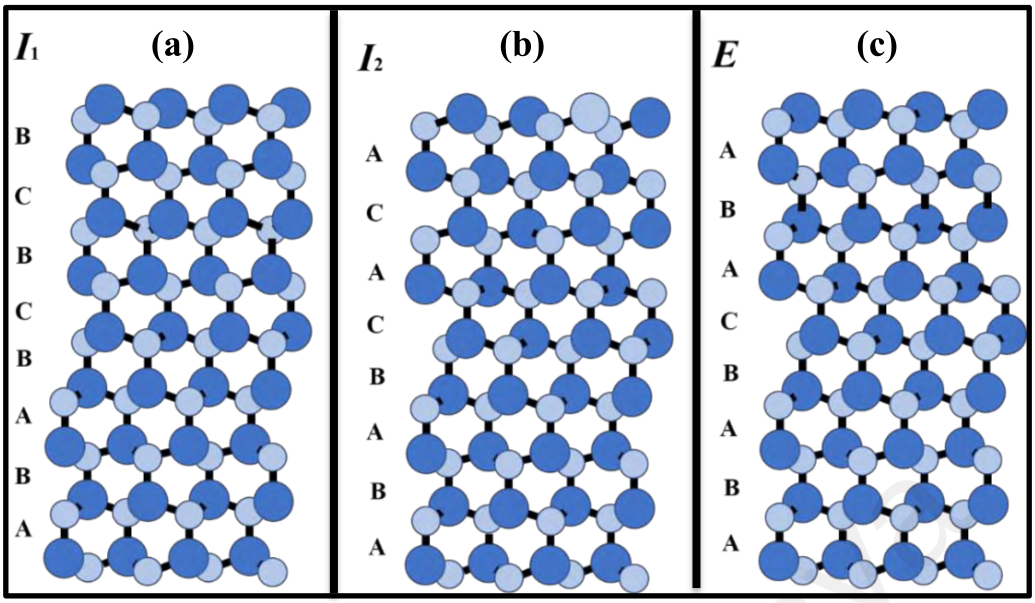

Figure 2.11: Atomic models of stacking sequence in the wurtzite structure, illustrating BSFs types of (a) the intrinsic I_1, (b) the intrinsic I_2 and (c) the extrinsic *E*. (Lähnemann et al., 2014; Zakharov et al., 2005).

It is noteworthy that the energy formation of BSFs increases as the presented order (Stampfl & Van de Walle, 1998). This has been already concluded by Frank and Nicholas (Frank & Nicholas, 1953), in which the increment of the number of breaches in the WZ stacking rule has the highest energy formation. The I_1 type of BSF are the most discerned defects owing its lowest energy formation (Lähnemann et al., 2014). However, the occurrence of the I_2 type of BSFs might be attributed due to a single slip in the basal plane (post-growth deformation) (Frank & Nicholas, 1953; Lähnemann et al., 2014). In contrast, the *E* type of BSF could occur in the case of growing nanowire (free surface) (Lähnemann et al., 2014).

BSFs of the type I_1 must be bounded by Frank–Shockley partial dislocations (PDs) 1/3⟨11-00⟩, I_2 type BSFs bounded by Shockley PDs and can be formed by 1/6⟨20-23⟩, and E-type BSFs occurs owing to the insertion of an extra basal plane and bounded by Frank PDs (1/2⟨1000⟩) as tabulated in Table 2.4 (Bougrioua et al., 2007; Dasilva et al., 2010; Moram et al., 2009; Moram & Vickers, 2009; Zakharov et al., 2005). While, the

BSFs of the type I_1 can also be in connection with one prismatic stacking fault (PSF) by (1/2⟨10-11⟩) displacement vector (Zakharov et al., 2005).

Table 2.4: The types of the BSFs with the displacement vectors as well as the bounded partial dislocation (Dasilva et al., 2010).

Type	**Displacement vector**	**Stacking sequence**	**Bounded type of dislocation**
I_1	1/3 [1-100]	ABABCBCBC	Frank-Shockley partial dislocation
I_2	1/6 [20-23]	ABABCACAC	Shockley partial dislocation
E	1/2 [0001]	ABABCABAB	Frank partial dislocation

2.6 Chemical Vapor Deposition (CVD)

The increase in the demand for the modern industries in the electronic, optoelectronic as well as optical applications have encouraged the development for several film deposition techniques. The chemical vapor deposition (CVD) technique have been widely employed to deposit wide range of materials (Beshkov et al., 2002; Funato et al., 2006; Kim et al., 2019; Koynov et al., 1997; Park & Sudarshan, 2001). Basically, this technique involves a flow of precursor or gas into the chamber, which the chemical reaction takes place and results in deposition of thin film (Park & Sudarshan, 2001). However, the deposition techniques have different advantages as compared one to another (Devi, 2013; Park & Sudarshan, 2001; Wiest et al., 2006). Generally, the CVD process mechanism involves chemical reaction and/or gaseous dissociation reactants in activated environment such as light, plasma and heat, etc. The CVD process consists of several types including atmospheric pressure (APCVD), low pressure (LPCVD), plasma enhanced chemical vapor deposition (PECVD) and metal organic chemical vapor deposition (MOCVD) as tabulated in Table 2.5.

Table 2.5: Limitation and capabilities of CVD techniques.

Technique	Capability	Limitation
APCVD	• Si-compound films • Metal oxide	Low deposition rate Film uniformity High pressure Contamination
LPCVD	• Si-compound films • Metal oxide	Low deposition rate Low pressure and temperature Contamination Pinhole defect
PECVD	• Si-compound films • Metal oxide	Plasma induced-reaction Low Temperature Surface impurities
MOCVD	• III-V • II-IV • SiN	Unsuitable for Metal oxide deposition Hazardous sources and waste gases

Note: Si-compound films include SiO_2, SiN, SiO_xN_y and amorphous Si films.

Recent advancement in CVD have shown the capability of high-quality thin film could be achieved via the mentioned techniques. However, certain material depositions require specific CVD techniques. For instance, APCVD and LPCVD have shown the ability to deposit the SiN or SiO_2 with various properties such as film and mask layers (Beshkov et al., 2002). Nevertheless, such techniques exhibit an additional pinhole defect occurrence within the layers (Koynov et al., 1997).

On the other hand, PECVD is employed to produce SiO_2 mask (Xi et al., 2018; Lee et al., 2016) and SiN_x (Beshkov et al., 2002; Kim et al., 2019; Zhang et al., 2019). However, via the PECVD method, traces of surface impurities can be observed; in which N-H, and O-H dangling bonds were present due to the plasma affecting the deposited layer. Studies have also shown the successful growth of GaN via PECVD. However, gallium oxide (Ga_2O_3) was present, deduced a mixed Ga-compounds indicating low crystal quality of GaN (Gholampour et al., 2015). Therefore, this technique would not be of interest to grow GaN epitaxial layer with high crystal quality. Alternatively, the MOCVD technique would be capable of attaining high crystal quality of GaN epitaxial layers and related nitride alloys (SiN, AlN, AlGaN, InN, InGaN, and InAlGaN) (Dai et al., 2017; Hatui et al., 2015; Jeong et al., 2013; Khoury et al., 2017; Pradeep et al., 2018; Zhao et al., 2016).

2.6.1 Metal Organic Chemical Vapor Deposition (MOCVD)

In a remarkable contrast to other CVD techniques, the metal organic compounds are utilized as the precursors in MOCVD. The initial MOCVD growth was accomplished by Manasevit & Simpson in 1971, who firstly use the term “metal-organic” (MO). Thereafter, several publications were obtained, describing the use of III-V materials in the MOCVD growth including GaN and GaAs (Takahashi et al., 1984). Thus far, MOCVD technique has become dominant for the industrial purposes to be used for the growth of optoelectronic devices (Funato et al., 2006; Nakamura et al., 2013).

The MOCVD possesses unique flexibilities to control wide range of operating conditions as well as source of the materials as compared to the other CVD techniques. This in turn contributes in producing state of the art performance such as LEDs, LDs and high electron mobility transistors (HEMTs) (Bae et al., 2011; Schmidt et al., 2007; Wang et al., 2005). In addition, the reaction in the MOCVD can be deposited at higher temperature namely more than 1100°C. This in turn allows the thermochemical reaction to be stable, which is believed to be the reason why the MOCVD is preferable for commercial application of optoelectronic devices. In addition, other CVD techniques would endure higher surface impurity incorporation whereas the MOCVD exhibited less due the simple interchangeable quartz flow channel (FC) for different material depositions. Furthermore, the deposition rate of MOCVD is relatively higher as compared to other CVD techniques. Therefore, the MOCVD is deemed suitable for the growth of semi-polar (11-22) epitaxial layers. Further elaboration of the MOCVD working principle will be presented in the next Chapter of the thesis.

2.7 Epitaxial Growth of Semi-polar (11-22)

The growth of the semi-polar (11-22), (10-11) and (10-13) epitaxial layers have been accomplished on several substrates such as semi-polar GaN substrate, spinal substrate as well as m-plane substrate (Baker et al., 2005; Hylton et al., 2009; Lee et al., 2014; Park, 2015). However, semi-polar (11-22) epitaxial layers suffer from high densities of defect and dislocations such as TDs and BSFs. Therefore, it is challenging to grow semi-polar with high crystal quality and surface morphology. Additionally, mixed phase of semi-polar (11-22) and (10-13) orientations might present during the growth of AlN nucleation layer (Hatui et al., 2015; Stellmach et al., 2012). This in turn leads to low crystal quality and morphological properties due to the twinning of the grains (Ploch et al., 2010). The growth of the AlN at a temperature less than 1000°C would result in low crystal quality since the growth is dependent on the nitridation temperature (Pristovsek et al., 2016; Sun et al., 2009a).

On the other hand, it was reported that the semi-polar GaN epitaxial layers would be grown with low defect densities using semi-polar GaN bulk substrate (Fujito et al., 2009a; Funato et al., 2006; Sato et al., 2008). These bulk substrates can be acquired by cleaving a c-oriented (0001) thick GaN substrate with a few millimeters of thickness along non- and semi-polar direction. Hence, the obtained semi-polar bulk GaN substrates will be in small sizes.

Alternatively, the epitaxial lateral overgrowth (ELOG) technique was introduced to obtain the growth of semi-polar (11-22) epitaxial layer with proper crystal quality (Jang et al., 2012; Min et al., 2013; Tendille et al., 2014; Wang et al., 2013). Although high crystal quality could be obtained using this technique, this technique requires additional steps and regrowth process (*ex-situ*). For instance, prior to the growth of the MOCVD, the r-sapphire substrates underwent several processes to obtain the desired pattern of cones such as photolithography and dry etching (Wang et al., 2013). However, the pattern of the cones must be controlled with certain dimension in order to obtain the c-plane facets, resulting in semi-polar (11-22) epitaxial layer. In addition, the ELOG technique was performed using three-step growth. The first-step was to deposit SiO_2 layer using RF sputtering. Then, the strip-like structures were obtained using standard photolithography and inductive-coupled plasma (ICP). Finally, the semi-polar (11-22) GaN was achieved using MOCVD (Jang et al., 2012; Tendille et al., 2014). However, this technique could be performed after the growth of GaN epitaxial by depositing thick layer of SiO_2 using e-beam evaporation (Hollander et al., 2007). Then, the wet chemistry photolithography was accomplished to obtain the strip-like structure. Finally, the overgrown GaN was achieved with high V/III ratio, in which it was required to perform. In contrast, recent studies on improvement of the crystal quality for GaN-based LEDs have shown that the insertion of multi-layer (ML) proved enhancement of the crystal quality (Sun et al., 2005; Xu et al., 2009; Xu et al., 2012). These MLs can effectively improve the crystal quality by acting as a filter for defects and dislocations as well as reduce or even eliminate the cracking for further application of GaN-based LED devices (Wang et al., 2002). In addition, these MLs could be utilized to investigate the strain state for the epitaxial layer (Gleize et al., 1999).

In this thesis, the use of AlN/GaN multi-layer (ML) is demonstrated to enhance the crystal quality of semi-polar (11-22) epitaxial layers. When a stack of two materials with different lattice constant are coherently grown, strong strain between different lattice constant (AlN and GaN epitaxial layers) is produced. Hence, it is presumed that the defects and dislocations might be blocked from propagating upwards if they are bent by the strain and a close-loop is generated.

CHAPTER 3: EXPERIMENTAL AND CHARACTERIZATION METHODS

This chapter discusses the experimental methods and material utilized in this study. In Section 3.1, the metal organic chemical vapor deposition system is described thoroughly including the reaction and the metal organic used in this study. The vapor phase reaction for the III-nitride materials is presented in Section 3.2. After that, the growth methodology of the epitaxial layer is presented in Section 3.3. Finally, the utilized characterization methods for investigation of the grown epitaxial layers are presented in Section 3.4.

3.1 Metal-Organic Chemical Vapor Deposition (MOCVD)

So far, metal-organic chemical vapor deposition (MOCVD) has been substantially used to grow III-V materials. In this study, the Taiyo Nippon Sanso SR-2000 MOCVD was utilized to grow III-V epitaxial layers as shown in Figure 3.1 (a) & (b). It is noteworthy that the reactor of the MOCVD has a laminar flow, in which precise control of the epitaxial layer as well as materials composition are attained.

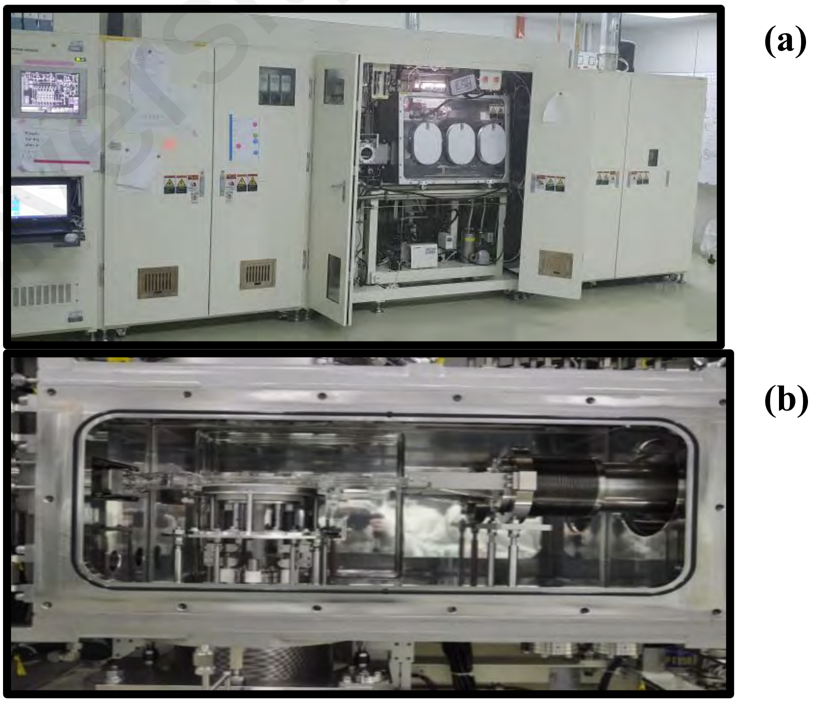

Figure 3.1: Images of Taiyo Nippon Sanso SR-2000 MOCVD of (a) The full system and (b) The horizontal Reactor.

The MOCVD reactor possesses a specific design, in which only the same specification of the reactor would have the same results in terms of the quality of the deposited epitaxial layers. Based on the flow of the gas into the reactor, the MOCVD reactors can be classified into two categories, namely vertical and horizontal MOCVD. The flow in the former is downward perpendicularly onto the substrate, while the flow in the latter is horizontal from three layers of gas injection nozzle inlet. The horizontal MOCVD reactor possesses the ability over the vertical MOCVD reactor to produce very uniform growth of epitaxial layer, especially for multi-layers (MLs). Figure 3.2 illustrates the schematic diagram for the process of the gases and the metal-organic (MO) sources entering the horizontal flow reactor through the three-layered gas injection inlets. As illustrated, the carrier gases of hydrogen (H_2) and nitrogen (N_2) will be carried in the top nozzle inlet, thus it counterbalances the pressure of the other two nozzle inlets. Moreover, the MOs enter through the middle nozzle inlet, while the ammonia (NH_3) that utilized as nitride is carried by the bottom nozzle inlets. The injection of the MO source and the NH_3 gas occur separately and then mixed together by the molecular diffusion. As a typical flow condition for the SR-2000 MOCVD, the design and the spacing for the gas separators as well as the position were made in a specific way; where the MOs diffuse laterally to the flow direction and then reach the substrate. Thus, a sheath of gas stream would isolate the mainstream of adduct $(CH_3)_3$: NH_3 from the heated reactor wall until it reaches the growth condition, in which the unfavorable upstream parasitic reaction is prevented (Ehrentraut et al., 2010; Matsumoto & Tachibana, 2004).

In contrast, to avoid the chemical reactions and physical abrasions, a graphite susceptor coated with silicon carbide (SiC) is utilized. The susceptor has a capacity of 1×2-inch wafer to be put on the top. The rotation speed of the susceptor is constant (10 rpm) against the steady gas stream during the growth to attain a uniform growth of epitaxial layers. In addition, the heater is positioned beneath the susceptor in order to assure a desired temperature for the growth.

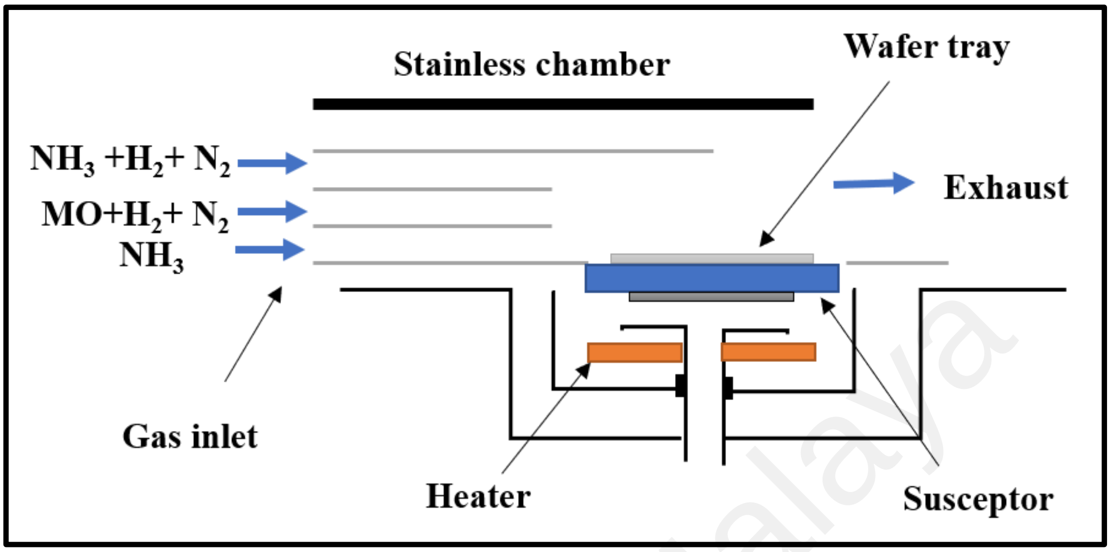

Figure 3.2: The process of the gases and the MO sources entering the horizontal flow reactor through the three-layered gas injection inlet (Ehrentraut et al., 2010).

The working principle for the MOCVD is that the MOs are carried into the reaction chamber, by which they are uniformly deposited onto the substrate. In turn, they decompose via pyrolysis in order to produce the epitaxial layers grown on the substrate. The H_2 and N_2 gases are employed as the carrier gases along the epitaxial growth and constantly utilized in certain reaction during the growth. It must be also pointed out that the H_2 and N_2 gases used during the growth must be purified by H_2 and N_2 purifiers.

The MO precursors employed in this study are trimethylgallium (TMG), trimethylaluminum (TMA), trimethylindium (TMI) and triethylgallium (TEG), whilst the NH_3 is utilized for the N source. In addition, the doping sources utilized for the p-type and n-type epitaxial layers were bicyclopentadienemagnesium (Cp_2Mg) and disilane (Si_2H_6) respectively. In general, the MO precursors are provided in sealed metal container (bubblers) due to the pyrophoric nature. The MO materials are carried to the reactor by flowing the gas into the bubbler, in which the gas enters the submerged dip tube in the MO. When the bubbling process occurs through the liquid MO, the carrier gas will be saturated with the vapor phase of the MOs, thus the MOs will be carried into the reactor. In addition, the carried amount of the MO materials will be dependent on the vapor pressure; whereas the flux of the MOs taken from the bubblers is determined as follows:

$$M_{MO}(mol/\,min) = \frac{F_C(sccm)}{22{,}400(cm^3/mol)} \times \frac{P_V}{P_T - P_V} \tag{3.1}$$

in which F_C , P_T and P_V are the carrier gas flow rate, the total pressure above the MO and the MO vapor pressure, respectively. Furthermore, the P_V demonstrated for a certain material at absolute temperature *T*, in which the parameters a and b are utilized as follows:

$$log(P_V) = a - b/T \tag{3.2}$$

It must be noted that the bubblers must be kept in chiller water, which is necessary for the exponential temperature dependence of P_V ; whereby the fluctuation in the temperature is avoided, thus the MO constant uniform delivery is not disturbed. Table 3.1 lists the abbreviation and the molecular formulas for some of the III-V precursors used in this study.

Table 3.1: Name and molecular formulas for some of the III-nitride precursors.

Abbreviation	Name	Formula
TMG	Trimethylgallium	$Ga(CH_3)_3$
TMA	Triethylaluminium	$(Al(CH)_3)_3)_2$
TMI	Trimethylindium	$In(CH_3)_3$
Cp_2Mg	Bicyclopentadienyl magnesium	$Mg(C_5H_5)_2$

In contrast, the NH_3 is considered as an ideal gas and can be calculated as follow:

$$M_{NH_3}(mol/\,min) = \frac{F_{NH_3}(sccm)}{22{,}400(cm^3/mol)} \tag{3.3}$$

Therefore, by using the Equations (3.1) and (3.3), M_{NH_3}/M_{MO} ratio can be calculated, which is referred as the V/III ratio.

The H_2 pellets and NH_3 cylinders are stored at high pressure that controlled by a flow of systematic pressure regulators, located at the gas yard. While, the N_2 is stored in a big tank as a form of liquid, which is then pressurized to be gas for the purpose of utilizing that in the MOCVD system. In addition, the pneumatic valves, the mass flow controllers (MFCs) and the pressure controllers are employed to electronically control the flux of the gases and MOs.

Furthermore, a computer is connected to the MOCVD through a mainboard system, which is called programmable logic controller (PLC). This in turn acts as a buffered interface between the computer and the gas as well as the MOs, allowing to handle components such as MFCs and valves. In general, the PLC performs safety interlocks, which mainly checked before the commands are given from the computer. It also possesses the ability to warn the user in case of mistakes and/or malfunctions such as leakage of toxic gases occurred in the system.

A two-inch m-plane sapphire substrate is introduced for the whole experimental procedure. As mentioned earlier, the MFC controls the amount of the MO source to be reacted with the NH_3 on the heated substrate. The basic thermodynamics during the deposition of GaN epitaxial layers in the MOCVD can be expressed in the chemical reaction as follows:

$$NH_3 \longrightarrow \frac{1}{2}N_2 + \frac{3}{2}H_2 \tag{3.4}$$

$$(CH_3)_3Ga + NH_3 \xrightarrow{T\,°C} GaN + 3(CH_4) \tag{3.5}$$

3.2 Vapor Phase Reaction: Quantum Chemical Study

This section prescribes the elementary process that is responsible for the parasitic reactions. Also, the methane unimolecular elimination of the TMG under the presence of the NH_3 will be discussed. The coordination interaction between the TMG and NH_3 is shown earlier in Equation (3.6). Here $M(CH_3)_3$ molecule, in which each molecule denotes as **1a**, **1i** and **1g** and M is designated for Al, In and Ga, and so forth. This $M(CH_3)_3$ molecule form with NH_3 owing to the coordinate bond of the M-N as seen in Equation (3.6).

$$M(CH_3)_3(\mathbf{1}) + NH_3 \longrightarrow M(CH_3)_3M{:}\,NH_3\ (\mathbf{2}) \tag{3.6}$$

The stabilization energy in the complex formation of the TMA: NH_3 is -23.17 kcal/mol (largest), while -18.92 kcal/mol and -18.22 kcal/mol for TMG: NH_3 and TMI: NH_3, respectively (Ehrentraut et al., 2010; Nakamura et al., 2000). The TMG can form a stable complex with the excess of the NH_3, which is attributed to its coordination bond with the molecules of NH_3 without a barrier of potential energy as follows:

$$Ga(CH_3)_3(\boldsymbol{1g}) + NH_3 \longrightarrow Ga(CH_3)_3{:}\,NH_3\ (\boldsymbol{2g}) \tag{3.7}$$

$$Ga(CH_3)_3 :\ NH_3\ (\boldsymbol{2g}) + NH_3 \longrightarrow H_3N:\ Ga(CH_3)_3{:}\,NH_3\ (\boldsymbol{3g}) \tag{3.8}$$

Under the excess of NH_3, the methane molecule can be eliminated by either the intermolecular collision of an NH_3 molecule and the complex **2g**, or the intermolecular reaction of the complex **3g**.

$$\begin{aligned} &H_3N:\ Ga(CH_3)_3Ga(CH_3)_3 \\ &\qquad\qquad :\ NH_3\ (\boldsymbol{3g}).or\ [(CH_3)_3Ga{:}\,NH_3(\boldsymbol{2g}) + NH_3] \\ &\longrightarrow Transition\ State1[\boldsymbol{TS1}] \longrightarrow\ H_3N:\ Ga(CH_3)_3{:}\,NH_2\ (\boldsymbol{4g}) + CH_4 \end{aligned} \tag{3.9}$$

Figure 3.3 illustrates the **TS1** geometry, where a molecule **3g** fragment was observed by Quadruple Mass Spectrometer spectroscopy as reported by (Bergmann et al., 1999).

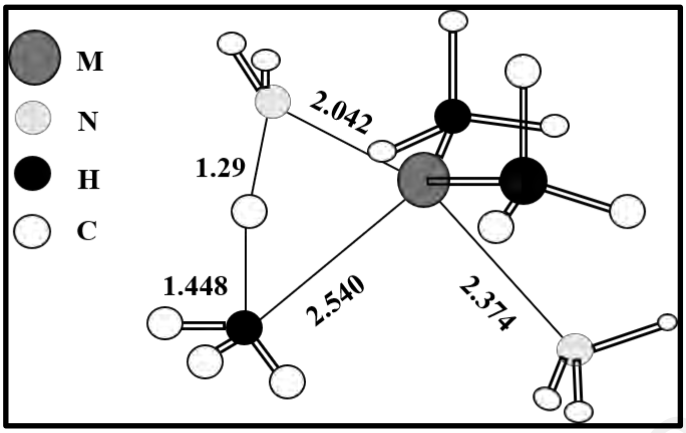

Figure 3.3: The TS1 geometry of M=Ga (Ehrentraut et al., 2010; Nakamura et al., 2000). Note: All the lengths of bonds in Angstrom.

As described in Equation (3.9), the reaction energy diagram is illustrated in Figure 3.4. It was found that under the presence of NH_3, the barrier of the potential energy is decreased through the **TS1** for each $M(CH_3)_3 + 2NH_3$. For instance, the gas-phase reaction for the TMA occurs fast with the excess of NH_3 since the barrier of the potential energy is decreased to 4.67 kcal/mol (Ehrentraut et al., 2010; Nakamura et al., 2000).

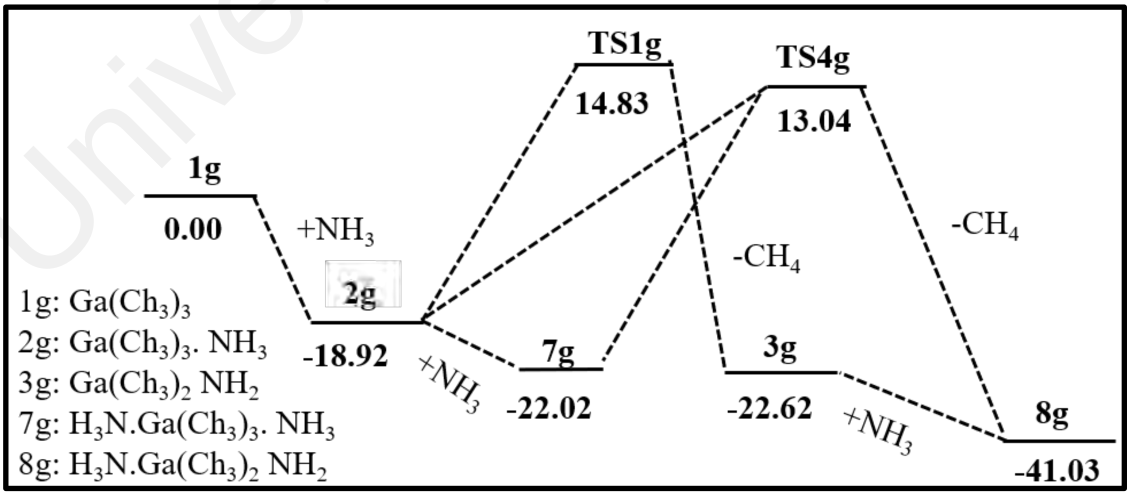

Figure 3.4: Potential energy for methane elimination diagram of TMG/NH_3 as described in equation (3.9) (Ehrentraut et al., 2010; Nakamura et al., 2000).

It is noteworthy that the stabilization energy of the coordination by the second molecule as mentioned in Equation (3.8) is relatively small; the reaction mainstream in Equation (3.9) will be the intermolecular reaction between an NH_3 molecule and the complex **2** along with effective energy transfer owing to the collision (Ehrentraut et al., 2010).

In contrast, the gas-phase reaction between the TMG and NH_3 was investigated using quantum chemical calculation (Watwe et al., 2000). It was estimated that the TMG:$(CH_3)_2GaNH_2$: NH_3 species possess the lowest barrier of the standard energy activation of the methane elimination. Furthermore, the spatial distribution and the elemental process of species was calculated in each step using computational fluid dynamics by Hirako and Ohkawa (Hirako et al., 2005). The main reaction pathway was proposed, namely (i) TMG: NH_3 adduct formation, (ii) elimination of methane from TMG: NH_3, and further followed by another elimination of methane and (iii) formation of GaN molecule as shown in Figure 3.5.

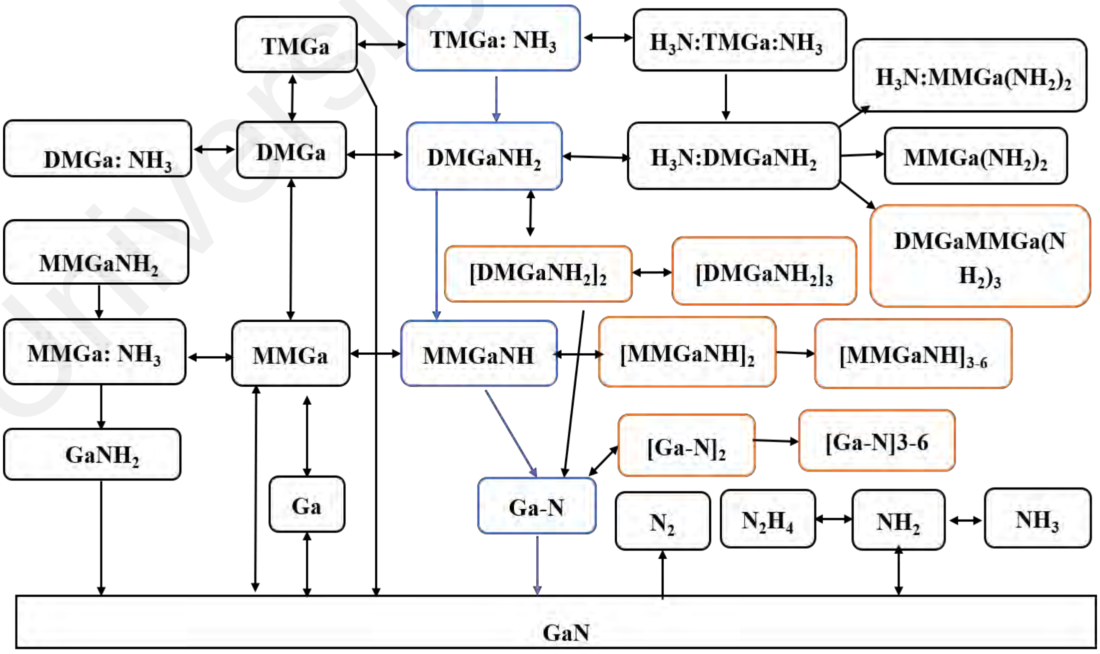

Figure 3.5: Schematic diagram for the GaN pathway reaction: Blue lines designated for the main pathway of the GaN and orange lines denoted for the plural Ga atoms (Ehrentraut et al., 2010; Hirako et al., 2005).

3.3 Growth Methodology

In this study, semi-polar (11-22) epitaxial layers were grown on m-plane sapphire substrate via SR-2000, Taiyo Nippon Sanso, Japan, MOCVD system. The growth procedure is divided into two parts, namely semi-polar (11-22) GaN templates and LED structures. The former deals with the H_2 thermal cleaning at 1125 °C, nitridation process 1050 °C, optimization of the uid-GaN with growth temperature of 1050 °C, the AlN nucleation layer at 1050 °C and the AlN/GaN ML at 1050 °C as illustrated in Figure 3.6. Whilst, the latter discusses the optimization of n-type GaN at 1050 °C and p-type GaN 1000 °C epitaxial layers, the multi-quantum well (MQW) InGaN/GaN at 700 °C and the full structure of light emitting-diode (LED) device as demonstrated in Figure 3.7. The pressure of the said growth methodology and annealing processes remained at 13.3 KPa.

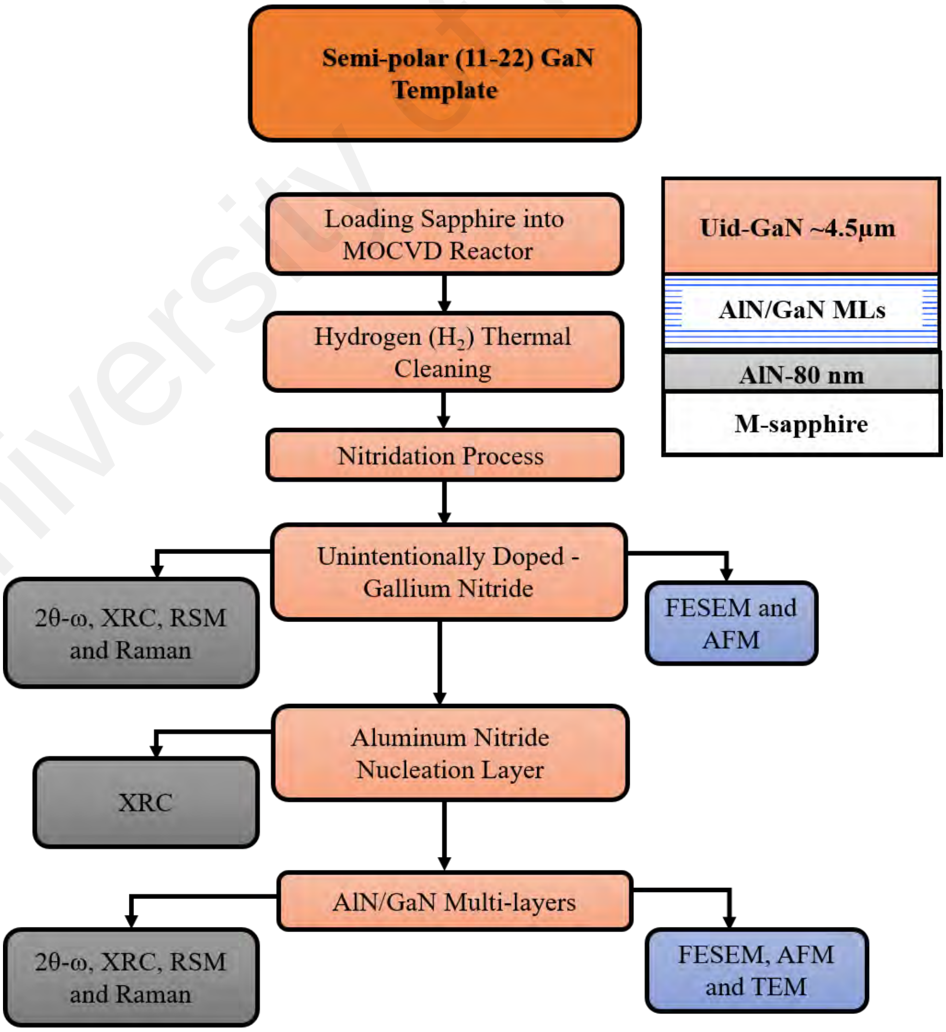

Figure 3.6: Methodology flowchart of semi-polar (11-22) GaN templates.

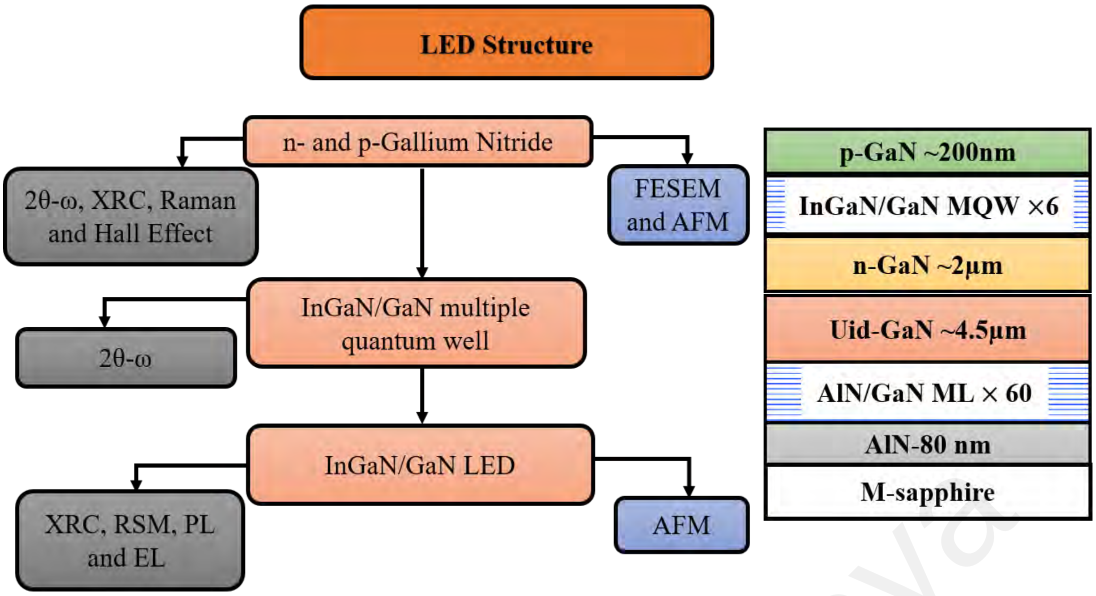

Figure 3.7: Methodology flowchart of LED structure.

3.4 Characterization Methods

The as-grown samples will be analyzed to study the stepwise improvement of the crystal quality and the surface morphology. The strain/stress states of the as-grown samples were characterized via room temperature Raman spectroscopy. The high resolution- x-ray diffraction (HR-XRD), involving $2\theta/\omega$ phase analysis (PA), on- and off-axis x-ray rocking curve (XRC) and reciprocal space mapping (RSM) were employed to examine the crystal quality. Whilst, the analysis of the surface morphology was conducted using AFM5000II atomic force microscopy (AFM), SU8220, Hitachi, field emission scanning electron microscopy and (FESEM). In addition, JEM-2100F, Jeol, transmission electron microscopy (TEM) was implemented to further study the reduction mechanism of defects and dislocations. Finally, the optical and the electrical analysis were conducted using room temperature photoluminescence (PL), electroluminescence (EL) and Hall Effect measurements.

3.4.1 Raman Spectroscopy

In the measurement of Raman spectroscopy, the main measured output is resulted from the Raman effect. The occurrence of possible scattering process would be resulted from an interaction of the incident beam projection and a matter that is being radiated. Figure 3.8 illustrates the three cases, namely (a) Rayleigh scattering, (b) Stokes and (c) anti-Stokes. In the case of Rayleigh scattering (a), a photon of a frequency v_0 is absorbed by a molecule, which in turn changes the state of photon from the basic vibrational energy state to virtual energy state. Then, the molecule returns to its vibrational energy state while the radiation is similarly emitted with the frequency of the incident photon v_0. In addition, the case of the Rayleigh scattering occurs the most as the photons scatter in such a manner. In this process, the distortion of the electron cloud is taken into consideration with no nuclear motion involved. However, energy transferred between the molecule and photons is observed when the nuclear motion is involved in the scattering process, in which the energy of the scattered photon is different from the incident photon, leading to Raman scattering.

In this case, the Raman scattering can be observed in the case of Stokes and anti-Stokes, where the photons are reduced, as shown in Figure 3.8 (b) & (c), respectively. In the case of Stokes as seen in Figure 3.8 (b), when the molecule is radiated to the state of virtual energy, it returns back to a higher vibrational energy, where less photon energy is released; a portion of the photon energy is transferred to the molecule and therefore the nuclear motion releases less irradiation of a photon. However, in the case of anti-Stokes (c), the molecule which is in excited vibrational energy state, transfers a part of its energy to the released photon during the reradiated emission. In this case, the anti-Stokes will have a higher energy of reradiated photons as compared to the incident photons.

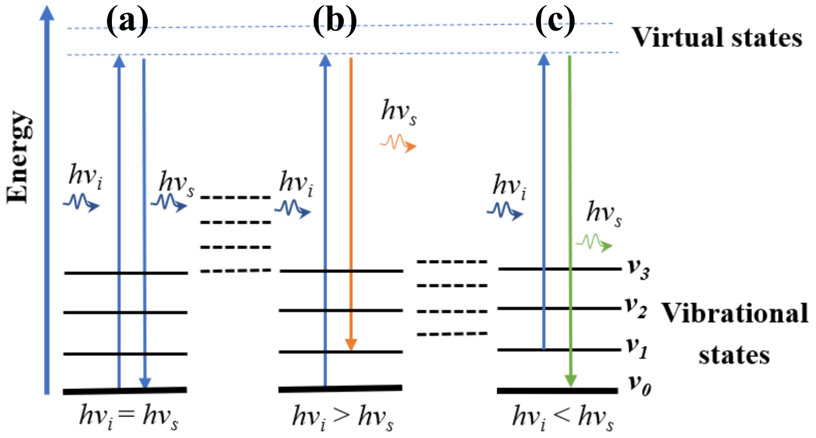

Figure 3.8: Schematic diagram of scattering effect induced in (a) Rayleigh scattering, (b) Stokes and (c) Anti-Stokes. Note: $h\nu_i$ and $h\nu_s$ are the incident and emitted photon energies, respectively.

In the Raman spectroscopy, the desired sample is radiated using a single frequency of radiation, where the radiation is scattered from the molecule. The vibrational unit of energy difference to the incident radiation is observed, thus the molecular identification of radiated material is obtained. In other words, the wurtzite (WZ) crystal structure of GaN possesses optical phonon modes of E_1 (TO), A_1 (TO), E_2 (high), in which the atomic displacement of phonon modes is changed. Hence, the shift in these phono modes is mainly caused by the relaxation state of the as-grown epitaxial layer.

The general working principle and the utilized Raman spectroscopy system in this study are displayed in Figure 3.9 (a) & (b), respectively. The incident light from a laser is utilized as a radiation source, which is commonly observed in Raman spectroscopy. The main challenges in the Raman spectroscopy is the difficulty of separating Raman scattering from the intense Rayleigh scattering. In order to remove the stray light from the Rayleigh scattering, the notch filters are employed. If the sample is being focused by the microscope, the radiation of the sample is obtained with the incoming laser, resulting in scattered photons to be collected at the CCD detector as shown in Figure 3.9 (a). The charged created on the CCD converted to light pattern digital copy before the Raman spectra is generated.

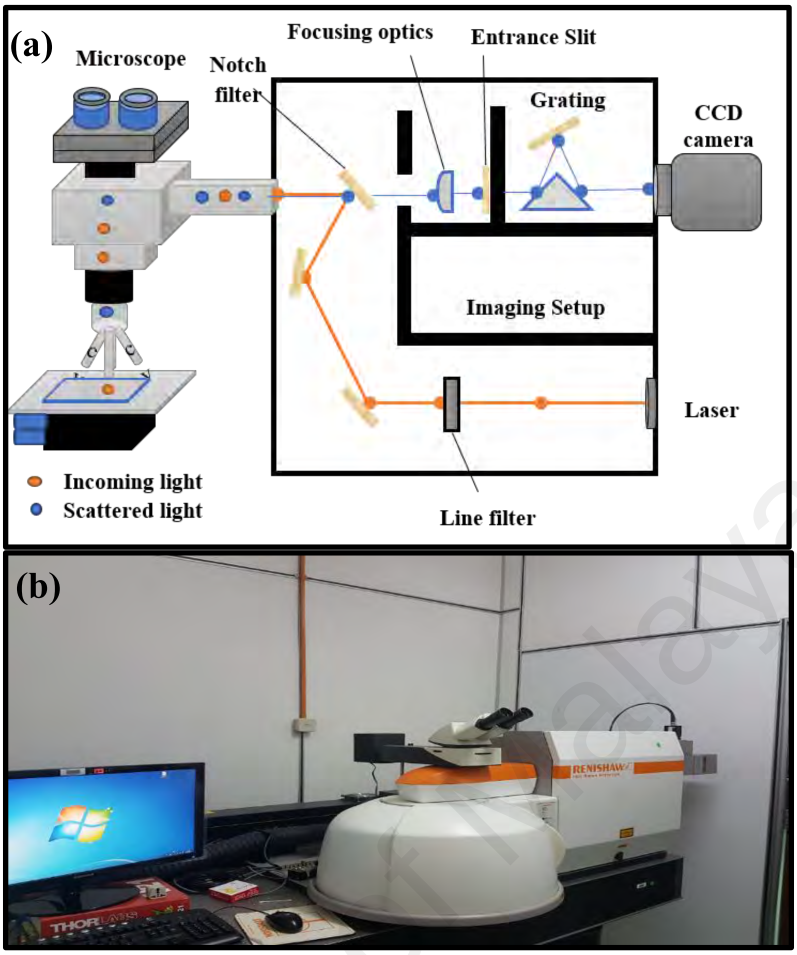

Figure 3.9: (a) Schematic diagram of Raman spectroscopy working principles and (b) The Raman spectroscopy instrument (Renishaw in Via Raman Microscope).

In this work, the usage of Renishaw in Via Raman microscope (Gloucestershire, UK) is seen to analyze the compressive stress/strain state. The Raman microscope used in this study is equipped with a He-Cd laser of 325 nm with a scanning range of 200-800 cm^{-1}. Prior to the measurement, the 2-inch sample will be placed on the sample holder underneath the microscope where the alignment and calibration will be conducted.

3.4.2 High-Resolution X-ray Diffraction (HR-XRD)

HR-XRD is a conventionally multipurpose non-destructive crystal characterization tool that can be utilized to examine the crystal quality, strain/stress state and the surface orientation of the as-grown epitaxial layer. Basically, the HR-XRD differs from the normal XRD in the utilized components in the during the measurement such as 2-bounce or 4-bounce monochromator, goniometer and 1D or 2D detectors. These advanced components are usually utilized to study deviations from the ideal crystal structure, the structure of individual diffraction peaks, defects and dislocations. However, the principle is the same as for any XRD. The XRD measurement is based on the monochromatic constructive interference, which is diffracted by the crystal sample. The x-rays are generated by a cathode ray tube, which then filtered to produce a monochromatic radiation. Then, they are collimated to a concentrated beam and focused towards the tested sample. Thus, the constructive interference of the x-rays is generated from the interaction between the incident beam and the tested sample, satisfying Bragg's Law as follows:

$$2d\ sin\,\theta = n\lambda \tag{3.10}$$

whereby λ, n, θ and d are the x-ray wavelength, the diffraction order, the incident angle, and interplanar spacing of the reflecting planes, respectively.

It should be noted that the scattered x-rays will undergo destructive interference in case of other angles than θ, thus the signals are not distinguished by the detector. Therefore, the interplanar spacing of the crystal phase is revealed by the θ determination. As shown in Figure 3.10, in general, the HR-XRD instruments comprise three main parts, namely x-ray source, goniometer (sample stage) and x-ray detector. Here, there are two main parts were utilized as established by Rigaku HR-XRD, which were incident optics (Ge (220) two-bounce monochromator) and receiving optics for high resolution measurement. The x-rays are mainly generated by an x-ray tube (vacuum tube), in which high voltage is utilized (10-40kV). This is due to the fact that a hot cathode would accelerate the released electrons to a high velocity. Then, the high-velocity electron will hit the metal target (anode), thus the x-ray is generated. In the current study, the XRD measurement were carried out using Rigaku HR-XRD system as shown in Figure 3.10.

Prior the measurement, the 2-inch specimen was placed on sample stage with calibrated alignment by performing the manual of phi (*φ*) and omega as to define the zero degree of the azimuthal angle (*Φ*).

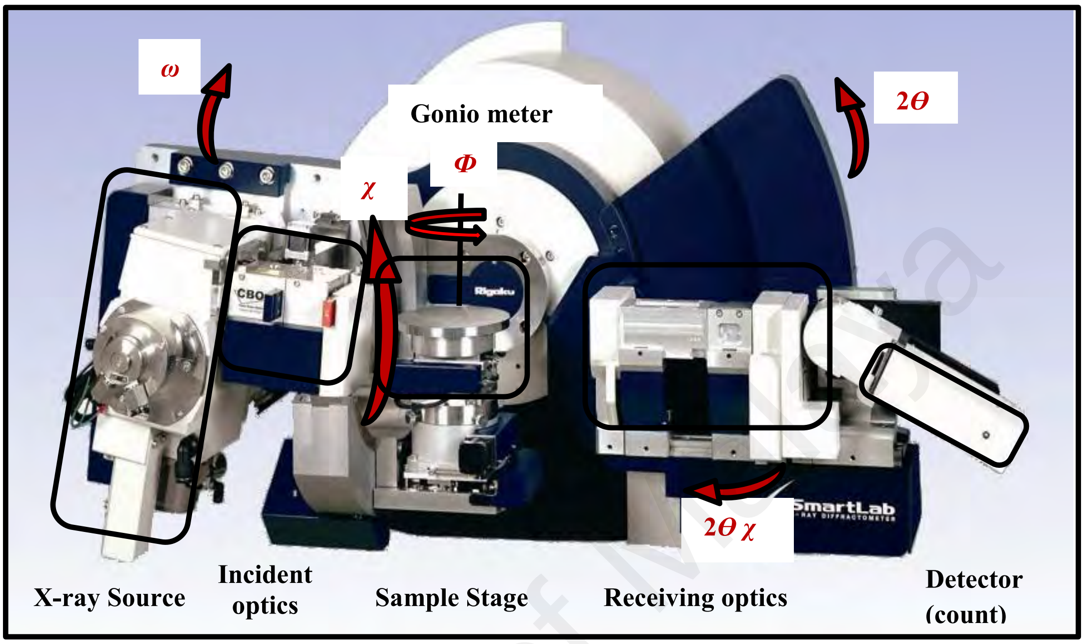

Figure 3.10: Rigaku HR-XRD system employed in this study.

3.4.2.1 X-ray Rocking Curve (*ω*-scan)

In the XRC measurement, the distributions of the diffraction intensity along the reciprocal lattice vector is measured. This measurement does not require incident and the exit angles of the x-ray relative to the surface is equal to each other. In the XRC measurement, the $2\theta/\omega$ is scanned, where the change in the diffraction angle 2θ is twice the change in the incident angle ω. The XRC measurement is used to evaluate the epitaxial layer crystallinity; the diffraction peak at a specific angle would be broadened due to defect in the crystals, resulting from the tilt in the Bragg's angle. There are two types of scan in the XRC measurement introduced in this study, namely symmetric plane (on-axis) and asymmetric plane (off-axis). The standard on- and off-axis XRC measurements are employed to investigate the anisotropic characteristics and the planar defects of the epitaxial layers. Figure 3.11 (a-c) illustrates the schematic diagram of the experimental setup, on-axis plane and off-axis plane, respectively.

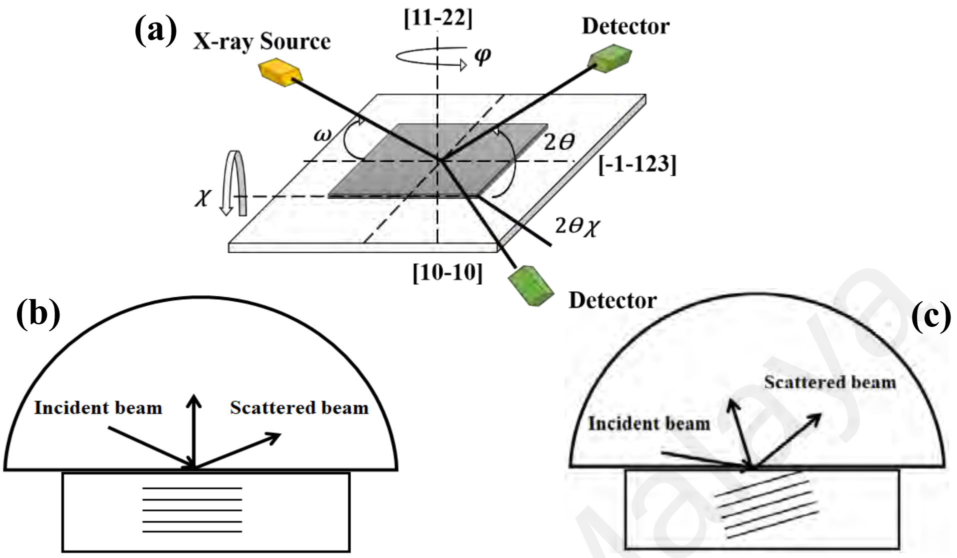

Figure 3.11: (a) Schematic diagram of the experimental setup, (b) The on-axis plane and (c) The off-axis plane.

The first scan assessed here is the M-shapes azimuthal dependence of FWHM over 360°. The detector should be stationary and the sample stage is rotating with *Φ* around the surface normal. The on-axis XRC of the (11-22) reflection of the as-grown epitaxial layer is carried out as a function of *Φ*. In addition, the incident beam projection was parallel to [-1-123] as the angle was set at 0°, while parallel to [1-100] when the angle was set at 90°. In contrast, the off-axis XRC is introduced to investigate the other types of defects such as basal stacking faults (BSFs), partial dislocations (PDs) and/or perfect dislocation since the on-axis XRC was reported to be insensitive to BSFs based on the visibility criteria (Moram & Vickers, 2009; Sun, et al., 2009b; Williams & Carter, 1996). As reported in the literature, the BSFs are present in the microstructure of the semi-polar (11-22) epitaxial layer and might result from the mismatches between the as-grown epitaxial layers and the sapphire substrate (Moram et al., 2009; Moram & Vickers, 2009; Vennegues et al., 2007).

The anisotropic characteristics and the planar defects of a semi-polar (11-22) GaN epitaxial layer can be studied based on the reflection planes as shown in Figure 3.12 and Table 3.2. The off-axis diffraction planes assessed in this study are (10-11), (10-10), (11-20) and (0002). In order to obtain these diffraction planes, the tilt (χ) with respect to the surface normal and Φ must be aligned.

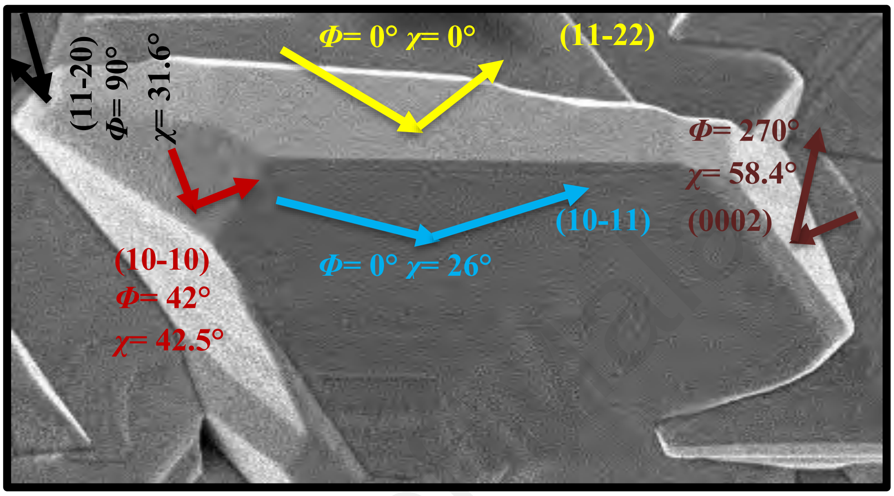

Figure 3.12: FESEM side-view image of semi-polar (11-22) GaN labelled with different diffraction planes for on- and off-axis XRC measurements (Leung, et al., 2009b).

Table 3.2: The values of ω, 2θ and χ for each diffraction plane in the off-axis XRC measurements.

Diffraction Plane	ω°	2θ°	χ°	**Incident Beam Direction**
(10-11)	18.43	36.95	26.18	(101)
(10-10)	16.24	32.48	42.48	(100)
(11-20)	28.97	57.95	31.61	(110)
(0002)	17.35	34.70	58.38	(002)

3.4.2.2 Phase Analysis ($2\theta/\omega$ scan)

Unlike the XRC measurement, the $2\theta/\omega$ scan cannot be utilized to investigate the crystal quality. It is, however, utilized to estimate the composition of a ternary alloy, a structure of multi-layer, a layer thickness and the crystal orientation of the as-grown epitaxial layer. For instance, a structure of semi-polar (11-22) AlN and GaN with a thickness of 100 nm and 1 μm, respectively, can be detected by rotating the 2θ and ω at the 2:1 ratio in the same direction. The HR-XRD $2\theta/\omega$ scan is done by rotating the sample stage by ω, while the detector by 2θ. In this study, the HR-XRD $2\theta/\omega$ scans were obtained to elucidate the crystal orientation for the as grown epitaxial layers.

3.4.2.3 Reciprocal Space Mapping (RSM)

The RSM measurements were implemented to investigate the crystal orientation, relaxation state and the type of defects forming in semi-polar (11-22). In the RSM measurement, the distributions of the diffraction intensity are obtained by scanning the sample rotation and the diffraction angle, then plotting the results in the reciprocal space. The peak position and shape of the reciprocal lattice points (RLPs) are obtained by scanning the 2θ and ω in the scattering plane by specific values of χ and Φ. The (11-22) measurements were carried out along [-1-123] and [1-100] as the tilt in RLP would be examined for both directions. As reported in the literature, the RSM measurement could be utilized to investigate prismatic stacking faults (PSF) via the peak elongation of the diffuse scattering (DS) streaks along [-1-123] (Lazarev et al., 2013; Pristovsek et al., 2016). As illustrated in Figure 3.13 (a) & (b), the diffracted beams resulted from the epitaxial layer and the sapphire substrate generate a distribution in the reciprocal space along [1-100] and [-1-123], respectively. In a view of this situation, therefore, a one can study the occurrence of the streak in the RLP and investigate the defect and relaxation state in the as-grown epitaxial layer. In addition, the measurement of RSM is performed by the scanning the ω and 2θ axes in the scattering plane as specified by certain values of χ and Φ. The RSM measurement in this study consists of three scanning methods as illustrated in Figure 3.13 (c): i) $2\theta/\omega$ step ω scan, which change the $2\theta/\omega$ gradually while repeat ω scan; ii) ω step $2\theta/\omega$ scan, which repeat the $2\theta/\omega$ scan while gradually change ω; iii) Mesh measurement, in which the axes are scanned while the step intervals in the coordinates (q) are maintained constant.

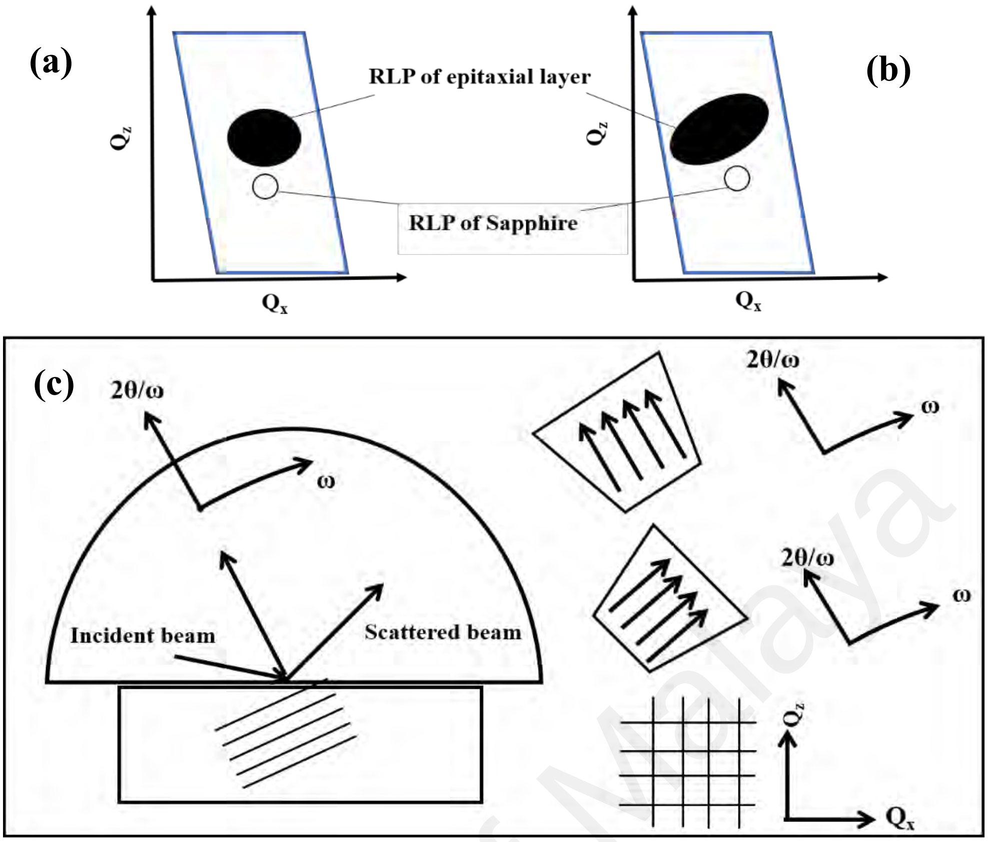

Figure 3.13: Reciprocal space mapping of (11-22) reflection along (a) [1-100] direction, (b) [-1-123] direction and (c) the type of measurement performed for the RSM.

3.4.3 Atomic Force Microscopy (AFM)

The surface morphology analysis of the epitaxial layers was characterized by AFM measurement. AFM is a type of high-resolution scanning probe microscopy that is utilized to provide 2D and 3D information of surface in the atomic scale. The AFM measurement is divided into three modes, namely contacting, non-contacting and tapping modes. In the contacting mode, the tip would be in a direct contact with the surface of the thin film, which may destruct either the surface of the thin film or the tip. A deformation between the tip and the surface of the thin film to different extend is resulted as the tip scan across the surface. Furthermore, there is a tiny laser located in the tip, whereby the reflected phase of a laser varies with the deformation. In contrast, in the non-contact mode, the tip hovers 5-10 nm over the sample surface, leading to low-resolution images. Furthermore, the provided imaged might be affected by the contaminant layers, resulting in an interference with the phase of the oscillation. On the other hand, in the tapping mode, high-resolution images will be obtained since the tip is in contact with the surface. The tip will be lifted off the surface to prevent dragging across the surface. The cantilever tip will be oscillating approximately at its resonance frequency.

Basically, the AFM comprises of feedback system, position-sensitive photodetector, a sample stage as well as a laser beam as schematically illustrated in Figure 3.14 (a). As it can be observed from the Figure, the tip will in contact with the specimen to scan across the surface. Then, the deflection of the cantilever is according to the Hooke's law is resulted from the atomic force between the surface and the tip. Meanwhile, the focused laser on the back side of the cantilever will be reflected to the photodetector. Then, the cantilever deflection degree will be measured by the detector, while a constant deflection between the specimen and the tip remained by the feedback system using the adjustment of the tip position; the information of this position will be transferred to the software to produce the surface morphology. In this study, AFM5000II instrument is used as illustrated in Figure 3.14 (b). Additional sample preparation is required prior to the AFM measurement. This includes i) sample cleaving from 2-inch to 1×1 cm, ii) ozone cleaning of the pre-cut specimen for thirty minutes to remove the possible contaminations, iii) loading of the sample into the chamber, while performing a rough scan to determine the accurate positioning of tip.

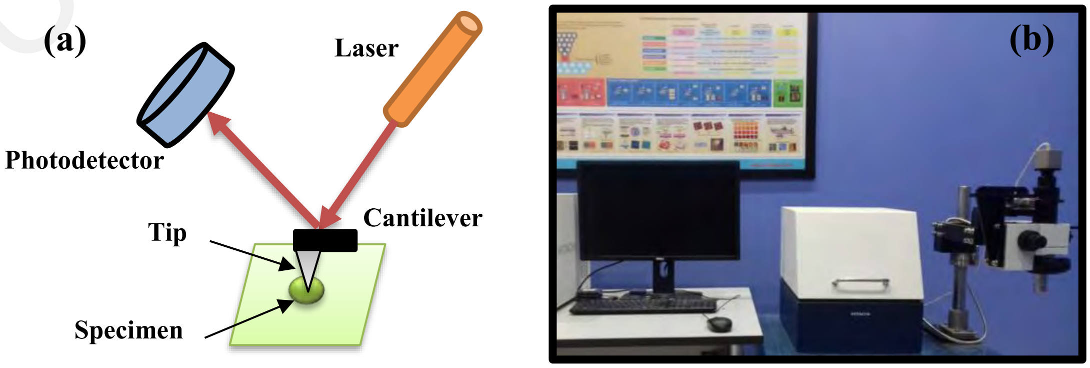

Figure 3.14: Schematic representation of AFM working principle and (b) AFM instrument used in this study.

3.4.4 Field Emission Scanning Electron Microscopy (FESEM)

FESEM measurement was implemented to further analyze the surface morphology of the as-grown epitaxial layers. FESEM measurement is an electron microscopy that generates images of the measured samples by scanning focused electron beam on the sample; whereby it measures the signals that possesses information of the surface morphology using the detector. It is noteworthy that the main advantage of the FESEM measurement as compared to the optical microscope is the FESEM possesses higher magnification and resolution, leading to very small scan size inspection (down to nano-meter). FESEM is considered similar to the scanning electron microscopy (SEM), in which the electrons are utilized to illuminate the samples. However, the FESEM is able to produce less electrostatically distorted images owing to the FE source, a smaller electron beam is produced. In addition, the use of an extremely thin and sharp electron gun is introduced in the FESEM, while the heating of the tungsten filament is used in the SEM. The FESEM works, as an electron microscopy, in a vacuum situation in order to remove the contaminants from the electron column. Figure 3.15 illustrates a schematic diagram of the general working principle of FESEM, while Figure 3.16 shows the FESEM (SU8220 Hitachi, Tokyo, Japan) instrument used in this study.

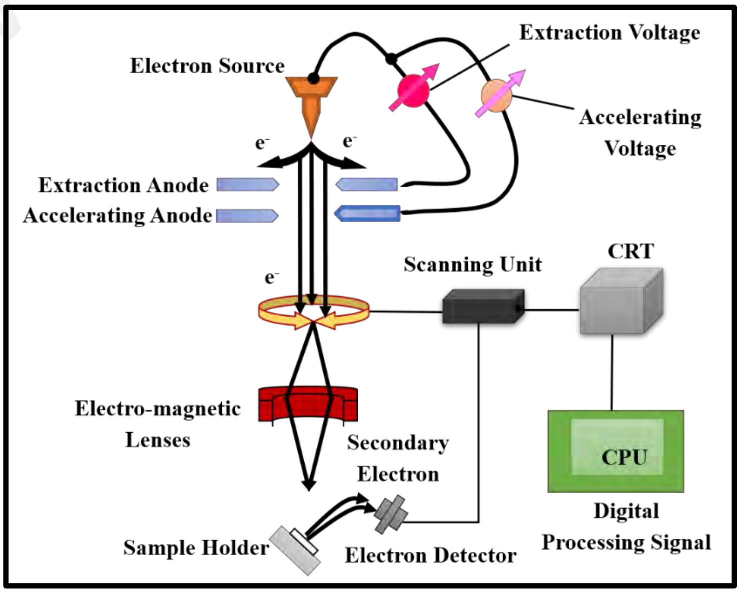

Figure 3.15: Schematic illustration of the FESEM working principle.

Figure 3.16: Image of FESEM instrument (SU8220, Hitachi, Tokyo, Japan).

As displayed in Figure 3.15, when the extraction voltage is applied, the electron emitted from the cathode is extracted, leading to more efficient extraction as the anode is presented. Subsequently, the accelerating voltage will be applied to the anode, whereby the electron beam travels down to the column. The resulted electron beam will pass through the electro-magnetic lens, creating a narrow beam of electrons that focuses on the specimen. Next, the emission of a secondary electron will be obtained from the specimen when the bombardment occurs. At this stage, a secondary electron is captured by the electron detector and transduced to a signal, which it is fed to the cathode ray tube (CRT). Finally, the as-obtained signals will be amplified and converted to an image, which can be displayed on the monitor.

Additional sample preparation is required prior to the FESEM measurement, which includes sample cutting similar to the AFM sample preparation as well as the ozone cleaning. Upon loading the specimen, beam alignment of the electron beam is accomplished by changing the z-axis of the sample stage as well as manipulating the optimum beam in accordance to the sample requirement.

FESEM has several advantages as compared to AFM. The most crucial advantage is the image captured form the FESEM is much larger scale size compared to AFM. Furthermore, the measurement of the FESEM usually takes few seconds unlike AFM, taken several minutes, which is considered time-consuming. In contrast, it should be also noted that the AFM has some advantages over the FESEM measurement such as i) 2D and 3D images can be obtained from AFM, while only 2D images can be achieved from FESEM and ii) AFM can be operated at atmospheric pressure, whilst FESEM must be operated in a high vacuum condition.

3.4.5 Transmission Electron Microscopy (TEM)

In a remarkable contrast to FESEM, TEM was used to allow a direct imaging for the structure of as-grown epitaxial layers on m-plane sapphire substrate. Using TEM, the direct imaging can be obtained since the electrons are accelerated by high voltage source of 200 kV. A very powerful magnification as well as high resolution image can be obtained from the TEM analysis, however, the TEM measurement is limited to a very small sample. Hence, a careful procedure must be executed in order to obtain ultra-thin with a small size samples, in which the electron beam passes through. Yet, the TEM measurement possesses a wide range of applications in semiconductors, whereas it is beneficial for crystal quality and morphological properties. In addition, the characterization of TEM can be accomplished in an atomic dimension owing to the high spatial resolution. Therefore, the structural defects and dislocation such as BSFs and TDs in the crystal lattice can be observed.

Five of the main parts in TEM instrument (Jeol, JEM-2100F) are electron source (illumination system), magnetic lens (electromagnetic system), the stage of the sample, projection lens (projection system), as well as the imaging plate as shown in Figure 3.17 (a) & (b). The TEM measurement is initiated when the electrons are generated from the illumination system. These electrons will be accelerated to high energies, and focused towards the sample then. The beam direction can be acquired by the electromagnetic system. It must be noted that the sample stage is placed into the electron beam path, in which the sample should be very thin to let the electron beam pass through. When the electron beam in contact with a sample, it traverses through the specimen. Therefore, it will scatter through the projection lens, and it will be further reached to the scintillator plate. In turn it will be converted to different light energies, resulting in various contrast imaging that defines the atomic structure of a specimen. However, for TEM imaging, a complex yet elaborate sample preparation is required: focused ion beam (FIB). The main stages of the sample preparation include i) cleaving the 2-inch sample to 1×1 cm. It should be noted that the orientation direction must be determined based on the required displacement vector as the thinning via the FIB would be conducted on that specific direction. ii) The loading of the specimen into the FIB chamber, whilst assuring the desired imaging side of the specimen. In order to extract a significantly small area of the specimen (as the TEM stage requires relatively small specimen), the ion beam must first bombard the surface of the specimen to the desired depth (thickness) at both end of the specimen. It is noteworthy that the beam exhibits a curve projection, in which upon reaching the desired depth it can be aligned to meet the opposite end of the specimen (ready for extraction). iii) The extracted specimen will now be attached to a cooper grid (specimen holder for TEM). iv) Lastly, thinning of the specimen to a desired thickness via the ion beam will be conducted prior to the TEM measurement.

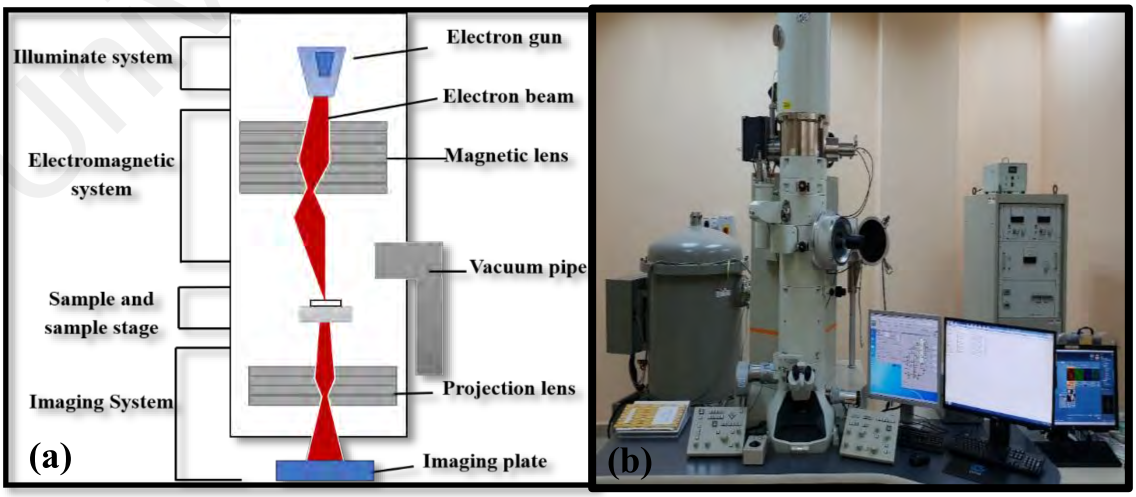

Figure 3.17: (a) Schematic illustration of the TEM working principle and (b) Jeol, JEM-2100F TEM instrument utilized in this study.

3.4.6 Photoluminescence Spectroscopy (PL)

The photon emission resulted from a photon excitation process is known as photoluminescence. PL measurement is a spectroscopy technique that can be utilized to investigate the electrical and optical properties of a III-V semiconductor. As mentioned in Chapter 2, the bandgap energy of a III-V semiconductor is given by the energy difference between the valence and conduction bands. In this study, the PL measurement is utilized to study the luminescence properties of the semi-polar (11-22) InGaN/GaN-based LED. As illustrated in Figure 3.18, the process of the PL emission is given as the electron are excited to a higher state of energy by photon, they jump to the excited state. Due to the non-stability of the excited state, these electrons will fall to a stable state (conduction band). Then, these electrons will fall back to the valence band. Since the process mostly occur between the states of valence and conduction band, the emitted photon energy is equal to the bandgap of III-V semiconductor. In contrast, other forms of energy might be released rather than photons by the transition of electron such as electronic excitation and lattice vibrations, known as non-radiative transitions process. Similar sample preparation to Raman spectroscopy was performed in PL measurement.

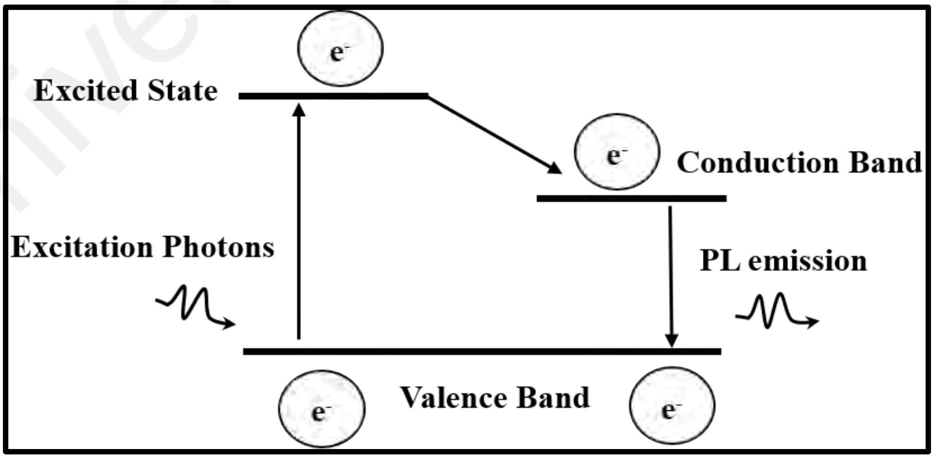

Figure 3.18: A basic Photoluminescence theory interpretation.

3.4.7 Hall Effect Measurement

Hall effect analysis is employed in order to measure the carrier concentration (n or p) as well as the mobility (μ) for semi-polar (11-22) n- and p-type GaN. In the equilibrium state, the intensity of the electric field (resulted from the Hall effect) will exert a force on the carriers, in which the magnetic force is balanced, given as follows:

$$qE = Bqv \tag{3.11}$$

in which, q and v are the magnitude of the charge on the carriers and the drift velocity, respectively. From $E = V_H/d$ and $J = nqv = I/wd$, where d and w the thickness and the width of the specimen, while J and n are the current density and charge density, respectively. (Millman & Halkias, 1972). By combining these equations:

$$V_H = Ed = Bvd = \frac{BJd}{n} = \frac{B.I}{nqw} \tag{3.12}$$

The charge density (n) is determined if V_H, B, I, as well as d are measured. Thus, the Hall coefficient can be defined by:

$$R_H = \frac{1}{nq} \tag{3.13}$$

This will lead to:

$$R_H = \frac{\mathrm{V_H d}}{\mathrm{B.I}} \tag{3.14}$$

In addition, the conductivity is related to the mobility as mentioned by Millman and Halkias (Millman & Halkias, 1972), as follows:

$$\sigma = nq\mu \tag{3.15}$$

Hence, the mobility is determined as the conductivity and the Hall coefficient are measured, given as:

$$\mu = \sigma R_H \tag{3.16}$$

The principle of the Hall effect measurement is shown in Figure 3.19, in which the B and I are in the positive direction of X and Z, respectively. While the force is exerted towards the negative direction of Y. As shown in the Figure, the current I might be either due to the free electrons traveling from right to left, or holes moving from left to right. Hence, regardless the movement of the hole and electrons, they will be forced downwards. In case of semiconductor with n-type material, the current is carried by the electrons, and these electrons are accumulated on the right side as depicted in the Figure. This in turn lead to negatively charged as compared to the left side, resulting in a potential between the two sides called Hall voltage V_H. However, if the left side becomes positively charged as compared to the right side, the semiconductor is a p-type material. A standard Van Der Pauw sample preparation was conducted prior to the measurement, including sample cleaving to 1×1 cm, standard metal contacts deposition, and finally probe adjustment to the edge of the specimen.

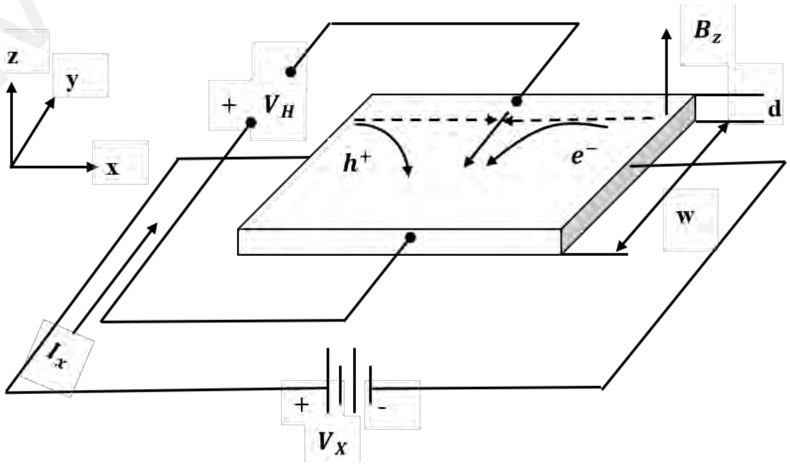

Figure 3. 19: Hall effect working principle.

CHAPTER 4: THE GROWTH OF SEMI-POLAR (11-22) UID-GAN

In this study, the effect of ammonia (NH_3) flux towards the enhancement of crystal quality of unintentionally doped-gallium nitride (uid-GaN) grown on m-plane sapphire substrate is presented in Section 4.1. The impact of NH_3 flux for the growth of aluminum nitride (AlN) nucleation layer is shown in Section 4.2. Finally, the growth of AlN/GaN multi-layer (ML) sandwiched between the nucleation layer AlN and uid-GaN epitaxial layer was attained and demonstrated in Section 4.3. The number of pairs for semi-polar (11-22) AlN/GaN ML was varied to examine its influence towards the enhancement of semi-polar (11-22) uid-GaN epitaxial layer. The crystal quality of the semi-polar (11-22) epitaxial layers grown on m-plane sapphire substrates was studied by high resolution-x-ray diffraction (HR-XRD), inclusive of $2\theta/\omega$, on- and off-axis x-ray rocking curve (XRC) and reciprocal space mapping (RSM), while the strain/stress properties were examined by room temperature (RT) Raman spectroscopy. In addition, the surface morphology of the grown epitaxial layers on m-plane sapphire substrates were characterized using field emission scanning electron microscopy (FESEM) and atomic force microscopy (AFM). Finally, transmission electron microscopy (TEM) was further utilized to investigate the reduction mechanism of the defects and dislocations.

4.1 Optimization of NH_3 Flux for the Growth of Semi-polar (11-22) Uid-GaN

4.1.1 Growth Methodology

The growth of semi-polar (11-22) uid-GaN epitaxial layers was accomplished by varying NH_3 flux as illustrated in Figure 4.1. Four samples of different NH_3 flux were introduced to investigate the effect of NH_3 flux towards the quality of semi-polar (11-22) uid-GaN epitaxial layers, namely S1, S2, S3 and S4 grown on top of AlN nucleation layer. The trimethylgallium (TMG) flow of the growth of uid-GaN epitaxial layers remained constant at 59.5 standard cubic centimeters per minute (sccm), while the NH_3 flux was varied from 8.3 to 0.7 standard liter per minute (slm). After annealing the m-plane sapphire substrate for 10 minutes at 1125 °C in hydrogen (H2) ambience, the nitridation process was carried out at 1050 °C. Then, the AlN nucleation layer of 80 nm thickness was grown on the m-plane sapphire substrate, followed by the 4.5 µm thickness of uid-GaN growth. The growth temperature of both AlN nucleation layer and uid-GaN epitaxial layer was 1050 °C.

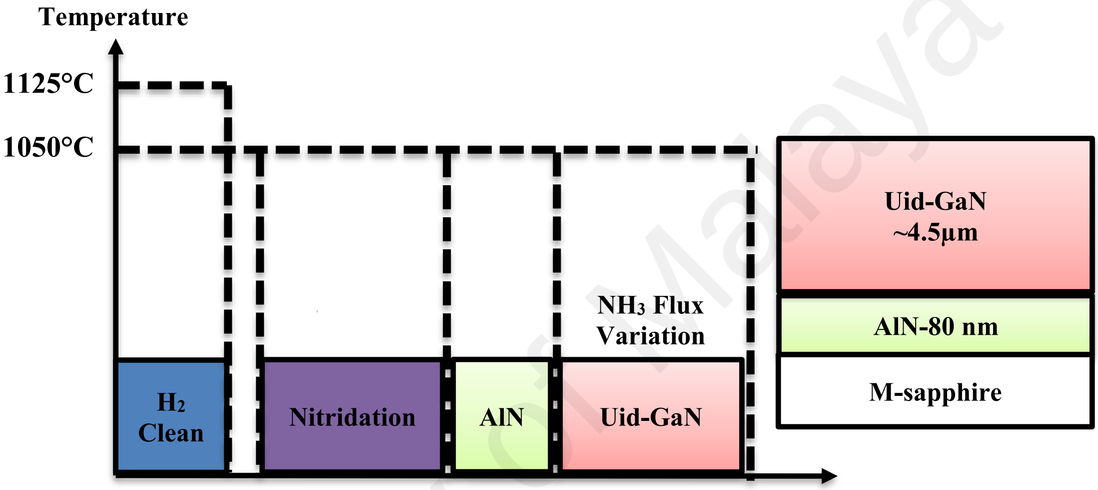

Figure 4.1: Illustration of the growth procedure of the uid-GaN epitaxial layers.

4.1.2 Effect of the NH_3 Flux on the Crystal Orientation

A measurement of HR-XRD $2\theta/\omega$ scan was performed to investigate the crystal orientation of the uid-GaN epitaxial layers grown on m-plane sapphire substrates. The abbreviations of the uid-GaN epitaxial layers are tabulated in Table 4.1 with the flow rate of the TMG, NH_3 flux as well as the diffraction peaks.

Table 4.1: Summary of the NH_3, TMG flow as well as diffraction peaks for the grown uid-GaN epitaxial layers (S1-S4) on m-plane sapphire substrate.

Samples	**S1**	**S2**	**S3**	**S4**
TMG Flow (sccm)	9.5	59.5	59.5	59.5
NH_3 Flux (slm)	8.3	5.3	2.6	0.7
Diffraction peaks	(10-10) (10-13) (11-22)	(10-10) (10-13) (11-22)	(10-10) (10-13) (11-22)	(11-22)

The HR-XRD $2\theta/\omega$ scans of the uid-GaN epitaxial layers grown on m-plane sapphire substrates are demonstrated in Figure 4.2. As shown in the Figure, three common diffraction peaks for S1-S4 can be clearly seen at 71.4°, 69.0°, and 68.2°, ascribing to semi-polar (11-22) AlN, semi-polar (11-22) GaN and m-plane sapphire substrate, respectively. As a high NH_3 flux (S1) was utilized for the growth of uid-GaN, a main peak of semi-polar (11-22) GaN located at 69.0° and minor peaks of semi-polar (10-13) GaN as well as m-plane (10-10) GaN located at 64.0° and 32.4° were observed, respectively. This could be attributed to the twinned GaN crystallites (Ploch et al., 2010). In contrast, when the NH_3 flux was decreased (S2), the intensities of diffraction peak for m-plane GaN (10-10) and semi-polar (10-13) GaN slightly diminished, which in turn shows a slight enhancement in the crystal orientation as it can be further discussed in the structural and morphological analysis.

After further decrease in the NH_3 flux (S3), the diffraction peak of (10-13) GaN was absent and no changes to (10-10) GaN were observed due to incomplete growth coalescence. When the lowest NH_3 flux (S4) was used, only the diffraction peaks attributed to semi-polar (11-22) GaN and AlN as well as m-plane sapphire were attained. This in turn suggested the complete coalescence of the semi-polar (11-22) uid-GaN growth. Therefore, the lowest NH_3 flux of 0.7 slm induces that the unwanted semi-polar (10-13) and m-plane (10-10) GaN phase orientations could be disappear.

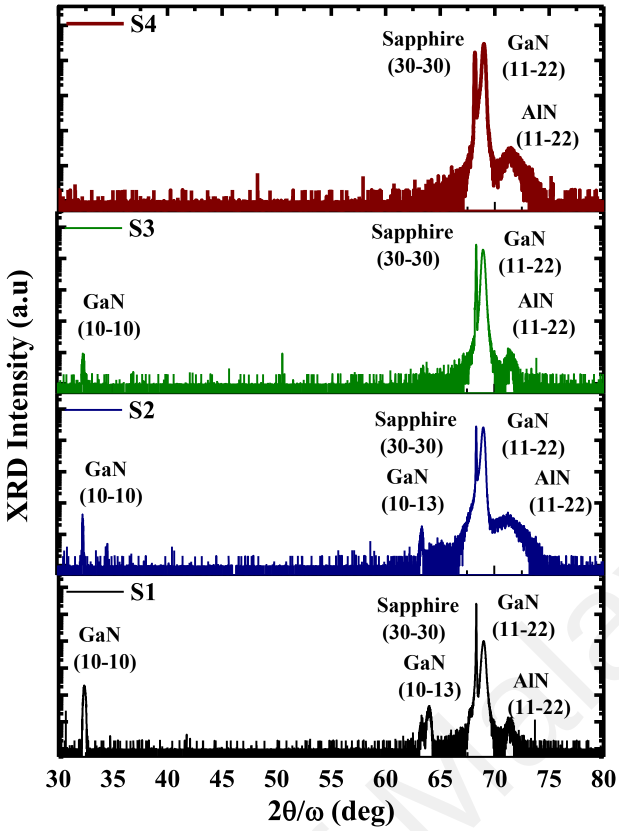

Figure 4.2: The HR-XRD 2*θ/ω* scan of uid-GaN epitaxial layers grown on m-plane sapphire substrate.

4.1.3 NH₃ Flux Influence on the Surface Evolution

The surface morphology analysis of the uid-GaN epitaxial layers grown on m-plane sapphire substrate was investigated via FESEM and AFM measurements. Two samples with different NH_3 flux for the growth of uid-GaN epitaxial layer is presented (S1 and S4), respectively. As observed in the HR-XRD 2*θ/ω* scans, these two samples clearly exhibited a remarkable change from poly-to single crystal structure. Hence, a huge transition of uid-GaN epitaxial layers from 2D to 3D growth modes is clearly discerned.

The morphological surface analysis using FESEM for the uid-GaN epitaxial layers grown on m-plane sapphire is demonstrated in Figure 4.3 (a-d). Figure 4.3 (a) & (b) illustrates the cross-sectional FESEM images of S1 and S4, respectively. As it can be obviously seen in the inset Figures, S1 and S4 exhibited appropriate 2D structures for the AlN nucleation layers, indicating the proper morphological surface quality of AlN (highlighted in green square). This is resulted from the use of the high NH_3 flux during the growth of AlN (Stellmach et al., 2012). In contrast, the growth of the uid-GaN epitaxial layer in S1 showed irregular surface morphology, promoting a 3D growth mode owing to the lack of the coalesced region; which it could be resulted from the micro twinning due to the difference in the crystallographic direction. Sample S4 illustrated a uniform 2D growth mode structure of the semi-polar (11-22) uid-GaN epitaxial layer, indicating a proper surface morphology. It is speculated that the reduction in the NH_3 flux for the growth of the uid-GaN would enhance the surface morphology by promoting a 2D growth structure.

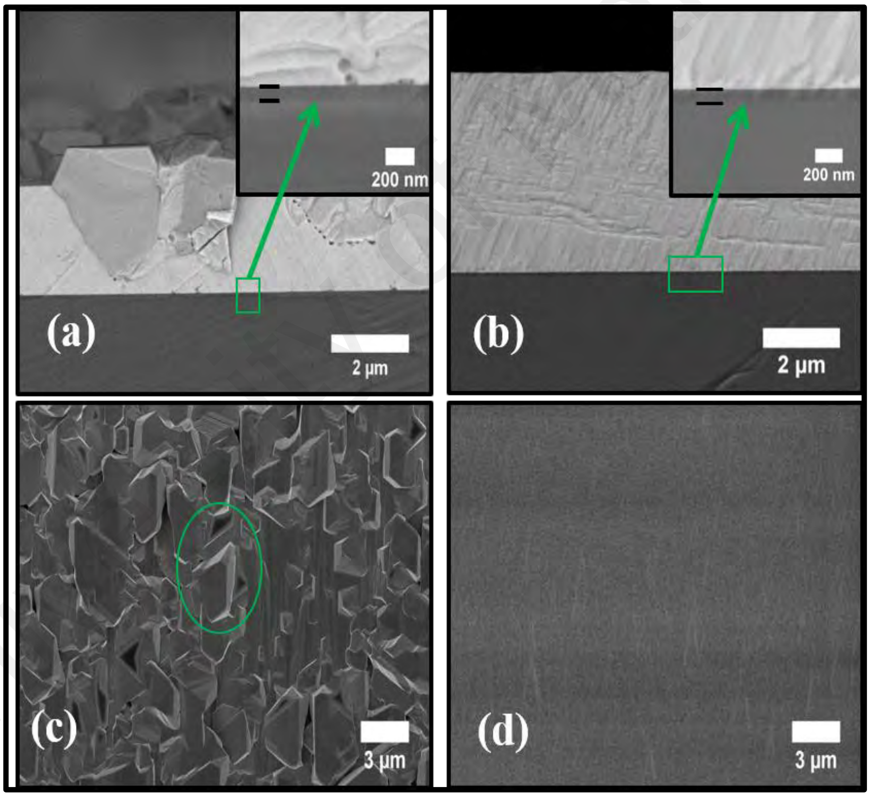

Figure 4.3: (a, b) Cross-sectional view of FESEM images with insets representing AlN nucleation layer for S1 and S4 and (c, d) Plane view of FESEM images of S1 and S4.

Figure 4.3 (c) & (d) shows the plain view FESEM images of the uid-GaN epitaxial layers for S1 and S4, respectively. Grains of the uid-GaN epitaxial layer in S1 can be clearly observed in Figure 4.3 (c) (highlighted in green circle), which in turn promoted

3D growth mode. This is mainly resulted from the bonding configuration and adatom diffusion length. However, the surface morphology of S4 illustrated a flat surface as the NH_3 reduced to 0.7 slm, indicating the complete coalescence of the GaN growth.

Figure 4.4 (a) & (b) shows the typical 10 × 10 µm AFM 2D and 3D images for S1 and S4, respectively. As shown in Figure 4.4 (a), S1 exhibited a very rough surface morphology with root mean square (RMS) surface roughness of 437.05 nm. This is due to the pronounced grain-structure, resulting from the high NH_3. However, smooth surface morphology of S4 was attained with the RMS roughness of 6.05 nm as illustrated in Figure 4.4 (b). Therefore, these results strongly suggest that the amelioration of the surface roughness was successfully obtained after reducing the NH_3 flux for the growth of semi-polar (11-22) uid-GaN epitaxial layer with surface roughness of as low as 6.05 nm as tabulated in Table 4.2.

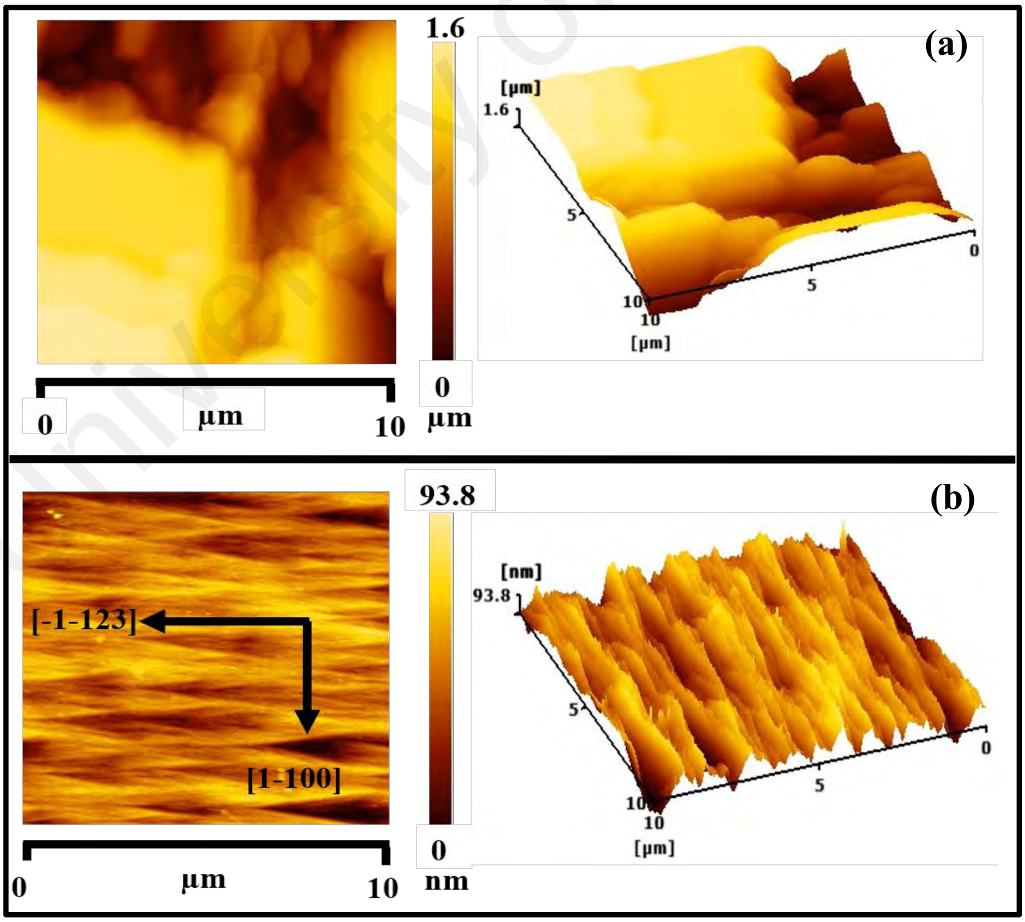

Figure 4.4: 2D and 3D images of 10 ×10 µm scan size AFM for (a) S1 and (b) S4.

Table 4.2: RMS roughness values for S1 & S4.

Sample	**S1**	**S4**
RMS Roughness (nm)	437.05	6.05

The growth mechanism of the uid-GaN epitaxial layers grown on m-plane sapphire substrate is elaborated to further understand the enhancement of the surface quality. It must be noted that the mechanism of the growth condition for semi-polar (11-22) GaN epitaxial layer on m-plane sapphire substrate covers the nitridation treatment process, optimization of AlN nucleation layer and NH_3 flow rate for uid-GaN epitaxial layer. As previously mentioned in the literature, the nitridation treatment process prior to the growth of the semi-polar (11-22) epitaxial layer is substantial; whereby it promotes the growth via forming nano-sized protrusions with slanted facets (highlighted in black square) as shown in cross-sectional TEM images taken along [1-100] zone axis in Figure 4.5 (a) (Frentrup et al., 2011; Won et al., 2014). As the substrate is exposed to nitridation process, the topmost O atoms in the sapphire substrate (Al_2O_3) is most probable to be substituted by N resulted from the nitridation process to obtain the protrusion (Wang et al., 2017). This in turn promoted the tilt of the orientation to obtain semi-polar (11-22) epitaxial layer as can be clearly observed in Figure 4.5 (b), in which the lattice plane tilted towards the semi-polar (11-22) orientation. In addition, these protrusions have the tendency to further help in reducing the lattice mismatch (Wang et al., 2017). This fact might be due to the temperature of the nitridation treatment process, in which if the m-plane sapphire substrate is exposed to a nitridation temperature less than 1000 °C, it tends to facilitate the growth of semi-polar (10-13) and m-plane (10-10) epitaxial layers (Ploch et al., 2010; Vennéguès & Beaumont, 1999; Vennéguès et al., 2010). In addition, the misfit dislocation (MD) shown in black circles can be observed in Figure 4.5 (b), and the number of the lattice plane is not consistent. This in turn indicates that there is an anisotropic strain relaxation between the sapphire and AlN nucleation layer (Dasilva et al., 2010).

On the other hand, the use of low NH_3 flux for the growth of GaN promotes gallium (Ga)-rich surface condition. This in turn will affect the bonding configuration between nitrogen (N) and Ga, which might impact the adatom diffusion on the surface as schematically illustrated in Figure 4.5 (c). Hence, the NH_3 flux is an important key success to control the surface morphology, by which the polarity of the epitaxial layer is monitored (Nakamura et al., 2000; Smith et al., 1999). Therefore, we assume that the low NH_3 flux for the GaN growth would promote the migration of the Ga atoms to the surface as supported by the cross-sectional FESEM image shown in Figure 4.3 (b).

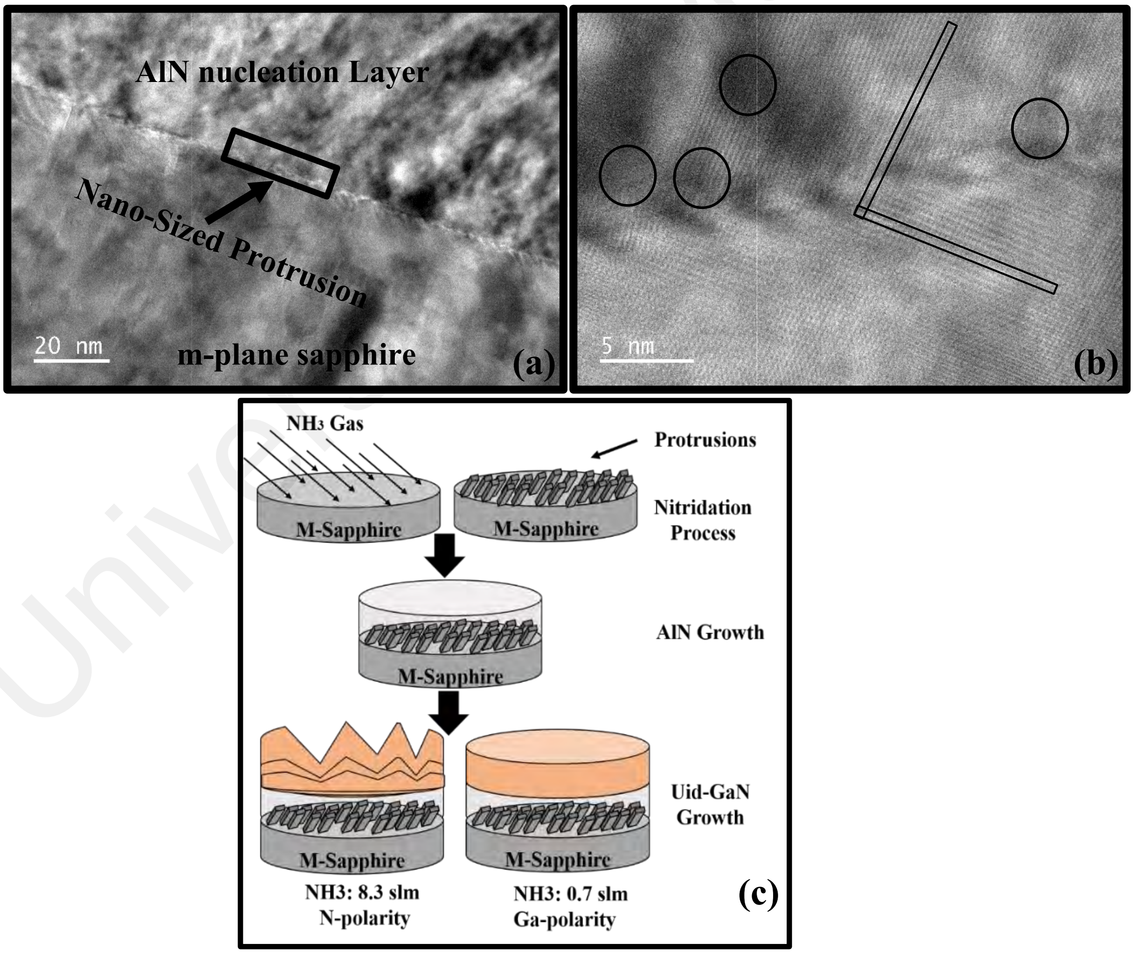

Figure 4.5: (a) & (b) Cross-sectional views of TEM images of AlN/sapphire interface taken closed to [10-10] zone axis showing the nano-sized protrusions and orientation tilt, respectively (the circles indicate the misfit dislocations and the box indicates the protrusions), and (c) The growth mechanism of the epitaxial layers on m-plane sapphire.

4.1.4 The Impact of NH_3 Flux on the Structural Properties

The anisotropic characteristics of the uid-GaN epitaxial layers grown on m-plane sapphire substrates were investigated using on-axis XRC as shown in Figure 4.6 (a) & (b). Figure 4.6 (a) shows the M-shape azimuthal dependence of full width at half maximum (FWHM) over 360° for S1-S4. As the azimuthal angle (*Φ*) was set at 0°, the incident beam projection was parallel to [-1-123] direction (surface striation direction), while the incident beam projection was parallel to [1-100] direction when the angle was set at 90°. As it can be obviously seen from Figure 4.6 (a), the FWHM values of S1, S2, S3 and S4 along [-1-123] directions were 0.43°, 0.30°, 0.24° and 0.17°, respectively, whilst the FWHMs along [1-100] direction were 0.54°, 0.48°. 0.46° and 0.40°, respectively. The decrement trends for the FWHMs as a function of NH_3 flux along [-1-123] and [1-100] for S1-S4 is shown in Figure 4.6 (b), while the XRC FWHMs along [-1-123], [1-100], [11-2-3] and [-1100] directions for S1-S4 are tabulated in Table 4.3.

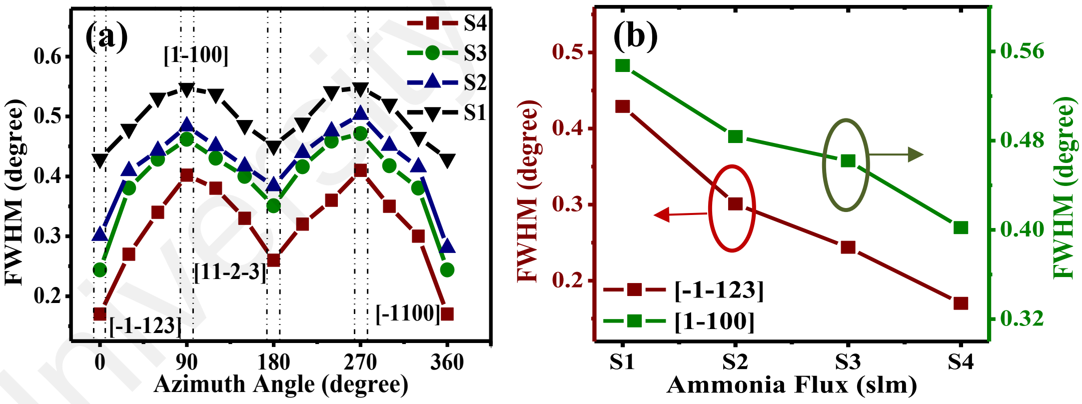

Figure 4.6: On-axis XRC FWHM values (a) As a function of azimuthal angle (*Φ*) and (b) Along [-1-123] and [1-100] directions as a function of NH_3 flux.

Table 4.3: On-axis XRC FWHMs along [-1-123], [1-100], [11-2-3] and [-1100] directions for as-grown GaN epitaxial layers (S1-S4).

Samples	FWHM (deg)			
	[-1-123]	**[1-100]**	**[11-2-3]**	**[-1100]**
S1	0.43	0.54	0.45	0.54
S2	0.30	0.48	0.38	0.50
S3	0.24	0.46	0.35	0.47
S4	0.17	0.40	0.26	0.41

It is noted that the values of FWHM for S4 along [-1-123] and [1-100] were remarkably low as compared to other samples, suggesting that the use of low NH_3 flux has considerably reduced the anisotropic properties. As compared to S1, the reductions in the XRC FWHMs of S4 were approximately 26.5% along [-1-123] and 15% along [1-100]. However, it is noteworthy that the broadening in the FWHM parallel to [1-100] is due to the GaN lattice distortion, resulting from the threading dislocation (TDs), anisotropic twist and tilt, and grain size distribution (Kriouche et al., 2010; Moram et al., 2009).

The off-axis XRC FWHM is implemented since on-axis (11-22) XRC measurement is insensitive to basal stacking faults (BSFs) (Moram & Vickers, 2009; Sun et al., 2009b). It must be noted that the BSFs always exist in the semi-polar (11-22), which might be resulted from the interface between the epitaxial layer and the substrate (Moram & Vickers, 2009; Vennegues et al., 2007); whereby the perfect dislocation is dissociated to compensate the mismatch between the as-grown epitaxial layers and the sapphire substrate. As previously reported, the type I_1 BSFs is bounded by Shockley partial dislocations (PDs) and formed by 1/3⟨10-10⟩, the type I_2 BSFs is bounded by Frank-Shockley PDs b = 1/6⟨20-23⟩, and E-type BSFs is bounded by Frank PDs (1/2⟨0001⟩), which occurs due to an insertion of extra basal plane (Sun et al., 2009a; Vennegues et al., 2007). In addition, the type I_1 BSFs are connected with one prismatic stacking fault (PSF) by (1/2⟨10-11⟩) displacement vector, while the density of partial dislocation (PDs)/perfect dislocations are connected with Burgers vector of b = 1/3<11-20> (Dasilva et al., 2010).

Figure 4.7 (a) shows the off-axis XRC FWHMs of (10-11) and (11-20) planes at different Φ with χ with respect to the surface normal for S1-S4. As it can be observed that the XRC FWHM values along (10-11) and (11-20) for S4 reduced approximately by 30% and 15%, respectively, as compared to S1. It is presumed that the low NH_3 flux of 0.7 slm would positively impact the decrement of the PSFs and PDs.

Previous studies have also reported that a series measurement of off-axis XRC FWHM with diffraction order (*n*) could be influenced by BSFs and the PDs and/or perfect dislocation (Sun et al., 2009a; Sun et al., 2009b; Vennegues et al., 2007). This was implemented on the m- and c-plane directions as shown in Figure 4.7 (b) & (c), respectively.

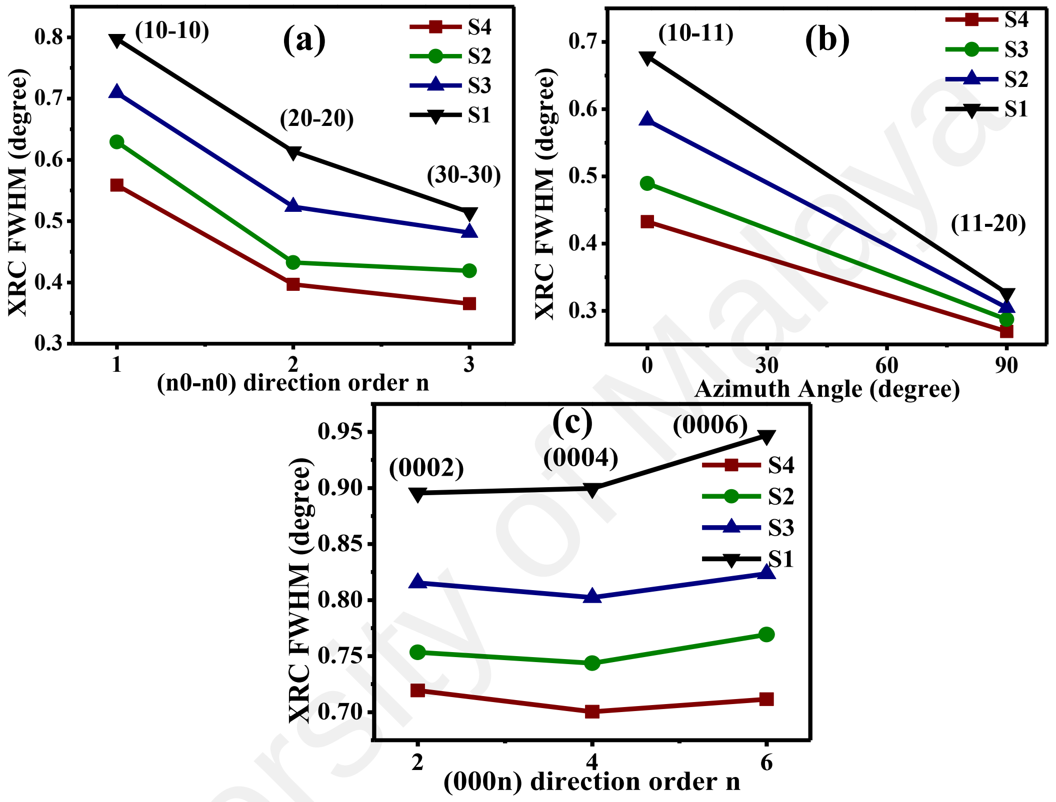

Figure 4.7: Off-axis XRC (a) FWHMs as a function of azimuthal angle (*Φ*), (b) M-plane (*n*0-*n*0) FWHMs (*n* = 1, 2, and 3) and (c) C-plane (000*n*) FWHMs (*n* = 2, 4, and 6).

Figure 4.7 (b) illustrates the (n0-n0) XRC FWHMs with the diffraction order n increased from 1 to 3 for S1-S4. It can be clearly discerned that the FWHMs along (10-10) and (20-20) planes for S4 decreased almost 35% as compared to S1 as NH_3 flux lowered to 0.7 slm. Such narrowing in the XRC FWHMs might be due to the decrement of the BSFs, indicating the enhancement of the crystal qualities (Sun et al., 2009b). As previously mentioned, however, the (10-10) and (20-20) XRC FWHM values are correlated with the BSFs, while (30-30) XRC FWHM values are insensitive to BSFs based on the visibility criteria and do not follow the same trend as the (10-10) and (20-20) data points (McLaurin et al., 2008; Moram et al., 2009; Sun et al., 2009c).

Next, the (000n) XRC FWHM values for S1-S4 are illustrated in Figure 4.7 (c). The (000n) off-axis XRC FWHM values increase as we increase the diffraction order, which is attributed to PDs and/or perfect dislocation (Jang et al., 2012; Vennegues et al., 2007; Zhao et al., 2016). It is evident that a large enhancement was obtained, in which the reduction of the NH_3 flux (S4) would positively influence the PDs and/or perfect dislocation.

It is speculated that the transition from 2D to 3D growth mode possesses a positive impact towards the improvement of the crystal quality, whereby these results are well correlated with surface morphology and might be due to improvement of the bonding configuration between N and Ga. Thus, it is evidenced that the two-step growth with an optimized NH_3 flux during the growth would improve the crystal quality of semi-polar uid-GaN grown on m-plane sapphire substrate.

On-axis RSM measurements were implemented to further study the crystal orientation, crystal quality and the relaxation state of the as-grown epitaxial layers along the principle in-plane directions of [1-100] and [-1-123]. In this subsection, two samples were presented to illustrate a complete understanding of the broadening mechanism in the as-grown epitaxial layers grown on m-plane (10-10) sapphire substrate.

Figure 4.8 (a) & (b) illustrates the RSM measurement along [1-100] direction for S1 and S4, respectively. As a comparison between S1 and S4, the peak position of the S1 exhibited a polycrystalline structure, namely semi-polar (11-22) GaN and AlN as well as semi-polar (10-13) GaN as illustrated in Figure 4.8 (a). This indicates that the high NH_3 flow rate during the growth of the uid-GaN epitaxial layer promotes a polycrystalline orientation of semi-polar (11-22) and (10-13) planes, resulting from rough surface due to the twining grain (Ploch et al., 2010). However, upon utilizing the low NH_3 flux (S4) during the growth of uid-GaN as shown Figure 4.8 (b), the peak of (10-13) was absent, suggesting a single crystal structure of semi-polar (11-22) GaN was attained. This in turn proved the enhancement of the crystal orientation quality as mentioned earlier in the 2*θ/ω* scans. Furthermore, a microscopic tilt between the semi-polar (10-13) peak and m-plane sapphire peak in S1 was clearly seen, while the semi-polar (10-13) peak was not present in S4. This is in turn signifying that S4 exhibited no lattice tilt between semi-polar (11-22) uid-GaN and m-plane sapphire substrate along [1-100]. This fact strongly suggested that AlN and uid-GaN were coherently grown along (11-22) plane, and relaxed semi-polar epitaxial layers are achieved as shown in Figure 4.8 (b) (Farrell et al., 2012).

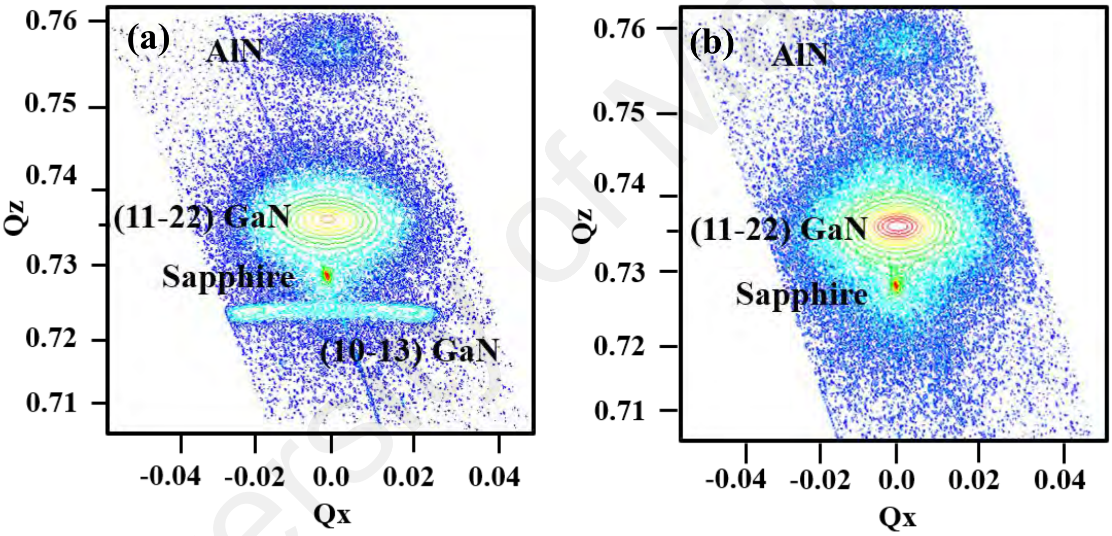

Figure 4.8: X-ray reciprocal space mapping of semi-polar (11-22) along [1-100] direction for (a) S1 and (b) S4.

In contrast to the (11-22) RSM symmetric reflection along the [1-100] direction, the (11-22) symmetric RSM along [-1-123] was performed for S1 and S4 as shown in Figure 4.9 (a) & (b), respectively. As mentioned in the literature, a tilt between the sapphire substrate and the as-grown epitaxial layer is obtained in the (11-22) symmetric RSM along [-1-123], which might be due to the cumulative effect of the Burgers vectors (Farrell et al., 2012; Young et al., 2010). As shown in Figure 4.9 (a), the tilt between the as-grown GaN and the m-plane (10-10) sapphire in S1 is roughly 0.47°, while the lattice tilt between the semi-polar (11-22) GaN and m-plane sapphire substrate for S4 is 0.63°. This suggests that the two are grown with the same crystal structure (Bauer & Richter, 2012; Young et al., 2010). The tilt value for the semi-polar (11-22) GaN and AlN peaks with the respect to m-plane sapphire substrate peaks are tabulated in Table 4.4.

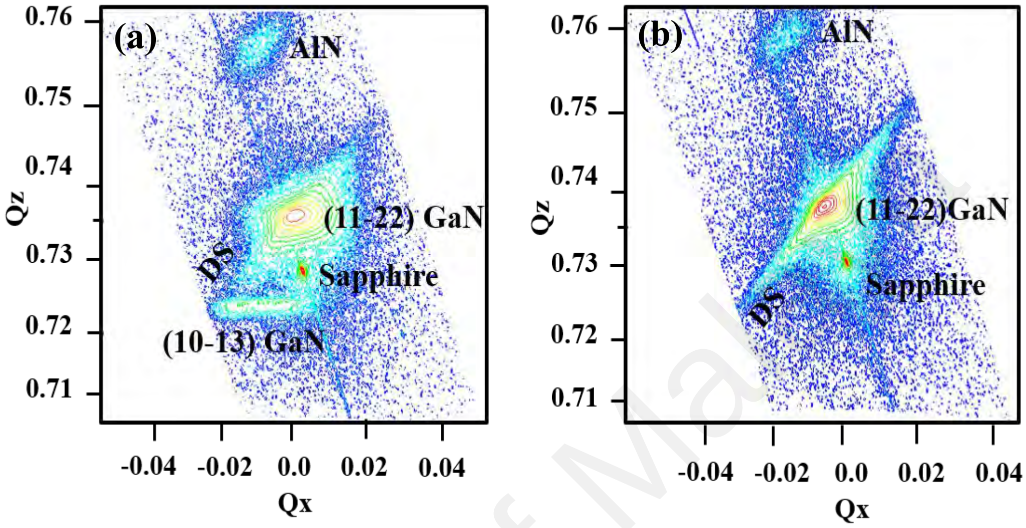

Figure 4.9: X-ray reciprocal space mapping of semi-polar (11-22) along [-1-123] for (a) S1 and (b) S4.

Table 4.4: Observed microscopic tilt of semi-polar GaN and AlN epitaxial layer taken along [-1-123] direction for S1 and S4.

Sample	Tilt of GaN with sapphire (°)	Tilt of AlN with sapphire (°)
S1	~0.47	~0.88
S4	~0.63	~1.27

Figure 4.10 (a) & (b) demonstrates the RT Raman spectroscopy measurement for S1-S4 to study the compressive and tensile stress/strain. As illustrated in Figure 4.10 (a), three unambiguous peaks located at 379, 416 and 742 cm^{-1} were seen and assigned by asterisks (*), resulting from the phonon mode of the m-plane (10-10) sapphire substrate. Meanwhile, the E_1 (TO), E_2 (high) for GaN and E_2 (high) AlN were located at 541, 570 and 644 cm^{-1}, respectively. As it can be observed from Figure 4.10 (a), the as-grown

samples shows dual E2 (high) phonon modes, which were corresponded to the GaN E_2 (high) and AlN E_2 (high), respectively (Demangeot et al., 1998; Kuball, 2001). The E_2 (high) modes of the GaN and AlN for S1-S4 were located at 570 and 644 cm^{-1}, respectively. It was reported that the standard compressive stress-free for GaN E_2 (high) is located at 568 cm^{-1}, in which the shift is proportional to that compressive and tensile stress (Jiang et al., 2016; Yan et al., 2007). Hence, it is confirmed that the as-grown samples exhibited compressive stress/strain phenomena. In contrast, Figure 4.10 (b) shows the FWHM of the GaN E_2 (high) mode peaks for S1-S4 as a function of NH_3 flux. It can be clearly seen that a direct relationship between the FWHM and the NH_3 flux was obtained. This phenomenon shows that the enhancement of the GaN E_2 (high) peak for S4 is attained with higher peak intensity as compared with S1-S3. This fact is due to the use of the low NH_3 flux of 0.7 (S4), which is well correlated with the surface morphology and crystal quality analysis.

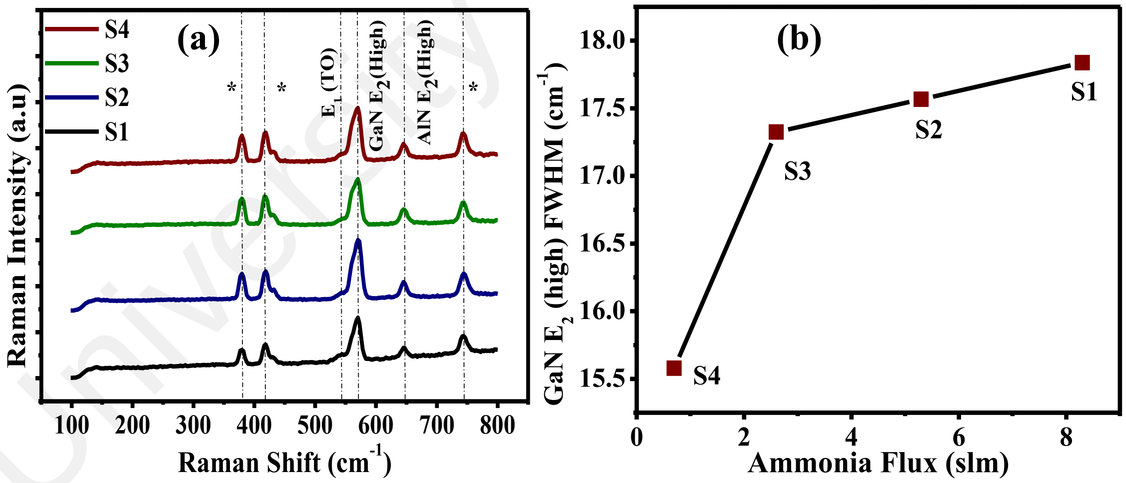

Figure 4.10: (a) Room temperature Raman spectra of uid-GaN epitaxial layers & (b) FWHM of GaN E_2 (high) as a function of NH_3 flux.

4.2 Optimization of NH_3 Flux for the Growth of AlN Nucleation Layer

4.2.1 Growth Procedure

The effect of AlN nucleation layer towards the crystal quality of semi-polar (11-22) uid-GaN epitaxial layers was investigated using with and without AlN nucleation layer.

The former was optimized using low NH_3 flux of 1 slm (A1) and high NH_3 flux of 2.3 slm (A2), while the latter was designated as A3 (without AlN nucleation layer). The trimethylaluminum (TMA) flow of the AlN nucleation layer growth remained constant at 98.5 sccm. After the H_2 annealing and the nitridation process (similar to section 4.1), the 80 nm thickness of AlN nucleation layer was deposited at a temperature of 1050 °C, followed by the growth of the uid-GaN (similar to section 4.1). The growth procedure of the AlN nucleation layer grown on m-plane sapphire is shown in Figure 4.11. The crystal qualities of the epitaxial layer were examined using on- and off-XRC analysis.

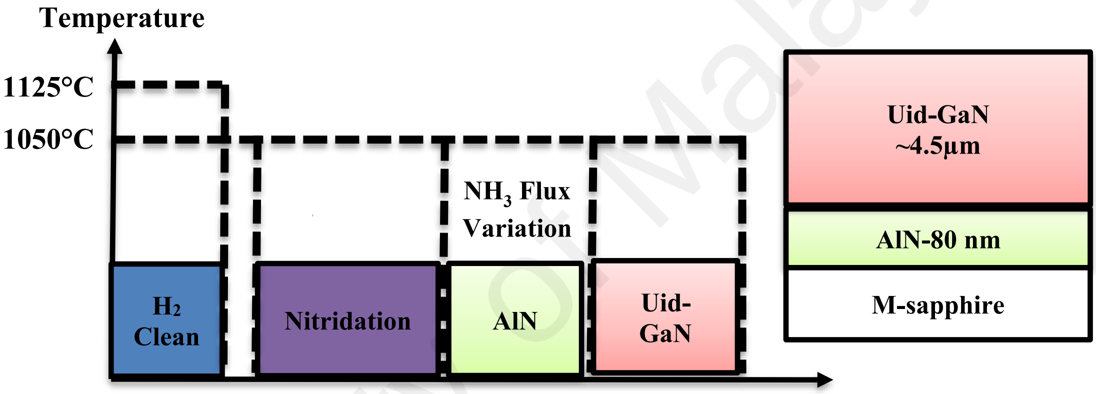

Figure 4.11: The growth procedure of AlN nucleation layer grown on m-plane sapphire.

4.2.2 Influence of the AlN Nucleation Layer on the Crystal Qualities

The crystal qualities for A1-A3 were examined by on- and off-axis XRC to understand the anisotropic properties and planar defects of semi-polar (11-22) uid-GaN epitaxial layers grown on m-plane sapphire substrate with optimization of AlN nucleation layer. The M-shape azimuthal angle dependence of FWHMs over 360° for A1, A2 and A3 is illustrated in Figure 4.12 (a). The FWHMs along [-1-123] were 0.18°, 0.17° and 0.19° for A1, A2 and A3, respectively. Whilst, the FWHMs were 0.41°, 0.40° and 0.47° for A1, A2 and A3, along [1-100] direction, respectively. Figure 4.12 (b) shows the FWHMs along [-1-123] and [1-100] directions as a function of NH_3 flux during the growth of the AlN nucleation layer. In addition, Table 4.5 presents the FWHM along [-1-123], [1-100], [11-2-3] and [-1100] for A1, A2 and A3. These results indicate that the high NH_3 flux (2.3 slm) for the growth of the AlN nucleation layer positively influenced the reduction of the anisotropic properties of semi-polar (11-22) uid-GaN epitaxial layers.

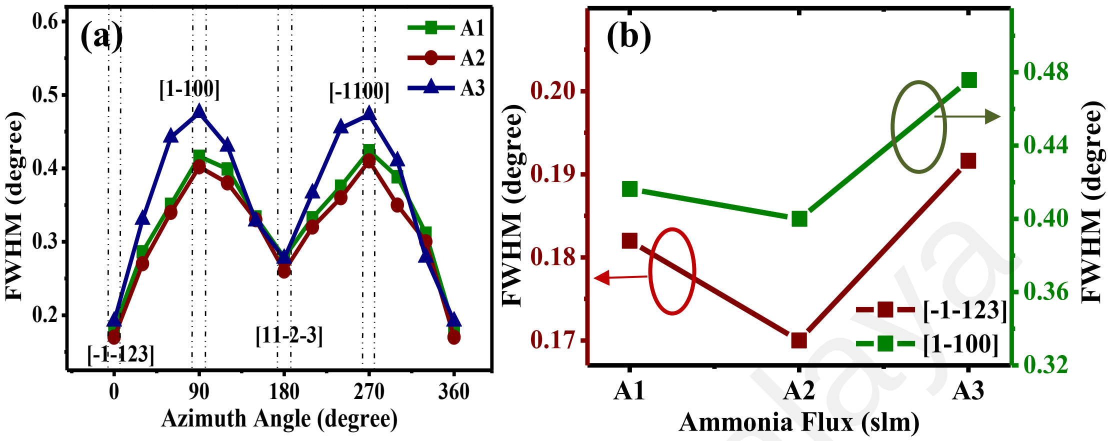

Figure 4.12: On-axis XRC FWHMs (a) As a function of azimuthal angle (*Φ*) and (b) Along [-1-123] and [1-100] directions as a function of NH_3 flux.

Table 4.5: On-axis XRC FWHMs along [-1-123], [1-100] [11-2-3] and [-1100] directions for A1-A3.

Samples	**FWHM (deg)**			
	[-1-123]	**[1-100]**	**[11-2-3]**	**[-1100]**
A1	0.18	0.41	0.27	0.42
A2	0.17	0.40	0.26	0.41
A3	0.19	0.47	0.27	0.48

The off-axis XRC FWHM measurement is performed for (10-11) and (11-20) planes. As it can be seen from Figure 4.13 (a), A2 recorded the XRC FWHMs to be lowered by 25% and 40% for (10-11) and (11-20), respectively, as compared to A3. It is safe to presume this phenomenon is attributed to the enhancement of crystal quality, resulting from the high NH_3 flux of 2.3 slm. This is in turn resulted from the reduction of the PSFs and PDs.

Figure 4.13 (b) shows the (*n*0-*n*0) XRC FWHMs implemented along the m-plane direction with an increment of *n* from 1 to 3. The off-axis XRC FWHMs suggested that the A2 exhibited lower FWHMs as compared to A1 and A3. This in turn indicated that the BSFs reduced upon utilizing the high NH_3 flux of 2.3 slm. In contrast, Figure 4.13 (c) demonstrates the (000*n*) XRC FWHMs with increased *n* from 2 to 6. As it can be obviously discerned, the values of the FWHM for A2 decreased upon the use of NH_3 flux of 2.3 slm. This is attributed to the decrement in PDs and/or perfect dislocation (Kriouche et al., 2010; McLaurin et al., 2008).

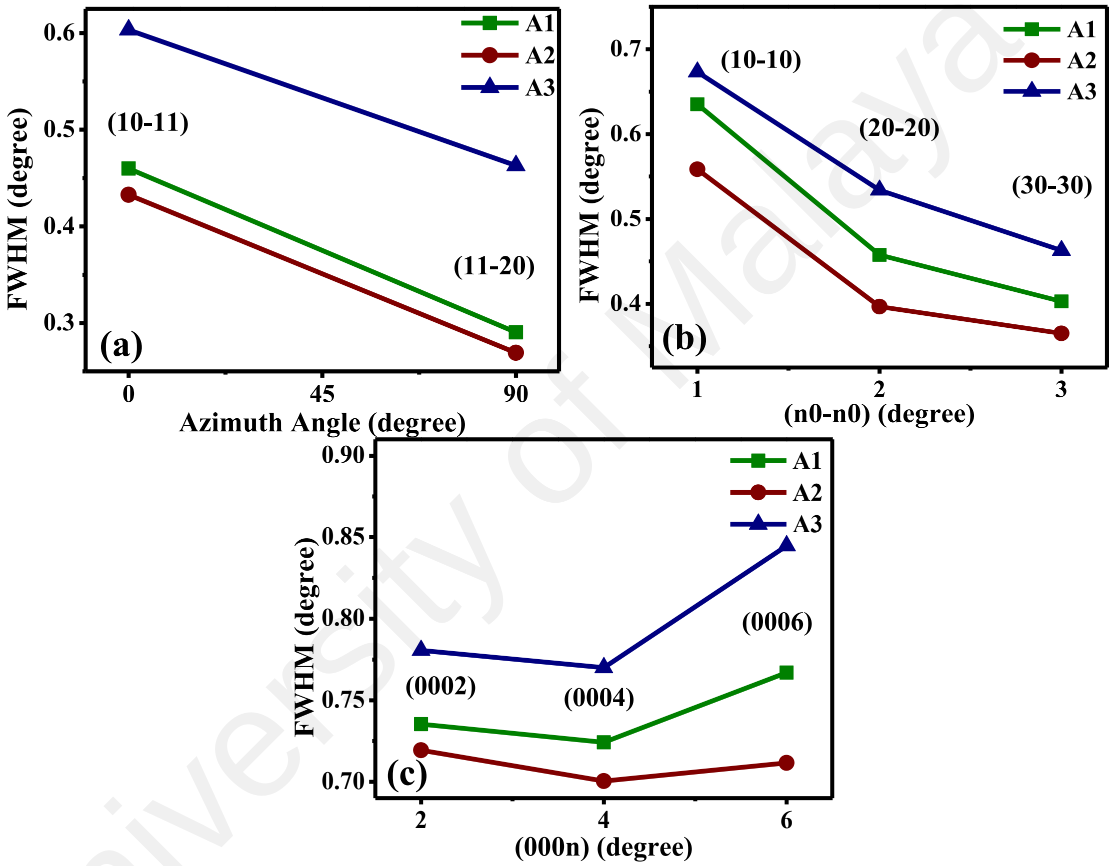

Figure 4.13: Off-axis XRC (a) FWHMs as a function of azimuthal angle (Φ), (b) M-plane (*n*0-*n*0) (*n* = 1, 2, and 3) FWHMs and (c) C-plane (000*n*) FWHMs (*n* = 2, 4, and 6).

This in-depth mechanism of obtaining high crystal quality of semi-polar (11-22) uid-GaN here surrounds the use of AlN nucleation layer. As previously mentioned, the use of AlN nucleation prior to the growth of semi-polar (11-22) GaN is crucial (Davidsson et al., 2005; Leung, et al., 2009). It is envisaged that the growth of AlN nucleation layer prior to the growth of uid-GaN would help to facilitate Ga-mobility (Davidsson et al., 2005). Therefore, it is assumed that the growth of uid-GaN epitaxial layer without AlN nucleation layer might suffer from deterioration of crystal quality as observed in Figure 4.12 and Figure 4.13 (A3). It was also reported by Sun et.al., the growth of AlN nucleation prior to the growth of semi-polar uid-GaN is substantial to attain 2D growth mode by rendering a smooth surface for the subsequent growth (Sun, et al., 2009c). As previously reported that the tensile strain is avoided by implementing the growth of thin film of AlN nucleation layer (Waltereit et al., 1999). In other words, the lattice mismatch between the AlN nucleation layer and the sapphire substrate is smaller than the lattice mismatch between the GaN nucleation layer and the sapphire substrate (Wang et al., 2017). This in turn leads to less disorientation in the AlN grains as compared to GaN epitaxial layer.

On the other hand, high NH_3 flux with a high TMA is preferred to promote a smooth surface, leading to the dominance of a single crystal orientation and suppression of other phases such as (10-10) and (10-13) orientations (Mogilatenko et al., 2014). This is due to the fact the growth of AlN nucleation layer at low NH_3 and TMA flux would induce the growth of (10-13) and (10-10) AlN crystallites; presuming that the vertical growth rate of the semi-polar (11-22) crystallites is slower than (10-13) and (10-10) AlN crystallites (Mogilatenko et al., 2014). Therefore, it is confirmed that the crystal quality of semi-polar (11-22) uid-GaN was further improved as the high NH_3 and TMA flux (A2) introduced during the growth of the AlN nucleation layer. The said optimization will further confirm the ability of the SR-2000 Taiyo Nippon Sanso MOCVD system to produce a high quality proper 2D growth mode of high temperature AlN to be utilized further for the AlN/GaN ML growth.

4.3 Optimization of AlN/GaN Multi-Layers

4.3.1 Growth Methodology

Next, in order to further enhance the crystal quality and morphological properties of semi-polar (11-22) uid-GaN grown on m-plane sapphire substrate, the AlN/GaN

(5nm/25nm) MLs were introduced with different number of pairs as shown in Figure 4.14. Three samples were proposed, namely 20, 40 and 60 pairs, and denoted as M1, M2 and M3, respectively. Prior to the growth of AlN/GaN MLs, the annealing process of H_2 and nitridation process were performed as mentioned in Section 4.1, followed by the growth of AlN nucleation layer as stated in Section 4.2. Then, growth temperature of the AlN/GaN was implemented at 1050 °C, followed by the growth of semi-polar (11-22) uid-GaN. The AlN/GaN MLs were sandwiched between the semi-polar (11-22) AlN nucleation layer and uid-GaN epitaxial layers to investigate the influence of the AlN/GaN MLs on the semi-polar (11-22) uid-GaN epitaxial layer.

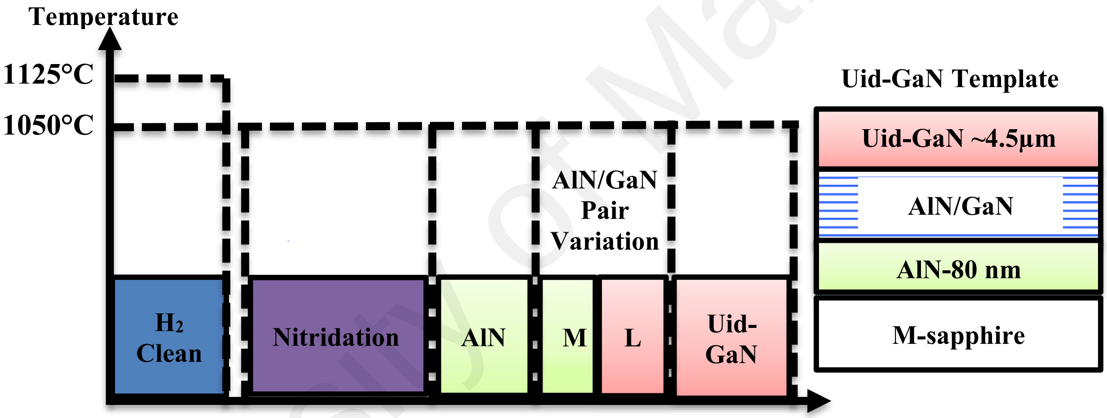

Figure 4.14: The growth Methodology of the AlN/GaN multi-layer.

4.3.2 Influence of the AlN/GaN Pairs on the Diffracted Fringes

The measurement of HR-XRD $2\theta/\omega$ scans is utilized to clarify the crystal orientations of semi-polar (11-22) uid-GaN grown on m-plane sapphire. Also, the satellite peaks of the 20, 40 and 60 pairs of the AlN/GaN ML were confirmed. Figure 4.15 shows the HR-XRD $2\theta/\omega$ scans profiles from the symmetric (11-22) plane for samples of M1, M2 and M3.

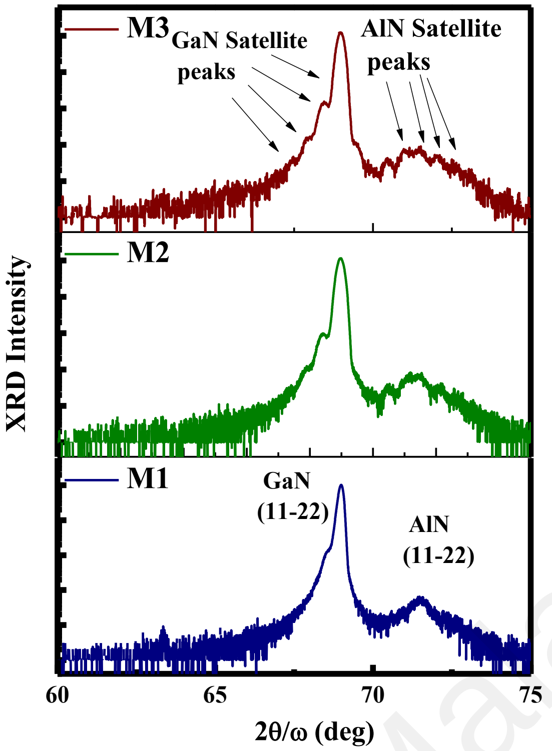

Figure 4.15: HR-XRD 2*θ/ω* scans of semi-polar (11-22) AlN/GaN MLs.

It can be clearly seen that diffracted fringes are corresponding to the interface of the AlN/GaN ML abruptness, which is sandwiched between the semi-polar (11-22) AlN nucleation layer and the uid-GaN. As it can be observed, M3 recorded proper diffracted fringes ascribed to the 60 pairs of AlN/GaN ML, while M2 exhibited a fewer number of fringes owing to the less abruptness occurred in the ML. However, the diffracted fringes in M1 almost were non-existent, which is mainly attributed to the inappropriate abruptness of the 20 pairs AlN/GaN ML. Based on these results, samples M3 proved that the use of AlN/GaN 60 pairs was substantial to achieve a structure of ML with an abrupt interface between AlN/GaN. These results will be further confirmed using cross-sectional images of FESEM and TEM.

4.3.3 Influence of AlN/GaN MLs towards the Undulation Features

Figure 4.16 (a-c) shows the FESEM plain view images for M1, M2 and M3, respectively. As it can be clearly seen that M1 and M2 suffer from undulated features.

However, these features were progressively seen to be overcome after the AlN/GaN pairs were increased to 60. This is due to the fact that the 60 of AlN/GaN ML further reduces the lattice mismatch between the m-plane sapphire substrate and the semi-polar (11-22) uid GaN epitaxial layers, in turn decreasing the densities of the undulated features (Song et al., 2013). These features will be further discussed in the AFM surface morphology analysis.

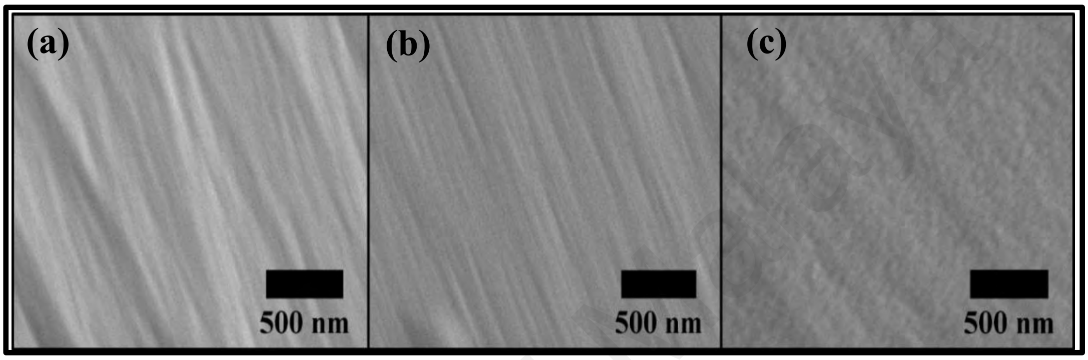

Figure 4.16: FESEM surface morphology analysis of (a) M1, (b) M2 and (c) M3

Cross-sectional FESEM analysis of 60 pairs (M3) was performed to further examine the quality of AlN/GaN ML as presented in Figure 4.17 (a-d). Figure 4.17 (a) & (b) illustrates the cross-sectional FESEM image of semi-polar (11-22) epitaxial layers and its schematic diagram, respectively. As it can be discerned that the 4.5 µm-thick uid-GaN was properly grown on top of AlN/GaN 60 pairs, exhibiting a 2D growth mode. As observed in Figure 4.17 (c), the AlN/GaN 60 pairs displayed a non-abrupt structure from the base of the AlN/GaN 60 pairs until the 20th pair (highlighted in orange). Nevertheless, the AlN/GaN after the 20th pair progressively exhibited an abrupt structure as highlighted in green circle. The improvement of AlN/GaN pairs as shown in Figure 4.17 (d) is thought to be attributed to the decrement of defects and dislocations, which mainly resulted from the mismatch between the epitaxial layer and the sapphire substrate (Leung et al., 2012).

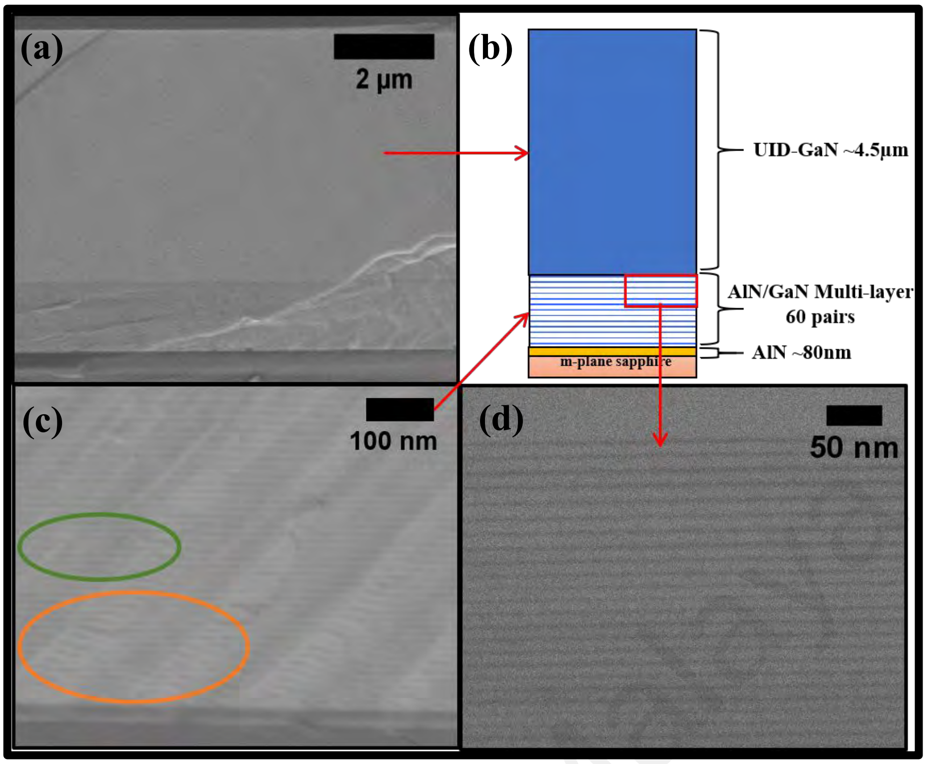

Figure 4.17: (a) Cross-sectional FESEM images of the full structure with 60 pairs of AlN/GaN, (b) the schematic diagram of the full structures and (c, d) higher magnification of the AlN/GaN multi-layers.

The surface morphology analysis of the as-grown M1, M2 and M3 was further investigated using 2D and 3D images of AFM measurement over a 10×10 µm scan size as illustrated in Figure 4.18 (a-c). The arrow-head like features for the typical as-grown semi-polar (11-22) GaN epitaxial layer on m-plane sapphire were unambiguously seen for M1, M2 and M3. These features might be resulted from the anisotropic incorporation and the adatom diffusion length towards the crystallographic direction [-1-123] and [1-100] (Leung et al., 2012; Oh et al., 2011; Ploch et al., 2012). However, these features were reduced after the AlN/GaN 60 pairs were introduced due to the reduction of the lattice mismatch between the m-plane sapphire substrate and the semi-polar (11-22) uid-GaN epitaxial layer as depicted in Figure 4.18 (c), in which the RMS roughness was drastically decreased from 16.24 nm to 6.08 nm. The reduction of the RMS surface roughness is mainly due to the decrease in the arrowhead like features and the enhanced abruptness of the AlN/GaN ML in M3. However, the negligible increment of the RMS surface roughness from 6.00 nm (M2) to 6.08 (M3) is mainly due to the accumulation of defects and dislocations, in which the AlN/GaN ML has promoted an annihilation process as it will be further discussed in the TEM analysis. The values of the RMS roughness and peak-to-valley for M1-M3 are listed in Table 4.6.

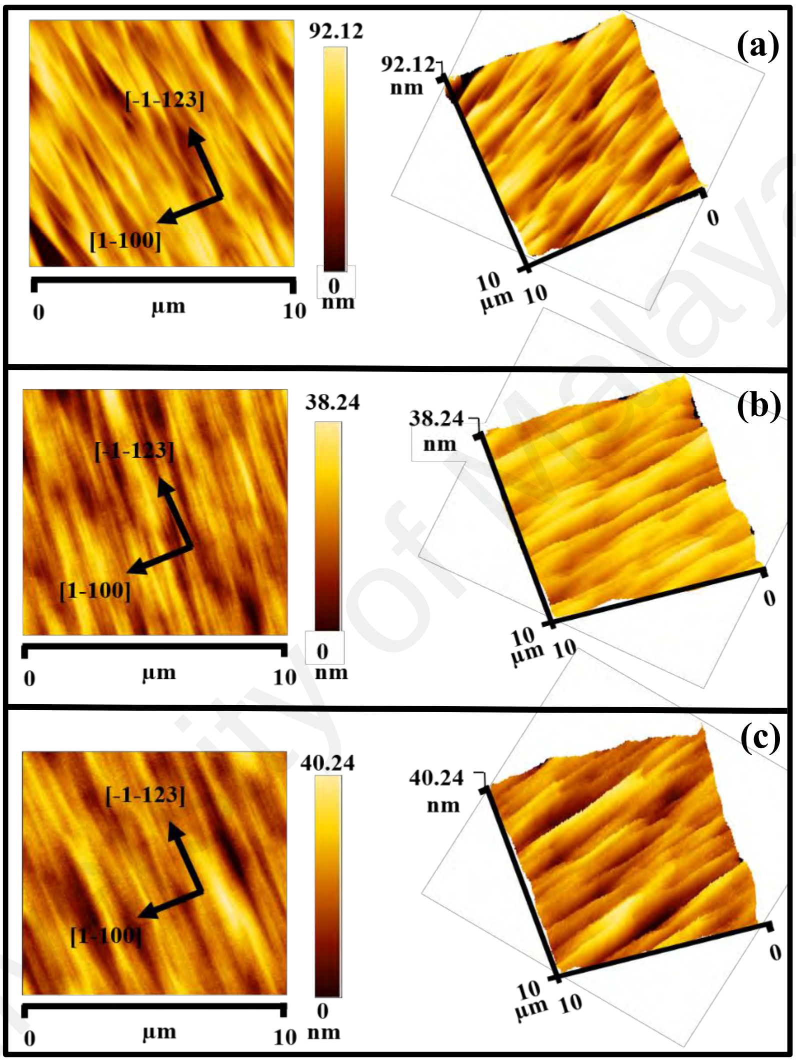

Figure 4.18: 2D and 3D images of 10 ×10 µm scan size AFM for (a) M1, (b) M2 and (c) M3.

Table 4.6: RMS roughness values for M1, M2 and M3.

Sample	**M1**	**M2**	**M3**
Number of Pairs	20	40	60
RMS Roughness (nm)	16.24	6.00	6.08

To further investigate the enhancement of surface morphology of semi-polar (11-22) GaN epitaxial layers grown on m-plane sapphire substrate, the bright field (BF) cross-sectional TEM analysis was utilized. Figure 4.19 (a-f) illustrates the BF cross-sectional TEM images for M3 taken along [10-10] zone axis with g = [11-20] using different magnifications. Figure 4.19 (g) demonstrates the selected area electron diffraction pattern (SAED) for M3. As it can be obviously seen in Figure 4.19 (a) & (b) (highlighted in green circles) that the initial interface of AlN/GaN ML (20th pairs) was rather undergoing 3D growth mode, leading to accumulation of the BSFs. It must be noted that these BSFs along with its associated PDs are originating from the AlN/sapphire interface and propagating along the c-plane to the subsequent epitaxial layer. The discerned defects observed from the Figure 4.19 (b) and (c) were the I_1-type BSFs with the associated PDs and a few PSFs. As it can be clearly seen from Figure 4.19 (a-e), those BSFs were deviated from their original propagation directions (slanted vertical). Higher magnification imaging depicted in Figure 4.19 (b) reveals the numerous defects generated from the AlN NL and sapphire interface was seen propagating/accumulating towards the first pair of the AlN/GaN ML causing a disturbance during the epitaxial layer growth. Such phenomenon continued to reoccur until ~20th pair of the AlN/GaN.

Furthermore, the PDs were affected by the alternating ML, leading to a propagation in unison deviating from its original path. This can be clearly observed as the consequent 40th AlN/GaN pairs exhibited significant interfacial abruptness (Figure 4.19 (e) & (f)). Moreover, the PDs associated BSFs started to accumulate and propagate unitedly into the 60th ML pair and uid-GaN interface as shown in Figure 4.19 (a) (highlighted in orange circles). It was also seen that the unison of these defect were bent towards their original path, promoting closed-loop effect (highlighted in red arrows) (Wu et al., 2017a). Figure 4.19 (g) illustrates SAED of M3, suggesting the high crystal quality semi-polar (11-22) GaN epitaxial layer.

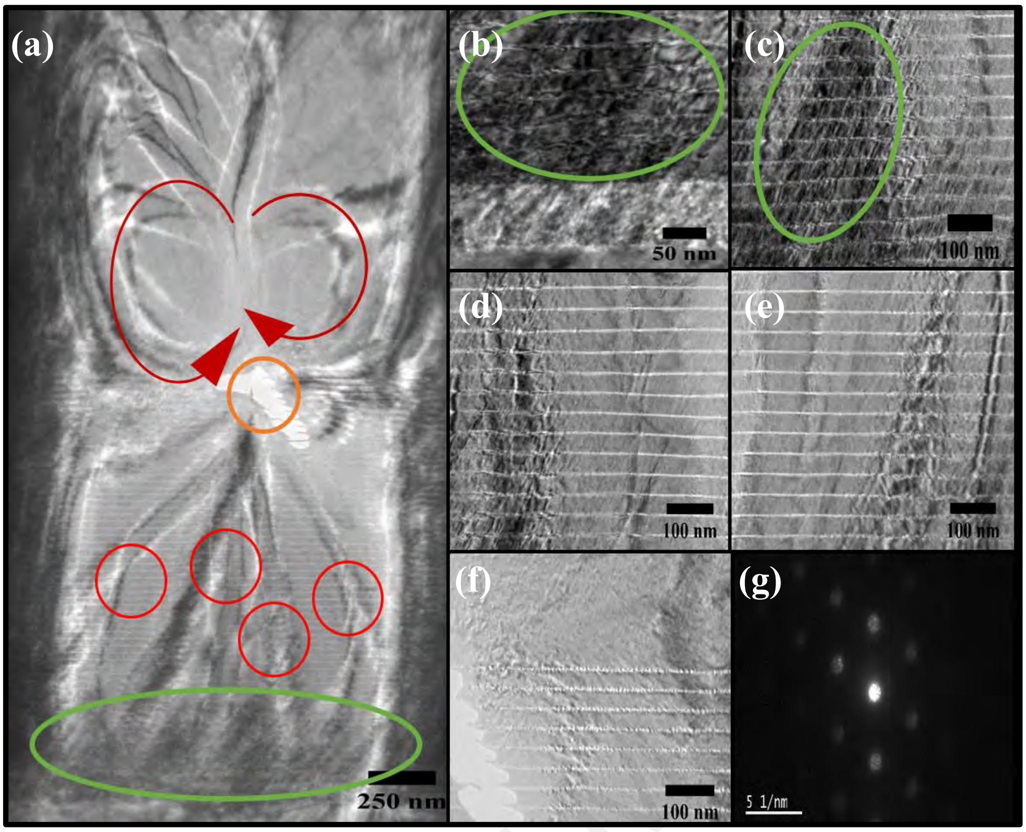

Figure 4.19: Cross-sectional TEM images of M3 taken closed to [1-100] with g = [11-20]. (a) The whole structure using AlN/GaN ML of 60 pairs, (b) The initial growth of the AlN/GaN ML, (c, d) Middle part of the AlN/GaN ML, (e, f) The upper part of the AlN/GaN ML and (g) Selected area electron diffraction pattern of the uid-GaN/ML.

To elaborate the mechanism of the defect reduction, schematic diagram of the full structure for M3 is sketched in Figure 4.20. The BSFs along with its associated PDs generated from the AlN nucleation layer and the m-plane sapphire substrate interface were observed to be reduced and accumulated due to the rough surface of the 20 pairs of AlN/GaN ML. In addition, the propagated BSFs were further terminated by their associated PDs owing to the the tensile/compressive strain exerted by the subsequent AlN/GaN ML. This is also due to the fact that the I_1-type BSFs can be terminated by the PDs or folded by the PSFs as shown in Figure 4.20 (Dasilva et al., 2010; Vennegues et al., 2007). Subsequently, these defects will be further affected by the difference in the strain state of the AlN/GaN, resulting in unison deviating from its original path to an undesired propagation direction. Hence, the consequent 40th AlN/GaN pairs and above exerting significant interfacial abruptness, depicting prominent absence of the mentioned defect in certain areas. Furthermore, BSFs and their associated PDs started to converge around the 60th ML pair and unitedly propagate into the semi-polar GaN epitaxial layer. As the propagation enters the semi-polar (11-22) uid-GaN interface, the strain difference separates the union whilst bending them in a manner which loops the propagation creating a closed-loop effect of the defects. Thus, this led to the improvement of the defect annihilation owing to the line bending of the basal plane. However, certain propagation of defects still reaches the surface of the epitaxial layer conversely with a lower density.

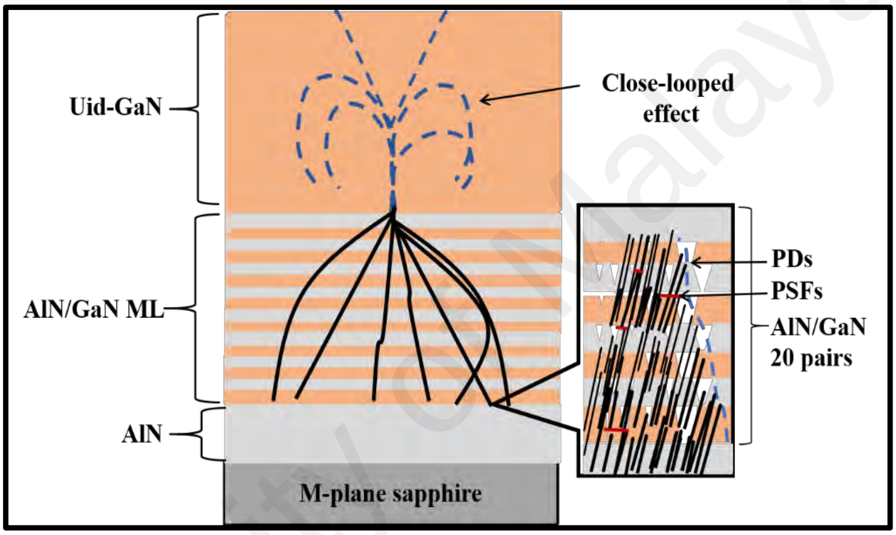

Figure 4.20: Schematic diagram of the full structure illustrating the defect reduction in M3.

These results are in good agreement with FESEM and AFM measurements, in which the insertion of AlN/GaN 60 pairs would reduce the undulation and the arrowhead-like features by reducing the dislocations and defects. It must be noted that if the growth of the semi-polar uid-GaN was accomplished on AlN/GaN 20 pairs, the defects would continue to propagate, resulting in rough surface. However, with further increment of AlN/GaN to 60 pairs, the closed-loop effect was further reducing the defect propagation.

4.3.4 Impact of Pair Numbers on the Structural Properties

On-axis XRC measurements were performed to reveal the anisotropic reduction for the semi-polar (11-22) uid-GaN epitaxial layer grown on m-plane sapphire substrate after the insertion of AlN/GaN ML. The M-shape azimuthal dependence of FWHMs over 360° for M1, M2 and M3 is shown in Figure 4.21 (a). The FWHMs along [-1-123] direction were 0.15°, 0.14° and 0.13° for M1, M2 and M3, respectively. While, the FWHM values along [1-100] direction were 0.39°, 0.37° and 0.36° for M1, M2 and M3, respectively. In order to further clarify the reduction trend of the FWHMs, Figure 4.21 (b) shows the FWHMs parallel to [-1-123] and [1-100] directions as a function of AlN/GaN pair increment, while the XRC FWHMs along [-1-123], [1-100], [11-2-3] and [-1100] directions are tabulated in Table 4.7.

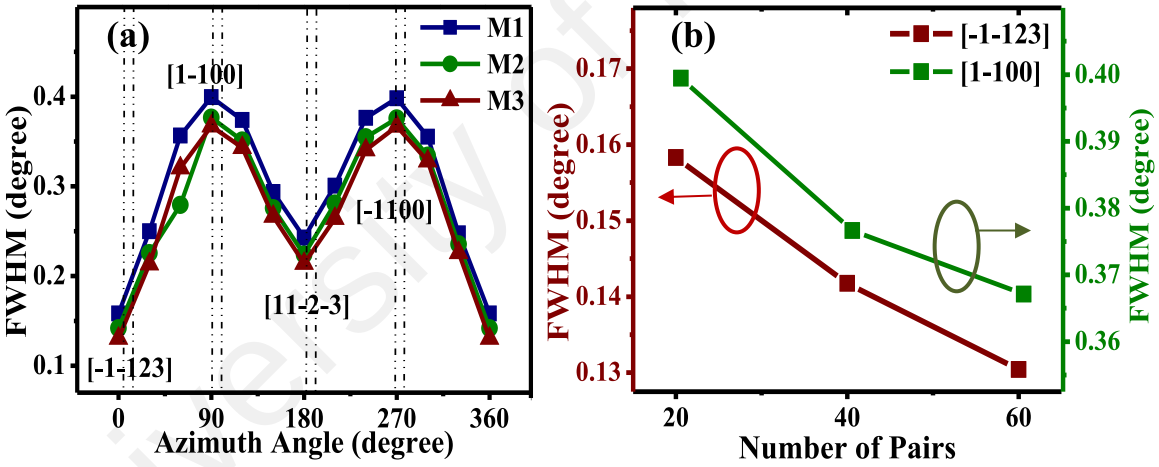

Figure 4.21: On-axis XRC FWHM values (a) As a function of azimuthal angle (Φ) and (b) Along [-1-123] and [1-100] directions as a function of AlN/GaN pairs.

Table 4.7: On-axis XRC FWHMs along [-1-123], [1-100], [11-2-3] and [-1100].

Samples	**FWHM (deg)**			
	[-1-123]	**[1-100]**	**[11-2-3]**	**[-1100]**
M1	0.15	0.39	0.24	0.39
M2	0.14	0.37	0.22	0.37
M3	0.13	0.36	0.21	0.36

As shown in Figure 4.21 (b), linear decrement trends of [-1-123] and [1-100] directions are obtained with the increment of the AlN/GaN pairs. The decrement of the FWHMs for M3 as compared to M1 and M2 were almost 8% along [-1-123] and [1-100] directions, respectively. This in turn proves the reduction of undesired defects such as TDs, larger mosaic tilt and/or reduction in coherent length (Moram et al., 2009).

The off-axis XRC FWHM measurement is performed for (10-11) and (11-20) planes for M1, M2 and M3 as shown in Figure 4.22 (a). As it can be seen from Figure 4.22 (a), the FWHMs of the (10-11) and (11-20) diffraction planes for M3 were enhanced by at least 20% as compared to M1. This is attributed to the increment of AlN/GaN pairs, in which the PSFs and partial dislocations (PDs) and/or perfect dislocation were reduced (McLaurin et al., 2008; Sun et al., 2009c).

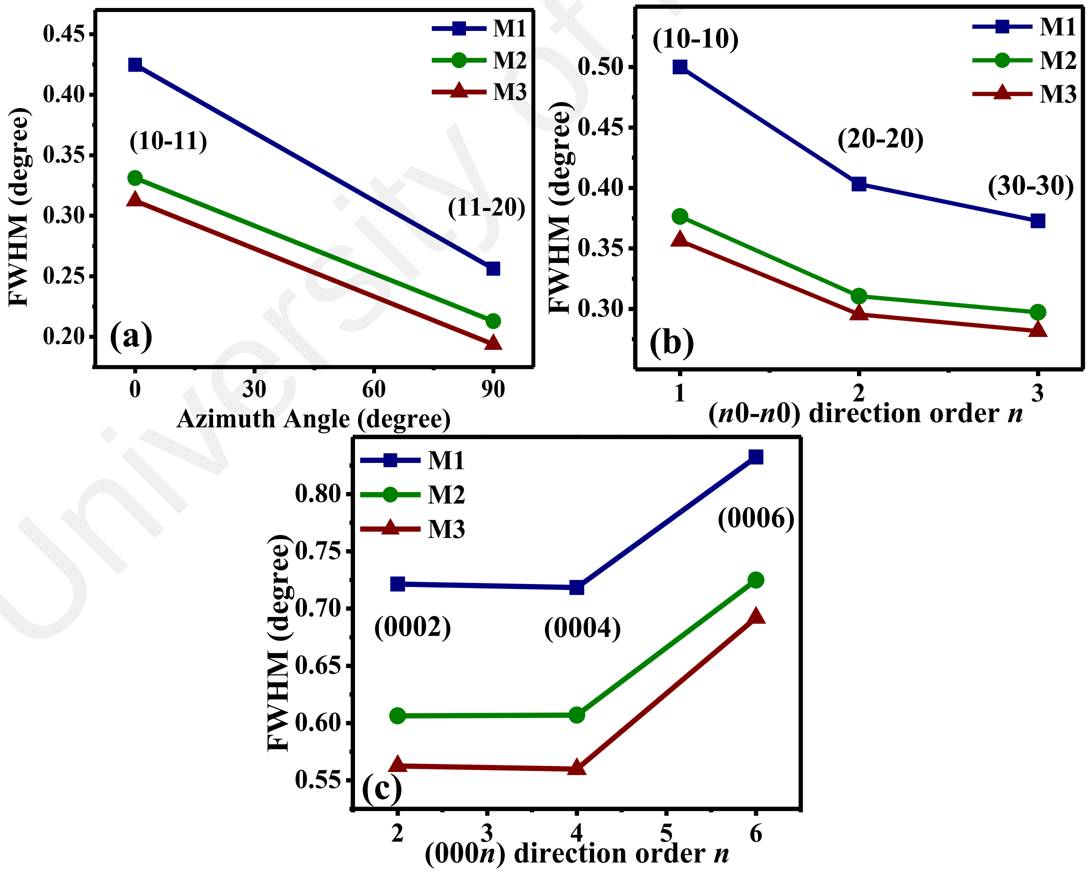

Figure 4.22: Off-axis XRC (a) FWHMs as a function of azimuthal angle (*Φ*), (b) M-plane (*n*0-*n*0) (*n* = 1, 2, and 3) FWHMs and (c) C-plane (000*n*) (*n* = 2, 4, and 6) FWHMs.

As shown in Figure 4.22 (b), the off-axis XRC FWHM values along m-plane direction for M3 recorded the lowest value as compared to M1 and M2 with the insertion of AlN/GaN 60 pairs. Furthermore, the off-axis XRC FWHMs along c-plane direction for M1, M2 and M3 are shown in Figure 4.22 (c). As it can be clearly observed from the Figure, the FWHM of M3 decreased as compared to M1 and M2 with the increment of the AlN/GaN pairs. These reductions might be attributed to BSFs and connected to PDs and/or perfect dislocation (Sun et al., 2009c).

These results are in good agreement with the measurements of HR-XRD $2\theta/\omega$, FESEM, AFM and TEM, in which the AlN/GaN 60 pairs suggested a proper interface abruptness between the GaN and AlN. It is speculated that the growth of a stack of two materials with dissimilar lattice constant produces strong strain, whereby the dislocation and defect might be averted from propagating upwards (Gian et al., 1996).

Here, the periodic peaks, relaxation state and crystal quality of the uid-GaN epitaxial layers with embedded AlN/GaN ML were investigated using the symmetric (11-22) RSM measurement along the [1-100] and [-1-123] directions. The RSM measurement along [1-100] direction for M1, M2 and M3 is shown in Figure 4.23 (a-c), respectively. As it can be discerned from Figure 4.23 (a) & (b), there is a slight tilt between the as-grown semi-polar (11-22) epitaxial layers (AlN and GaN) and the m-plane sapphire substrate for M1 and M2, respectively. In addition, fewer periodic peaks of AlN/GaN ML were observed in M1 and M2, resulting from the less abruptness in the AlN/GaN ML. However, it can be clearly observed from Figure 4.23 (c) that the peak positions corresponding to the semi-polar (11-22) nucleation layer AlN and uid-GaN are coherently grown along the semi-polar (11-22) plane (no tilt seen), indicating that the epitaxial films are along the same direction with a relaxed state (Farrell et al., 2012; Young et al., 2010; Zhao et al., 2016). Furthermore, the periodic peaks of AlN/GaN ML can be clearly observed in Figure 4.23 (c) due to the abruptness in the AlN/GaN ML. These results are in good agreement with the HR-XRD 2θ/ω scans and cross-sectional images of FESEM and TEM, in which the satellite peaks can be seen in M3 (60 pairs of AlN/GaN).

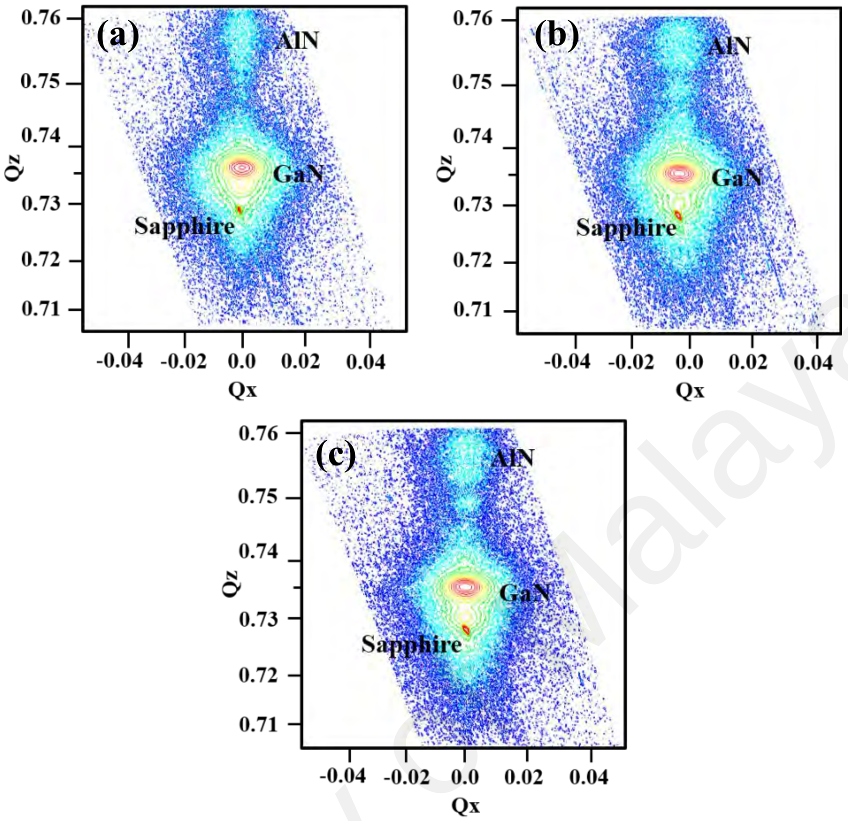

Figure 4.23: X-ray reciprocal space maps of semi-polar (11-22) along [1-100] direction for (a) M1, (b) M2 and (c) M3.

Figure 4.24 (a-c) illustrates the (11-22) RSM scans along [-1-123] direction for M1, M2 and M3, respectively. The semi-polar (11-22) epitaxial layer in the three samples exhibited tilts with the respect to the m-plane sapphire substrates unlike the [1-100] direction, in which with [-1-123] direction cumulative effect of the Burgers vectors is seen (Farrell et al., 2012). This is in turn indicating that relaxed epitaxial layers were attained, which might be resulting from the cumulative effect of the Burgers vectors (Farrell et al., 2012). The use of AlN/GaN 60 pairs was found to be more effective to reduce the lattice mismatch between the semi-polar (11-22) epitaxial layer and m-plane sapphire substrate, resulting from different state of strained states at AlN/GaN MLs. This is in turn promoting higher microscopic tilt for M3 as compared to M1. These results are in good agreement with the surface morphology analysis, in which the undulated-like features significantly receded.

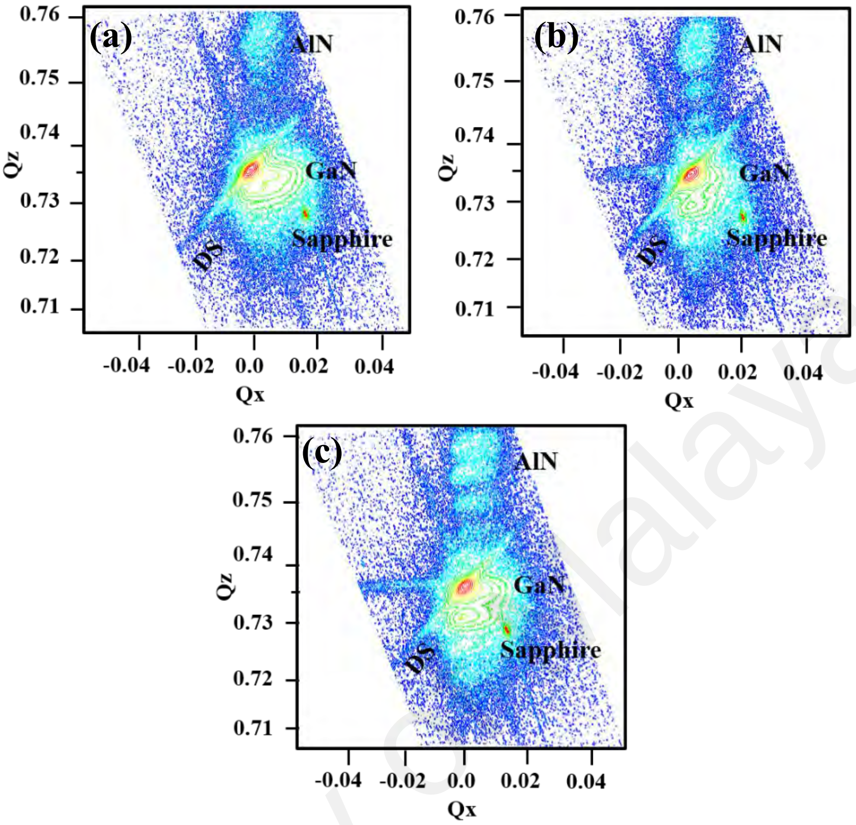

Figure 4.24: X-ray reciprocal space maps of semi-polar (11-22) along [-1-123] direction for (a) M1, (b): M2 and (c): M3.

The DS streaks in M1, M2 and M3 are visible as shown in Figure 4.24 (a-c). These streaks were clearly elongated in M1 and M2 and appear to be extended by almost 0.036 Å^{-1} and 0.03 Å^{-1}, respectively. While, the length of the DS streak for sample M3 did not exceed 0.025 Å^{-1}. As previously reported in the literature (Lazarev et al., 2013; Pristovsek et al., 2016), the length of the streaks is well correlated with the densities of the PSFs, the longer and clearer the streak, the higher the densities of the PSFs. Table 4.8 tabulates the tilt values and DS streaks of semi-polar (11-22) GaN and AlN peaks with respect to the m-plane sapphire peaks. Therefore, it is speculated that the PSFs decreased with the use of AlN/GaN 60 pairs, which is well correlated with the folding effect shown in the TEM analysis.

Table 4.8: Observed lattice tilt of semi-polar GaN and AlN epitaxial layer taken along [-1-123] direction as well as the elongated streaks for M1-M3.

Sample	GaN tilt with sapphire (°)	AlN tilt with sapphire (°)	DS Streak ($Å^{-1}$)
M1	~1.37	~1.15	~0.036
M2	~1.45	~1.19	~0.03
M3	~1.50	~1.25	~0.025

RT Raman spectroscopy measurement was utilized to investigate the compressive stress for M1, M2 and M3 as shown in Figure 4.25 (a) & (b). As displayed in Figure 4.25 (a), three peaks located at 379, 416, 742 cm^{-1} assigned by asterisks (*), were associated with the phonon mode of the m-plane sapphire substrate. While, the active phonon modes of the as-grown semi-polar (M1-M3) were E_2 (high), E_1 (TO) as well as A_1 (TO). The E_2 (high) phonon modes for M1 and M2 were shifted to 570 cm^{-1}, whilst the E_2 (high) phonon modes for M3 was located at 568 cm^{-1}. It was previously reported that the standard compressive stress-free GaN E_2 (high) is located at 568 cm^{-1} (Jiang et al., 2016; Yan et al., 2007). The shift in the E_2 (high) phonon modes is proportional to the compressive (blue-shifted) and tensile (red-shifted) strain (Jiang et al., 2016). This in turn suggests that the M1 and M2 suffer from compressive strain, while M3 indicates a strain -free state after the use of AlN/GaN 60 pairs. It is speculated that the difference in the stain level between the AlN/GaN and the uid-GaN reduced the stress in semi-polar (11-22) uid-GaN. Figure 4.25 (b) shows the FWHM of the GaN E_2 (high) mode peaks for M1, M2, and M3, in which an inverse relationship between the FWHM values and increment of the AlN/GaN pairs is observed. The improvement of the FWHM value of GaN E_2 (high) mode peak for M3 agrees with the enhancement of the structural properties obtained from the on and off-axis XRC measurement. This in turn indicates that the possibility of the interaction between the defects and dislocations, by which the enhanced crystal quality was attained (Yang et al., 2016).

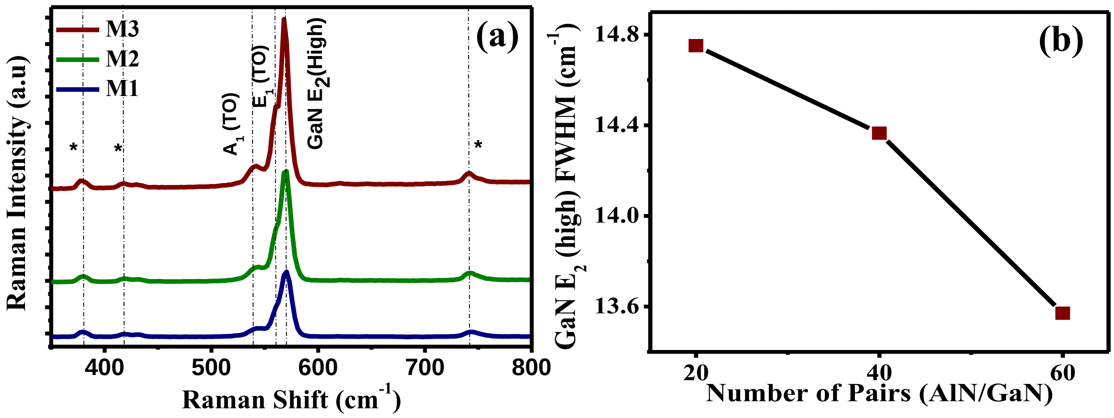

Figure 4.25: (a) Room temperature Raman spectra of as-grown GaN & (b) FWHM of GaN E_2 (high) as function of AlN/GaN pairs.

4.4 Conclusion

In summary, the use of AlN/GaN ML sandwiched between AlN and uid-GaN epitaxial layer (M3) enhances the crystal qualities of the uid-GaN by roughly 30% and 10% towards [-1-123] and [1-100], respectively as compared to the uid-GaN without AlN/GaN ML (S4). Hence, the reduction of the dislocation and defects was attained by introducing the 60 pairs of AlN/GaN ML. These results are compared with previous studies, in which Zhao et al., reported the FWHMs along [-1-123] and [1-100] to be 0.22° at and 0.42° (Zhao et al., 2016). In addition, comparison with ELOG technique as reported by Jae-Hwan Lee et al., showed that our results are comparable along [-1-123] and [1-100] (Lee et al., 2017). Additionally, our results further compared with SiN_x technique reported by Sheng-Rui Xu et al., whereby embedding the AlN/GaN ML demonstrates further enhancement of crystal quality (Xu et al., 2016). These results are well-correlated with the surface morphology analysis, whereby upon using the 60 pairs of AlN/GaN was found to be effectively reducing the arrowhead-like features. These results promote an effective approach to decrease the BSFs and associated PDs through the use of AlN/GaN ML 60 pairs. Hence, the semi-polar (11-22) GaN template with the use of 60 pairs AlN/GaN ML will be further utilized in the growth of semi-polar (11-22) LED.

CHAPTER 5: THE GROWTH OF N- AND P-TYPE SEMI-POLAR GAN

In this chapter, a series of n- and p-type gallium nitride (GaN) epitaxial layers is introduced in order to optimized the flow rates of disilane (Si_2H_6) and bicyclopentadienyl magnesium (Cp_2Mg). In Section 5.1, the n-type semi-polar (11-22) GaN epitaxial layers were optimized using different flow rates of Si_2H_6. On the other hand, the optimization of the semi-polar (11-22) p-type GaN epitaxial layers using different Cp_2Mg flow rates is presented in Section 5.2. The crystal orientation for n- and p-type GaN grown on m-plane sapphire substrates was examined by high resolution-x-ray (HR-XRD) diffraction $2\theta\omega$ scans. In addition, the on- and off-axis x-ray rocking curve (XRC) as well as the room temperature (RT) Raman spectroscopy were utilized to characterize the crystal quality of the epitaxial layers grown on m-plane sapphire substrates. Whilst, field emission scanning electron microscopy (FESEM) and atomic force microscopy (AFM) were further used to characterize the morphological properties of n- and p-type GaN epitaxial layers. Finally, the Hall effect measurement was employed to investigate the electrical characteristics of n- and p-type semi-polar (11-22) GaN epitaxial layers.

5.1 Optimization of the Si_2H_6 Flow Rates for n-Type GaN

5.1.1 Growth Methodology

The n-type semi-polar (11-22) GaN epitaxial layers were grown on the optimized uid-GaN templates as shown in Figure 5.1. The growth temperature was maintained at 1050 °C, with 59.5 standard cubic centimeters per minute (sccm) of trimethylgallium (TMG) and 0.7 standard liter per minute (slm) of ammonia (NH_3) as to ensure the same growth condition to the uid-GaN was maintained; to avoid the regeneration of defects and dislocations. In turn, the properties of n-type GaN will purely influenced by the doping concentration. In this work, Si_2H_6 was utilized as dopant, whereby the Si_2H_6 flow rates were varied to determine the impact of doping concentration towards the structural and electrical properties of the n-type GaN. Three dissimilar n-type GaN were prepared and denoted as N1, N2 and N3, where Si_2H_6 flow was varied at 10, 15, and 20 sccm, respectively.

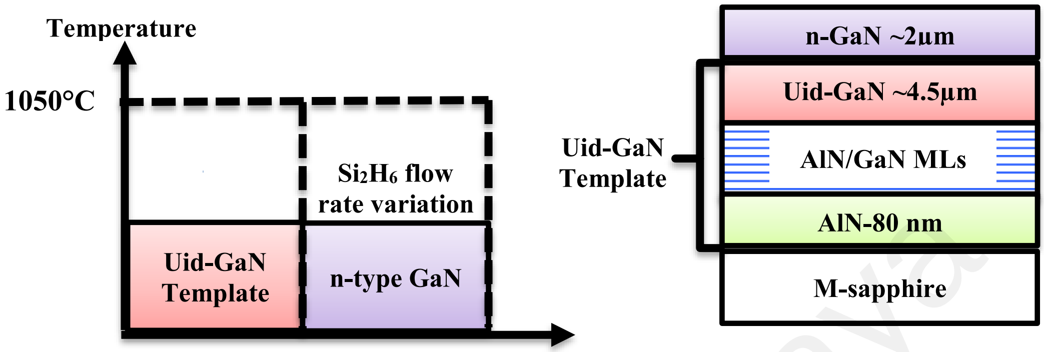

Figure 5.1: The growth methodology of n-type GaN grown on top of uid-GaN template.

5.1.2 The Influence of the Si_2H_6 Flow Rates on the Crystal Orientation

The HR-XRD 2*θ*/*ω* scans were implemented to elucidate the crystal orientation for N1, N2 and N3 as shown in Figure 5.2. Table 5.1 presents the n-type samples used in this study with different Si_2H_6 flow rates and the obtained diffraction peaks.

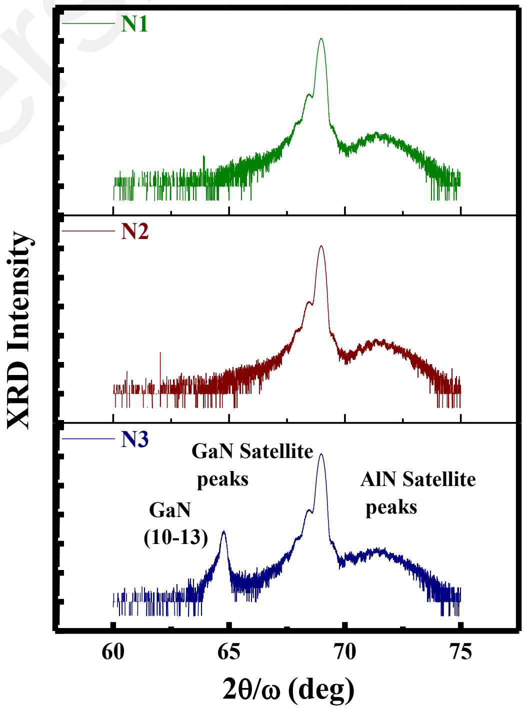

Figure 5.2: HR-XRD 2*θ*/*ω* scans of n-type GaN epitaxial layers grown on m-plane (10-10) sapphire substrate.

Table 5.1: Disilane (Si_2H_6) flow rates and the diffraction peaks for as-grown n-type GaN epitaxial layers (N1-N3) on m-plane sapphire substrate.

Samples	**N1**	**N2**	**N3**
Si_2H_6 Flow (sccm)	10	15	20
GaN Diffraction peaks	(11-22)	(11-22)	(10-13) (11-22)

The diffracted fringes for N1, N2 and N3 were visible and uniform due to the interface and the abruptness of AlN/GaN multi-layer (ML), which were mentioned in Subsection 4.3.2. However, at high flow rate of Si_2H_6 (N3), a peak of semi-polar (10-13) was existed due to the rough surface of the n-type GaN, which might be resulting from the twinned crystallites. It is speculated that the excess of high flow rate of Si_2H_6 would induce higher strain, resulting in poorer crystal orientation. In contrast, the peak of semi-polar (10-13) GaN was absent for N1 and N2, in which only the diffracted fringes of semi-polar GaN and AlN were attained. Therefore, it is suggested that upon using the low flow rate of Si_2H_6 of 10 and 15 sccm, single crystal of n-type GaN epitaxial layer was obtained.

5.1.3 Impact of the Si_2H_6 Flow Rates on Morphological Properties

The morphological properties of the semi-polar (11-22) n-type GaN grown on m-plane sapphire substrate with different Si_2H_6 flow rates were investigated using AFM and FESEM analysis. Figure 5.3 (a-i) illustrate the morphological properties for N1, N2 and N3. It is unambiguously discerned that the typical arrowhead-like features of the semi-polar (11-22) epitaxial layer grown on m-plane sapphire substrate were prevailing. When the flow rate of 10 sccm Si_2H_6 flow rate (N1) was utilized as shown in Figure 5.3 (a), the arrowhead-like features were dense with a root mean square (RMS) surface roughness of 6.6 nm over a 10×10 μm scan size AFM. In order to reveal the origin of undulated features, a higher magnification of 1×1 μm scan size AFM imaging was utilized. Figure 5.3 (b) demonstrates presence of small terrace sizes with loosely packed steps, inducing longer intervals between the protruding terraces. This in turn leads to increased valley formations (highlighted in white circles), which results in the observable undulated features in the FESEM plain view image (c) as well as 10×10 µm scan size AFM image (a). However, as the Si_2H_6 flow rate was increased to 15 sccm (N2), density of the arrowhead-like features was observed to reduce, resulting in RMS surface roughness of 5.7 nm as shown in Figure 5.3 (d) as well as the plain view FESEM image (f). This is mainly owing to formation of larger terrace sizes (as shown in 1×1 µm scan size AFM image (e)), inducing closely-packed (in length) step terraces. Conversely, further increasing the dopant flow to 20 sccm Si_2H_6, the arrowhead-like feature further increases, resulting in RMS surface roughness of 7.6 nm as shown in Figure 5.3 (g).

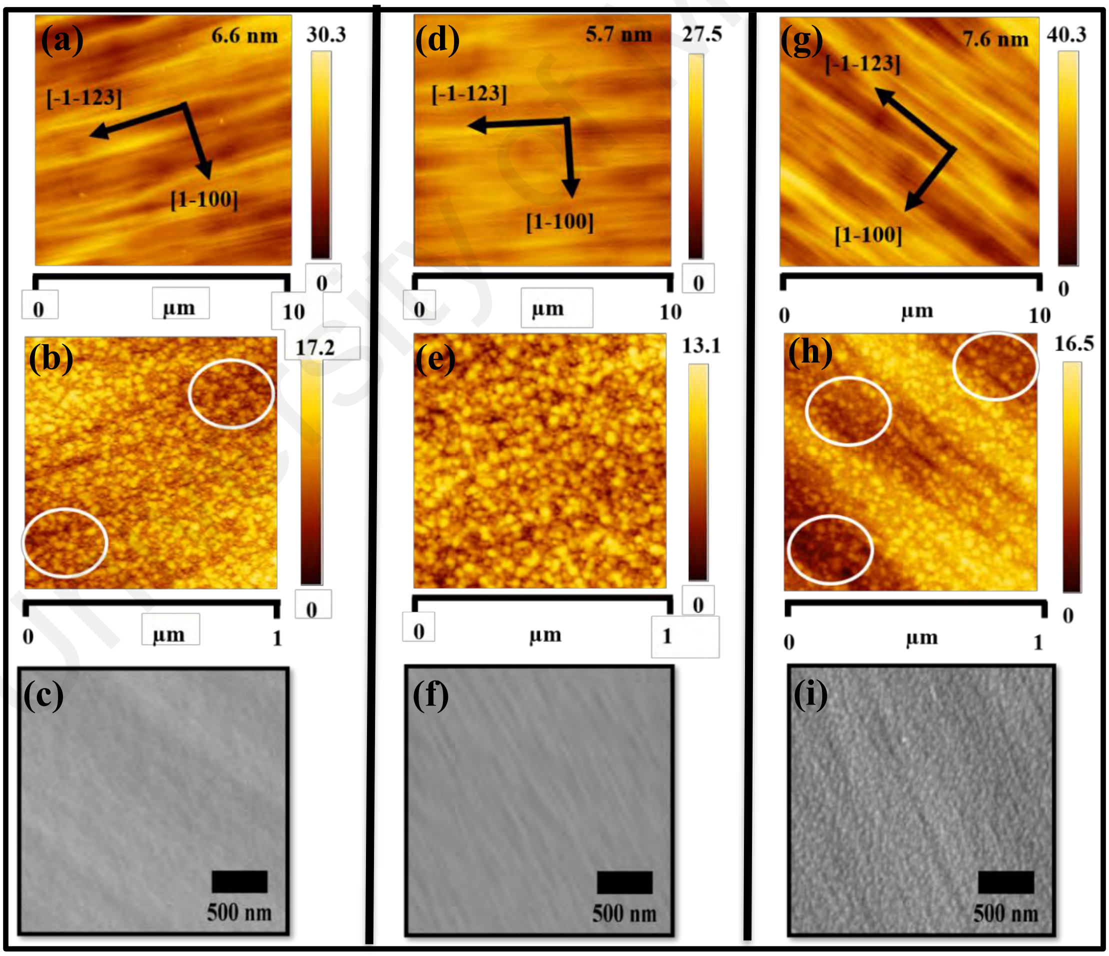

Figure 5.3:Surface morphology analysis for (a-c) N1, (d-f) N2 and (g-i) N3.

The 1×1 μm scan size AFM image (h) reveals the evolution of the terrace to a highly irregular distribution constituting loosely packed terrace steps. This in turn results in larger areas of valleys (highlighted in white circles), increasing the undulated features as observed in the FESEM plain view image (i). This is due to the fact that the growth mode slightly changed from 2D to 3D when the heavily-doped is introduced, which is well correlated with the HR-XRD $2\theta/\omega$ scans. In order to further understand the mechanism involved in the surface evolution, on- and off-axis XRC analysis is implemented to determine the causality of the phenomenon in the microstructure.

5.1.4 Effect of the Si_2H_6 Flow Rates on the Structural Properties

The on-axis XRC measurement is accomplished to illustrate the reduction of anisotropic properties for N1-N3. Figure 5.4 (a) & (b) illustrates the measurement of the symmetric XRC using the M-shape azimuthal (Φ) dependence of full width at half maximum (FWHM) over 360° and the FWHMs as a function of Si_2H_6 flow rates for N1-N3, respectively. The FWHMs along [-1-123] for N1, N2 and N3 were 0.14°, 0.13°, 0.15°, respectively, while the FWHMs along [1-100] were 0.32°, 0.31°, 0.33°, respectively. It is noted that the value of the FWHM along [-1-123] and [1-100] for N2 were reduced with the use of 15 sccm Si_2H_6 flow rate as compared to N1. This is attributed to reduction of the anisotropic properties, resulted from the enhanced of the dislocation movements as the 15 sccm Si_2H_6 flow rate promoted climbing or gliding of the dislocations (Dai et al., 2017). However, upon the use of 20 sccm Si_2H_6 flow rate, the FWHMs increased due to the valleys from high flow rate of Si_2H_6 dopant as highlighted in the surface morphology analysis. This is well correlated with the HR-XRD $2\theta/\omega$ and the surface morphology analysis, in which rougher surface would induce higher dislocation densities. The FWHMs along [-1-123], [1-100], [11-2-3] and [-1100] directions for N1-N3 are shown in Table 5.2.

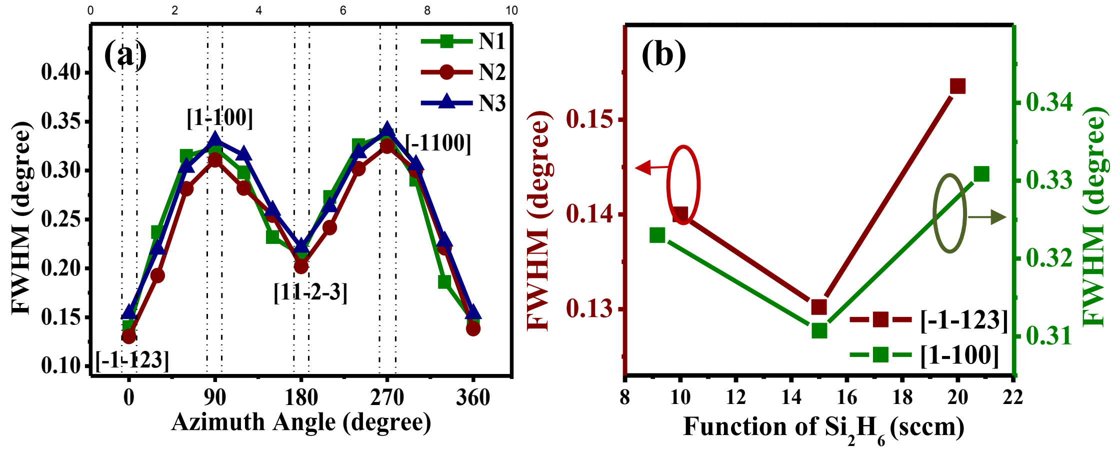

Figure 5.4: On-axis XRC FWHM values (a) As a function of azimuthal angle (*Φ*) and (b) Along [-1-123] and [1-100] directions as a function of Si_2H_6.

Table 5.2: On-axis XRC FWHMs along [-1-123], [1-100] [11-2-3] and [-1100] directions for n-type GaN epitaxial layers (N1-N3).

Samples	FWHM (deg)			
	[-1-123]	[1-100]	[11-2-3]	[-1100]
N1	0.14	0.32	0.21	0.33
N2	0.13	0.31	0.20	0.32
N3	0.15	0.33	0.22	0.34

In contrast, Figure 5.5 (a) shows the off-axis XRC FWHMs of the (10-11) and (11-20) planes for N1-N3. As it can be obviously discerned, the FWHM of the (10-11) and (11-20) planes for N2 illustrate a slight enhancement as compared to N1 and N3, which indicate the reduction of the prismatic stacking faults (PSFs), partial dislocations (PDs) and/or perfect dislocation. Figure 5.5 (b) shows the off-axis XRC FWHMs along m-direction with increasing diffraction order (*n*) from 1 to 3 for N1-N3. As it can be seen that the (n0- n0) XRC FWHMs for N2 were narrowed as compared to N1 and N3. The decrement is believed to be associated with the reduction of the basal stacking faults (BSFs) based on the visibility criteria. Additionally, the (000n) XRC FWHMs for N1-N3 with an increased *n* from 2 to 6 is shown in Figure 5.5 (c). As the Si_2H_6 flow rate was 15 sccm (N2), the (000n) XRC FWHM illustrated the lowest value, which might be due the decrement in the PDs and/or perfect dislocation densities (Sun et al., 2009c). However, it can be seen that upon using the 20 sccm of Si_2H_6 flow rate, the (000n) XRC FWHM increased suggesting the increment of the PDs and/or perfect dislocations.

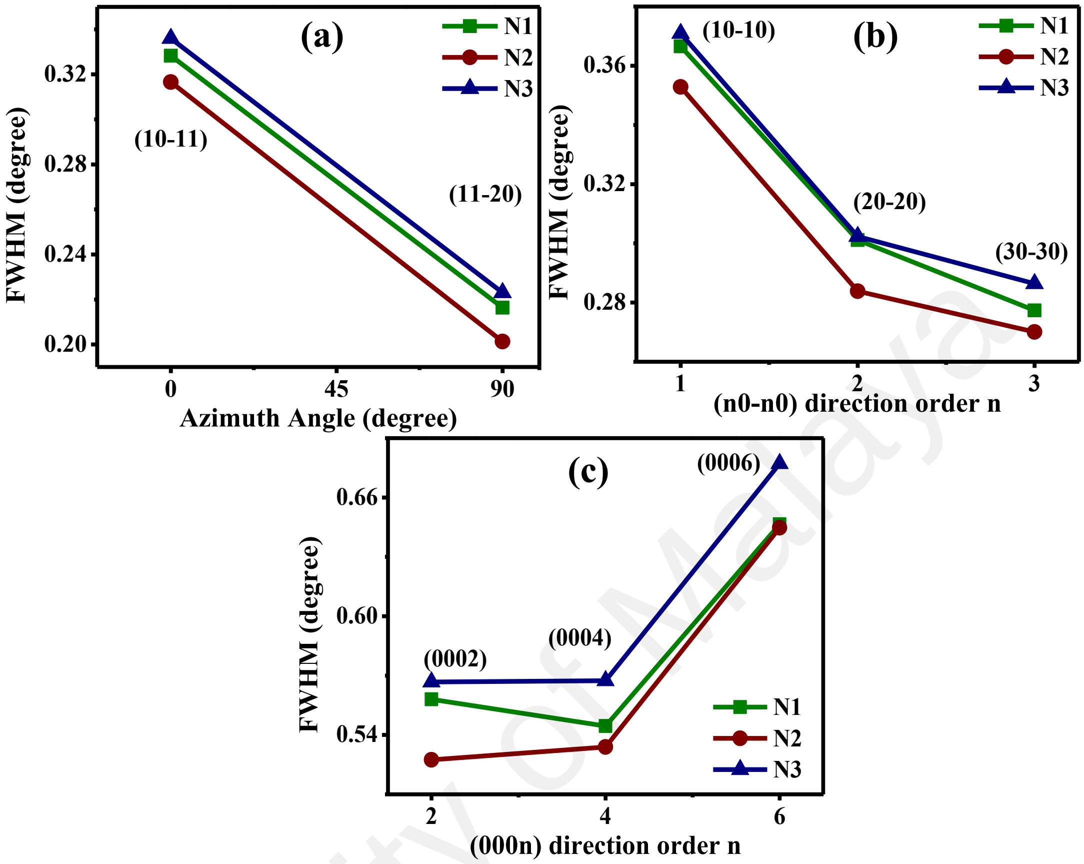

Figure 5.5: Off-axis XRC (a) FWHMs as a function of azimuthal angle (Φ), (b) M-plane (n0-n0) (n = 1, 2, and 3) FWHMs and (c) C-plane (000n) (n = 2, 4, and 6) FWHMs.

It is speculated that the excessive Si_2H_6 flow rate of 20 sccm (N3) might increase defects and dislocations by forming SiN_x-related dislocation cores (Dai et al., 2017; Wang et al., 2016). However, upon using the 15 sccm Si_2H_6 high flow rate (N2), the crystal quality was improved owing to the dislocation movements; the optimum Si_2H_6 high flow rate of 15 sccm might promote climbing and/or gliding of the defects and dislocations, in turn induces the interaction and annihilation of the defects (Dai et al., 2017; Manning et al., 2009). These results are in good agreement with the surface morphology analysis in which the triangular-like and undulated features appeared on the surface deduced more defects and dislocation.

Raman spectroscopy was accomplished for the as-grown n-type of N1, N2 and N3 to study the effect of Si_2H_6 flow rate towards the compressive strain. Figure 5.6 (a) & (b) illustrates the RT Raman spectroscopy for N1, N2 and N3. As it can be seen, three obvious peaks of sapphire were seen for N1-N3 and located at 377.5, 415.8, 742.2 cm^{-1}, denoted as (*). Whilst, the E_1 (TO), A_1 (TO) and E_2 (high) peaks were attributed to semi-polar GaN epitaxial layer for N1-N3. The E_2 (high) peak for N2 was located at 568.5 cm^{-1}, while the E_2 (high) peak for N1 and N3, were located at 569.5 cm^{-1} and 570 cm^{-1}, respectively. As mentioned in the literature, the E_2 (high) for GaN and AlN were located at 568 and 643 cm^{-1}, whereby the shift in the E_2 (high) peak is proportional to the compressive and tensile stress (Jiang et al., 2016; Yan et al., 2007). Hence, it is presumed that N1 suffered from a compressive strain, which could be reduced upon using the 15 sccm Si_2H_6 flow rate. This in turn concluded the relaxation state of the compressive strain in the n-type semi-polar (11-22) GaN epitaxial layer was attained. Nevertheless, at high Si_2H_6 flow rate of 20 sccm, the doping efficiency was degraded owing to the formation of local self-compensation centers, resulted from the compressive strain (Dai et al., 2017; Yang et al., 2016).

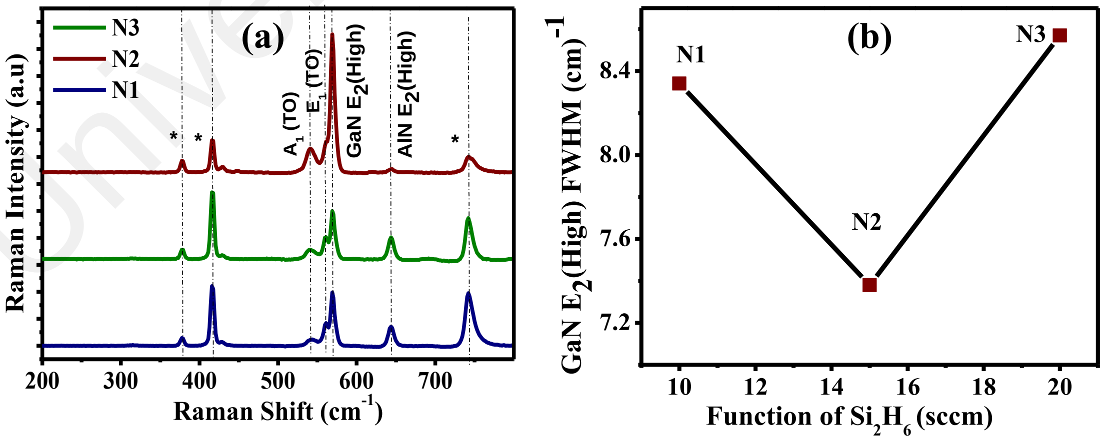

Figure 5.6: (a) Room temperature Raman spectra of n-type semi-polar (11-22) GaN & (b) FWHM of GaN E_2 (high) as a function of Si_2H_6 flow rate.

Figure 5.6 (b) shows FWHM of the GaN E_2 (high) mode peaks for N1-N3 as a function of Si_2H_6 flow rate. The FWHMs of GaN E_2 (high) peaks for N1, N2 and N3 were 8.3, 7.3 and 8.5 cm^{-1}, respectively. This phenomenon in turn suggests the enhancement of the GaN E_2 (high) peak for N2, which agrees with the on- and off-axis XRC measurement (Yang et al., 2016). This is well correlated with the enhancement of the crystal and morphological properties, whereby the interaction and/or annihilation of the defects would be promoted due to the climbing or gliding of dislocations (Dai et al., 2017).

5.1.5 Impact of the Si_2H_6 Flow Rates on the Electrical Properties

The electrical properties for semi-polar (11-22) n-type GaN epitaxial layers grown on m-plane with different Si_2H_6 flow rates were characterized by room temperature (RT) Hall effect measurement. The electron concentration and the mobility as a function of Si_2H_6 flow rate for three samples were examined as shown in Figure 5.7. It is obviously discerned that the electron concentration with elevating the Si_2H_6 flow rate from 10 to 20 sccm, the electron concentration increased from 8.1×10^{17} to 1.6×10^{18} cm^{-3}. In addition, upon using a moderate incorporation of Si_2H_6 flow rate of 15 sccm, resulting in an increment of electron mobility from 76.9 to 99.3 cm^2. V^{-1}. S^{-1}. However, the electron mobility for N3 decreased to 96.4 cm^2. V^{-1}. S^{-1} although the electron concentration increased as we further increased the Si_2H_6 flow rate to 20 sccm. This might be due to dopant-related dangling bonds along the existing dislocations, which act as acceptor traps forming negatively charged scattering centers. Thus the electron mobility decreased upon the use of heavily doped n-type GaN (20 sccm Si_2H_6 flow rate) (Dai et al., 2017; Ng et al., 1998).

The decrement in the mobility upon using the heavily doping of 20 sccm Si_2H_6 flow rate might be also due to the increment of ionized impurity scattering centers, resulting from the excessive Si_2H_6 flow rate (Dai et al., 2017; Liu et al., 2019; Yang et al., 2016).

In other words, the ionized Si impurities became scattering centers, thus the mobility would be decreased. Therefore, it is inferred that the mobility properties would be highly affected by the impurity-related scattering centers as well as crystal quality enhancement, which in turn induce the formation of acceptor traps. These assumptions agree completely with the morphological and crystal properties, in which it is evidenced that the 15 sccm Si_2H_6 flow rate promotes a moderate doping of semi-polar (11-22) n-type GaN. Table 5.3 lists the values of electron concentration, electron mobility, carrier density and conductivity for the N1-N3.

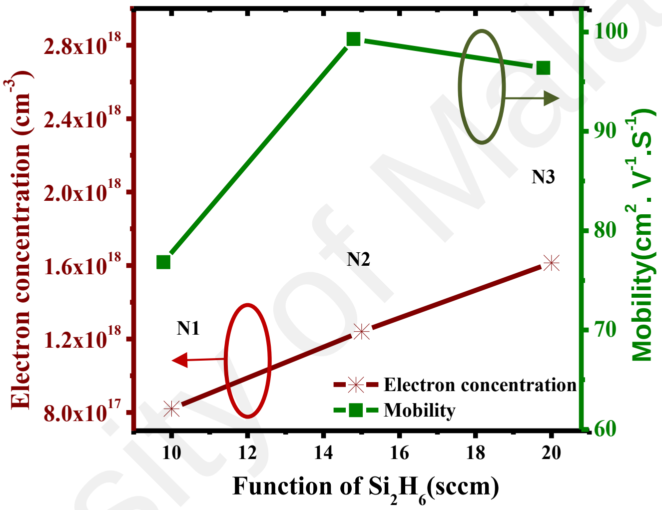

Figure 5.7: The electron concentration and the electron mobility as a function of the Si_2H_6 flow rate for N1-N3.

Table 5.3:The values of electron concentration and electron mobility for N1-N3.

Sample	**N1**	**N2**	**N3**
Si_2H_6 flow rate (sccm)	10	15	20
Electron concentration (cm^{-3})	8.2 ×10^{17}	1.3 ×10^{18}	1.6 ×10^{18}
Electron mobility (cm^2. V^{-1}. S^{-1})	76.9	99.3	96.4

5.1.6 Summary

It is convincing to presume that the variation of the Si_2H_6 would impact the morphological, structural and electrical properties of the n-type GaN. Based on the results, the moderately Si_2H_6 doped n-type GaN exhibited the most enhanced microstructural properties, resulting in a relatively superior electrical characteristics compared to the lightly and heavily doped samples. These results are comparable with previous studies, where it was seen that the use of n-AlGaN alloys for enhanced of n-type properties (Dai et al., 2017). In this study, however, the use of n-GaN was implemented with enhanced properties. The process involved during the preparation of n-type GaN consists of simultaneous flow of TMG (Ga), NH_3 (N) and Si_2H_6 (Si), whereby the Si atom will be incorporated within the GaN matrix; the doping concentration is highly dependent on flow of Si_2H_6. It is presumed that excessive flow of Si_2H_6 would endure a dominant substitution of the Ga atom, forming SiN_x related dislocation cores, thus increasing the dislocations and defects densities. In addition, such occurrences would facilitate mixed-orientated growth directions, leading to slight transition from 2D to 3D growth mode. Hence, the moderately doped n-GaN (N2) will be further utilized for the LED deposition.

5.2 Optimization of the Cp_2Mg Flow Rates for p-Type GaN

5.2.1 Growth Procedure of p-type GaN

Similar to the n-type GaN, the doping rate of the p-type GaN would also undergo an optimization phase, whereby the Cp_2Mg flow would be varied. Growth of the p-type GaN is as shown in Figure 5.8, in which the template of uid-GaN was further utilized. The growth temperature was kept at 1000 °C as the full LED structure in the later would employ slightly lower temperature for the p-type GaN growth to avoid the indium dissociation. In contrast to the n-type preparation, the p-type GaN requires a slightly lower growth rate to help facilitate the magnesium (Mg) incorporation within the GaN matrix. The TMG and NH_3 flow were 22.6 sccm and 0.7 slm, respectively. Simultaneously, the Cp_2Mg was flowed at different flow rates of 20, 30 and 40 sccm, and designated as P1, P2 and P3, respectively.

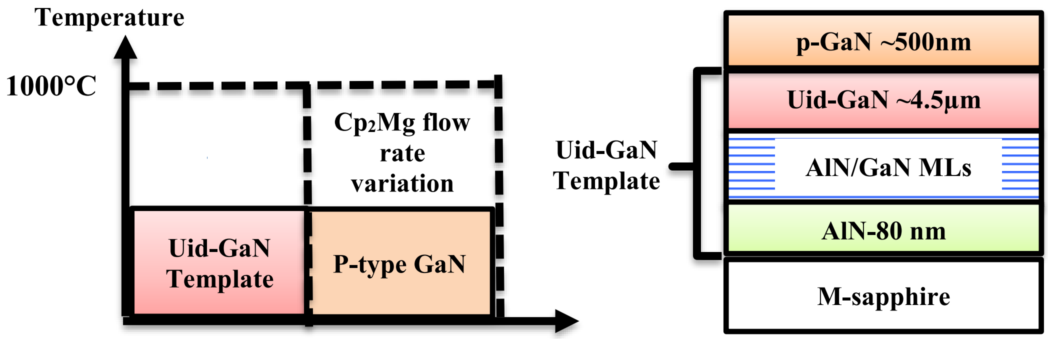

Figure 5.8: The growth procedure for p-type GaN grown on top of uid-GaN template.

5.2.2 Effect of the Cp_2Mg Flow Rates on the Crystal Orientation.

HR-XRD $2\theta/\omega$ scans were performed on all the p-type GaN epitaxial layer to ensure the crystal orientation of semi-polar (11-22) GaN. Figure 5.9 illuminates that the growth orientation was maintained to precede along (11-22) without any deviation in the crystal phase for P1-P3.

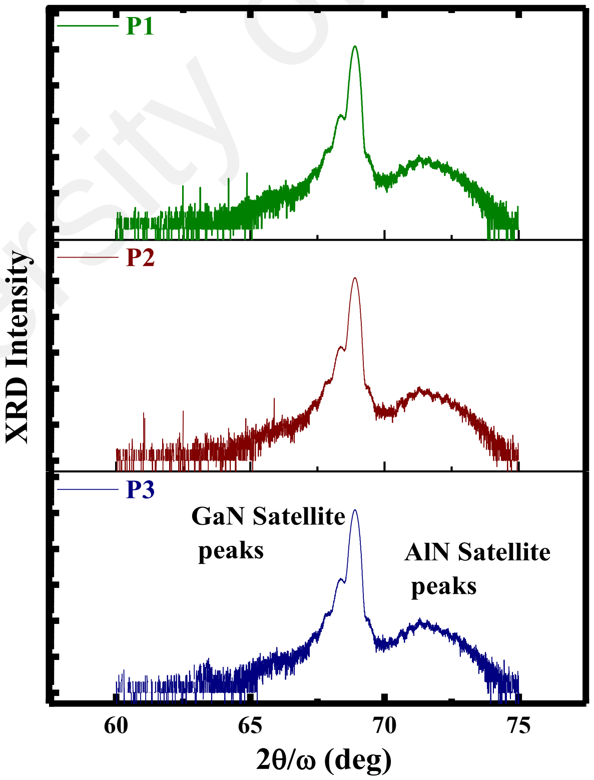

Figure 5.9: HR-XRD $2\theta/\omega$ scans for semi-polar (11-22) p-type GaN epitaxial layers grown on m-plane sapphire substrate.

As shown in the Figure, even with excessive doping of Mg would somehow attain the single crystal phase of (11-22) unlike n-type GaN. This is mainly due to the dissimilar doping behavior between the Mg and Si. It is well known, that the doping of GaN epitaxial layers with Mg would not significantly deteriorate the crystal properties. Hence, variations in the doping concentration would rarely effect the crystal phase orientation of the GaN epitaxial layers (Song et al., 2011).

5.2.3 Impact of the Cp_2Mg Flow Rates on the Morphological Properties

The analysis of the morphological properties of the p-type semi-polar (11-22) GaN grown on m-plane sapphire substrate using various Cp_2Mg flow rates were studied by AFM and FESEM analysis. Figure 5.10 (a-i) shows the surface morphology analysis for P1, P2 and P3. The RMS surface roughness of P1 was recorded to be 6.4 nm over a 10×10 µm scan size AFM with the use of 20 sccm Cp_2Mg flow rate as shown in Figure 5.10 (a). The higher magnification scan area over 1×1 µm scan size AFM for P1 (b) reveals that there is indeed a lower scale surface evolution with non-uniform terraces. This phenomenon is mainly due to the lengthy and inhomogeneous step-like structures, inducing relatively wide valleys (highlighted in white circles). These obvious features are well correlated with the observable undulation feature in FESEM plain view image (c), in which exhibiting higher density of undulation. In contrast, when the 30 sccm of Cp_2Mg flow rate was introduced, the RMS surface roughness for P2 slightly reduced to 6.0 nm for 10×10 µm scan size AFM as shown in Figure 5.10 (d). Furthermore, it can be unambiguously observed with higher magnification of 1×1 µm scan size AFM imaging (e) that the uniformity of the step-like structures was enhanced, resulting in narrowing of the valleys. This in turn promotes a closely-packed step terraces, which reduces the undulation features as observed from the FESEM plain view image (f).

Furthermore, the increase of Cp_2Mg flow rate to 40 sccm deteriorated the surface roughness with increased density of the arrowhead-like features as illustrated in Figure 5.10 (g). Figure 5.10 (h) depicts the higher magnification AFM image, which reveals that the step-like structures evolving to an inferior state, whereby the length and distribution of the terraces becomes poorer. This in turn formed a significantly wider valley length (highlighted in white circles) with increased density. These features are correlated with the undulation feature as it is seen from the FESEM plain view images (i). Further details surrounding the Mg doping mechanism will be discussed in the XRC analysis.

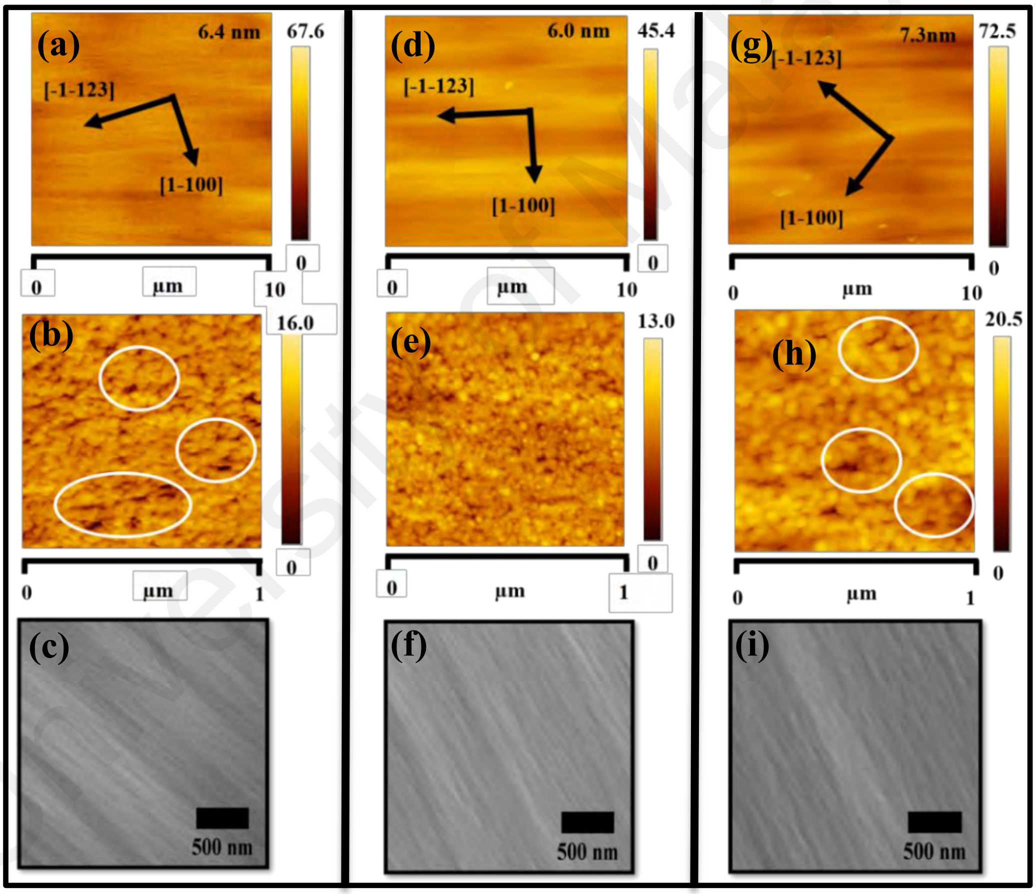

Figure 5.10: Surface morphology analysis for (a-c) P1, (d-f) P2 and (g-i) P3.

5.2.4 Effect of the Cp_2Mg Flow Rates on the Structural Properties

Figure 5.11 (a) & (b) represents the on-axis XRC measurement in order to study the influence of Cp_2Mg flow rates towards the crystal quality of P1, P2 and P3. As it can be seen that the M-shape azimuthal dependence of FWHM over 360° was illustrated in

Figure 5.11 (a), while Figure 5.11 (b) shows the FWHMs along [-1-123] and [1-100] as a function of Cp_2Mg flow rates. As shown in Figure 5.11 (a), as the Cp_2Mg flow rate increased to 30 sccm (P2), the FWHMs decreased from 0.134° to 0.132° along [-1-123] and from 0.330° to 0.326° along [1-100]. However, the FWHMs increased to 0.136° along [-1-123] and 0.347° along [1-100] with 40 sccm Cp_2Mg flow rate (P3). The FWHM value along [-1-123], [1-100], [11-2-3] and [-1100] are listed in Table 5.4.

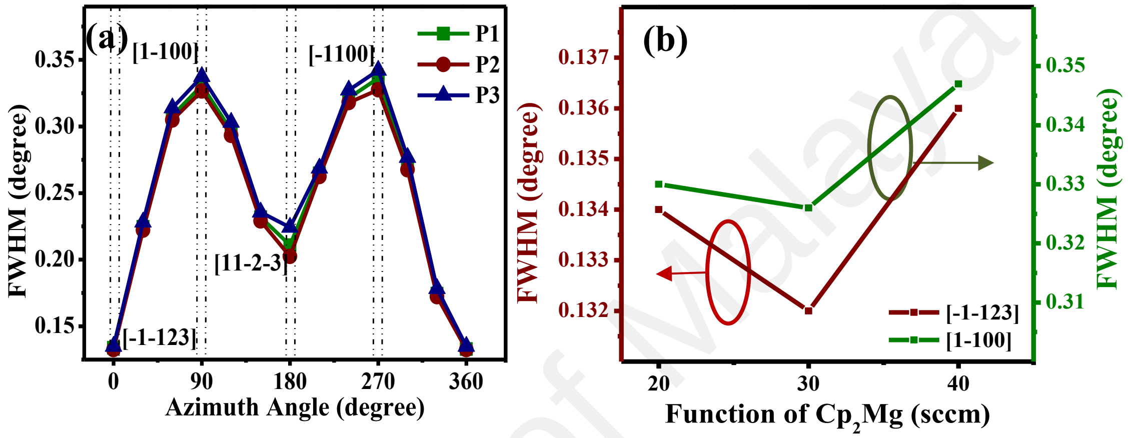

Figure 5.11: On-axis XRC FWHM values of (11-22) *ω*-scan (a) As a function of azimuthal angle (*Φ*) and (b) Along [-1-123] and [1-100] as a function of Cp_2Mg.

Table 5.4: On-axis XRC FWHMs along [-1-123], [1-100] [11-2-3] and [-1100] directions for p-type GaN epitaxial layers (P1-P3).

Samples	FWHM (deg)			
	[-1-123]	[1-100]	[11-2-3]	[-1100]
P1	0.134	0.330	0.211	0.336
P2	0.132	0.326	0.202	0.327
P3	0.136	0.347	0.224	0.342

The off-axis XRC FWHMs of (10-11) and (11-20) planes for P1-P3 are shown in Figure 5.12 (a-c). As it can be seen from Figure 5.12 (a), the FWHM values of the (10-11) and (11-20) planes for 20 and 40 sccm of Cp_2Mg flow were observed to higher than 30 sccm. This indicates that the PSFs, PDs and/or perfect dislocation were increased with non-moderate Cp_2Mg flow rate (20 and 40 sccm).

Figure 5.12 (b) demonstrates (*n*0-*n*0) XRC FWHM value along the m-direction with increasing of *n* from 1 to 3. As it can be observed that the FWHM for P2 was slightly lower compared to P1. However, as the Cp_2Mg flow rate was increased to 40 sccm (P3), the FWHM values were significantly broadened, indicating an increased density of BSFs. The (000n) XRC FWHMs for P1-P3 with increment of *n* from 2 to 6 portrayed similar trend to (*n*0-*n*0), signifying the poor crystal quality upon the use of high Cp_2Mg flow rate of 40 sccm as shown in Figure 5.12 (c).

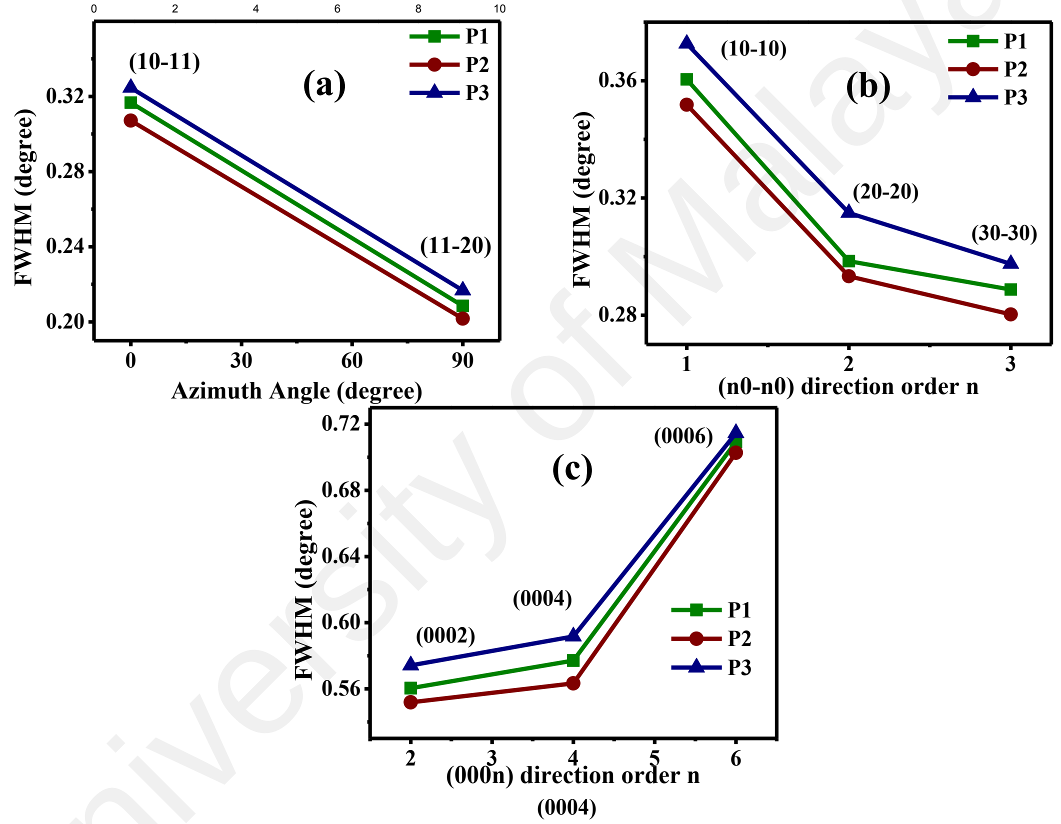

Figure 5.12: Off-axis XRC (a) FWHMs as a function of azimuthal angle (*Φ*), (b) M-plane (*n*0-*n*0) (*n* = 1, 2, and 3) and (c) C-plane (000*n*) (*n* = 2, 4, and 6).

It is safe to assume that the crystal qualities were maintained upon with 30 sccm of Cp_2Mg flow, resulting in the improvement of surface morphology with uniformly distributed terraces. On the other hand, the excessive Cp_2Mg flow rate into the GaN epitaxial layers induced the generation of additional dislocations and defects, leading to increased valley formations on the surface. This is attributed to the irregular distribution of the terraces, resulting from the difference in the atomic size between Mg and Ga (Dai et al., 2017). In turn a lattice distortion will be generated between the Mg and Ga atoms, leading to the newly generated dislocations and defects.

Figure 5.13 (a) & (b) demonstrates the RT Raman spectroscopy to investigate the impact of Cp_2Mg flow rate on the compressive strain/stress for P1-P3. As shown in Figure 5.13 (a), the peaks of sapphire substrate for P1-P3 were located at 377.5, 415.8, 742.2 cm^{-1} and assigned by (*). Furthermore, it was found that the E_2 (high) for all three samples (P1-P3) clearly exhibited dual mode behaviors, which identified to be E_2 (high) GaN and E_2 (high) AlN. The peaks of the A_1 (TO) and E_1 (TO) for all the three samples were located at 540.7 and 561.1 cm^{-1}, respectively. In contrast, the peak of E_2 (high) GaN for P1 and P3 were located at 570.5 cm^{-1}, whilst the E_2 (high) GaN for P2 was blue-shifted to 568.5 cm^{-1}. It was reported that higher or lower than the critical value would suggest a tensile or a compressive stress/strain (Demangeot et al., 1998; Kuball, 2001). Hence, it could be deduced that P1 and P3 suffer from compressive strain, conversely with P2.

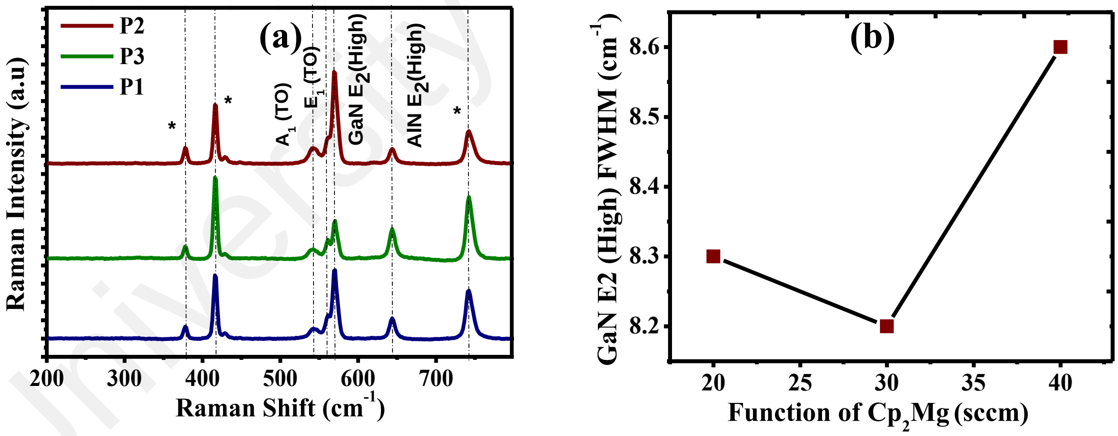

Figure 5.13: (a) Room temperature Raman spectra of p-type semi-polar (11-22) GaN and (b) FWHM of GaN E_2 (high) as a function of Cp_2Mg flow rate.

Figure 5.13 (b) shows the FWHMs of GaN E_2 (high) peaks for P1-P3 as a function of Cp_2Mg flow rate. The FWHMs for P1-P3 were 8.3, 8.2 and 8.6 cm^{-1}, indicates that the enhancement of crystal quality was attained upon using the 30 sccm of Cp_2Mg flow rate. It is assumed that upon using 30 sccm Cp_2Mg flow rate, a uniform distribution terrace was attained, resulting in a relaxed state of compressive strain. Nevertheless, at high Cp_2Mg flow rate (P2), the doping behavior was degraded owing to the formation of local self-compensation centers, resulted from the compressive strain (Dai et al., 2017; Yang et al., 2016).

5.2.5 The Influence of Cp_2Mg Flow Rates on the Electrical Properties

The RT Hall effect measurement was carried out to investigate the electrical properties of p-type semi-polar (11-22) GaN epitaxial layers grown on m-plane with different Cp_2Mg flow rates. Figure 5.14 shows the hole concentration and the hole mobility as a function of Cp_2Mg flow rates for P1-P3. The hole concentration for P1-P3 increased almost linearly from 3.1×10^{19} to 5.1×10^{19} cm^{-3} by increasing the Cp_2Mg flow rate to 40 sccm. However, the hole mobility for P2 increased to 1.8 $cm^2.V^{-1}.S^{-1}$ upon using 30 sccm of Cp_2Mg flow rate, while the mobility for P3 reduced to 0.6 $cm^2.V^{-1}.S^{-1}$.

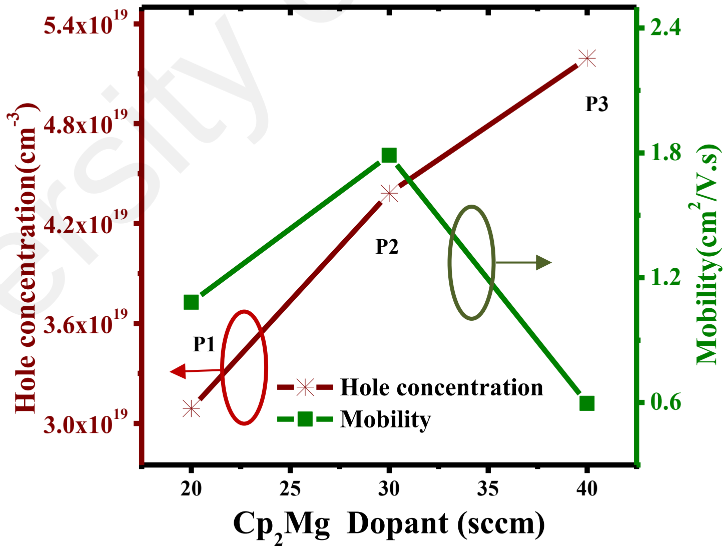

Figure 5.14: The hole concentration and the hole mobility as a function of the Cp_2Mg flow rate for P1-P3.

Table 5.5: The values of hole concentration and hole mobility for the P1-P3.

Sample	P1	P2	P3
Cp_2Mg flow rate (sccm)	20	30	40
Hole concentration ($\times 10^{19} cm^{-3}$)	3.1	4.4	5.1
Hole mobility ($cm^2. V^{-1}. s^{-1}$)	1.1	1.8	0.6

The degradation in the mobility for P3 might be due to the increment of the dislocation and defect densities as well as the ionized impurity scattering since the Cp_2Mg flow rate was increased (Lee et al., 2003; Wu et al., 2017b). As seen in the XRC analysis, the generation of additional defects and dislocation would negatively impact the mobility with excessive Cp_2Mg flow. On the other hand, similar to the n-type GaN, as the doping concentration was increased, the carrier concentration was also increased as mentioned in Table 5.5.

5.2.6 Summary

In summary, as an enhanced crystal quality of p-type GaN was achieved, the electrical properties were observed to be improved. As observed in the results, the moderate Cp_2Mg flow rate would positively influence distribution of terraces, leading to the relaxation of compressive strain and termination of defects and dislocation (Nakarmi et al., 2003; Wu et al., 2019). Similar to the n-type GaN, the growth of p-type GaN involve the flow of TMG (Ga), NH_3 (N), and Cp_2Mg (Mg); in which the incorporation of the Mg atoms will be within the GaN matrix. Upon using high flow rate of Cp_2Mg (40 sccm), regeneration of defects and dislocations is induced. This might be resulted from the atomic size difference between the Mg and gallium (Ga) atoms, leading to a lattice distortion (Dai et al., 2017; Lee et al., 1998). The results in this study are comparable with Qian Dai et al., whereby it was reported that the use of p-AlGaN alloy was employed to attain enhanced p-type characteristics (Dai et al., 2017). Based on these assumptions, the moderate Cp_2Mg of 30 sccm for the p-GaN (P2) will be further employed for the LED structure.

CHAPTER 6: SEMI-POLAR (11-22) INGAN/GAN-BASED LED

In Section 6.1, a series of three samples for the growth of semi-polar (11-22) InGaN/GaN multi-quantum well (MQW) was introduced in order to study the interfacial abruptness of the InGaN/GaN MQW. The impact of trimethylindium (TMI) flow rates towards the crystal, morphological, optical and electrical properties of the semi-polar (11-22) InGaN/GaN MQW-based light emitting diode (LED) was presented in Section 6.2. Finally, a comparative investigation of the semi-polar (11-22) InGaN/GaN MQW-based LEDs using gallium nitride (GaN) templates of with and without AlN/GaN multi-layer (ML) is presented in Section 6.3. The crystal quality of the epitaxial layer grown on m-plane sapphire substrates was studied by high resolution-x-ray diffraction (HR-XRD), inclusive of $2\theta/\omega$, on- and off-axis x-ray rocking curve (XRC) and reciprocal space mapping (RSM). While, the surface morphology of the as-grown epitaxial layer on m-plane sapphire substrate was characterized using atomic force microscopy (AFM). Finally, the optical and electrical properties were characterized using room temperature photoluminescence (RTPL) and electroluminescence (EL) measurements.

6.1 The Optimization of InGaN/GaN Multi Quantum Well (MQW)

6.1.1 The Growth Procedure

Six pairs of InGaN/GaN (3nm/12nm) MQW epitaxial layers were grown on semi-polar (11-22) uid-GaN templates without AlN/GaN ML to ensure presence of the satellite peaks as shown in Figure 6.1. The growth temperature of the InGaN/GaN MQW was maintained at 700 °C, while the flow rates of ammonia (NH_3) and triethylgallium (TEG) were 6.5 standard liter per minute (slm) and 114 standard cubic centimeters per minute (sccm), respectively. However, TMI flow rate for the growth of the InGaN quantum well (QW) was varied at 134, 270 and 403 sccm for In1, In2 and In3, respectively, to yield 1:1, 1:2 and 1:3 ratios. Therefore, the impact of dissimilar ratios of TEG to TMI flow rates were presented to attain different indium incorporations. Table 6.1 list the flux of TMI and TEG utilized in this study.

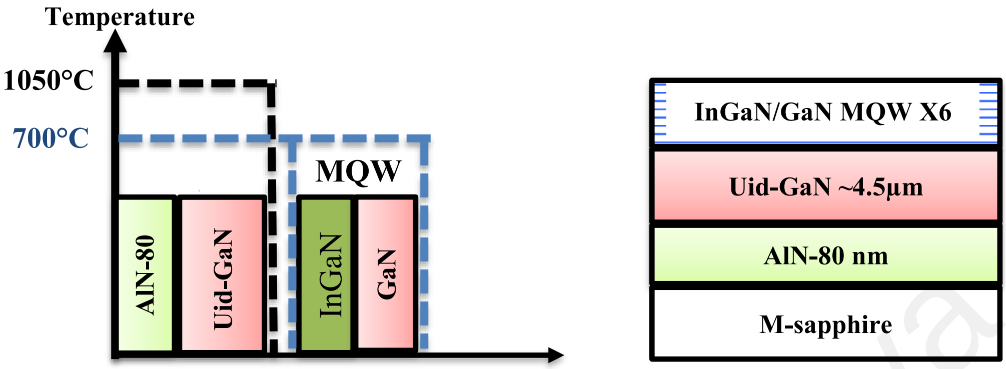

Figure 6.1: The growth procedure for the InGaN/GaN MQW grown on top of uid-GaN without AlN/GaN ML.

Table 6.1: The TEG: TMI ratios used for the growth of InGaN/GaN MQW for In1-In3.

Sample	TEG: TMI flow rate ratio	TEG flow rate ratio (sccm)	TMI flow rate ratio (sccm)
In1	1:1	114	134
In2	1:2	114	270
In3	1:3	114	403

6.1.2 Effect of the TMI Flow Rates on the Indium Incorporations

HR-XRD $2\theta/\omega$ scans from the symmetric plane of (11-22) for the semi-polar (11-22) InGaN/GaN MQW grown on m-plane sapphire substrate are shown in Figure 6.2. It can be seen that the main peak attributes to the semi-polar (11-22) thick GaN, while the satellite peaks and the broader shoulder at the lower angle were ascribed to the semi-polar (11-22) InGaN/GaN MQWs. The number of the satellite peaks were -4 to +2, and the 0th peak is the one next to the semi-polar (11-22) GaN epitaxial layer. As observed from the Figure, the 0th for In1 and In3 were closer to the main peak, indicating lower average of In incorporation, whilst the 0th peak of In2 was farther to the main peak of semi-polar (11-22) GaN (Zhao et al., 2018). Additionally, the diffracted satellite peaks for In2 exhibit proper fringes, while the diffracted satellite peaks for In1 and In3 illustrated non-uniform fringes due to the interfacial abruptness of InGaN/GaN MQW in In2. As previously mentioned in the literature, the interfacial abruptness of the epitaxial layer would exhibit proper diffracted fringes (Lee et al., 2014). The In2 was proven to obtain the proper interfacial abruptness of the growth of the InGaN/GaN MQW.

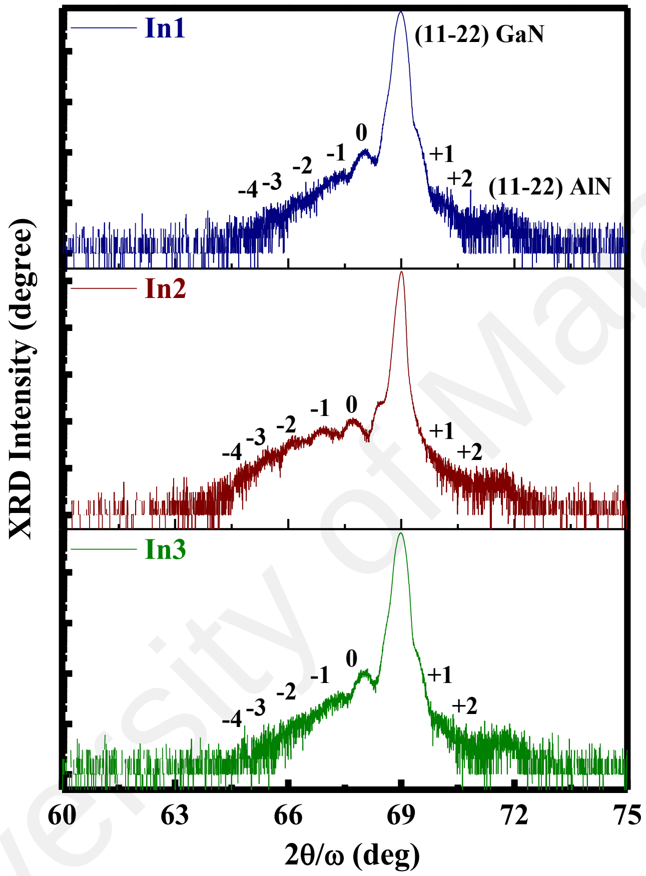

Figure 6.2: The HR-XRD $2\theta/\omega$ scan of semi-polar (11-22) InGaN/GaN MQW top of uid-GaN without AlN/GaN ML.

6.2 InGaN/GaN MQW-Based LEDs with Different TMI Flow Rates

6.2.1 Growth Methodology

Three samples with different TMI flow rates were introduced into the full structure of the LED. The InGaN/GaN MQW-based LEDs were grown with the AlN/GaN ML on m-plane sapphire substrate. As mentioned earlier, the growth temperature for the InGaN/GaN MQW was at 700 °C. The TMI flow rates were varied as 134 sccm (L1), 270 sccm (L2), and 403 sccm (L3) to achieve the TEG: TMI ratio of 1:1, 1:2 and 1:3 as previously presented in Table 6.1. The growth methodology of the InGaN/GaN MQW-based LED is illustrated in Figure 6.3. Prior to the six pairs of InGaN/GaN MQW, the optimized n-type GaN was grown for 20 minutes to yield a thickness of 2 µm. Subsequently, ramping down the temperature to 700 °C was conducted for the growth of MQW. Finally, a 200 nm thickness of p-type GaN was grown utilizing the pre-optimized growth condition as mentioned in the previous chapter.

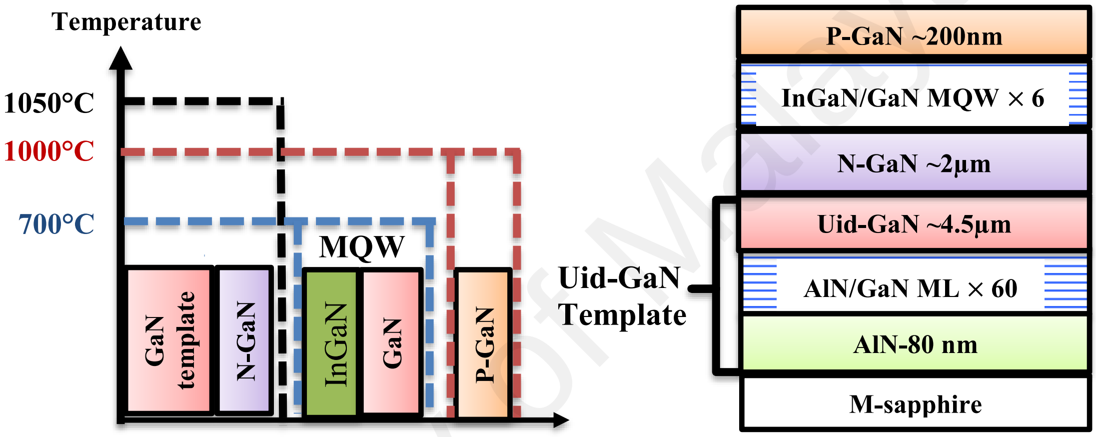

Figure 6.3: Schematic diagram for growth procedure of the InGaN/GaN MQW-based LEDs.

6.2.2 Effect of the TMI Flow Rates on the Surface Evolution

The morphological properties of L1-L3 were investigated via AFM images of 10×10 µm and 1×1 µm scan sizes as shown in Figure 6.4 (a-f). It can clearly be observed from Figure 6.4 (a, c, e) that the arrow-head like features for exhibited similar densities with slight variation in the undulation length along [1-100]. Figure 6.4 (a) (L1) possessed the longest undulation length as compared to L2 (c) and L3 (e). It is presumed that such occurrence is in direct correlation with the irregularities of the terrace features.

Figure 6.4 (b, d, f) depicts the 1×1 µm AFM scan sizes portraying the occurrence of atomic-size terrace evolution. Figure 6.4 (b) (L1) demonstrates a highly irregular terrace sizes (in length) and arrangement. This in turn leads to longer undulation along [1-100] as shown in Figure 6.4 (a). On the other hand, Figure 6.4 (d) (L2) exhibited a rather uniformly distributed terrace steps, resulted from the constant terrace sizes. However, Figure 6.4 (f) (L3) displayed degradation in the terrace sizes as well as distributions. The dissimilarities among L1-L3 signifies the impact of TMI flow variation towards the surface atomic-size terraces, leading to increase/decrease in the undulation length of the arrowhead like features along [1-100] direction. The origin of such phenomenon is well correlated with the indium adsorption rates, whereby different TMI flows would endure dissimilar indium compositions within the InGaN QW. Conclusively, in order to further evaluate the causality of the occurring observation, structural and optical characterizations will be analyzed.

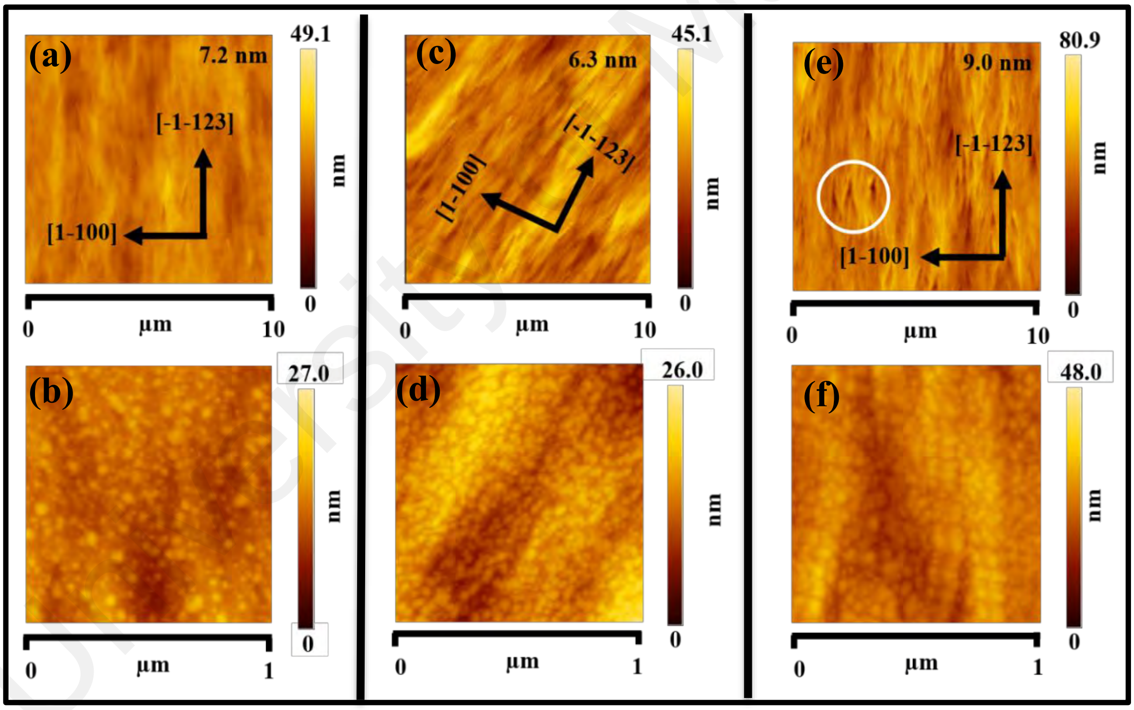

Figure 6.4: Surface morphology analysis of AFM 2D images of 10×10 µm and 1×1 µm scan sizes for (a-b) L1, (c-d) L2 and (e-f) L3.

6.2.3 The Influence of the TMI Flow Rates on the Structural Properties

On-axis XRC measurements were implemented to investigate the anisotropic properties for L1-L3 as shown in Figure 6.5 (a) & (b). It can be observed from the Figure that the use of low TMI flow (L1), the XRC FWHMs were found to be 0.14° and 0.32°

along [-1-123] and [1-100] directions, respectively. Meanwhile, L2 exhibited a narrowing in the FWHMs along [-1-123] and [1-100] as tabulated in Table 6.2. Conversely, XRC FWHMs of L3 were broadened to 0.15° and 0.33° along [-1-123] and [1-100] directions, respectively. It is seen that the FWHMs for L2 along [-1-123] and [1-100] directions portrayed the narrowest peaks, indicating the use of moderate TMI flow possesses a positive impact towards the reduction in the anisotropic properties.

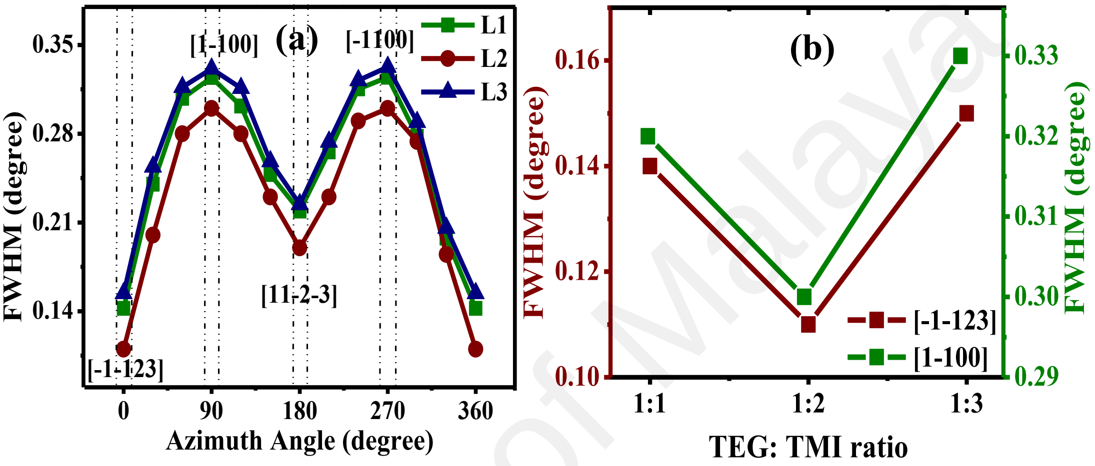

Figure 6.5: On-axis XRC FWHMs for L1-L3 (a) As a function of azimuthal angle (Φ) and (b) Along [-1-123] and [1-100] directions as a function of TEG: TMI ratio.

Table 6.2: On-axis XRC FWHM values along [-1-123], [1-100], [11-2-3] and [-1100] direction for L1-L3.

Samples	**FWHM (deg)**			
	[-1-123]	**[1-100]**	**[11-2-3]**	**[-1100]**
L1	0.14	0.32	0.21	0.32
L2	0.11	0.30	0.19	0.30
L3	0.15	0.33	0.22	0.33

In order to evaluate the defects and dislocations with TMI flow variations (L1-L3), off-axis XRC measurements were implemented as shown in Figure 6.6 (a-c). Figure 6.6 (a) illustrates the diffraction planes of (10-11) and (11-20) for L1-L3. As a comparison with L1, the FWHMs of the off-axis XRC for sample L2 was seen to be reduced, indicating the decrement of prismatic staking faults (PSFs), partial dislocations (PDs) and/or perfect dislocation (Kriouche et al., 2010; Moram et al., 2009). On the other hand, upon using higher TMI flow rate (L3), the off-axis XRC FWHMs of (10-11) and (11-20) increased as compared to L2, indicting a degradation in the crystal qualities.

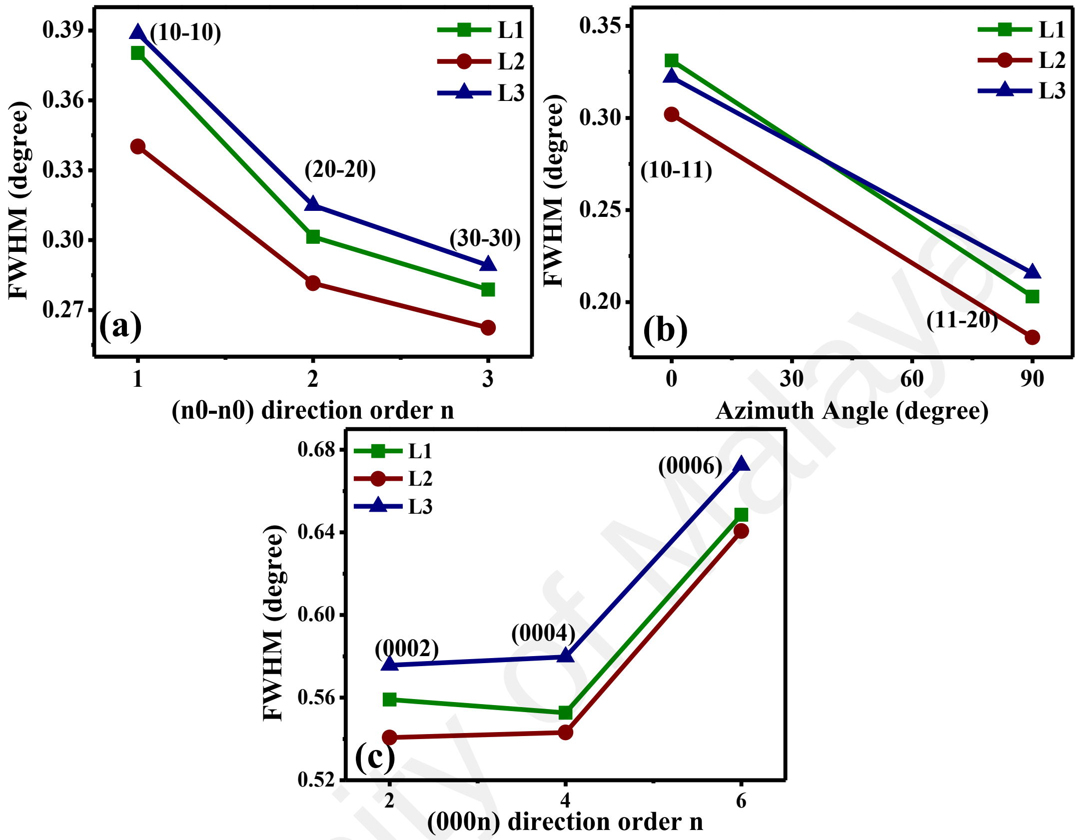

Figure 6.6: Off-axis XRC (a) FWHMs as a function of the azimuthal angle (*Φ*), (b) M-plane (*n*0-*n*0) (*n* = 1, 2, and 3) FWHMs and (c) C-plane (000*n*) (*n* = 2, 4, and 6) FWHMs.

Off-axis XRCs with different diffraction orders (*n*) was performed along m- and c-plane directions as shown in Figure 6.6 (b) & (c), respectively. As shown in Figure 6.6 (b), as *n* increased from 1 to 3 for L1-L3, the broadening in the FWHM peaks in L1 suggested higher number of basal stacking faults (BSFs) in the epitaxial layers. However, after introducing the moderate TMI flow rate (L2), the FWHMs were narrowed down, suggesting a reduction in BSFs. In contrast, the crystal quality for L3 was degraded, which might be resulting from the generated additional defects with higher TMI flow. Figure 6.6 (c) shows the (000*n*) off-axis XRC FWHM with the increment of the *n* from 2 to 6 for L1-L3. It can be observed that the FWHMs of (000*n*) for L1 and L3 were observed to be higher than L2 due to the presence of PDs and/or perfect dislocation in the epitaxial layers.

Additionally, the (11-22) symmetric reflection RSM along [-1-123] direction for L1-L3 was measured to further elucidate the relaxation state of LEDs in conjunction to its related defects as displayed in Figure 6.7 (a-c) and Table 6.3. The RSMs taken along [-1-123] direction exhibit a tilt between the m-plane sapphire and semi-polar (11-22) epitaxial layers. This in turn indicate a relaxed state of the as-grown epitaxial layers, which might be resulted from the cumulative effect of the Burgers vectors (Farrell et al., 2012; Young et al., 2010).

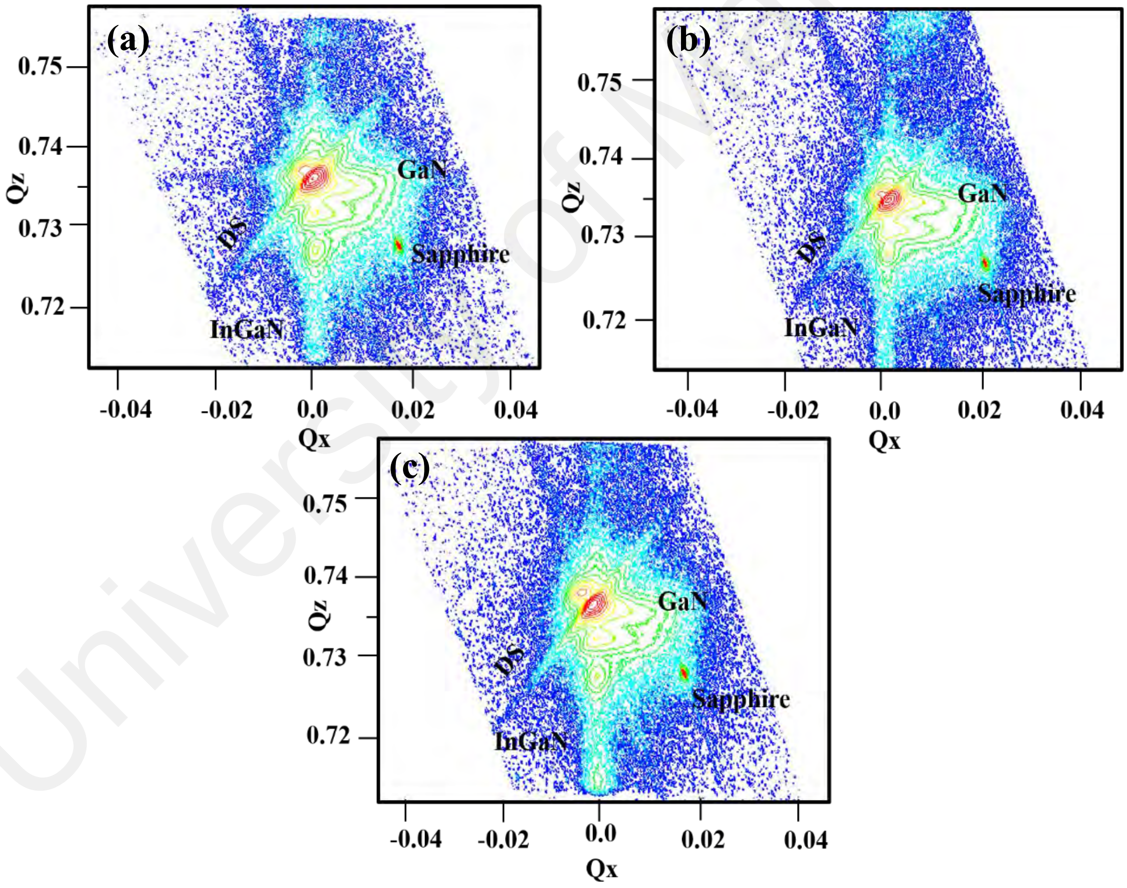

Figure 6.7: X-ray reciprocal space mapping of semi-polar (11-22) along [-1-123] direction for (a) L1, (b) L2 and (c) L3.

Table 6.3: Observed lattice tilts of semi-polar GaN and InGaN epitaxial layer taken along [-1-123] direction as well as the elongated DS streaks for L1-L3.

Sample	**GaN Tilt with sapphire (°)**	**InGaN Tilt with sapphire (°)**	**DS Streak ($\mathring{A}^{-1}$)**
L1	~1.41	~1.35	~0.031
L2	~1.69	~1.71	~0.025
L3	~1.52	~1.51	~0.029

Additionally, the different magnitudes of a tilt might be resulted from the strain and/or defects (Dinh et al., 2012); the existence of the misfit dislocations (MDs) and the lattice tilt within the InGaN/GaN MQW would minimize the strain energy, leading to either partially or fully relaxed layers (Dinh et al., 2012; Tyagi et al., 2009). As tabulated in Table 6.3, L2 possesses the largest tilt between the InGaN and the sapphire, suggesting that L2 possesses the highest relaxed state as compared to L1 and L3. This mainly due to the moderate TMI flow rate introduced during the growth of semi-polar (11-22) InGaN MQW, whereby the excessive TMI flow (L3) induced larger strain into the epitaxial layers.

In addition, the diffuse scattering (DS) streaks for L1-L3 were investigated along [-1-123] direction. Upon utilizing low TMI flow rate (L1) as shown in Figure 6.7 (a), the DS streaks was extended to be around ~0.031 $\mathring{A}^{-1}$, while the DS streak for L2 decreased to 0.025 $\mathring{A}^{-1}$ as the TMI flow was moderately increased (Figure 6.7 (b)). However, the DS streak for L3 was elongated with excessive TMI flow rate as illustrated in Figure 6.7 (c). Therefore, it is presumed that the with an optimized TMI flow, the defect densities such PSFs for L2 were sequestered (Lazarev et al., 2013; Pristovsek et al., 2016; Zhao et al., 2016).

6.2.4 TMI Flow Rates towards the Enhancement of the Optical Properties

In order to examine impact of the TMI flow variations towards the luminescence capability, RTPL measurement was conducted and illustrated in Figure 6.8. The PL wavelength emission for L1 was located at 497 nm with moderate intensity, while, L2 was red-shifted to 510 nm with higher intensity owing to the decrease in the defects and dislocation with the use of optimum TMI flow rate (L2). It can be deduced that yielding high indium incorporation/composition (within the active region) with higher TMI flow would endure a longer wavelength emission. However, L3 exhibited dual peaks located at 490 nm and 580 nm, respectively, with significantly low intensity. Such occurrence is mainly attributed to the degradation of the crystal qualities (as observed in the XRCs). This is due the compositional fluctuations in the relatively high TMI flow during the growth of InGaN epitaxial layer. Furthermore, the red-shift in wavelength emission as well as the enhanced PL intensity of L2 would be in direct correlation with the defect confinement during the growth of QW (optimized indium adsorption).

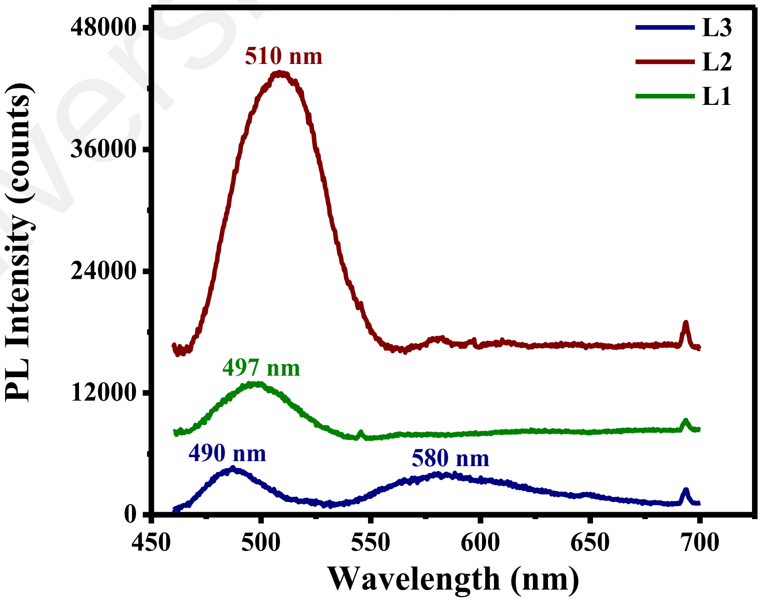

Figure 6.8: Room temperature photoluminescence spectra for (a) L1, (b) L2 and (c) and L3.

6.2.5 Summary

In summary, the pre-optimization of the indium incorporation probability in conjunction to the PL emission reveals that the enhanced luminescence properties would be attained with moderate TMI flow. However, it should be noted the importance of the n-type GaN surface morphology as mentioned in the previous chapter would play a huge role in enabling enhanced indium incorporation during the InGaN QW growth. Although the indifferent n-type GaN epitaxial layer were utilized for the growth of dissimilar QWs, a superior PL emission was exhibited with the use of an intermediate TMI flow (L2). As low TMI flow was utilized (L1), insufficient supply of indium atoms was seen, resulting in the highly irregular step-terraces as observed in the morphological analysis. This also indicates that the slight degradation of the structural properties hindering the PL emission. Excessive flow of TMI (L3), on the other hand, would further degrade the PL emission as the indium atom supply was relatively too high, regenerating new defects and dislocations as observed in the XRC. In addition, such phenomena would also result in the surface deterioration by forming huge terrace-steps, presumably indium clustering sites. This in turn leads to the observable dual peaks in the PL emission, whereby the longer wavelength peak corresponds to as said indium clusters. Based on these results, the superior properties exhibited by L2 will be further utilized in the growth of two indifferent LEDs via the use of two dissimilar templates, which will elucidate the significance of an enhanced semi-polar (11-22) GaN template.

6.3 Growth of Semi-polar (11-22) InGaN/GaN LED on Different Templates

6.3.1 Growth Methodology

Two LED samples namely with and without AlN/GaN ML templates were grown to investigate the impact of AlN/GaN ML towards the enhancement of crystal, morphological, optical and electrical properties of semi-polar (11-22) InGaN/GaN LED, and denoted as T1(without) and T2 (with). The indifferent 6 periods of InGaN/GaN

MQW structure, introduced in previous section (L2), were adopted to grow the LEDs. Figure 6.9 (a) & (b) represents the schematic illustration of the as-grown structures for T1 and T2, respectively. The pre-optimized MQW was inserted between the optimized n-type and p-type GaN, whereby the impact of dissimilar semi-polar (11-22) GaN templates would be analyzed.

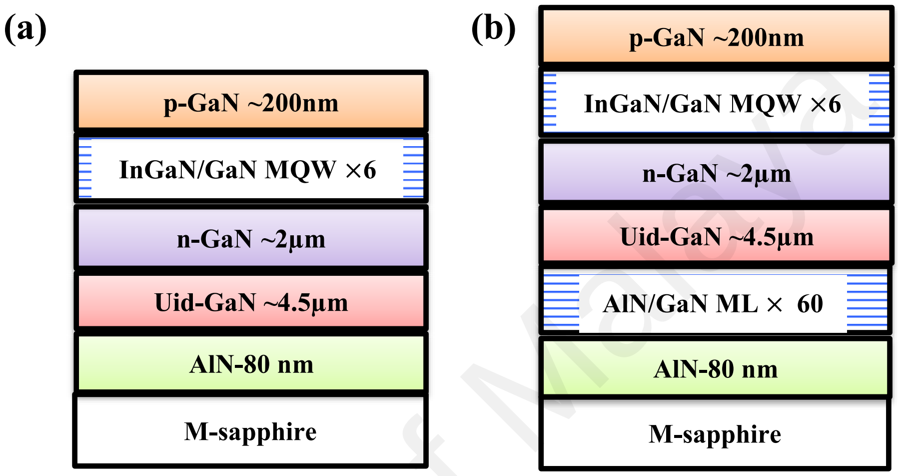

Figure 6.9: Schematic diagram of LED structures for (a) T1 and (b) T2.

6.3.2 Effect of Different Templates on the Surface Morphology

An investigation of the surface morphology via AFM imaging over 10×10 µm and 1×1 µm scan sizes for T1 and T2 is illustrated in Figure 6.10 (a-d). It can be discerned that the surface morphologies for both samples exhibited arrowhead-like features. As illustrated in Figure 6.10 (a), T1 exhibited longer undulated length along [1-100] with an estimated peak-to-valley depth of around 72.0 nm, leading to surface roughness of 10.05 nm. Conversely, a decrement in the peak-to-valley to around 45.1 nm was observed for T2, whereby significant surface roughness enhancement of 6.3 nm was recorded as shown in Figure 6.10 (c). Due to the implementation of the indifferent growth condition of the LED, such variation in the surface properties would be in direct correlation with utilization of dissimilar templates. Therefore, higher magnification of 1×1 µm AFM imaging would further elucidate the occurring phenomenon.

Figure 6.10 (b) & (d) depicts the higher magnification of the 10×10 µm AFM image, revealing random distributions of the terrace-like features for T1, while T2 exhibited a rather uniformly distributed terrace arrangement, respectively. As seen in the previous chapters, such features would either facilitate the loosely- or closely-packed terrace steps, inducing wider or narrower valley formations, respectively. As the terrace-like features in T1 exhibited numerous exposed valleys within the surface, it can be presumed lower number of indium atoms were embedded. However, T2 displayed significant terrace-step interconnections, portraying successful indium adsorption at a higher rate (Strittmatter et al., 2011). This would be further elaborated in the subsequent sub-chapter.

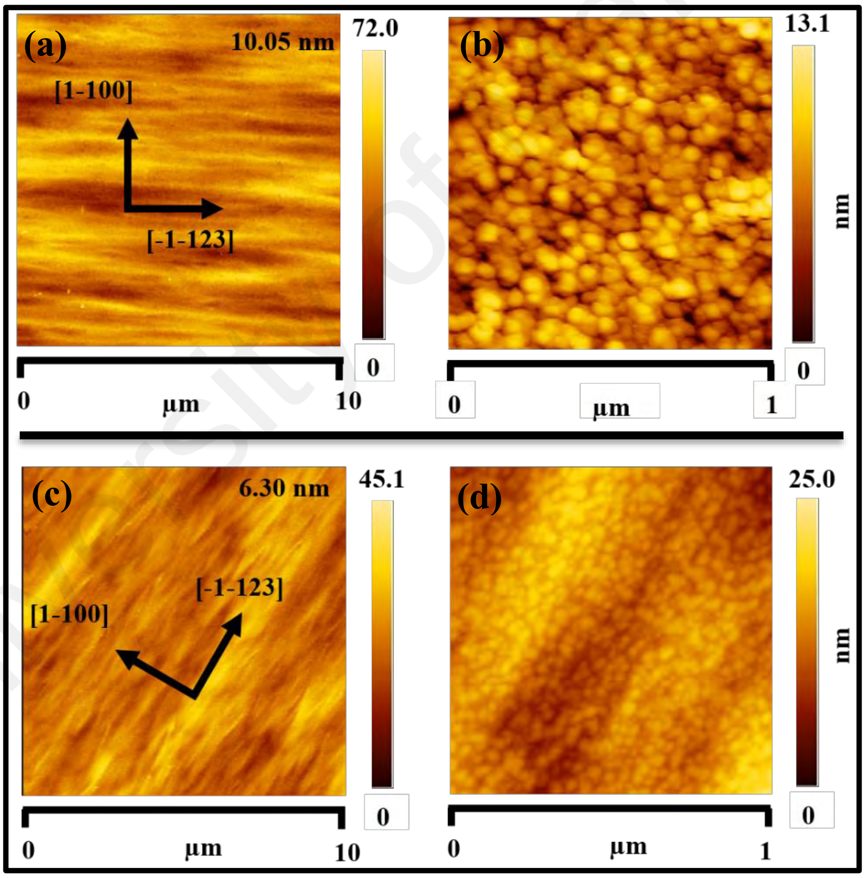

Figure 6.10: Surface morphology analysis of AFM 2D images of 10×10 µm and 1×1 µm scan sizes for (a) & (b) T1 and (c) & (d) T2.

6.3.3 Impact of Different Templates on the Structural Properties

The anisotropic properties and planar defects were investigated using on- and off-axis XRC measurements for T1 and T2 as illustrated in Figure 6.11 (a-d). Figure 6.11 (a) illustrates the M-shaped *Φ* dependence of FWHMs from 0° to 360°. The FWHMs for T1 were observed to be as high as 0.17° and 0.45° along [-1-123] and [1-100] directions, respectively. However, T2 exhibited a remarkable narrowing in the FWHMs to 0.11° and 0.30° along [-1-123] and [1-100] directions, respectively. This indicates that the AlN/GaN promoted effective anisotropic reductions, whereby the degree of narrowing in the FWHMs along [1-100] for T2 was enhanced as compared to T1 (tabulated in Table 6.4).

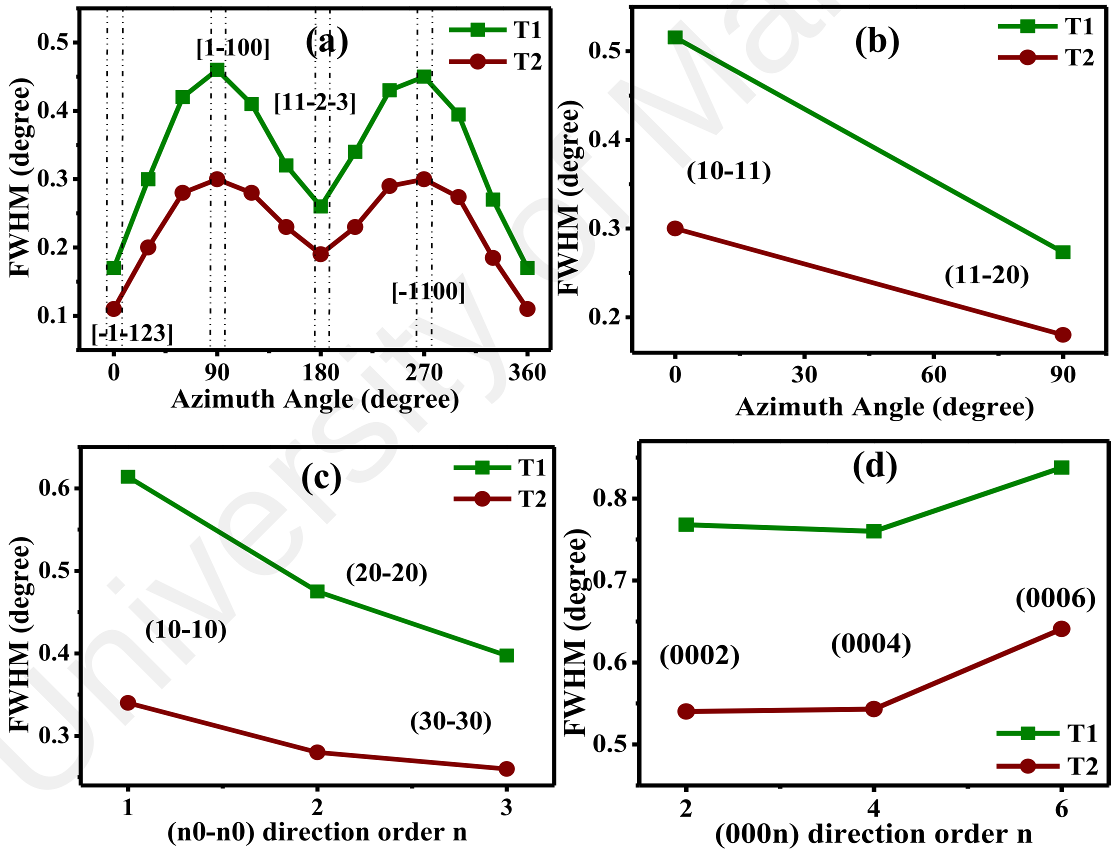

Figure 6.11: XRC FWHMs of (a) On-axis as a function of azimuthal angle (*Φ*), (b) off-axis as a function of azimuthal angle (*Φ*), (c) off-axis M-plane (n0-n0) (*n* = 1-3) and (d) off-axis C-plane (000n) (*n* = 2, 4, and 6).

Table 6.4: On-axis XRC FWHM values along [-1-123], [1-100], [11-2-3] and [-1100] for T1 and T2.

Samples	**FWHM (deg)**			
	[-1-123]	**[1-100]**	**[11-2-3]**	**[-1100]**
T1	0.17	0.45	0.26	0.45
T2	0.11	0.30	0.19	0.30

Figure 6.11 (b) represents the off-axis diffraction planes of (10-11) and (11-20). As expected, T1 exhibited substantial broadening in the FWHMs compared to T2 by almost 40% and 25% for (10-11) and (11-20) planes, respectively. Additionally, the m-and c-plane XRC FWHMs (as *n* increased) for T1 and T2 portrayed a similar trend, in which T2 exerted superior narrowing as shown in Figure 6.11 (c) & (d).

Based on these results, it is assumed that the use of the AlN/GaN template induced the reduction of the defects and dislocation, resulting in uniform arrangements of the crystal structure as previously discussed (Chapter 4).

Furthermore, in order to further support the XRCs, RSM measurements along [-1-123] directions were implemented to elucidate the relaxation state of the InGaN/GaN active region as opposed to the dissimilar templates used. Figure 6.12 (a) & (b) illustrates the RSM plots for T1 and T2, respectively. A larger lattice tilt between the epitaxial layers and sapphire substrate would indicate higher degree of relaxation state within the epitaxial layers (Dinh et al., 2012). T2 exhibited larger tilts of semi-polar (11-22) GaN and InGaN epitaxial layer with respect to the m-plane sapphire substrate as listed in Table 6.5. Additionally, the DS streaks for T1 and T2 were seen to be extended by approximately 0.042 $Å^{-1}$ and 0.025 $Å^{-1}$, respectively, deducing that the defect densities of PSFs were decreased with the use of AlN/GaN ML template (T2).

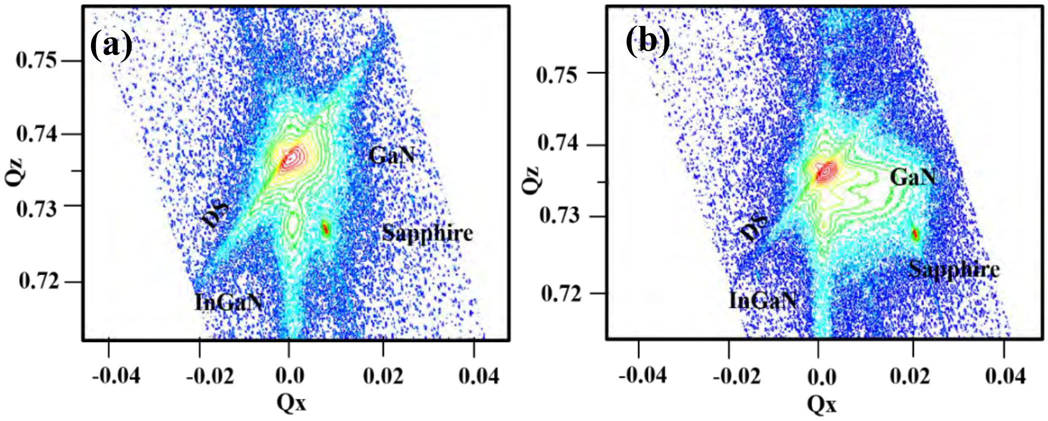

Figure 6.12: X-ray reciprocal space mapping along [-1-123] direction for (a) T1 and (b) T2.

Table 6.5: Observed lattice tilts of semi-polar GaN and InGaN epitaxial layer taken along [-1-123] direction as well as the elongated DS streaks for T1 and T2.

Sample	GaN tilt (°)	InGaN Tilt (°)	DS Streaks (Å^{-1})
T1	~0.64	~0.60	~0.042
T2	~1.69	~1.71	~0.025

6.3.4 Influence of the AlN/GaN Template on the Optical and Electrical Properties

In order to examine the optical and the electrical properties of T1 and T2, the PL and EL measurements were conducted and illustrated in Figure 6.13 (a-d). Figure 6.13 (a) shows the PL analysis for T1 and T2, respectively, in which the PL intensity of T2 was observed to be remarkably higher compared to T1. This would be owing to the improvement of the crystal quality, resulting from the decrement in the defect and dislocations densities. This is mainly due to the orderly arranged crystal structures as seen in the surface morphology analysis. In addition, T2 exhibited longer wavelength emission by 15 nm from T1 owing to the enhanced indium atom incorporation during the growth of the InGaN/GaN MQW.

The indium composition (x) can be calculated via maximum peak position of the PL spectrum. The expression for the InGaN bandgap E_g^{InGaN} was assessed as follows (Denton & Ashcroft, 1991):

$$E_g^{InGaN}(x) = xE_g^{InN} + (1-x)\,E_g^{GaN} - bx(1-x) \tag{6.1}$$

in which the E_g^{InN} and E_g^{GaN} are the bandgaps for InN and GaN, respectively, while b is the bowing parameter. Based on the theoretical calculation accomplished by (Moses et at., 2011), b would be 1.44 and the bandgap values for GaN as well as InN are 3.42 eV and 0.7 eV, respectively (Morkoç, 2009). Based on the equation, the x for T2 was calculated to be 26.5%, while the indium composition for T1 was 22.5%. This indicates an enhanced indium incorporation was achieved with the use of the AlN/GaN template, elucidating the shift in the PL peak emission between T1 and T2.

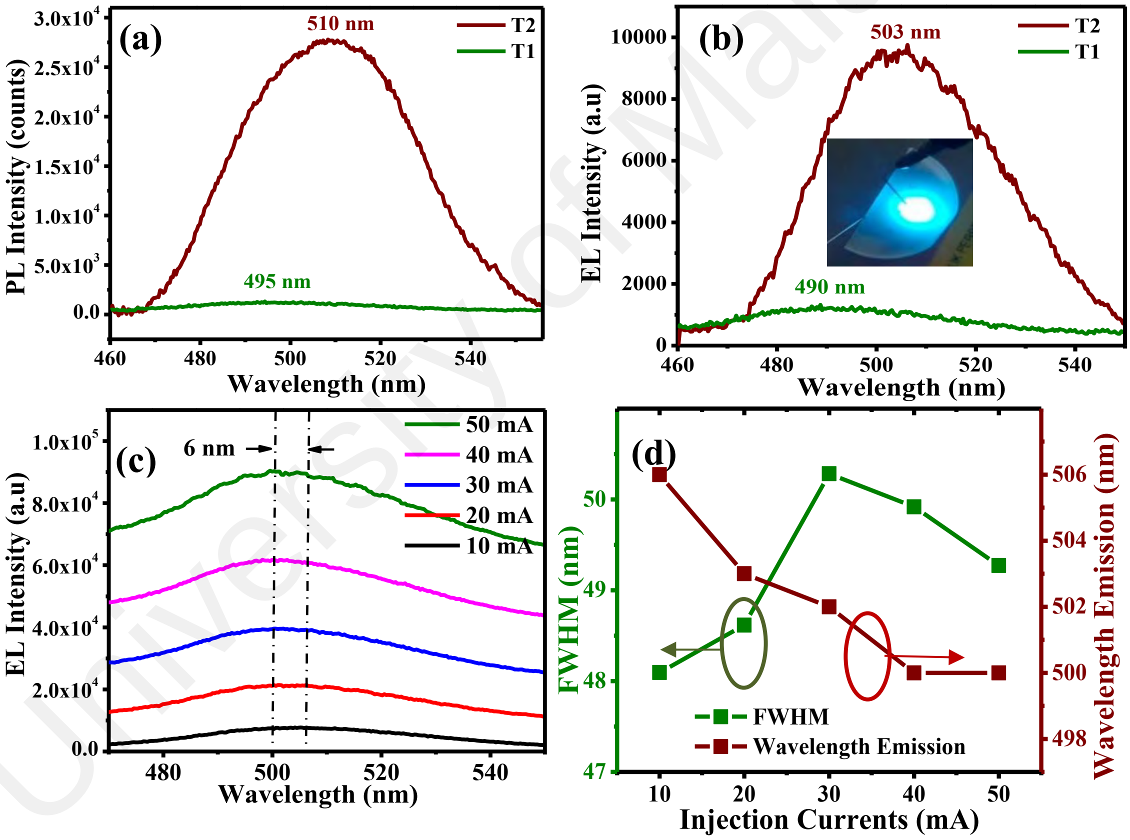

Figure 6.13: Room temperature photoluminescence and electroluminescence spectra. (a) PL analysis for T1 and T2, (b) EL analysis for T1 and T2 at 20 mA injection current, (c) EL data for T2 at different injection current and (d) Blue-shift and FWHM for T2 as a function of injection current.

Furthermore, it is speculated that the strain states by T1 and T2 would affect the incorporation of indium atoms (Strittmatter et al., 2011), which is well correlated with RSM analysis. In other words, the indium incorporation in T1 might require higher chemical potential than T2 due to the non-uniform distribution of the terraces. These results are well correlated with the AFM analysis, presuming that the enhanced terrace-like features endure better indium occupation, which would exhibit longer wavelength emission.

Moreover, Figure 6.13 (b) demonstrates the EL measurement for T1 and T2, by which the peak position of the EL slightly shifted from the PL peak emission around ~10 nm. This might be due to the fact the RTPL solely emits its corresponding luminescence without being affected by the presence of defects and dislocations. In addition, the use of the PL measurement was conducted to estimate the indium composition within the active region. On the other hand, EL emission will be affected by such defects and dislocations, whereby excitation source (injection current) depends on the structural quality of the active region. It is well known that the EL measurement is preferably utilized upon having a complete structure of a device, whereby the full functionality of the device can be evaluated.

From the Figure, the EL intensity for T2 was drastically elevated as compared to T1 due to the presence of lower defect densities. Additionally, the EL spectra exhibited a blue shift for T1, indicating the existence of residual compressive strain, in which the energy the energy band gap would be affected (Xu et al., 2012). The inset Figure illustrates the emission of 503 nm (cyan) for T2 at 20 mA injection current.

Furthermore, the EL spectra of the semi-polar (11-22) InGaN/GaN-based LED for T2 as a function of injection currents were investigated as shown Figure 6.13 (c). The LED exhibited a blue-shift in the emission from 506 nm at 10 mA to 500 nm at 50 mA, indicating a net shift of 6 nm as shown in Figure 6.13 (d). The weak shift in the EL would be attributed to a weak quantum confined stark effect (QCSE), indicating low piezoelectric polarization electric field (Chen et al., 2006; Masui et al., 2010). Moreover, the FWHM of the wavelength emission peak for T2 was recorded to be as low as 48 nm at 10 mA, 51 nm at 30 mA, and further decreased to 49 nm at 50 mA. The results indicate that the use of AlN/GaN template would endure comparable findings without the use of prior *ex-situ* and complex processes (Li et al., 2017).

CHAPTER 7: CONCLUSION AND FUTURE WORK

7.1 Conclusions

The InGaN/GaN MQW-based light emitting diodes (LEDs) have attracted research interest owing to the tremendous application prospects. Commercially, the growth of GaN-based LEDs is accomplished along c-plane (0001) direction with remarkably improved performance over recent years. However, the conventional LEDs grown along the c-plane directions suffer the quantum-confinement Stark-effect (QCSE). This is due the spontaneous (P^{sp}) and piezoelectric polarization (P^{pz}), thus leads to a separation of the electron-hole wave function. Such phenomenon hampers the device efficiency more significantly in longer wavelength LEDs grown along c-plane directions. In order to circumvent such limitations, growth along the semi-polar (11-22) orientation is preferable, by which the QCSE is expected to significantly improve. However, semi-polar GaN-based LEDs suffer from high defect densities, which is challenging to attain very high crystal qualities for enhanced device performance. Several groups have reported to improve the crystal quality of the semi-polar GaN-based LEDs by using free-standing GaN substrates and epitaxial lateral overgrowth (ELOG). However, the former technique requires high in production cost as well as its availability in mass production remains an obstacle, while the latter required additional steps and regrowth process (*ex-situ*). Therefore, it is encouraged to consider the *in-situ* techniques to acquire enhanced crystal quality and emission efficiency. The main study of this thesis is about the high quality semi-polar (11-22) GaN epitaxial layers to be used as templates for the growth of InGaN/GaN MQW-based LED with longer wavelength emission.

The first approach was to optimize the ammonia (NH_3) flux for the growth of semi-polar (11-22) GaN epitaxial layers grown on m-plane sapphire substrate. The NH_3 flux for the growth of semi-polar (11-22) GaN epitaxial layers was varied from 0.7 to 8.3

standard liter per minute (slm). The low NH_3 flux for the growth of semi-polar (11-22) GaN epitaxial layers was seen to have a positive impact in terms of the crystal and morphological qualities. The influence of NH_3 flux towards the enhancement of the crystal orientation was investigated using high-resolution x-ray diffraction (HR-XRD) $2\theta/\omega$ scans, in which a single crystal semi-polar (11-22) GaN was attained upon using 0.7 slm NH_3 flux. In addition, the transition from 3D to 2D growth mode was clearly observed when the NH_3 flux was decreased to 0.7 slm as shown in the cross-sectional images of field emission scanning electron microscopy (FESEM). The 10 × 10 µm atomic force microscopy (AFM) measurements clearly illustrated the enhancement of the surface morphology analysis with a reduction of root mean square (RMS) roughness from 437.05 to 6.05 nm. This is attributed to the decrement of NH_3 flux for the growth of semi-polar (11-22) GaN epitaxial layer, in which the structure of the pronounced grains was suppressed. To further confirm the nano-sized protrusion resulted from the nitridation process, the transmission electron microscopy (TEM) was utilized.

The full width at half maximum (FWHM) values of the on-axis x-ray rocking curve (XRC) along [-1-123] were reduced from 0.45° to 0.17°, while the FWHMs along [1-100] were decreased from 0.54° to 0.40°. This in turn suggested the enhancement of crystal quality upon using the low NH_3 flux of 0.7 slm. The off-axis XRC FWHMs indicated the improvement of the semi-polar (11-22) epitaxial layer due to the reduction of basal stacking faults (BSFs), prismatic stacking faults (PSFs), partial dislocations (PDs) and/or perfect dislocations with use of 0.7 slm NH_3 flux. Furthermore, the enhancement of the crystal quality was further proven with the RSM along [1-123] tilt values of 1.27° and 0.63° for the AlN nucleation layer and uid-GaN, respectively, with the respect to the m-plane sapphire substrate.

The AlN/GaN multi-layer (ML) was sandwiched between the semi-polar (11-22) AlN nucleation layer and uid-GaN. The optimization of the AlN/GaN multi-layer pairs was achieved by varying the number of pairs from 20 to 60. The HR-XRD $2\theta/\omega$ scans were employed to confirm the diffracted fringes, which are corresponding to the interface of AlN/GaN ML abruptness upon using the AlN/GaN 60 pairs. The undulation structure of the typical semi-polar (11-22) epitaxial layers grown on m-plane sapphire substrate was reduced with the use of AlN/GaN 60 pairs due to the decrement of undesirable defects and dislocations. The cross-sectional images of FESEM were further utilized to prove the interfacial abruptness of the AlN/GaN upon using 60 pairs, which were well correlated with the HR-XRD $2\theta/\omega$ scans. The arrow-head features were found to be well correlated with the enhancement of crystal qualities, whereby the AlN/GaN 60 pairs exhibited less arrow-head like features with RMS roughness of 6.05 nm. Furthermore, the cross-sectional images of TEM measurement taken close to [10-10] direction with g = [11-20] was found to be consistent with the structural measurement since the use of AlN/GaN ML 60 pairs was proven to be a key success for the reduction of dislocations and/or defects.

The correlation between the crystal quality and morphological properties was proven with the use of AlN/GaN 60 pairs. The on-axis XRC measurements asserted the enhancement of the crystal quality by 30% and 10% as for the [-1-123] and [1-100] directions, respectively, as compared to the bare GaN template (without AlN/GaN template). The off-axis XRC FWHMs suggested the enhancement of the crystal quality by the insertion of AlN/GaN ML 60 pairs due to the decrement of the BSFs, PSFs, PDs and/or perfect dislocations. The RSM measurement along [1-100] indicated that the peak positions corresponding to the semi-polar (11-22) nucleation layer AlN and uid-GaN are coherently grown along the semi-polar (11-22) plane. The RSM measurement along [1-123] indicated the improvement of the crystal quality and the relaxation state by embedding the 60 pairs of AlN/GaN, in which the diffuse scattering (DS) streaks reduced to roughly 0.025 Å^{-1} and a tilt values of ~1.50 and ~1.25 for the semi-polar (11-22) AlN nucleation layer and uid-GaN, with the respect to the m-plane sapphire substrate. In addition, the room temperature Raman spectroscopy suggested a stress-free state semi-polar (11-22) GaN upon using the AlN/GaN 60 pairs with the E_2 (high) mode peak located at located at 568 cm^{-1}.

The InGaN/GaN MQW was further optimized to obtain the abrupt interface between the InGaN and GaN. It was found that the growth of InGaN/GaN MQW using the ratio of 1:2 of TEG to TMI would promote proper diffracted fringes, corresponding to abrupt interface. In addition, the surface morphology analysis strongly suggested that the use of 1:2 ratio would reduce the undulated features with an RMS roughness of 6.30 nm, resulting from the uniform distribution of terrace-like steps (closely packed steps). This indicating that these results are well correlated with the enhancement of the crystal qualities.

It was also found that InGaN/GaN MQW-based LED exhibited lower FWHMs along [-1-123] and [1-100] using 1:2 ratio as compared to other ratios, which was in a good agreement with the improvement of surface morphology analysis. The off-axis XRC measurements suggested that with the use of 1:2 ratio, the undesirable defects and dislocations were reduced as compared to other ratios. Further studies using RSM measurements along [-1-123] reveal larger lattice tilt between the GaN and InGaN with respect to the m-plane (10-10) sapphire substrate, namely ~1.69° and ~1.71°, respectively. This is in turn substantiating relaxation state upon using the 1:2 ration although a full device is grown. This is indicating that this method is an effective way to improve the crystal quality as well as relaxation state simultaneously for producing semi-polar (11-22) LEDs.

Further studies of the optical properties suggested that the use of 1:2 ratio would enhance the PL intensity upon using 1:2 ratio by factor ~5 and ~6 as compared to 1:1 and 1:3, respectively. This is well correlated with the crystal and morphological properties, in which the fewer arrow-head like features, the better the indium incorporation. It was found that 1:2 ratio would have a positive impact towards the improvement of the indium incorporation due to the uniform distribution of the terrace-like structures.

The comparison between semi-polar (11-22) InGaN/GaN MQW-based LEDs deposited on with and without AlN/GaN templates suggested the enhancement of the surface morphology upon using AlN/GaN template. The RMS surface roughness of the semi-polar (11-22) InGaN/GaN MQW-based LED was reduced from 10.05 to 6.3 nm with closely packed terraces. The enhancement of the crystal quality using on and off-axis XRC FWHM by at least 17%. The RSM measurement along [-1-123] strongly indicated the relaxed strain state of the semi-polar LED upon using the AlN/GaN templates, in which the ~1.69° and ~1.71° with a DS streak of ~0.025.

The PL measurements of the both LEDs strongly proved the enhancement of the PL intensity with the use of AlN/GaN ML. It was also found that the indium incorporation increased upon using the AlN/GaN templates, indicating less residual compressive strain and orderly arranged crystal structures. In addition, it was found that semi-polar (11-22) InGaN/GaN-based LED using the AlN/GaN template exhibited longer wavelength emission by 15 nm, mainly owing to the enhanced indium incorporation. The indium composition (x) values of LEDs were 26.5 and 22.5 for AlN/GaN template and bare GaN template, respectively.

Finally, a significant improvement of EL intensity was obtained with the use of AlN/GaN ML, which is well correlated with the enhancement of the crystal and morphological qualities. The LED device exhibited a blue-shift from 506 nm at 10 mA to 500 nm (cyan) at 50 mA. This is in turn confirming the a weak QCSE resulted from the low piezoelectric polarization electric field. The FWHM of the wavelength emission peak was observed to be at 48 nm at 10 mA, while it increased up to 51 nm at 30 mA, and then decreased down to 49 nm at 50 mA.

7.2 Future Works

Although the embedded AlN/GaN ML enhances the overall crystal, morphological, optical and electrical properties, there is a wide possibility for further improvement by combining this technique with *in-situ* SiN_x interlayer or NH_3 treatment. The said techniques were found to drastically improve the crystal quality by reducing the defect and dislocation densities. Therefore, it is believed that combining those techniques with the current one proposed in this study may further decrease the defect and dislocation densities.

On the other hand, the bulk InGaN and InGaN strained-superlattice layers prior to the InGaN/GaN MQW may be tried as a relaxation layer. Furthermore, the composition of the indium into either bulk InGaN, or strained-superlattice layers can be implemented.

The growth of the semi-polar (11-22) InGaN/GaN MQW have been grown on the AlN/GaN templates. However, the growth conditions for the semi-polar (11-22) InGaN/GaN MQW can be further optimized by tuning the thickness of the well and/or barrier. The NH_3 flux for the growth of semi-polar (11-22) InGaN MQW might be further optimized in order to increase the indium incorporation. Finally, the pre-cap GaN can be introduced to further enhance the quality of the InGaN/GaN MQW.

REFERENCES

Ahmed, R., Hashemifar, S. J., Akbarzadeh, H., & Ahmed, M. (2007). Ab initio study of structural and electronic properties of III-arsenide binary compounds. *Computational Materials Science, 39*(3), 580-586.

Alhassan, A. I., Farrell, R. M., Saifaddin, B., Mughal, A., Wu, F., DenBaars, S. P., & Speck, J. S. (2016). High luminous efficacy green light-emitting diodes with AlGaN cap layer. *Optics Express, 24*(16), 17868-17873.

Amano, H., Kito, M., Hiramatsu, K., & Akasaki, I. (1989). P-type conduction in Mg-doped GaN treated with low-energy electron beam irradiation (LEEBI). *Japanese Journal of Applied Physics, 28*(12A), L2112-L2114.

Amano, H., Sawaki, N., Akasaki, I., & Toyoda, Y. (1986). Metalorganic vapor phase epitaxial growth of a high quality GaN film using an AlN buffer layer. *Applied Physics Letters, 48*(5), 353-355.

Amilusik, M., Sochacki, T., Lucznik, B., Fijalkowski, M., Smalc-Koziorowska, J., Weyher, J. L. & Grzegory, I. (2014). Homoepitaxial HVPE-GaN growth on non-polar and semi-polar seeds. *Journal of Crystal Growth, 403*, 48-54.

Arbouche, O., Belgoumène, B., Soudini, B., Azzaz, Y., Bendaoud, H., & Amara, K. (2010). First-principles study on structural properties and phase stability of III-phosphide (BP, GaP, AlP and InP). *Computational Materials Science, 47*(3), 685-692.

Armitage, R., & Hirayama, H. (2008). M-plane GaN grown on m-sapphire by metalorganic vapor phase epitaxy. *Applied Physics Letters, 92*(9), Article#092121.

Arslan, E., Ozturk, M. K., Duygulu, Ö., Kaya, A. A., Ozcelik, S., & Ozbay, E. (2009). The influence of nitridation time on the structural properties of GaN grown on Si (111) substrate. *Applied Physics A, 94*(1), 73-82.

As, D., Potthast, S., Fernandez, J., Lischka, K., Nagasawa, H., & Abe, M. (2006). Cubic GaN/AlGaN Schottky-barrier devices on 3C-SiC substrates. *Microelectronic Engineering, 83*(1), 34-36.

Avramescu, A., Lermer, T., Müller, J., Eichler, C., Bruederl, G., Sabathil, M., Strauss, U. (2010). True green laser diodes at 524 nm with 50 mW continuous wave output power on c-plane GaN. *Applied Physics Express, 3*(6), Article#061003.

Bae, S., Lee, D., Kong, B., Cho, H., Kaeding, J., Nakamura, S., & Speck, J. (2011). Electroluminescence enhancement of (11-22) semipolar GaN light-emitting diodes grown on miscut m-plane sapphire substrates. *Current Applied Physics, 11*(3), 954-958.

Bai, J., Xu, B., Guzman, F., Xing, K., Gong, Y., Hou, Y., & Wang, T. (2015). (11-22) semipolar InGaN emitters from green to amber on overgrown GaN on micro-rod templates. *Applied Physics Letters, 107*(26), Article#261103.

Baker, T. J., Haskell, B. A., Wu, F., Fini, P. T., Speck, J. S., & Nakamura, S. (2005). Characterization of planar semipolar gallium nitride films on spinel substrates. *Japanese Journal of Applied Physics, 44*(7L), L920-L922.

Bauer, G., & Richter, W. (2012). *Optical characterization of epitaxial semiconductor layers*. Berlin, Germany: Springer Science & Business Media.

Bergmann, U., Reimer, V., & Atakan, B. (1999). An experimental study of the reactions of trimethylgallium with ammonia and water over a wide temperature range. *Physical Chemistry Chemical Physics, 1*(24), 5593-5599.

Bernardini, F., Fiorentini, V., & Vanderbilt, D. (1997). Spontaneous polarization and piezoelectric constants of III-V nitrides. *Physical Review B, 56*(16), R10024-R10027.

Bernardini, F., & Fiorentini, V. (1999). Spontaneous versus piezoelectric polarization in III–V nitrides: conceptual aspects and practical consequences. *Physica Status Solidi (b), 216*(1), 391-398.

Beshkov, G., Lei, S., Lazarova, V., Nedev, N., & Georgiev, S. J. V. (2002). IR and Raman absorption spectroscopic studies of APCVD, LPCVD and PECVD thin SiN films. *Vacuum, 69*(1-3), 301-305.

Beyer, A., Stolz, W., & Volz, K. (2015). Metastable cubic zinc-blende III/V semiconductors: growth and structural characteristics. *Progress in Crystal Growth and Characterization of Materials, 61*(2-4), 46-62.

Bougrioua, Z., Laügt, M., Vennégués, P., Cestier, I., Gühne, T., Frayssinet, E., Leroux, M. (2007). Reduction of stacking faults in (11-20) and (11-22) GaN films by ELO techniques and benefit on GaN wells emission. *Physica Status Solidi (a), 204*(1), 282-289.

Cao, X., LeBoeuf, S., D'evelyn, M., Arthur, S., Kretchmer, J., Yan, C., & Yang, Z. (2004). Blue and near-ultraviolet light-emitting diodes on free-standing GaN substrates. *Applied Physics Letters, 84*(21), 4313-4315.

Chakraborty, A., Haskell, B. A., Keller, S., Speck, J. S., Denbaars, S. P., Nakamura, S., & Mishra, U. K. (2005). Demonstration of nonpolar m-plane InGaN/GaN light-emitting diodes on free-standing m-plane GaN substrates. *Japanese Journal of Applied Physics, 44*(1L), L173-L175.

Chandrasekhar, D., Smith, D. J., Strite, S., Lin, M., & Morkoç, H. (1995). Characterization of Group III-nitride semiconductors by high-resolution electron microscopy. *Journal of Crystal Growth, 152*(3), 135-142.

Chen, H. S., Lu, C. F., Yeh, D. M., Huang, C. F., Huang, J. J., & Yang, C. C. (2006). Orange-red light-emitting diodes based on a prestrained InGaN-GaN quantum-well epitaxy structure. *IEEE Photonics Technology Letters, 18*(21), 2269-2271.

Chen, J., Han, X., Huang, P., Chen, W., Liang, J., Zhong, C., Zhang, B. (2017). Schottky performance variation on r-plane and c-plane of GaN micro truncated-pyramid grown by selective area MOCVD. *Materials Science in Semiconductor Processing, 63*, 248-252.

Cherns, D., Henley, S., & Ponce, F. (2001). Edge and screw dislocations as nonradiative centers in InGaN/GaN quantum well luminescence. *Applied Physics Letters, 78*(18), 2691-2693.

Chitnis, A., Chen, C., Adivarahan, V., Shatalov, M., Kuokstis, E., Mandavilli, V., Khan, M. A. (2004). Visible light-emitting diodes using a-plane GaN–InGaN multiple quantum wells over r-plane sapphire. *Applied Physics Letters, 84*(18), 3663-3665.

Cimalla, V. (2017). Label-Free Biosensors Based on III-Nitride Semiconductors. In *Label-Free Biosensing* (pp. 59-102). London, UK: Springer.

Craven, M., Lim, S., Wu, F., Speck, J., & DenBaars, S. (2002). Structural characterization of nonpolar (1120) a-plane GaN thin films grown on (1102) r-plane sapphire. *Applied Physics Letters, 81*(3), 469-471.

Dadgar, A., Poschenrieder, M., Bläsing, J., Contreras, O., Bertram, F., Riemann, T., Krtschil, A. (2003). MOVPE growth of GaN on Si (111) substrates. *Journal of Crystal Growth, 248*, 556-562.

Dadgar, A., Schulze, F., Wienecke, M., Gadanecz, A., Bläsing, J., Veit, P., Krost, A. (2007). Epitaxy of GaN on silicon-impact of symmetry and surface reconstruction. *New Journal of Physics, 9*(10), 389-399.

Dai, Q., Zhang, X., Wu, Z., Yang, G., Liang, Z., Zhao, J., & Cui, Y. (2017a). Effects of Mg-doping on characteristics of semi-polar (11-22) plane p-AlGaN films. *Materials Letters, 209*, 472-475.

Dai, Q., Zhang, X., Zhao, J., Luan, H., Liang, Z., & Cui, Y. (2017b). Effects of Si-doping on characteristics of semi-polar (11-22) plane $Al_{0.45}Ga_{0.55}N$ epi-layers. *Materials Science in Semiconductor Processing, 58*, 30-33.

Dasilva, Y. A. R., Chauvat, M.-P., Ruterana, P., Lahourcade, L., Monroy, E., & Nataf, G. (2010). Defect structure in heteroepitaxial semipolar (11-22)(Ga, Al) N. *Journal of Physics: Condensed Matter, 22*(35), Article#355802.

Davidsson, S., Fälth, J., Liu, X., Zirath, H., & Andersson, T. (2005). Effect of AlN nucleation layer on the structural properties of bulk GaN grown on sapphire by molecular-beam epitaxy. *Journal of Applied Physics, 98*(1), Article#016109.

De Mierry, P., Guehne, T., Nemoz, M., Chenot, S., Beraudo, E., & Nataf, G. (2009). Comparison between Polar (0001) and Semipolar (1122) Nitride Blue-Green Light-Emitting Diodes Grown on c-and m-Plane Sapphire Substrates. *Japanese Journal of Applied Physics, 48*(3R), Article#031002.

DeCuir Jr, E., Manasreh, M., Tschumak, E., Schörmann, J., As, D., & Lischka, K. (2008). Cubic GaN/AlN multiple quantum well photodetector. *Applied Physics Letters, 92*(20), Article#201910.

Demangeot, F., Groenen, J., Frandon, J., Renucci, M., Briot, O., Clur, S., & Aulombard, R. (1998). Coupling of GaN-and AlN-like longitudinal optic phonons in $Ga_{1-x}Al_xN$ solid solutions. *Applied Physics Letters, 72*(21), 2674-2676.

Denton, A. R., & Ashcroft, N. W. (1991). Vegard's law. *Physical Review A, 43*(6), 3161-3164.

Devi, A. (2013). 'Old Chemistries' for new applications: perspectives for development of precursors for MOCVD and ALD applications. *Coordination Chemistry Reviews, 257*(23-24), 3332-3384.

Dinh, D. V., Skuridina, D., Solopow, S., Frentrup, M., Pristovsek, M., Vogt, P., Szczepańska, A. (2012). Growth and characterizations of semipolar (11-22) InN. *Journal of Applied Physics, 112*(1), Article#013530.

Drechsel, P., Stauss, P., Bergbauer, W., Rode, P., Fritze, S., Krost, A., Riechert, H. (2012). Impact of buffer growth on crystalline quality of GaN grown on Si (111) substrates. *Physica Status Solidi (a), 209*(3), 427-430.

Ehrentraut, D., Meissner, E., & Bockowski, M. (2010). *Technology of gallium nitride crystal growth* (Vol. 133). Berlin, Germany: Springer Science & Business Media.

Farrell, R., Young, E., Wu, F., DenBaars, S., & Speck, J. (2012). Materials and growth issues for high-performance nonpolar and semipolar light-emitting devices. *Semiconductor Science and Technology, 27*(2), Article#024001.

Fichter, F. (1907). Über aluminiumnitrid. *Zeitschrift für anorganische Chemie, 54*(1), 322-327.

Fiorentini, V., Bernardini, F., Della Sala, F., Di Carlo, A., & Lugli, P. (1999). Effects of macroscopic polarization in III-V nitride multiple quantum wells. *Physical Review B, 60*(12), 8849-8858.

Frank, F., & Nicholas, J. (1953). CXXVIII. Stable dislocations in the common crystal lattices. *The London, Edinburgh, and Dublin Philosophical Magazine and Journal of Science, 44*(358), 1213-1235.

Frentrup, M., Ploch, S., Pristovsek, M., & Kneissl, M. (2011). Crystal orientation of GaN layers on (1010) m-plane sapphire. *Physica Status Solidi (b), 248*(3), 583-587.

Fu, Y., Gulino, D. A., & Higgins, R. (2000). Residual stress in GaN epilayers grown on silicon substrates. *Journal of Vacuum Science & Technology A: Vacuum, Surfaces, and Films,18*(3), 965-967.

Fujita, M. (2013). Silicon photonics: Nanocavity brightens silicon. *Nature Photonics, 7*(4), 264-265.

Fujito, K., Kubo, S., & Fujimura, I. (2009a). Development of bulk GaN crystals and nonpolar/semipolar substrates by HVPE. *MRS Bulletin, 34*(5), 313-317.

Fujito, K., Kubo, S., Nagaoka, H., Mochizuki, T., Namita, H., & Nagao, S. (2009b). Bulk GaN crystals grown by HVPE. *Journal of Crystal Growth, 311*(10), 3011-3014.

Funato, M., Ueda, M., Kawakami, Y., Narukawa, Y., Kosugi, T., Takahashi, M., & Mukai, T. (2006). Blue, green, and amber InGaN/GaN light-emitting diodes on semipolar {11-22} GaN bulk substrates. *Japanese Journal of Applied Physics, 45*(7L), L659-L662.

Gerthsen, D., Neubauer, B., Dieker, C., Lantier, R., Rizzi, A., & Lüth, H. (1999). Molecular beam epitaxy (MBE) growth and structural properties of GaN and AlN on 3C-SiC (001) substrates. *Journal of Crystal Growth, 200*(3-4), 353-361.

Gholampour, M., Abdollah-zadeh, A., Shekari, L., & Poursalehi, R. (2015). From nanoparticles to nanowires of GaN with different hydrogen gas flow rates by PDC-PECVD. *Procedia Materials Science, 11*, 304-308.

Gian, W., Skowronski, M., & Rohrer, G. S. (1996). Structural defects and their relationship to nucleation of GaN thin films. *MRS Online Proceedings Library Archive, 423*, 475-486.

Gleize, J., Demangeot, F., Frandon, J., Renucci, M., Widmann, F., & Daudin, B. (1999). Phonons in a strained hexagonal GaN-AlN superlattice. *Applied Physics Letters, 74*(5), 703-705.

Hangleiter, A., Hitzel, F., Netzel, C., Fuhrmann, D., Rossow, U., Ade, G., & Hinze, P. (2005). Suppression of nonradiative recombination by V-shaped pits in GaInN/GaN quantum wells produces a large increase in the light emission efficiency. *Physical Review Letters, 95*(12), Article#127402.

Hatui, N., Frentrup, M., Rahman, A. A., Kadir, A., Subramanian, S., Kneissl, M., & Bhattacharya, A. (2015). MOVPE growth of semipolar (11-22) $Al_{1-x}In_xN$ across the alloy composition range (0≤ x≤ 0.55). *Journal of Crystal Growth, 411*, 106-109.

Heikman, S., Keller, S., Wu, Y., Speck, J. S., DenBaars, S. P., & Mishra, U. K. (2003). Polarization effects in AlGaN/GaN and GaN/AlGaN/GaN heterostructures. *Journal of Applied Physics, 93*(12), 10114-10118.

Hirako, A., Kusakabe, K., & Ohkawa, K. (2005). Modeling of reaction pathways of GaN growth by metalorganic vapor-phase epitaxy using TMGa/NH_3/H_2 system: a computational fluid dynamics simulation study. *Japanese Journal of Applied Physics, 44*(2R), 874-879.

Hirth, J. P & Lothe J. (1982). *Theory of dislocations*. New Jersey, United State: John Wiley & Sons.

Hollander, J. L., Kappers, M. J., & Humphreys, C. J. (2007). Epitaxial lateral overgrowth of off-basal GaN thin-film growth orientations. *Physica B: Condensed Matter, 401*, 307-310.

Hylton, N. P., Dawson, P., Johnston, C. F., Kappers, M. J., Hollander, J. L., McAleese, C., & Humphreys, C. J. (2009). Optical and microstructural properties of semi-polar (11-22) InGaN/GaN quantum well structures. *Physica Status Solidi (c), 6*(S2 2), S727-S730.

Ishikawa, H., Yamamoto, K., Egawa, T., Soga, T., Jimbo, T., & Umeno, M. (1998). Thermal stability of GaN on (111) Si substrate. *Journal of Crystal Growth, 189*, 178-182.

Jain, S., Willander, M., Narayan, J., & Overstraeten, R. V. (2000). III–nitrides: Growth, characterization, and properties. *Journal of Applied Physics, 87*(3), 965-1006.

Jang, J., Lee, K., Hwang, J., Jung, J., Lee, S., Lee, K., & Nam, O. (2012). Improvement of crystal quality and optical property in (11-22) semipolar InGaN/GaN LEDs grown on patterned m-plane sapphire substrate. *Journal of Crystal Growth, 361*, 166-170.

Jeong, J., Jang, J., Hwang, J., Jung, C., Kim, J., Lee, K., & Nam, O. (2013). Improved performance of semi-polar (11-22) GaN-based light-emitting diodes grown on SiNx interlayer. *Journal of Crystal Growth, 370*, 114-119.

Jiang, T., Xu, S., Zhang, J., Li, P., Huang, J., Niu, M., & Zhao, Y. (2016). Temperature dependence of the Raman-active modes in the semipolar (11-22) plane GaN Film. *Journal of Applied Physics, 120*(24), Article#245706.

Johnson, M., Fujita, S., Rowland Jr, W., Bowers, K., Hughes, W., He, Y., & Ren, J. (1996). Molecular beam epitaxy growth and properties of GaN, Al$_x$Ga$_{1-x}$N, and AlN on GaN/SiC substrates. *Journal of Vacuum Science & Technology B: Microelectronics and Nanometer Structures Processing, Measurement, and Phenomena, 14*(3), 2349-2353.

Johson, W., Parsons, J., & Crew, M. (1932). Nitrogen coumponds of Gallium-III. Gallic nitride. *The Journal of Physical Chemistry, 36*, 2651-2654.

Juza, R., & Hahn, H. (1938). Über die kristallstrukturen von Cu3N, GaN und InN metallamide und metallnitride. *Zeitschrift für anorganische und allgemeine Chemie, 239*(3), 282-287.

Khoury, M., Li, H., Kuritzky, L. Y., Mughal, A. J., DeMierry, P., Nakamura, S., & DenBaars, S. P. (2017). 444 nm InGaN light emitting diodes on low-defect-density GaN templates on patterned sapphire. *Applied Physics Express, 10*(10), Article#106501.

im, J. G., Kang, S. H., Janicki, Ł., Lee, J. H., Ju, J. M., Kim, K. W., ...Lee, J. H. (2019). Growth of AlGaN/GaN heterostructure with lattice-matched AlIn(Ga)N back barrier. *Solid-State Electronics,152*, 24-28.

Koleske, D. D., Lee, S. R., Crawford, M. H., Coltrin, M. E., & Fini, P. T. (2013). Semi-polar GaN materials technology for high IQE green LEDs'. *Sandia Report,* 1-86.

Kordoš, P., Bernát, J., Marso, M., Lüth, H., Rampazzo, F., Tamiazzo, G., & Meneghesso, G. (2005). Influence of gate-leakage current on drain current collapse of unpassivated GaN/AlGaN/GaN high electron mobility transistors. *Applied Physics Letters, 86*(25), Article#253511.

Koukoula, T., Lotsari, A., Kehagias, T., Dimitrakopulos, G., Häusler, I., Das, A., & Komninou, P. (2012). Structure and strain state of polar and semipolar InGaN quantum dots. *Applied Surface Science, 260*, 7-12.

Koynov, S., Topf, M., Fischer, S., Meyer, B. K., Radojkovic, P., Hartmann, E., & Liliental-Weber, Z. (1997). Structural investigations of GaN grown by low-pressure chemical vapor deposition on 6H-SiC and Al_2O_3 from $GaCl_3$ and NH_3. *Journal of Applied Physics, 82*(4), 1890-1895.

Kriouche, N., Vennéguès, P., Nemoz, M., Nataf, G., & De Mierry, P. (2010). Stacking faults blocking process in (11-22) semipolar GaN growth on sapphire using asymmetric lateral epitaxy. *Journal of Crystal Growth, 312*(19), 2625-2630.

Kuball, M. (2001). Raman spectroscopy of GaN, AlGaN and AlN for process and growth monitoring/control. *Surface and Interface Analysis, 31*(10), 987-999.

Lähnemann, J., Jahn, U., Brandt, O., Flissikowski, T., Dogan, P., & Grahn, H. T. (2014). Luminescence associated with stacking faults in GaN. *Journal of Physics D: Applied Physics, 47*(42), Article#423001.

Lazarev, S., Bauer, S., Meisch, T., Bauer, M., Tischer, I., Barchuk, M., Baumbach, T. (2013). Three-dimensional reciprocal space mapping of diffuse scattering for the study of stacking faults in semipolar (11-22) GaN layers grown from the sidewall of an r-patterned sapphire substrate. *Journal of Applied Crystallography, 46*(5), 1425-1433.

Lebedev, V., Morales, F., Romanus, H., Krischok, S., Ecke, G., Cimalla, V., & Ambacher, O. (2005). The role of Si as surfactant and donor in molecular-beam epitaxy of AlN. *Journal of Applied Physics, 98*(9), Article#093508.

Lee, C.-R., Lee, I. H., Yeon, J. M., Seol, K. W., Ahn, H. K., & Baek, B.-J. (2003). Doping characteristics of $Al_{0.15}Ga_{0.85}N$ epilayers with various Mg incorporations. *Journal of Crystal Growth, 256*(1-2), 56-62.

Lee, C. R., Leem, J. Y., Noh, S. K., Park, S. E., Lee, J. I., Kim, C. S., & Leem, K. Y. (1998). Characteristics of Mg-doped GaN epilayers grown with the variation of Mg incorporation. *Journal of Crystal Growth,193*(3), 300-304.

Lee, H. J., Bae, S. Y., Lekhal, K., Mitsunari, T., Tamura, A., Honda, Y., & Amano, H. (2016). Improved crystal quality of semipolar (10-13) GaN on Si (001) substrates using AlN/GaN superlattice interlayer. *Journal of Crystal Growth, 454*, 114-120.

Lee, J. G., Kim, H. S., Seo, K. S., Cho, C. H., & Cha, H. Y. (2016). High quality PECVD SiO_2 process for recessed MOS-gate of AlGaN/GaN-on-Si metal-oxide-semiconductor heterostructure field-effect transistors. *Solid-State Electronics, 122*, 32-36.

Lee, J. H., Han, S. H., Song, K. R., & Lee, S. N. (2014). Optical and electrical improvements of semipolar (11-22) GaN-based light emitting diodes by Si doping of n-GaN template. *Journal of Alloys and Compounds, 598*, 85-88.

Lee, J. H., Han, S. H., Song, K. R., Ryou, J. H., Na, H., & Lee, S. N. (2017). Effect of SiO_2 hexagonal pattern on the crystal and optical properties of epitaxial lateral overgrown semipolar (11-22) GaN film. *Microelectronic Engineering, 168*, 32-36.

Lei, T., Fanciulli, M., Molnar, R., Moustakas, T., Graham, R., & Scanlon, J. (1991). Epitaxial growth of zinc blende and wurtzitic gallium nitride thin films on (001) silicon. *Applied Physics Letters, 59*(8), 944-946.

Lester, S., Ponce, F., Craford, M., & Steigerwald, D. (1995). High dislocation densities in high efficiency GaN-based light-emitting diodes. *Applied Physics Letters, 66*(10), 1249-1251.

Leung, B., Sun, Q., Yerino, C. D., Han, J., & Coltrin, M. E. (2012). Using the kinetic Wulff plot to design and control nonpolar and semipolar GaN heteroepitaxy. *Semiconductor Science and Technology, 27*(2), Article#024005.

Leung, B., Zhang, Y., Yerino, C. D., Han, J., Sun, Q., Chen, Z., & Li, Y. L. (2012). Optical emission characteristics of semipolar GaN light-emitting diodes grown on m-sapphire and stripe-etched r-sapphire. *Semiconductor Science and Technology, 27*(2), Article#024016.

Li, H., Cheng, H. Y., Chen, W. L., Huang, Y. H., Li, C. K., Chang, C. Y., & Chang, Y. M. (2017). Three dimensional characterization of GaN-based light emitting diode grown on patterned sapphire substrate by confocal Raman and photoluminescence spectromicroscopy. *Scientific Reports, 7*, Article#45519.

Li, H., Khoury, M., Bonef, B., Alhassan, A. I., Mughal, A. J., Azimah, E., & DenBaars, S. P. (2017). Efficient semipolar (11-22) 550 nm yellow/green InGaN light-emitting diodes on low defect density (11-22) GaN/sapphire emplates. *ACS Applied Materials & Interfaces, 9*(41), 36417-36422.

Li, J., Nam, K., Nakarmi, M., Lin, J., Jiang, H., Carrier, P., & Wei, S. H. (2003). Band structure and fundamental optical transitions in wurtzite AlN. *Applied Physics Letters, 83*(25), 5163-5165.

Li, Y., Wang, W., Li, X., Huang, L., Lin, Z., Zheng, Y., ...Li, G. (2019). Stress and dislocation control of GaN epitaxial films grown on Si substrates and their application in high-performance light-emitting diodes. *Journal of Alloys and Compounds, 771*, 1000-1008.

Liu, L., & Edgar, J. H. (2002). Substrates for gallium nitride epitaxy. *Materials Science and Engineering: R: Reports, 37*(3), 61-127.

Liu, S. T., Yang, J., Zhao, D. G., Jiang, D. S., Liang, F., Chen, P., ...Zhang, L. Q. (2019). The compensation role of deep defects in the electric properties of lightly Si-doped GaN. *Journal of Alloys and Compounds, 773*, 1182-1186.

Lu, H., Schaff, W. J., Eastman, L. F., Wu, J., Walukiewicz, W., Cimalla, V., & Ambacher, O. (2003). Growth of a-plane InN on r-plane sapphire with a GaN buffer by molecular-beam epitaxy. *Applied Physics Letters, 83*(6), 1136-1138.

Manasevit, H., Erdmann, F., & Simpson, W. (1971). The use of metalorganics in the preparation of semiconductor materials IV. The nitrides of aluminum and gallium. *Journal of the Electrochemical Society, 118*(11), 1864-1868.

Manning, I. C., Weng, X., Acord, J. D., Fanton, M. A., Snyder, D. W., & Redwing, J. M. (2009). Tensile stress generation and dislocation reduction in Si-doped Al_xGa_{1-x} N films. *Journal of Applied Physics, 106*(2), Article#023506.

Maruska, H. á., & Tietjen, J. (1969). The preparation and properties of vapor-deposited single-crystal-line GaN. *Applied Physics Letters, 15*(10), 327-329.

Masui, H., Nakamura, S., DenBaars, S. P., & Mishra, U. K. (2010). Nonpolar and semipolar III-nitride light-emitting diodes: achievements and challenges. *IEEE Transactions on Electron Devices, 57*(1), 88-100.

Matsumoto, K., & Tachibana, A. (2004). Growth mechanism of atmospheric pressure MOVPE of GaN and its alloys: gas phase chemistry and its impact on reactor design. *Journal of Crystal Growth, 272*(1-4), 360-369.

McLaurin, M. B., Hirai, A., Young, E., Wu, F., & Speck, J. S. (2008). Basal plane stacking-fault related anisotropy in X-ray rocking curve widths of m-plane GaN. *Japanese Journal of Applied Physics, 47*(7R), 5429–5431.

Millman, J., & Halkias, C. C. (1972). *Integrated electronics: Analog and digital circuits and systems*. New York, United States: McGraw-Hill.

Min, D., Yoo, G., Ryu, Y., Moon, S., Lee, K., & Nam, O. (2013). Improvement of crystal quality and optical property in (11-22) semipolar InGaN/GaN light emitting diodes grown on hemi-spherically patterned SiO_2 mask. *Journal of Ceramic Processing Research, 14*(4), 521-524.

Mogilatenko, A., Kirmse, H., Stellmach, J., Frentrup, M., Mehnke, F., Wernicke, T., Weyers, M. (2014). Analysis of crystal orientation in AlN layers grown on m-plane sapphire. *Journal of Crystal Growth, 400*, 54-60.

Mokkapati, S., & Jagadish, C. (2009). III-V compound SC for optoelectronic devices. (2009). III-V compound SC for optoelectronic devices. *Materials Today, 12*(4), 22-32.

Moram, M., Johnston, C., Hollander, J., Kappers, M., & Humphreys, C. (2009). Understanding x-ray diffraction of nonpolar gallium nitride films. *Journal of Applied Physics, 105*(11), Article#113501.

Moram, M., & Vickers, M. (2009). X-ray diffraction of III-nitrides. *Reports on Progress in Physics, 72*(3), Article#036502.

Morkoç, H. (2009). Handbook of nitride semiconductors and devices, materials properties, physics and growth (Vol. 1) New Jersey, United States: John Wiley & Sons.

Moses, P. G., Miao, M., Yan, Q., & Van de Walle, C. G. (2011). Hybrid functional investigations of band gaps and band alignments for AlN, GaN, InN, and InGaN. *The Journal of Chemical Physics, 134*(8), Article#084703.

Mukundan, S., Mohan, L., Chandan, G., Roul, B., & Krupanidhi, S. (2014). Semipolar and nonpolar GaN epi-films grown on m-sapphire by plasma assisted molecular beam epitaxy. *Journal of Applied Physics, 116*(20), Article#204502.

Murthy, M., Tegueu, A., Awaah, M. A., Wang, D., Park, M., Walker, F. J., & Kumar, D. (2006). Electrical characterization of blue light emitting diodes as a function of temperature. *Materials Research Society*, *892*, 251-257.

Nakamura, K., Hayashi, T., Tachibana, A., & Matsumoto, K. (2000). Regional density functional theory for crystal growth in GaN. *Journal of Crystal Growth, 221*(1), 765-771.

Nakamura, K., Makino, O., Tachibana, A., & Matsumoto, K. (2000). Quantum chemical study of parasitic reaction in III–V nitride semiconductor crystal growth. *Journal of Organometallic Chemistry, 611*(1-2), 514-524.

Nakamura, S. (1991). GaN growth using GaN buffer layer. *Japanese Journal of Applied Physics, 30*(10A), L1705-1707.

Nakamura, S., Mukai, T., & Senoh, M. (1994). Candela-class high-brightness InGaN/AlGaN double-heterostructure blue-light-emitting diodes. *Applied Physics Letters, 64*(13), 1687-1689.

Nakamura, S., Pearton, S., & Fasol, G. (2013). *The blue laser diode: The complete story*. Berlin, Germany: Springer Science & Business Media.

Nakamura, S., Senoh, M., Iwasa, N., & Nagahama, S.-I. (1995). High-brightness InGaN blue, green and yellow light-emitting diodes with quantum well structures. *Japanese Journal of Applied Physics, 34*(7A), L797-L799.

Nakamura, S., Senoh, M., & Mukai, T. (1993). P-GaN/N-InGaN/N-GaN double-heterostructure blue-light-emitting diodes. *Japanese Journal of Applied Physics, 32*(1A), L8-L11.

Nakamura, S., Senoh, M., Nagahama, S. I., Iwasa, N., Yamada, T., Matsushita, T., & Sugimoto, Y. (1996). InGaN-based multi-quantum-well-structure laser diodes. *Japanese Journal of Applied Physics, 35*(1B), L74-L76.

Nakarmi, M. L., Kim, K. H., Li, J., Lin, J. Y., & Jiang, H. X. (2003). Enhanced p-type conduction in GaN and AlGaN by Mg-δ-doping. *Applied Physics Letters, 82*(18), 3041-3043.

Narayan, J., Pant, P., Chugh, A., Choi, H., & Fan, J. (2006). Characteristics of nucleation layer and epitaxy in GaN/sapphire heterostructures. *Journal of Applied Physics, 99*(5), Article#054313.

Narukawa, Y., Ichikawa, M., Sanga, D., Sano, M., & Mukai, T. (2010). White light emitting diodes with super-high luminous efficacy. *Journal of Physics D: Applied Physics, 43*(35), Article#354002.

Ng, H. M., Doppalapudi, D., Moustakas, T. D., Weimann, N. G., & Eastman, L. F. (1998). The role of dislocation scattering in n-type GaN films. *Applied Physics Letters, 73*(6), 821-823.

Nishida, T., Saito, H., & Kobayashi, N. (2001). Efficient and high-power AlGaN-based ultraviolet light-emitting diode grown on bulk GaN. *Applied Physics Letters, 79*(6), 711-712.

Northrup, J. E. (2009). GaN and InGaN (11-22) surfaces: Group-III adlayers and indium incorporation. *Applied Physics Letters, 95*(13), Article#133107.

Oh, D. S., Jang, J. J., Nam, O., Song, K. M., & Lee, S. N. (2011). Study of green light-emitting diodes grown on semipolar (11-22) GaN/m-sapphire with different crystal qualities. *Journal of Crystal Growth, 326*(1), 33-36.

Ohtomo, A., Kawasaki, M., Koida, T., Masubuchi, K., Koinuma, H., Sakurai, Y., Segawa, Y. (1998). $Mg_xZn_{1-x}O$ as a II–VI widegap semiconductor alloy. *Applied Physics Letters, 72*(19), 2466-2468.

Ozturk, M. K., Arslan, E., Kars, İ., Ozcelik, S., & Ozbay, E. (2013). Strain analysis of the GaN epitaxial layers grown on nitridated Si (111) substrate by metal organic chemical vapor deposition. *Materials Science in Semiconductor Processing, 16*(1), 83-88.

Pampili, P., & Parbrook, P. J. (2017). Doping of III-nitride materials. *Materials Science in Semiconductor Processing, 62*, 180-191.

Park, J. H., & Sudarshan, T. (2001). *Chemical vapor deposition* (Vol. 2). Ohio, United States: ASM International.

Park, J. K., Lim, M. A., Kim, C. H., Park, H. D., Park, J. T., & Choi, S. Y. (2003). White light-emitting diodes of GaN-based Sr_2SiO_4: Eu and the luminescent properties. *Applied Physics Letters, 82*(5), 683-685.

Park, S. H. (2015). Polarization characteristics of 480-680 nm (11-22) InGaN/GaN quantum well structures with strain relaxation effects. *Superlattices and Microstructures, 86*, 531-535.

Parthé, E. (1964). *Crystal chemistry of tetrahedral structures*. Florida, United States: CRC Press.

Pearton, S., Zolper, J., Shul, R., & Ren, F. (1999). GaN: Processing, defects, and devices. *Journal of Applied Physics, 86*(1), 1-78.

Ploch, S., Frentrup, M., Wernicke, T., Pristovsek, M., Weyers, M., & Kneissl, M. (2010). Orientation control of GaN and grown on sapphire by metal-organic vapor phase epitaxy. *Journal of Crystal Growth, 312*(15), 2171-2174.

Ploch, S., Wernicke, T., Dinh, D. V., Pristovsek, M., & Kneissl, M. (2012). Surface diffusion and layer morphology of (11-22) GaN grown by metal-organic vapor phase epitaxy. *Journal of Applied Physics, 111*(3), Article#033526.

Pradeep, S., Loganathan, R., Surender, S., Prabakaran, K., Asokan, K., & Baskar, K. (2018). Effect of gamma irradiation on AlInGaN/AlN/GaN heterostructures grown by MOCVD. *Superlattices and Microstructures, 120*, 40-47.

Pristovsek, M., Frentrup, M., Han, Y., & Humphreys, C. J. (2016). Optimizing GaN (11-22) hetero-epitaxial templates grown on (10-10) sapphire. *Physica Status Solidi (b), 253*(1), 61-66.

Rahman, M. N. A., Yusuf, Y., Mansor, M., & Shuhaimi, A. (2016). Effect of nitridation surface treatment on silicon (111) substrate for the growth of high quality single-crystalline GaN hetero-epitaxy layer by MOCVD. *Applied Surface Science, 362*, 572-576.

Reuters, B., Strate, J., Hahn, H., Finken, M., Wille, A., Heuken, M., Vescan, A. (2014). Selective MOVPE of InGaN-based LED structures on non-planar Si (111) facets of patterned Si (100) substrates. *Journal of Crystal Growth, 391*, 33-40.

Romanov, A. E., Baker, T. J., Nakamura, S., Speck, J. S., & ERATO/JST UCSB Group. (2006). Strain-induced polarization in wurtzite III-nitride semipolar layers. *Journal of Applied Physics, 100*(2), Article#023522.

Rosner, S., Carr, E., Ludowise, M., Girolami, G., & Erikson, H. (1997). Correlation of cathodoluminescence inhomogeneity with microstructural defects in epitaxial GaN grown by metalorganic chemical-vapor deposition. *Applied Physics Letters, 70*(4), 420-422.

Ryou, J. H., Yoder, P. D., Liu, J., Lochner, Z., Kim, H., Choi, S., Dupuis, R. D. (2009). Control of quantum-confined stark effect in InGaN-based quantum wells. *IEEE Journal of Selected Topics in Quantum Electronics, 15*(4), 1080-1091.

Sasaki, T., & Zembutsu, S. (1987). Substrate-orientation dependence of GaN single-crystal films grown by metalorganic vapor-phase epitaxy. *Journal of Applied Physics, 61*(7), 2533-2540.

Sato, H., Chung, R. B., Hirasawa, H., Fellows, N., Masui, H., Wu, F., DenBaars, S. P. (2008). Optical properties of yellow light-emitting diodes grown on semipolar (11-22) bulk GaN substrates. *Applied Physics Letters, 92*(22), Article#221110.

Schmidt, M. C., Kim, K.-C., Farrell, R. M., Feezell, D. F., Cohen, D. A., Saito, M., Nakamura, S. (2007). Demonstration of nonpolar m-plane InGaN/GaN laser diodes. *Japanese Journal of Applied Physics, 46*(3L), L190-L191.

Scholz, F. (2012). Semipolar GaN grown on foreign substrates: A review. *Semiconductor Science and Technology, 27*(2), Article#024002.

Schubert, M. F., Chhajed, S., Kim, J. K., Schubert, E. F., Koleske, D. D., Crawford, M. H., Banas, M. A. (2007). Effect of dislocation density on efficiency droop in

GaIn/N/GaN light-emitting diodes. *Applied Physics Letters, 91*(23), Article#231114.

Schwarz, U. T., & Kneissl, M. (2007). Nitride emitters go nonpolar. *Physica Status Solidi (RRL)-Rapid Research Letters*, 1(3), A44-A46.

Smith, A., Feenstra, R., Greve, D., Shin, M.-S., Skowronski, M., Neugebauer, J., & Northrup, J. (1999). GaN (0001) surface structures studied using scanning tunneling microscopy and first-principles total energy calculations. *Surface Science, 423*(1), 70-84.

Song, K. R., Oh, D. S., & Lee, S. N. (2013). Optical and crystal improvements of semipolar (11-22) GaN/m-sapphire by in-situ thermal etching process. *Current Applied Physics, 13*(8), 1643-1646.

Song, K. M., Kim, J. M., Kim, C. Z., & Kim, H. (2011). Mg Doping Effect in Nonpolar a-Plane GaN. *Japanese Journal of Applied Physics, 50*(12R), Article#121002.

Speck, J., & Rosner, S. (1999). The role of threading dislocations in the physical properties of GaN and its alloys. *Physica B: Condensed Matter, 273*, 24-32.

Stampfl, C., & Van de Walle, C. G. (1998). Energetics and electronic structure of stacking faults in AlN, GaN, and InN. *Physical Review B, 57*(24), R15052-R15055.

Stellmach, J., Frentrup, M., Mehnke, F., Pristovsek, M., Wernicke, T., & Kneissl, M. (2012). MOVPE growth of semipolar AlN on m-plane sapphire. *Journal of Crystal Growth, 355*(1), 59-62.

Strittmatter, A., Northrup, J. E., Johnson, N. M., Kisin, M. V., Spiberg, P., El-Ghoroury, H., & Syrkin, A. (2011). Semi-polar nitride surfaces and heterostructures. *Physica Status Solidi (b), 248*(3), 561-573.

Sun, Q., Ko, T. S., Yerino, C. D., Zhang, Y., Lee, I. H., Han, J., &Wang, S. C. (2009a). Effect of controlled growth dynamics on the microstructure of nonpolar a-plane GaN revealed by x-ray diffraction. *Japanese Journal of Applied Physics, 48*(7R), Article#071002.

Sun, Q., Kong, B. H., Yerino, C. D., Ko, T. S., Leung, B., Cho, H. K., & Han, J. (2009b). Morphological and microstructural evolution in the two-step growth of nonpolar a-plane GaN on r-plane sapphire. *Journal of Applied Physics, 106*(12), Article#123519.

Sun, Q., Leung, B., Yerino, C. D., Zhang, Y., & Han, J. (2009c). Improving microstructural quality of semipolar (11 2_2) GaN on m-plane sapphire by a two-step growth process. *Applied Physics Letters, 95*(23), Article#231904.

Sun, W., Zhang, J., Yang, J., Maruska, H., Khan, M. A., Liu, R., & Ponce, F. (2005). Fine structure of AlN/AlGaN superlattice grown by pulsed atomic-layer epitaxy for dislocation filtering. *Applied Physics Letters, 87*(21), Article#211915.

Sun, Z., Song, P., Nitta, S., Honda, Y., & Amano, H. (2017). A-plane GaN growth on (11-20) 4H-SiC substrate with an ultrathin interlayer. *Journal of Crystal Growth, 468*, 866-869.

Suzuki, N., Uchida, T., Tanikawa, T., Hikosaka, T., Honda, Y., Yamaguchi, M., & Sawaki, N. (2009). HVPE growth of semi-polar (11-22) GaN on GaN template (113) Si substrate. *Journal of Crystal Growth, 311*(10), 2875-2878.

Takahashi, Y., Sakai, S., & Umeno, M. (1984). Selective MOCVD growth of GaAlAs on partly masked substrates and its application to optoelectronic devices. *Journal of Crystal Growth, 68*(1), 206-213.

Takeuchi, T., Amano, H., & Akasaki, I. (2000). Theoretical study of orientation dependence of piezoelectric effects in wurtzite strained GaInN/GaN heterostructures and quantum wells. *Japanese Journal of Applied Physics, 39*(2R), 413-416.

Tendille, F., De Mierry, P., Vennéguès, P., Chenot, S., & Teisseire, M. (2014). Defect reduction method in (11-22) semipolar GaN grown on patterned sapphire substrate by MOCVD: Toward heteroepitaxial semipolar GaN free of basal stacking faults. *Journal of Crystal Growth, 404*, 177-183.

Tyagi, A., Wu, F., Young, E. C., Chakraborty, A., Ohta, H., Bhat, R., & Speck, J. S. (2009). Partial strain relaxation via misfit dislocation generation at heterointerfaces in (Al, In) GaN epitaxial layers grown on semipolar (11-22) GaN free standing substrates. *Applied Physics Letters, 95*(25), Article#251905.

Van de Walle, C. G. (2012). *Wide-band-gap Semiconductors*. Amsterdam, Netherlands: Elsevier.

Vennéguès, P., & Beaumont, B. (1999). Transmission electron microscopy study of the nitridation of the (0001) sapphire surface. *Applied Physics Letters, 75*(26), 4115-4117.

Vennegues, P., Bougrioua, Z., & Guehne, T. (2007). Microstructural characterization of semipolar GaN templates and epitaxial-lateral-overgrown films deposited on m-plane sapphire by metalorganic vapor phase epitaxy. *Japanese Journal of Applied Physics, 46*(7R), 4089-4095.

Vennéguès, P., Zhu, T., Martin, D., & Grandjean, N. (2010). Study of the epitaxial relationships between III-nitrides and M-plane sapphire. *Journal of Applied Physics, 108*(11), Article#113521.

Waltereit, P., Brandt, O., Trampert, A., Ramsteiner, M., Reiche, M., Qi, M., & Ploog, K. (1999). Influence of AlN nucleation layers on growth mode and strain relief of GaN grown on 6H-SiC (0001). *Applied Physics Letters, 74*(24), 3660-3662.

Wang, H. M., Zhang, J. P., Chen, C. Q., Fareed, Q., Yang, J. W., & Khan, M. A. (2002). AlN/AlGaN superlattices as dislocation filter for low-threading-dislocation thick AlGaN layers on sapphire. *Applied Physics Letters, 81*(4), 604-606.

Wang, J., Xu, F., He, C., Zhang, L., Lu, L., Wang, X., & Shen, B. (2017). High quality AlN epilayers grown on nitrided sapphire by metal organic chemical vapor deposition. *Scientific Reports*, 7, Article#42747.

Wang, M. T., Brunner, F., Liao, K. Y., Li, Y. L., Tseng, S. H., & Weyers, M. (2013). Phase control of semi-polar (11-22) and non-polar (11-20) GaN on cone shaped r-plane patterned sapphire substrates. *Journal of Crystal Growth, 371*, 11-16.

Wang, X., Wang, C., Hu, G., Wang, J., Chen, T., Jiao, G., Li, J. (2005). Improved DC and RF performance of AlGaN/GaN HEMTs grown by MOCVD on sapphire substrates. *Solid-State Electronics, 49*(8), 1387-1390.

Wang, Y., Zhang, X., Luan, H., Yang, H., Wang, S., Dai, Q., & Cui, Y. (2016). Effects of Si-doping on structural and electrical characteristics of polar, semi-polar, and non-polar AlGaN epi-layers. *Materials Science in Semiconductor Processing, 42*, 344-348.

Watwe, R. M., Dumesic, J. A., & Kuech, T. F. (2000). Gas-phase chemistry of metalorganic and nitrogen-bearing compounds. *Journal of Crystal Growth, 221*(1-4), 751-757.

Weimann, N. G., Eastman, L. F., Doppalapudi, D., Ng, H. M., & Moustakas, T. D. (1998). Scattering of electrons at threading dislocations in GaN. *Journal of Applied Physics, 83*(7), 3656-3659.

Wiest, F., Capodieci, V., Blank, O., Gutsche, M., Schulze, J., Eisele, I., & Schmidt, U. (2006). Conformal aluminum oxide coating of high aspect ratio structures using metalorganic chemical vapor deposition. *Thin Solid Films, 496*(2), 240-246.

Williams, D. B., & Carter, C. B. (1996). *The transmission electron microscope. Transmission electron microscopy* (pp. 3-17). Berlin, Germany: Springer.

Won, Y., So, B., Woo, S., Lee, D., Kim, M., Nam, K., & Nam, O. (2014). Effect of nitridation on the orientation of GaN layer grown on m-sapphire substrates using hydride vapor phase epitaxy. *Journal of Ceramic Processing Research, 15*(2), 61-65.

Wu, J. (2009). When group-III nitrides go infrared: New properties and perspectives. *Journal of Applied Physics, 106*(1), Article#011101.

Wu, Z., Song, P., Shih, T., Pang, L., Chen, L., Lin, G., Design. (2017a). In situ site-specific gallium filling and nanograin growth for blocking of hreading efects in semipolar (11-22) GaN. *Crystal Growth & Design, 17*(9), 4687-4693.

Wu, Z., Zhang, X., Dai, Q., Zhao, J., Fan, A., Wang, S., & Cui, Y. (2017b). High hole concentration in nonpolar a-plane p-AlGaN films with Mg-delta doping technique. *Superlattices and Microstructures, 109*, 880-885.

Wu, Z., Zhang, X., Zhao, J., Fan, A., Chen, H., Chen, S., ...Cui, Y. (2019). Enhanced structural and electrical properties of nonpolar a-plane p-type AlGaN/GaN superlattices. *Superlattices and Microstructures, 125*, 310-314.

Xi, X., Yang, C., Cao, H., Yu, Z., Li, J., Lin, S., & Zhao, L. (2018). GaN nanocolumns fabricated by self-assembly Ni mask and its enhanced photocatalytic performance in water splitting. *Applied Surface Science, 462*, 310-315.

Xia, H., Xia, Q., & Ruoff, A. L. (1993). High-pressure structure of gallium nitride: Wurtzite-to-rocksalt phase transition. *Physical Review B, 47*(19), 12925-12928.

Xu, S. R., Zhao, Y., Jiang, T., Zhang, J. C., Li, P. X., & Hao, Y. (2016). Improved semipolar (1122) GaN quality grown on m-plane sapphire substrates by metal organic chemical vapor deposition using self-organized SiN_x interlayer. *Chinese Physics Letters, 33*(6), Article#068102.

Xu, S., Hao, Y., Zhang, J., Zhou, X., Yang, L., Zhang, J., Hu, S. (2009). Improvements in a-plane GaN crystal quality by AlN/AlGaN superlattices layers. *Journal of Crystal Growth, 311*(14), 3622-3625.

Xu, S., Zhang, J., Cao, Y., Zhou, X., Xue, J., Lin, Z., Hao, Y. (2012). Improvements in (11-22) semipolar GaN crystal quality by graded superlattices. *Thin Solid Films, 520*(6), 1909-1912.

Xu, X., Vaudo, R., Loria, C., Salant, A., Brandes, G., & Chaudhuri, J. (2002). Growth and characterization of low defect GaN by hydride vapor phase epitaxy. *Journal of Crystal Growth, 246*(3-4), 223-229.

Yamada, H., Iso, K., Saito, M., Fujito, K., DenBaars, S. P., Speck, J. S., & Nakamura, S. (2007). Impact of substrate miscut on the characteristic of m-plane InGaN/GaN light emitting diodes. *Japanese Journal of Applied Physics, 46*(12L), L1117-L1119.

Yamada, H., Iso, K., Saito, M., Masui, H., Fujito, K., DenBaars, S. P., & Nakamura, S. (2008). Compositional dependence of nonpolar m-plane $In_xGa_{1-x}N$/GaN light emitting diodes. *Applied Physics Express, 1*(4), Article#041101.

Yamamoto, S., Zhao, Y., Pan, C.-C., Chung, R. B., Fujito, K., Sonoda, J., Nakamura, S. (2010). High-efficiency single-quantum-well green and yellow-green light-emitting diodes on semipolar (2021) GaN substrates. *Applied Physics Express, 3*(12), Article#122102.

Yan, F., Gao, H., Zhang, H., Wang, G., Yang, F., Yan, J., Li, J. (2007). Temperature dependence of the Raman-active modes in the nonpolar a-plane GaN film. *Journal of Applied Physics, 101*(2), Article#023506.

Yang, H., Zhang, X., Wang, S., Wang, Y., Luan, H., Dai, Q., Cui, Y. (2016). Effects of Si-doping on structural, electrical, and optical properties of polar and non-polar AlGaN epi-layers. *Superlattices and Microstructures, 96*, 1-7.

Yeh, C. Y., Lu, Z., Froyen, S., & Zunger, A. (1992). Predictions and systematizations of the zinc-blende-wurtzite structural energies in binary octet compounds. *Physical Review B, 45*(20), 12130-12133.

Yoshida, S., Misawa, S., & Itoh, A. (1975). Epitaxial growth of aluminum nitride films on sapphire by reactive evaporation. *Applied Physics Letters, 26*(8), 461-462.

Young, E. C., Gallinat, C. S., Romanov, A. E., Tyagi, A., Wu, F., & Speck, J. S. (2010). Critical thickness for onset of plastic relaxation in (1122) and (2021) semipolar AlGaN heterostructures. *Applied Physics Express, 3*(11), Article#111002.

Zakharov, D. N., Liliental-Weber, Z., Wagner, B., Reitmeier, Z. J., Preble, E. A., & Davis, R. F. (2005). Structural TEM study of nonpolar a-plane gallium nitride grown on (11-20) 4H-SiC by organometallic vapor phase epitaxy. *Physical Review B, 71*(23), Article#235334.

Zhang, J., Sokolovskij, R., Chen, G., Zhu, Y., Qi, Y., Lin, X., Chemical, A. B. (2019). Impact of high temperature H2 pre-treatment on Pt-AlGaN/GaN HEMT sensor for H_2S detection. *Sensors and Actuators B: Chemical, 280*, 138-143.

Zhao, G., Wang, L., Li, H., Meng, Y., Li, F., Yang, S., & Wang, Z. (2018). Structural and optical properties of semi-polar (11-22) InGaN/GaN green light-emitting diode structure. *Applied Physics Letters, 112*(5), Article#052105.

Zhao, G., Wang, L., Yang, S., Li, H., Wei, H., Han, D., & Wang, Z. (2016). Anisotropic structural and optical properties of semi-polar (11-22) GaN grown on m-plane sapphire using double AlN buffer layers. *Scientific Reports*, 6, Article#20787.

Zimmermann, H. (2000). Basics of optical emission and absorption. *Integrated Silicon Optoelectronics* (pp. 1-10) Berlin, Germany: Springer.

LIST OF PUBLICATIONS AND PAPERS PRESENTED

Publications

1. **Omar, A. Z.**, Bakar, A. S. B. A., Makinudin, A. H. A., Khudus, M. I. M. A., Azman, A., Kamarundzaman, A., & Supangat, A. (2018). Effect of low NH_3 flux towards high quality semi-polar (11-22) GaN on m-plane sapphire via MOCVD. *Superlattices and Microstructures*, *117*, 207-214.

2. **Omar, A. Z.**, Shuhaimi, A., Makinudin, A. H. A., Khudus, M. I. A., & Supangat, A. (2018). Embedded AlN/GaN multi-layer for enhanced crystal quality and surface morphology of semi-polar (11-22) GaN on m-plane sapphire. *Materials Science in Semiconductor Processing*, *86*, 1-7.

Papers Presented

1. **Omar, A. Z.**, Ahmad Shuhaimi, Abdullah Haaziq Ahmad Makinudin, Muhammad I.M. Abdul Khudus, Azzuliani Supangat. (2018). *A reduction in the anisotropic characteristics of semi-polar (11-22) epitaxial layers by embedded AlN/GaN multi-layer via MOCVD.* Paper presented at the International Workshop on Nitride Semiconductors (IWN2018), 11-16 November, Kanazawa, Japan.

2. Abdullah Haaziq Ahmad Makinudin, Ahmad Shuhaimi, **Omar, A. Z.**, Adreen Azman, Anas Kamarundzaman1, Muhammad I.M. Abdul Khudus, Azzuliani Supangat. (2018). *Controlling the growth mode of semi-polar (11-22) GaN epi-layers utilizing ammonia flux variation via MOCVD*. Paper presented at the International Workshop on Nitride Semiconductors (IWN2018), 11-16 November, Kanazawa, Japan.

3. **Omar, A. Z.**, Ahmad Shuhaimi, Azman Adreen, Kamarundzaman Anas. (2017). *Optimization of V/III ratio of semipolar GaN grown on m-sapphire by MOCVD*. Paper presented at the 4th Meeting of Malaysia Nitrides Research Group (MNRG), University Sains Malaysia, Penang, Malaysia.

4. **Omar, A. Z.**, Ahmad Shuhaimi, Adreen Azman, Anas Kamarundzaman, Ikram Taib, Norzaini Zainal Saadah rahaman. (2016). *Improvement of growth and properties of semipolar GaN using three-step approach on m-plane sapphire substrate via MOCVD*. Paper Presented at the National Physics Conference (PERFIK), Kuala Lumpur, Malaysia, (Awarded of Best Oral Presenter).

5. **Omar, A. Z.**, Ahmad Shuhaimi, Adreen Azman, Anas Kamarundzaman, Ikram Taib, Norzaini Zainal, Saadah Rahaman. (2015). *Optimization of semipolar GaN nucleation layer and buffer layer GaN grown on m-plane sapphire by MOCVD*. Paper Presented at the International Conference on Nitride Semiconductors (ICNS-11), Peking University, Beijing, China.